AD-A189 503 AN INTERDISCIPLINARY APPROACH TO PREDICTIVE MODELING OF STRUCTURAL ADHESI. (U) VIRGINIA TECH CENTER FOR ADHESION SCIENCE BLACKSBURG J A FILBEY ET AL. OCT 87 1/4

UNCLASSIFIED CAS/CHEM-87-7 N00014-82-K-0185 F/G 11/1 NL

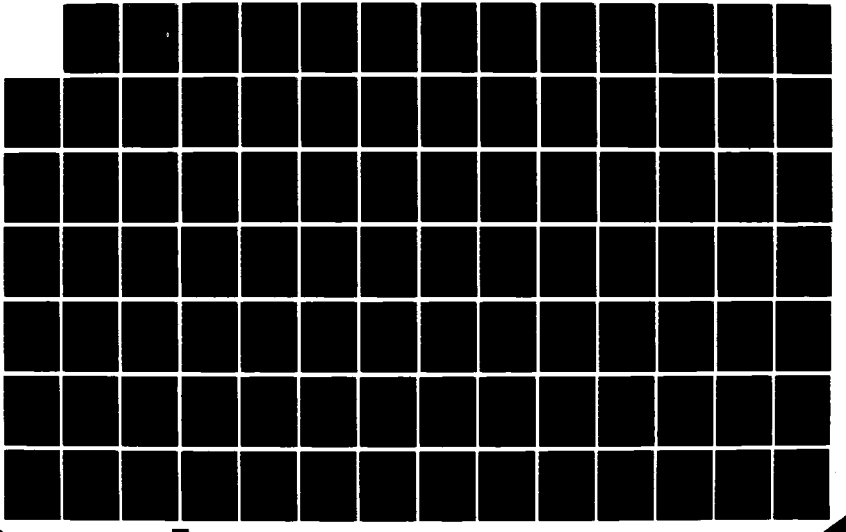

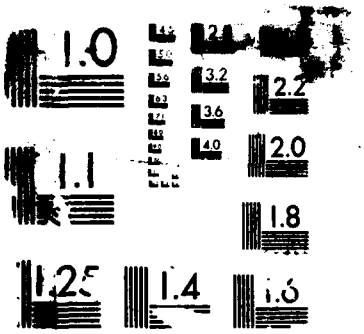

VIRGINIA TECH
CENTER FOR ADHESION SCIENCE

CAS/CHEM-87-7 OCTOBER 1987

SUMMARY REPORT

AN INTERDISCIPLINARY APPROACH TO PREDICTIVE MODELING OF STRUCTURAL ADHESIVE BONDING

FACTORS AFFECTING THE DURABILITY OF TITANIUM/EPOXY BONDS

by

J. A. Filbey
and
J. P. Wightman

Prepared under Contract No. N00014-82-K-0185
Dr. Larry H. Peebles, Jr., Project Monitor
Office of Naval Research
Code 431
800 N. Quincy Street
Arlington, VA 22217

VIRGINIA POLYTECHNIC INSTITUTE
AND STATE UNIVERSITY

216 NORRIS HALL
BLACKSBURG, VIRGINIA 24061

Telephone: (703) 961-6824
TLX: EZLINK 9103331861
VPI-BKS

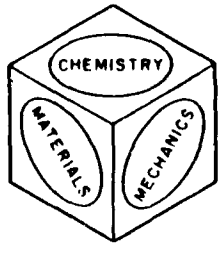

SECURITY CLASSIFICATION OF THIS PAGE

AD-A189 503

REPORT DOCUMENTATION PAGE

1a. REPORT SECURITY CLASSIFICATION Unclassified	1b. RESTRICTIVE MARKINGS
2a. SECURITY CLASSIFICATION AUTHORITY	3. DISTRIBUTION / AVAILABILITY OF REPORT
2b. DECLASSIFICATION / DOWNGRADING SCHEDULE	
4. PERFORMING ORGANIZATION REPORT NUMBER(S) CAS/CHEM-87-7	5. MONITORING ORGANIZATION REPORT NUMBER(S)
6a. NAME OF PERFORMING ORGANIZATION Virginia Polytechnic Institute and State University 6b. OFFICE SYMBOL (If applicable)	7a. NAME OF MONITORING ORGANIZATION
6c. ADDRESS (City, State, and ZIP Code) Center for Adhesion Science Department of Chemistry Blacksburg, VA 24061	7b. ADDRESS (City, State, and ZIP Code)
8a. NAME OF FUNDING / SPONSORING ORGANIZATION Office of Naval Research 8b. OFFICE SYMBOL (If applicable)	9. PROCUREMENT INSTRUMENT IDENTIFICATION NUMBER
8c. ADDRESS (City, State, and ZIP Code) 800 N. Quincy St. Arlington, VA 22217	10. SOURCE OF FUNDING NUMBERS PROGRAM ELEMENT NO. / PROJECT NO. / TASK NO. / WORK UNIT ACCESSION NO.

11. TITLE (Include Security Classification)
An Interdisciplinary Approach to Predicative Modeling of Structural Adhesive Bonding - Factors Affecting the Durability of Titanium/Epoxy Bonds

12. PERSONAL AUTHOR(S) Filbey, J. A. and Wightman, J. P.

13a. TYPE OF REPORT	13b. TIME COVERED FROM ____ TO ____	14. DATE OF REPORT (Year, Month, Day)	15. PAGE COUNT
		October, 1987	296

16. SUPPLEMENTARY NOTATION

17. COSATI CODES			18. SUBJECT TERMS (Continue on reverse if necessary and identify by block number)
FIELD	GROUP	SUB-GROUP	

19. ABSTRACT (Continue on reverse if necessary and identify by block number)

Factors influencing the durability of Ti-6-4/epoxy and Ti-6-4/metal alkoxide/epoxy interphases were studied by first determining chemical and physical properties of Ti-6-4 adherend surfaces; second by characterizing the strength and durability of Ti-6-4/epoxy bonds; and third by using aluminum and titanium alkoxides as possible adhesion promoters.

Ti-6-4 adherend surfaces were oxidized either by chemical etch or anodization. Four principal pretreatments were studied: chromic acid anodization (CAA), sodium hydroxide anodization (SHA), phosphate fluoride acid etch (P/F), and TURCO basic etch (TURCO). The oxides were characterized physically by SEM, STEM, profilometry, and contact angles; and chemically by XPS, AES, SIMS, and indicator dyes. The two anodically produced oxides were porous, with pore diameters of 40 to 50 nm, while P/F and TURCO pretreated adherends showed no porosity. Good reproducibility of oxide composition was seen by XPS. The acidity/basicity of the surfaces was found to be in order of increasing basicity CAA < P/F< TURCO< SHA

20. DISTRIBUTION / AVAILABILITY OF ABSTRACT ☒ UNCLASSIFIED/UNLIMITED ☐ SAME AS RPT. ☐ DTIC USERS	21. ABSTRACT SECURITY CLASSIFICATION
22a. NAME OF RESPONSIBLE INDIVIDUAL	22b. TELEPHONE (Include Area Code) / 22c. OFFICE SYMBOL

DD FORM 1473, 84 MAR 83 APR edition may be used until exhausted
All other editions are obsolete.

SECURITY CLASSIFICATION OF THIS PAGE

19. Abstract continued

All adhesive bonding was done with a structural epoxy, FM-300. Lap shear strengths showed no significant difference between pretreatments, reinforcing the opinion that the lap shear test is not surface sensitive. The stress durability and wedge test, however, showed vast differences in bond durability. The SHA and CAA pretreatments were equally durable in 80° C, 95% r.h. The TURCO pretreatment was slightly less durable than the P/F pretreatment which exhibited no durability in hot-wet environments. The characterization results point to the surface area of contact between the adhesive and adherend as the reason for variation in bond durability. CAA and SHA pretreated Ti-6-4 adherends were porous and thus possessed the highest surface area. TURCO was the roughest surface and therefore had a higher surface area than the smoother P/F surface.

Because the P/F surface was not durable, it was chosen as the substrate for testing the possible durability enhancement by titanium and aluminum alkoxide coatings. Sec-butyl aluminum alkoxide significantly enhanced the bond durability of the P/F pretreated bonds, while the titanium alkoxide primers showed no improvement in durability. The locus of failure and infrared studies indicate the enhancement in durability by the aluminum alkoxide was due to the high concentration of hydroxyl groups in the alkoxide available to interact with the titanium oxide and the epoxy.

SUMMARY REPORT

AN INTERDISCIPLINARY APPROACH TO PREDICTIVE MODELING OF STRUCTURAL ADHESIVE BONDING

FACTORS AFFECTING THE DURABILITY OF TITANIUM/EPOXY BONDS

BY

J. A. FILBEY AND J. P. WIGHTMAN

PREPARED FOR

OFFICE OF NAVAL RESEARCH
800 NORTH QUINCY STREET
ARLINGTON, VIRGINIA 22178

DR. L. H. PEEBLES, JR.

GRANT NO. N00014-82-K-0185 P00002

FROM

CENTER FOR ADHESION SCIENCE
VIRGINIA POLYTECHNIC INSTITUTE AND STATE UNIVERSITY
BLACKSBURG, VIRGINIA 24061

OCTOBER, 1987

FACTORS AFFECTING THE DURABILITY OF TITANIUM/EPOXY BONDS

(ABSTRACT)

Factors influencing the durability of Ti-6-4 / epoxy and Ti-6-4 / metal alkoxide / epoxy interphases were studied by first determining chemical and physical properties of Ti-6-4 adherend surfaces; second by characterizing the strength and durability of Ti-6-4 / epoxy bonds; and third by using aluminum and titanium alkoxides as possible adhesion promoters.

Ti-6-4 adherend surfaces were oxidized either by chemical etch or anodization. Four principal pretreatments were studied: chromic acid anodization (CAA), sodium hydroxide anodization (SHA), phosphate fluoride acid etch (P/F), and TURCO basic etch (TURCO). The oxides were characterized physically by SEM, STEM, profilometry, and contact angles; and chemically by XPS, AES, SIMS, and indicator dyes. The two anodically produced oxides were porous, with pore diameters of 40 to 50 nm, while P/F and TURCO pretreated adherends showed no porosity. Good reproducibility of oxide composition was seen by XPS. The acidity/basicity of the surfaces was found to be in order of increasing basicity CAA < P/F < TURCO < SHA.

All adhesive bonding was done with a structural epoxy, FM-300. Lap shear strengths showed no significant difference between pretreatments, reinforcing the opinion that the

lap shear test is not surface sensitive. The stress durability and wedge test, however, showed vast differences in bond durability. The SHA and CAA pretreatments were equally durable in 80° C, 95% r.h. The TURCO pretreatment was slightly less durable than the P/F pretreatment which exhibited no durability in hot-wet environments. The characterization results point to the surface area of contact between the adhesive and adherend as the reason for variation in bond durability. CAA and SHA pretreated Ti-6-4 adherends were porous and thus possessed the highest surface area. TURCO was the roughest surface and therefore had a higher surface area than the smoother P/F surface.

Because the P/F surface was not durable, it was chosen as the substrate for testing the possible durability enhancement by titanium and aluminum alkoxide coatings. Sec-butyl aluminum alkoxide significantly enhanced the bond durability of the P/F pretreated bonds, while the titanium alkoxide primers showed no improvement in durability. The locus of failure and infrared studies indicate the enhancement in durability by the aluminum alkoxide was due to the high concentration of hydroxyl groups in the alkoxide available to interact with the titanium oxide and the epoxy.

Table of Contents

	Page No.
Abstract	ii
Table of Contents	iv
List of Figures	ix
List of Tables	xv
I. Introduction	1
II. Literature Review	3
A. Titanium and its Oxides	3
1. Titanium	3
2. Titanium oxide	4
3. Pretreatments	9
B. Analysis Methods	11
1. Electron microscopy	11
a. SEM - Scanning Electron Microscopy	11
b. STEM - Scanning Transmission Electron Microscopy	15
2. XPS and AES - X-ray Photoelectron Spectroscopy and Auger Electron Spectroscopy	17
a. General description of technique	17
b. Instrumentation	19
c. Qualitative analysis	22
d. Quantitative analysis	31
e. Curve fitting	40
f. Angle dependent XPS	41
3. SIMS - Secondary Ion Mass Spectrometry	43
4. FTIR - Fourier Transform Infrared	47
a. Infrared phenomenon	47
b. Dispersive vs. Fourier transform	48
c. Techniques in infrared	52
d. External reflectance	54

e. Peak identification 56

C. Surface Energy of High Energy Surfaces 66

D. Acidity/Basicity of Solid Surfaces 73

E. Adhesive Bonding 80

1. General discussion 80
2. Roughness and pore penetration 84
3. Wedge test 85
4. Lap shear test 88
5. Stress durability test 89

F. Metal Alkoxides 89

1. Introduction 89
2. Alkoxides in adhesive bonding 92
3. Chemistry of alkoxides 93

G. EPON 828/DDS 96

III. Experimental 98

A. Materials 98

B. Sample Preparation 100

1. Pretreatments of Ti-6-4 100
2. Ferrotype plates 100
3. Polished Ti-6-4 101
4. Aluminum oxide preparation 101
5. Metal alkoxides 102
6. EPON828/DDS 103

C. Instrumental Techniques 104

1. SEM/STEM 104
2. XPS 105
3. AES 109
4. SIMS 109
5. FTIR 110

D. Roughness 110

E. Contamination 110

F. Surface Energy Determination 112

G. Indicator Dye Tests 114

H. Adhesive Bonding 115

1. FM-300 characterization 115
2. Pore penetration study 115
3. Lap shear test 116
4. Stress durability test 116
5. Wedge test 117

I. Statistical Analysis 118

IV. Results and Discussion 120

A. Part I - Physical and Chemical Properties of Ti-6-4 Oxides

1. Topography 120

a. Profilometry 120
b. SEM/STEM 120
c. Contamination 131

2. Surface energy 131

3. Acidity/basicity 134

4. Chemical composition 137

a. Oxide composition by XPS, AES, SIMS 137
b. Reproducibility of pretreatment 146
c. Stoichiometry by AES line shapes 150
d. Relative oxide thickness 155

5. Oxide thermal stability 158

B. Part II - Strength and Durability of Ti-6-4/ Epoxy Bonds

1. FM-300 characterization 164

2. Pore penetration study 166

3. Lap shear test 171
a. Lap shear strength 171
b. Locus of failure 172

4. Stress durability test 179

a. Time to failure 179
b. Locus of failure 181

5. Wedge test 183

a. Crack extension tests 183
b. Strain energy release rate, G_1 186
c. Locus of failure 189

6. Summary 191

C. Part III - Metal Alkoxides as Adhesion Promoters

1. Adhesive bonding 192

a. Wedge test 193
b. Stress durability test 200

2. Physical and chemical properties of the alkoxides 206

a. XPS 206

i. TNBT 206
ii. TIPT 208
iii. E-8385 210
iv. Model aluminum oxides 213
v. Angle dependent XPS studies - alkoxides 216

b. FTIR 221

i. TIPT 221
ii. TNBT 225
iii. E-8385 230

c. Acidity/basicity 238

3. Interaction of aluminum alkoxide with epoxy by FTIR 240

a. EPON 828 / DDS 240
b. EPON 828 / DDS on E-8385 254

V. Summary 257

VI. References 260

Appendix A 270
Appendix B 272
Appendix C 292
Appendix D 297

List of Figures

1 Electronic structure of the rutile crystalline form of TiO_2 [3].

2 Interatomic distances in anatase and rutile TiO_2 [11].

3 Oxygen 1s curve fit XPS peak of TiO_2 taken at 85° and 10° take-off angle [15].

4 Schematic drawing of SEM instrument [22].

5 Secondary electron detection system for a) SEM and b) STEM [28].

6 Schematic diagram of emission of an Auger electron from a solid [29].

7 Ti $L_{2,3}$,$M_{2,3}$,$M_{2,3}$ and $L_{2,3}$,$M_{2,3}$,V Auger line shapes for TiO, Ti_2O_3, and TiO_2 [33].

8 Molecular orbital energy diagram for titanium octahedrally coordinated to oxygen [35].

9 Titanium L_3 emission and absorption spectra for Ti, TiO, Ti_2O_3, and TiO_2 with peak labels corresponding to Figure 8 [34].

10 Schematic diagram of XPS spectrometer geometry used in angle dependent studies [37].

11 Ion bombardment-induced changes in the surface zone of the solid [49].

12 Stretch and bending modes of molecules interacting with infrared radiation [57].

13 Sadtler IR spectra of isopropyl alcohol, Titanium (4') salt, TIPT, (33830K), and of butyl titanate, TNBT, (15547K) [73,74].

14 Sadtler IR spectrum of 47948P, sec-butyl alcohol, aluminum salt, E-8385, [81].

15 Schematic diagram of the balance of forces when a liquid contacts a solid surface [128].

16 Schematic representation of water and oxide layers on a metal surface [99].

17 Series of sulphonephthalein indicator dyes [103].

18 Structural changes causing color changes in phenol red [103].

19 Adhesive fracture energy vs. bond line thickness for epoxy and rubber modified epoxy [110].

20 Basic loading modes [114].

21 Deformation of a lap shear joint when load is applied [118].

22 Shear stress in a lap shear joint [118].

23 Schematic diagram of grazing angle reflectance attachment used in all FTIR studies [129].

24 Schematic diagram of experimental set-up for interfacial contact angle measurements.

25 Profilometer tracings of (A) TURCO, (B) P/F, and (C) CAA pretreated Ti-6-4 coupons and (D) acid-cleaned glass slide.

26 SEM photomicrographs at 2000 x of CAA pretreated Ti-6-4.

27 SEM photomicrographs at 2000 x of SHA pretreated Ti-6-4.

28 SEM photomicrographs at 2000 x of P/F pretreated Ti-6-4.

29 SEM photomicrographs at 2000 x of TURCO pretreated Ti-6-4.

30 SEM stereophotomicrograph at 7800 x of SHA pretreated Ti-6-4.

31 SEM stereophotomicrograph at 7800 x of PSHA pretreated Ti-6-4.

32 STEM photomicrograph at 100,000 x of CAA pretreated Ti-6-4 surface.

33 STEM photomicrograph at 100,000 x of PSHA pretreated Ti-6-4 surface.

34 STEM photomicrograph at 100,000 x of SHA pretreated Ti-6-4 surface.

35 STEM photomicrograph at 50,000 x of P/F pretreated Ti-6-4 surface.

36 STEM photomicrograph at 50,000 x of TURCO pretreated Ti-6-4 surface.

37 AES elemental map of iron on a TURCO pretreated Ti-6-4 surface.

38 Graphical comparison of the titanium isotopic abundances of CAA pretreated Ti-6-4 sample for Ti^{+} and TiO^{+}.

39 CAA pretreated Ti-6-4 SIMS spectrum with an in-bleed of O_2.

40 CAA pretreated Ti-6-4 SIMS spectrum without an in-bleed of O_2.

41 AES narrow scan dN(E)/dE spectrum of the CAA pretreated Ti-6-4 surface.

42 Ti(LMM) and Ti(LMV) dN(E)/dE Auger spectra of Ti, TiO, and TiO_2 [34].

43 Narrow AES scan of CAA pretreated Ti-6-4.

44 Narrow AES scan of TiO_2 powder.

45 AES depth profile of CAA pretreated Ti-6-4 surface.

46 Ti 2p peak before and after heating P/F and TURCO pretreated Ti-6-4 surfaces.

47 STEM photomicrograph at 50,000 x of CAA pretreated Ti-6-4 after heating to 350° C for 10 min.

48 STEM photomicrograph at 50,000 x of PSHA pretreated Ti-6-4 after heating to 350° C for 10 min.

49 STEM photomicrograph at 50,000 x of P/F pretreated Ti-6-4 after heating to 350° C for 10 min.

50 STEM photomicrograph at 50,000 x of TURCO pretreated Ti-6-4 after heating to 350° C for 10 min.

51 STEM photomicrograph at 50,000 x of MFS of CAA pretreated Ti-6-4 foil peeled from FM-300.

52 STEM photomicrograph at 50,000 x of AFS of FM-300 peeled from CAA pretreated Ti-6-4 foil.

53 AES depth profile of AFS of FM-300 peeled from CAA pretreated Ti-6-4 foil.

54 SEM photomicrograph at 940 x of AFS from CAA pretreated Ti-6-4 lap shear bond.

55 SEM photomicrograph at 940 x of MFS from CAA pretreated Ti-6-4 lap shear bond.

56 Schematic representation of locus of failure for CAA pretreated Ti-6-4 lap shear bonded with FM-300.

57 SEM photomicrograph at 1000 x of AFS from P/F pretreated Ti-6-4 lap shear bond.

58 SEM photomicrograph at 1000 x of MFS from P/F pretreated Ti-6-4 lap shear bond.

59 SEM photomicrograph at 3200 x of AFS from TURCO pretreated Ti-6-4 lap shear bond.

60 SEM photomicrograph at 3200 x of MFS from TURCO pretreated Ti-6-4 lap shear bond.

61 Schematic representation of locus of failure for P/F and TURCO pretreated Ti-6-4 lap shear samples bonded with FM-300.

62 Time to failure windows from the stress-durability test at 80° C, 95% r.h.

63 Rate of crack extension vs. time for P/F samples in 95° C water.

64 Crack extension vs. time for P/F pretreated wedge samples bonded with FM-300 and immersed in basic buffer at pH = 11.8, and 80° C.

65 Crack extension vs. time for CAA and TURCO pretreated wedge samples bonded with FM-300 and immersed in acidic buffer at pH = 2, and 80° C.

66 Crack extension vs. time for P/F pretreated wedge samples coated with one and five coats of TNBT or E-8385, bonded with FM-300 and immersed in 95° C water.

67 Rate of crack growth vs. time for P/F pretreated wedge samples coated with five coats of E-8385, bonded with FM-300 and immersed in 95° C water.

68 Crack extension vs. time for P/F pretreated wedge samples coated with five coats of TNBT and TIPT, bonded with FM-300 and exposed to 80° C, 95% r.h.

69 Crack extension vs. time for P/F pretreated wedge samples coated with five coats of E-8385, bonded with FM-300 and exposed to 80° C, 95% r.h.

70 Time to failure windows for stress-durability test at 80° C, 95% r.h.

71 SEM photomicrograph at 1600 x of E-8385 film spun coat from a 2 wt% solution onto a ferrotype plate.

72 Theoretical curve with data from angle dependent XPS study on E-8385 film spun coat from a 1 wt% solution in toluene.

73 Grazing angle FTIR spectra from 4600 to 1200 cm^{-1} of TIPT on ferrotype plates, cured at 25° and 300° C.

74 Grazing angle FTIR spectra from 1200 to 400 cm^{-1} of TIPT on ferrotype plates, cured at 25° and 300° C.

75 Grazing angle FTIR spectra from 4600 to 1200 cm^{-1} of TNBT on ferrotype plates, cured at 25° and 300° C.

76 Grazing angle FTIR spectra from 1200 to 400 cm^{-1} of TNBT on ferrotype plates, cured at 25° and 300° C.

77 Transmission FTIR spectrum of neat TNBT between KBr crystals.

78 Transmission FTIR spectrum of neat E-8385 between KBr crystals.

79 Grazing angle FTIR spectra from 4600 to 1200 cm^{-1} of E-8385 from dry toluene on ferrotype plates, cured at 25° and 300° C.

80 Grazing angle FTIR spectra from 1200 to 400 cm^{-1} of E-8385 from dry toluene on ferrotype plates, cured at 25° and 300° C.

81 Grazing angle FTIR spectra from 4600 to 1200 cm^{-1} of E-8385 from wet toluene on ferrotype plates, cured at 25° and 300° C.

82 Grazing angle FTIR spectra from 1200 to 400 cm^{-1} of E-8385 from wet toluene on ferrotype plates, cured at 25° and 300° C.

83 Grazing angle FTIR spectrum of EPON 828 film on ferrotype plates.

84 Grazing angle FTIR spectrum of DDS film on ferrotype plates.

85 Grazing angle FTIR spectrum of uncured EPON 828 / DDS film on ferrotype plates.

86 Grazing angle FTIR spectrum of cured EPON 828 / DDS film on ferrotype plates.

87 Transmission FTIR spectrum of EPON 828 / DDS free-standing film.

88 Grazing angle FTIR spectrum of cured EPON 828/DDS film on polished Ti-6-4 plates.

89 Grazing angle FTIR spectrum of cured EPON 828/DDS film on 1 wt% E-8385 on polished Ti-6-4.

90 Grazing angle FTIR spectrum of cured EPON 828/DDS film on 1 wt% E-8385 on ferrotype plates.

Appendix C

C1. Representative spectra of C 1s, O 1s and Ti 2p peaks from a CAA pretreated surface.

C2. Representative spectra of C 1s, O 1s and Ti 2p peaks from a P/F pretreated surface.

C3. Representative spectra of C 1s, O 1s and Ti 2p peaks from a TURCO pretreated surface.

C4. Representative spectra of C 1s, O 1s and Ti 2p peaks from a SHA pretreated surface.

C5. Representative spectra of C 1s, O 1s and Ti 2p peaks from a PSHA pretreated surface.

List of Tables

I. Spectroscopic notation in XPS and AES for levels n = 1 - 3 [29].

II. Area ratios of XPS peaks [29].

III. IR peak positions in TIPT and TNBT spectra [73-76].

IV. IR peak positions in E-8385 spectrum [81].

V. IR peak positions and assignments for DGEBA [85-87].

VI. Specifications for Ti-6Al-4V.

VII. XPS analysis of polydimethyl siloxane standard.

VIII. XPS analysis of TiO_2 powder.

IX. Roughness measurement by profilometry of Ti-6-4 foil and lap shear coupon surfaces.

X. Dispersive and polar components of the surface energy of pretreated Ti-6-4, using the geometric mean (gm) and harmonic mean (hm).

XI. Calculated work of adhesion of Ti-6-4/epoxy bonds in air, W_A, and in water, W_{Aw}.

XII. Indicator dye test results.

XIII. AES wide scan elements and kinetic energies (K.E.) for CAA, P/F, TURCO, SHA, and PSHA pretreated Ti-6-4.

XIV. Oxygen to titanium ratios from peak heights at 512 ev and 382 ev.

XV. Isotopic abundance of titanium from dynamic SIMS spectra for CAA, TURCO, and P/F pretreated surfaces.

XVI. Chemical reproducibility of CAA, P/F, and TURCO pretreated Ti-6-4.

XVII. AES depth profile - Average Time to reach Ti-O signal intersection.

XVIII. XPS analysis of FM-300U epoxy film and protective cover sheets.

XIX. XPS analysis of MFS and AFS from pore penetration experiment.

XX. XPS analysis of stress durability failure surfaces of P/F bonded with FM-300U.

XXI. XPS analysis of stress durability failure surfaces of TURCO bonded with FM-300U.

XXII. XPS analysis of P/F pretreated wedge test failure surfaces bonded with FM-300U.

XXIII. XPS analysis of wedge test failure surfaces of P/F pretreated Ti-6-4 coated with alkoxides.

XXIV. XPS analysis for locus of failure of P/F pretreated wedge sample coated with TNBT.

XXV. XPS analysis for locus of failure of P/F primed with E-8385 exposed to 80° C, 95% r.h.

XXVI. XPS analysis of TNBT film on ferrotype plates.

XXVII. XPS analysis of TIPT film on ferrotype plates.

XXVIII. XPS analysis of E-8385 films from dry toluene brushed on ferrotype plates.

XXIX. XPS analysis of E-8385 films from wet toluene brushed on ferrotype plates.

XXX. XPS analysis of E-8385 films spun coat onto ferrotype plates.

XXXI. XPS analysis of model aluminum oxides.

XXXII. Calculated thickness and patchiness of alkoxide films on ferrotype plates.

XXXIII. Grazing angle FTIR peak positions and assignments for TIPT films on ferrotype plates.

XXXIV. Grazing angle and transmission FTIR peak positions and assignments for TNBT films on ferrotype plates and neat TNBT between KBr crystals.

XXXV. Transmission FTIR peak positions and assignments for neat E-8385 between KBr crystals.

XXXVI. Grazing angle FTIR peak positions and assignments for E-8385 films on ferrotype plates.

XXXVII. Results from Indicator Dye Test on E-8385 films

XXXVIII. Grazing angle FTIR peak positions and assignments for EPON 828 films on ferrotype plates.

XXXIX. Grazing angle FTIR peak positions and assignments for DDS films on ferrotype plates.

XL. Grazing angle FTIR peak positions and assignments for uncured EPON 828 / DDS films on ferrotype plates.

XLI. Grazing angle FTIR peak positions and assignments for cured EPON 828 / DDS films on ferrotype plates.

XLII. Transmission FTIR peak positions and assignments for EPON 828 / DDS free standing film.

Appendix B

BI. XPS analysis of CAA pretreated Ti-6-4.

BII. XPS analysis of P/F pretreated Ti-6-4.

BIII. XPS analysis of TURCO pretreated Ti-6-4.

BIV. XPS analysis of SHA pretreated Ti-6-4.

BV. XPS analysis of PSHA pretreated Ti-6-4.

BVI. SIMS results for CAA pretreated Ti-6-4.

BVII. SIMS results for P/F pretreated Ti-6-4.

BVIII. SIMS results for TURCO pretreated Ti-6-4.

BIX. SIMS results for SHA pretreated Ti-6-4.

BX. SIMS results for PSHA pretreated Ti-6-4.

BXI. SIMS results for TiO_2 powder.

BXII. XPS analysis of heating study of CAA pretreated Ti-6-4.

BXIII. XPS analysis of heating study of PSHA pretreated Ti-6-4.

BXIV. XPS analysis of heating study of P/F pretreated Ti-6-4.

BXV. XPS analysis of heating study of TURCO pretreated Ti-6-4.

BXVI. XPS analysis of lap shear failure surfaces of CAA, P/F, TURCO, and water soaked CAA bonded with FM-300U.

I. Introduction

In an adhesive bond, dissimilar materials are brought together to form an interface. Several molecular layers in one material will be influenced by the presence of the other material. Understanding the chemistry and physical structure of the interface region or "interphase" is vital in understanding the interaction between the materials.

The chemistry and topography of a metal adherend surface is primarily determined by the method of preparing the surface prior to bonding. The pretreatment will affect the surface chemical composition, roughness, acidity/basicity, surface energy, and oxide thickness. The chemical composition of the polymeric adhesive will dictate the mobility of the polymer chains during bonding and thus the ability of functional groups to interact with the metal surface. The addition of an alkoxide primer to the metal adherend surface will provide a new chemistry to interact with the adhesive while usually masking the topography of the metal surface.

The interactions occurring at the interface will ultimately determine the performance of the adhesive bond. In load bearing adhesive bonds exposed to heat and humidity, good durability is imperative for continued integrity of the structure. One of the primary goals in adhesion science

today is to predict real world performance from modeling studies of adhesively bonded samples. To effectively model, however, the parameters affecting the system must first be established.

The purpose of this study is to determine the factors which affect the hot-wet durability of Ti-6Al-4V / epoxy bonds. First, physical and chemical properties of different Ti-6-4 oxide surfaces were studied. Next, the hydrothermal durability of Ti-6-4 / epoxy bonds was determined. Finally, the use of metal alkoxide primers for enhancement of bond durability was investigated by both adhesive bonding and alkoxide surface characterization studies.

II. Literature Review

A. Titanium and its Oxides

1. Titanium

Titanium makes up 0.6% of the earth's crust in the form of ilmenite, $FeTiO_3$, and rutile, TiO_2. The Kroll process is necessary to extract the titanium from these ores. Here, the ilmenite or rutile is treated at red heat with carbon and chlorine forming $TiCl_4$, which is then reduced with magnesium at 800° C in an argon atmosphere. Upon removal of the magnesium and magnesium chloride at 1000° C, a spongy mass of titanium remains [3].

Titanium has a high strength to weight ratio, a high melting point of 1668° C, and good corrosion resistance. The α-phase is hexagonal close packed, while the ß-phase is body centered cubic and forms above 882.5° C. α-phase alloys possess high strength and toughness and are resistant to oxygen contamination, but show poor forming characteristics. ß-phase alloys are more easily formed, show good hot and cold strength, but are more susceptible to atmospheric contamination and have a lower strength to weight ratio due to their higher density.

Ti-6Al-4V is an α-ß alloy with Al stabilizing the α-phase, raising the α -> ß transition temperature and V stabilizing the ß-phase, raising the ß -> α transition temp-

erature. α-ß alloys show good formability and good cold and hot strength [4] making them excellent materials for high performance structures.

2. Titanium oxide

Titanium has an outer electronic structure of $3d^2 4s^2$. Because the energy required to remove four electrons is so high, Ti^{4+} ion does not exist in compounds, making Ti(IV) compounds covalent [3]. The ionic radius of Ti^{4+} is 0.68 Å with the octahedral covalent radius of Ti(IV) equal to 1.36 Å [5].

Rutile is one of three titanium oxide forms and is pictured in Figure 1 [3]. Each Ti^{4+} ion is surrounded by six oxygen anions, arranged in a distorted octahedron with each oxygen anion surrounded by three Ti^{4+} ions [6-9]. Anatase and brookite are the other two titanium dioxide crystalline forms. The number of edges shared by the octahedra is two for rutile, three for brookite, and four for anatase, while the number of corners shared is six, five and four for rutile, brookite and anatase, respectively [6,9,10]. Figure 2 shows the lattice separation distance for rutile and anatase [11]. Not all titanium oxides are crystalline. The amorphous TiO_2 films are made of microcrystallites with anatase-like or rutile-like $Ti-O_6$ octahedral configurations [12].

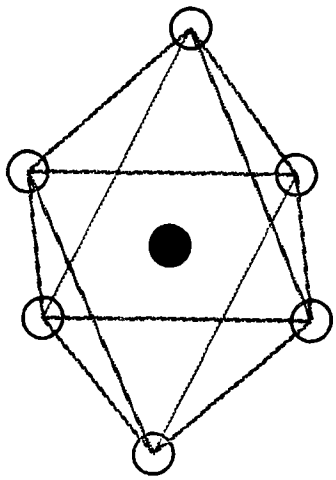

Figure 1. Electronic structure of the rutile crystalline form of TiO_2; small circle — titanium cations, large circles — oxygen anions [3].

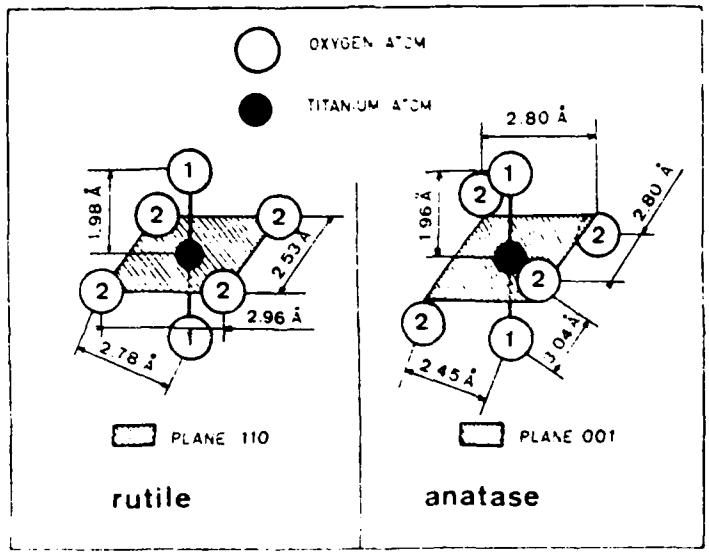

Figure 2. Interatomic distances in anatase and rutile TiO_2 [11].

While pretreated titanium surfaces are composed primarily of amorphous oxides, knowledge of the surface chemistry of crystalline titanium dioxide may provide insight into the nature of the pretreated surfaces.

Anatase and rutile have two types of hydroxyl groups on the surface. There is a basic Ti-OH group when the -OH is bound to one Ti^{4+} site, making it a terminal -OH. Here the sixth position of the octahedral coordination of the surface Ti^{4+} ion is filled by the -OH, with the other five positions occupied by lattice oxygens. When a hydroxyl group is bound to two Ti^{4+} sites in a tetrahedral coordination of the surface forming a bridged hydroxyl, the cations polarize the -OH group, making it more acidic [13-15].

Titanium dioxides have been well characterized by many techniques, two of which will be briefly discussed here - x-ray photoelectron spectroscopy, XPS and infrared spectroscopy, IR. In addition to the oxygen in the titanium oxide lattice, titanium oxide surfaces possess both acidic and basic hydroxyl groups. Sham and Lazarus [15] show an O 1s XPS peak with the oxygen's three components clearly resolved and labeled as shown in Figure 3. Comparing a titanium dioxide standard to an oxidized titanium electrode surface, Armstrong and Quinn [20] found the binding energy difference between O 1s and Ti 2p3 to be 71.5 eV for TiO_2.

Different types of hydroxyl groups on the surface of

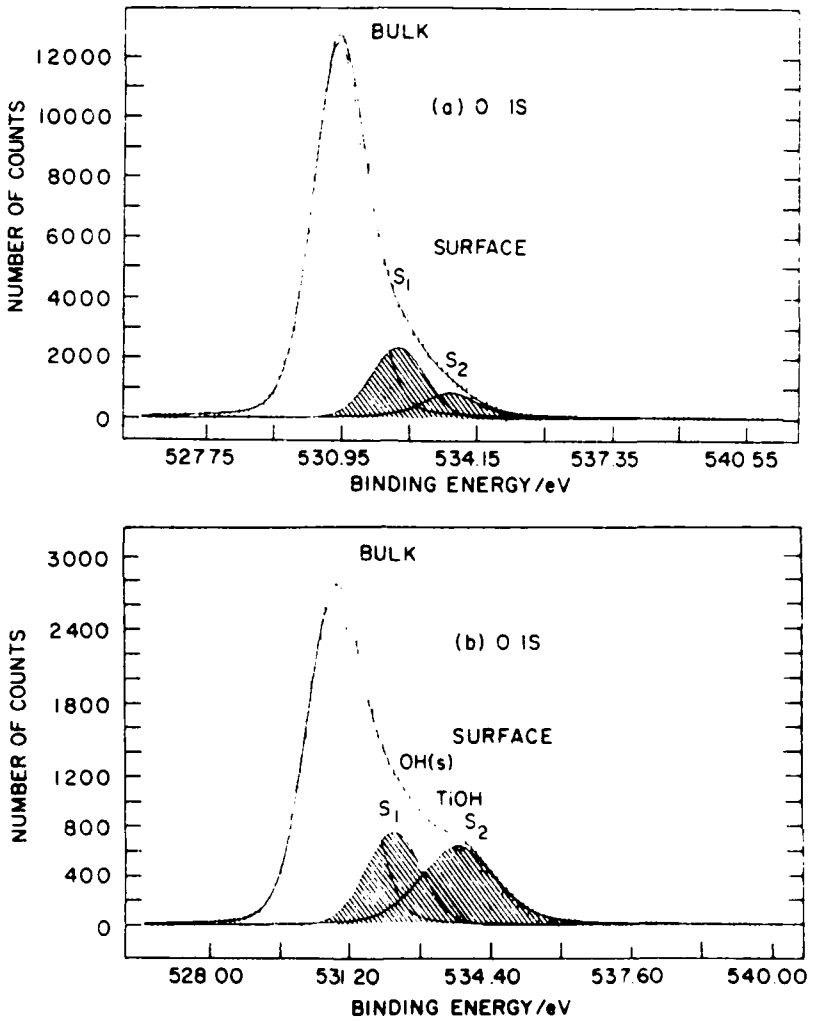

Figure 3. Oxygen 1s curve fit XPS peak of TiO_2 taken at 85° and 10° take-off angle [15].

titanium dioxides also absorb different frequencies of infrared radiation. When position 1 in Figure 2 is replaced by an -OH group and is isolated from other -OH groups, the stretching frequency occurs at 3715 cm^{-1} for anatase and at 3685 cm^{-1} for rutile. However, when hydroxyl groups occupy adjacent positions, the stretching frequency decreases to 3665 cm^{-1} for anatase and 3410 cm^{-1} for rutile due to hydrogen bonding [11]. Molecular water will also be present on hydroxylated titanium surfaces indicated by the presence of a bending vibration at 1625 cm^{-1} [14].

In air, titanium always is covered by a native oxide. This oxide can be modified by chemical or electrochemical pretreatment to produce a reproducible surface for adhesive bonding.

3. Titanium pretreatments

In preparing surfaces for adhesive bonding, a reproducible, durable oxide is desired. Typically titanium and its alloys are etched or abraded in acidic or basic media or anodized in acidic or basic electrolytes prior to adhesive bonding. Martin Marietta, AARADCOM, and NADC [16-18] have classified eight pretreatments of Ti-6-4 into three categories depending upon their performance when bonded and placed in a 60° C, 95% r.h. environment.

Representative pretreatments from each of the above

three categories chosen for this study in decreasing order of durability were chromic acid anodization (CAA), TURCO basic etch (TURCO), and phosphate/fluoride acidic etch (P/F). Anodization in a basic solution of sodium hydroxide (SHA) was also chosen for study due to its reported comparable, if not better, durability to the CAA in 50° C, 96% r.h. and the environmental benefits of no heavy metals, such as chromium in the anodization bath [19]. The optimum conditions for SHA chosen from Kennedy et al. [19] were 10 V, 30 min, at 20° C in 5M NaOH.

The mechanism of anodic oxidation of titanium has been studied. Kover and Musselin [8] showed by ^{18}O labeling studies that the primary mechanism by which an anodic oxide layer is formed is by metal cation migration through a stationary oxygen sublattice, with water as the main oxidizing agent. The growth of the film will be in a plane parallel to the electrode (or sample) surface and is rate limited by the applied voltage [20].

The mechanism of pore formation of the anodized surfaces is less clear, but is believed to be initiated by a preferential dissolution which is then subjected to localized heating due to its thinner interface. In the CAA pretreatment, HF serves as the activator for dissolution [21].

B. Analysis Methods

1. Electron microscopy

a. Scanning electron microscopy, SEM

SEM allows one to "see" what a surface looks like at the micrometer or nanometer level. Commonly used in adhesive bonding studies, SEM can be used to analyze post-failure surfaces and also to characterize surfaces prior to bonding. SEM provides excellent resolution and depth of field.

A rastered electron beam, typically from 2 to 30 kV, impinges on the sample, causing secondary electrons, back-scattered electrons, x-rays, and Auger electrons to be emitted. The secondary electrons can be detected and displayed as an image on a CRT (cathode ray tube) screen.

The basic components of a SEM are the vacuum system, lenses, electron gun, electron collector, CRT and associated electronics. Figure 4 [22] schematically illustrates the SEM instrument design. The electron beam is typically created from a tungsten filament cathode by thermionic emission. The electrons are accelerated by a grid cap, negatively biased with respect to the cathode, causing the electrons to converge at a crossover point. The condenser and objective lenses demagnify the electron image formed at the crossover (approx. 25 - 100 μm) to a probe size ranging from 5 nm to 1 μm. The condenser lens controls the beam

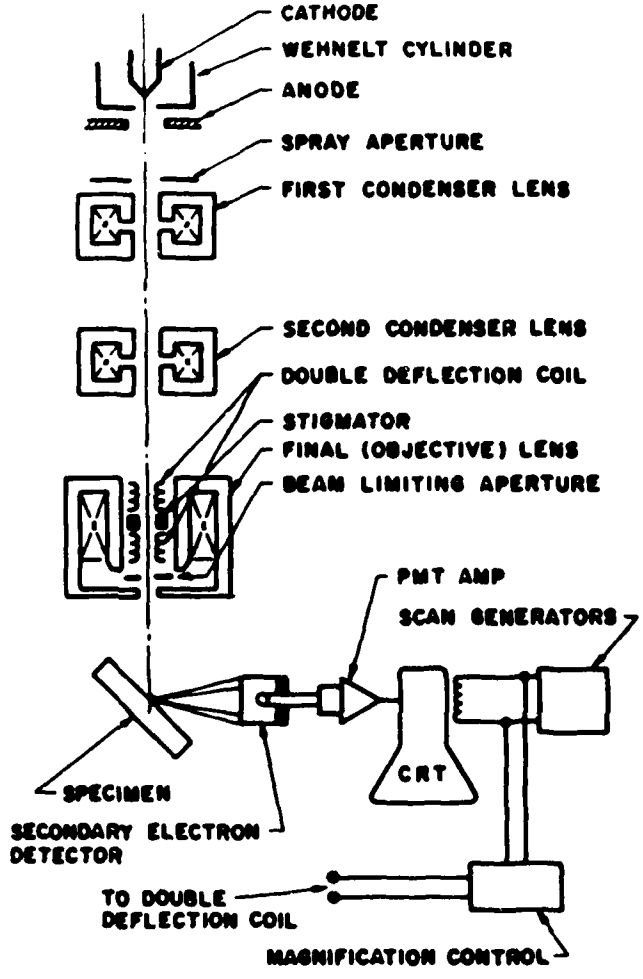

Figure 4. Schematic drawing of SEM instrument [22].

current, while the objective lens determines the final spot size. The electromagnetic lenses control the electron beam with an electromagnetic field. The depth of field is also controlled by the objective lens; however, the depth of field increases at the expense of resolution [23]. Once the electron beam hits the sample, a large number of interactions occur, with ejection of secondary electrons of interest in SEM. Secondary electrons are ejected from the top 5 to 10 nm of the surface with energies < 50 eV [24].

To form an image, a scanning system, signal detectors, amplifiers and CRT are needed. The scanning system, driven by a scan generator, consists of electromagnetic scanning coils which deflect the beam systematically . The CRT is scanned synchronously with the sample so that for each position on the sample, there is a unique position on the CRT. A detector will produce a signal from the secondary electrons emitted from each point on the sample. The amplified signal causes a point of particular brightness on the CRT. The detector consists of a scintillator which emits light when struck by high energy electrons. The light is internally reflected down a light pipe to a photomultiplier which serves to amplify the signal sent to the CRT. To detect low energy secondary electrons, the detector must be biased to accelerate the secondary electrons to the detector. The magnification of the resulting image is

simply a ratio of the area scanned on the CRT to the area scanned on the sample [25].

While single SEM photomicrographs yield some perception of depth, a three dimensional view is sometimes necessary for a truer picture of the surface topography. Depth can be perceived in SEM photomicrographs using a stereoscopic technique where two photographs are taken at different angles. The change in angle will change slightly the horizontal location of a corresponding image point in the two images creating parallax. Because the right eye sees more of the right sides of things than left sides and vice versa, the parallax between the two images will be interpreted as depth. Parallax, p, in a pair of photographs depends on the angle between the two photos, $\phi/2$, the magnification, m, and sample thickness or roughness, t, as shown by equation (1).

$$p = 2mt\ (\sin \phi/2) \qquad (1)$$

Generally, p should be equal to one-twentieth of the width of the photomicrograph or 6.5 mm for a 13 cm wide photograph. Thus, for a magnification of 9000 x, an approximate roughness of 3 μm, with a 7° tilt, the parallax is 6.6 mm [26].

Equation (1) simply provides a guide by which to begin stereomicroscopy. Typically, the angular separation of the two photomicrographs is between 5° and 10° [27]. When

viewing the two photos, the right eye should look at the right photo while the left eye looks at the left photo. Stereoglasses usually aid in viewing stereophotomicrographs [26].

b. Scanning transmission electron microscopy, STEM

A scanning transmission electron microscope has both SEM and TEM (transmission electron microscope) capabilities. The advantage of the STEM, run in the SEM mode, over the SEM is the enhanced resolution gained by the higher performance TEM lens system. Instead of a simple acceleration of the secondary electrons to the detector, as in SEM, the secondary electrons in the STEM travel a torical path through the lenses to the secondary electron detector, yielding better resolved photomicrographs and thus higher attainable magnifications. Figure 5 [28] illustrates the different placement of the detectors in SEM and STEM.

While SEM and STEM give a physical picture of a sample, a chemical picture is also necessary.

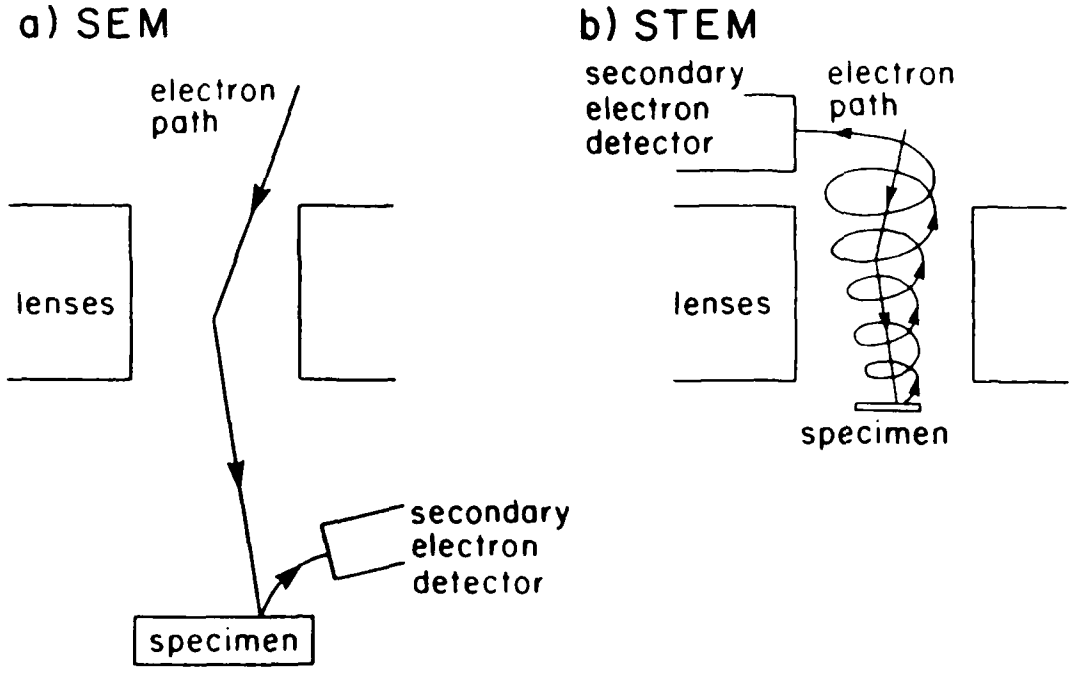

Figure 5. Secondary electron detection system for a) SEM and b) STEM [28]

2. X-ray photoelectron spectroscopy, XPS and Auger electron spectroscopy, AES

a. General description of techniques

X-ray photoelectron spectroscopy, or XPS, gives the elemental composition of approximately the top 5 nm of a sample's surface. X-rays of a characteristic energy impinge on the sample causing photoelectrons to be ejected and detected. The energy of a photoelectron is characteristic of a specific level of a particular atom, allowing for qualitative analysis of a surface.

Auger electron spectroscopy, AES, also provides elemental information of the top 5 nm of the surface. Here, an electron beam, typically 2 to 3 kV, impinges on the surface causing electrons to be ejected from a particular subshell. These ejections cause holes into which electrons from higher subshells fall releasing energy which can be used to eject Auger electrons which are then analyzed and detected. Figure 6 from reference [29] represents the three stages in the Auger process. The electron beam energy must be at least five times greater than the kinetic energy of the ejected electron for sufficient ionization to occur. In addition to Auger electrons, x-ray fluorescence can also occur; however, the Auger process is favored over the x-ray fluorescence for all elements below atomic number 35.

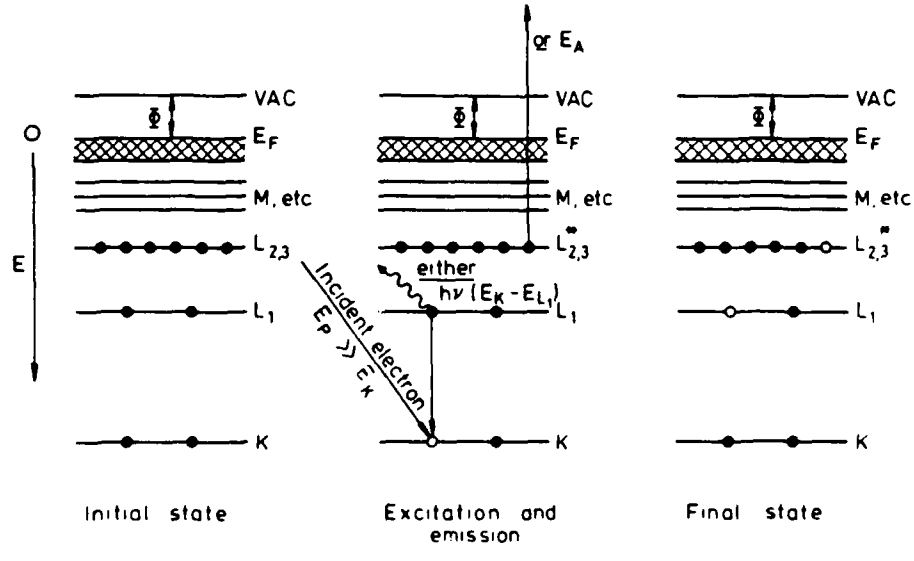

Figure 6. Schematic diagram of emission of an Auger electron from a solid [29].

b. **Instrumentation [29]**

A system used for XPS or AES must be under vacuum, contain a sample entry mechanism to maintain that vacuum, an x-ray or electron source, an energy analyzer, and a detector. Many of these components are computer controlled, allowing data to be stored and massaged.

A vacuum is necessary for two basic reasons. First, an ejected photoelectron or Auger electron needs to reach the energy analyzer without inelastically colliding with gas molecules. Secondly, if atomically clean surfaces are being studied, a high vacuum is necessary to keep the surfaces from adsorbing contaminants. For example, at a pressure of 10^{-6} torr, a monolayer of gas with a sticking coefficient of one, will adsorb on a surface in 1.5 seconds. There are various types of vacuum pumps which can produce system pressures $\leq 10^{-9}$ torr, provided the system can be "baked out". Bake-out at temperatures of approximately 300° C, allows adsorbed gases, such as water, on the walls of the vessel to be desorbed and pumped away.

There are three common types of vacuum pumps. Diffusion pumps require oil with vapor pressures $< 10^{-9}$ torr, with resistance to degradation and with low creep. Typically, poly phenyl ethers are used. Liquid nitrogen is necessary to cool the traps of the pump to prevent backstreaming of the oil. Turbo molecular pumps can pump any

gas, but are not as efficient with low molecular weight gases; however, no cooling is necessary. Titanium sublimation pumps are usually used to achieve the last order of magnitude in pressure, for example from 10^{-9} torr to 10^{-10} torr. Such pumps operate by reacting residual gases with elemental titanium.

Typical x-ray sources used in XPS spectrometers are magnesium and aluminum because of their narrow line widths and energies convenient for the study of core electrons. An electron beam with an energy about an order of magnitude higher than the x-ray energy is needed to efficiently produce the x-ray flux. Best results are achieved when the x-ray source is as close to the sample as possible. Electron guns, either the more common thermionic or field emission, are the usual sources for AES. The energy analyzer is the workhorse of the spectrometer, separating the energies or velocities of the photoelectrons ejected from the surface. Two analyzers are typically used - the concentric hemispherical analyzer (CHA), commonly used for XPS, and the cylindrical mirror analyzer (CMA), usually used in AES. Both analyzers are dispersive, deflecting the electron energies by an electrostatic field so that only energies of a narrow range are measured. The CHA is preferred for XPS as it "maintains adequate luminosity" [29] at high energy resolution. Because of the narrow acceptance angle, angle

dependent studies are possible with the CHA but not with the CMA which possesses a large acceptance angle.

Two retarding modes can be used by the CHA - fixed retarding ratio, FRR, or fixed analyzer transmission, FAT. In the FRR mode, electrons are decelerated from their initial energy by a constant ratio, thus operating at a constant relative energy resolution. The FAT mode decelerates electrons to a constant pass energy, operating at constant absolute resolution. The absolute resolution makes quantitation easier; however, the signal to noise at low kinetic energy or high binding energy is higher than in the FRR mode.

The CMA is generally used in Auger electron spectroscopy, due to its high transmission at only moderate energy resolution. Because the line widths of Auger transitions are usually wider than XPS linewidths, the moderate energy resolution does not pose a problem.

When depth profiling is needed, an ion gun is used to remove atomic layers from the sample's surface. Ion guns are electrostatic devices where rare gas ions, Ar^+, for example, are generated by collisional excitation with electrons from a hot filament. The Ar^+ ions are then accelerated to 0.5 to 5 KeV and focused on the sample with a beam width of 1 to 5 mm in diameter. The ion beam must raster the entire sample for XPS analysis, often making depth profiling

by XPS inefficient. Depth profiling is more commonly used with AES where a small rastered area creates a crater with a flat bottom for accurate AES analysis by an electron beam, which is narrower than the ion beam.

c. Qualitative analysis

The notation for the Auger transitions and the XPS photopeaks is different. Table I lists the quantum numbers, the x-ray suffix and level, and the spectroscopic level for n = 1 to 3 [29]. XPS peaks are described by the last column, whereas Auger peaks are described by the three x-ray levels involved in the transition. For example, if a 1s electron was ejected, a 2s electron dropped down to fill the hole causing a 2p electron to be ejected and detected, this Auger transition would be designated as $KL_1L_{2,3}$.

The elemental identity of the XPS photopeaks is obtained from their energy. The kinetic energy, KE, of the ejected photoelectron is a function of the incident x-ray energy, hw, the binding energy of the photoelectron, BE, and the work function, Φ.

$$KE = hw - BE - \Phi \qquad (2)$$

The work function term is a "catch-all" value which depends on the sample and the spectrometer. Equation 2 is valid if the photoemission is elastic, that is no energy is lost or gained between ejection and detection [29].

The binding energies for the various levels of most elements are well known and published [30]. The binding energy of an electron from a particular level will shift depending upon its environment, increasing with increasing formal oxidation number or for equal oxidation numbers, increasing as the electronegativity of the neighboring groups increases. This shift in binding energies allows bonding and elemental information to be obtained [29].

In order to properly determine the binding energy shifts, the spectra need to be calibrated. Typically either a metal, such as gold, is evaporated onto the sample and the binding energy of the 4f7 peak is assigned to 84 eV or the hydrocarbon contamination is assigned to a C 1s peak at 285 eV [31]. For carbon containing contamination of less than one monolayer, the binding energy may shift, causing variability in the calibration [32]. However, for samples analyzed in this study, a contamination layer of at least a monolayer is expected.

For subshells greater than s, that is for quantum level, l, greater than zero, doublet photopeaks occur due to spin-orbital j-j coupling. Two possible states are characterized by the quantum number $j = l + s$. The difference in energy states, E_j, arises from the parallel and antiparallel nature of the spin and orbital angular momentum. The magnitude of the energy separation is proportional to the spin-

orbit coupling. As the atomic number, z, increases for a given subshell, E_j increases. For a constant n, as l decreases, E_j increases. That is, a 3p doublet will be more widely separated than a 3d doublet. The area ratio of the doublets also changes with subshell and j value as shown in Table II [29].

In AES, elemental identity is also obtained from the measured energy of the Auger electrons. The kinetic energy of the Auger electron, $E_{Asc}(z)$, can be approximated as a function of the binding energies of each level, $E_i(z)$, and the binding energies of the same level of the next element on the periodic table, $E_i(z+1)$.

$$E_{ABC}(z) = E_A(z) - \tfrac{1}{2}[E_B(z) + E_B(z+1)] - \tfrac{1}{2}[E_C(z) + E_C(z+1)] \quad (3)$$

Auger electron peaks positions and intensities in the undifferentiated display are not as clearly defined as XPS peaks. Also, at the low kinetic energy end of an undifferentiated Auger spectrum, there is a broad background peak due to secondary electrons. For these reasons, Auger spectra are usually differentiated to clearly define the weak features of the spectra and to remove the background. By convention, the energy position of the Auger peak is measured at the "minimum in the high energy negative excursion" [29]. The Auger energies are more easily

TABLE I

Spectroscopic notation in XPS and AES for levels n = 1 - 3

Quantum No. n	l	j	X-ray Suffix	X-ray Level	Spectroscopic Level
1	0	1/2	1	K	1 s 1
2	0	1/2	1	L_1	2 s 1
2	1	1/2	2	L_2	2 p 1
2	1	3/2	3	L_3	2 p 3
3	0	1/2	1	M_1	3 s 1
3	1	1/2	2	M_2	3 p 1
3	1	3/2	3	M_3	3 p 3
3	2	3/2	4	M_4	3 d 3
3	2	5/2	5	M_5	3 d 5

TABLE II

Area ratios of XPS peaks [29]

Subshell	j Values	Area Ratio
s	1/2	-
p	1/2, 3/2	1:2
d	3/2, 5/2	2:3
f	5/2, 7/2	3:4

predicted than the intensities.

While derivative spectra are usually used in AES, bonding state information can be obtained from the undifferentiated line shapes, for example, the oxidation state of a particular metal.

The oxidation state of titanium can be determined by Auger line shapes, of both derivative and nondifferentiated spectra. Davis et al. [33] measured the derivative line shapes of titanium oxide powders and thin films in the kinetic energy range of 360 to 430 eV and they found that the peak amplitude at 411 - 415 eV changed with a change in oxidation state of the titanium, as shown in Figure 7. Care must be taken in the interpretation of line shape spectra, however, due to electron beam induced reduction of the titanium dioxide to lower oxidation states such as Ti_2O_3 or TiO. Davis et al. [33] found that while the titanium oxide powders were stable for 15 minutes exposure to electron or ion beams, anodized films were reduced with Ar^+ ion sputtering analyzed by an electron beam.

Thomas [36] shows significant electron beam reduction in only two minutes of electron beam bombardment as evidenced in the $L_3M_{2,3}V$ peak where the ratio of the 411 eV peak to the 417 eV peak shows a reduction of 3.2 to 1. Similar results were observed for Ar^+ ion beam bombardment, therefore making quantitative depth profile analysis

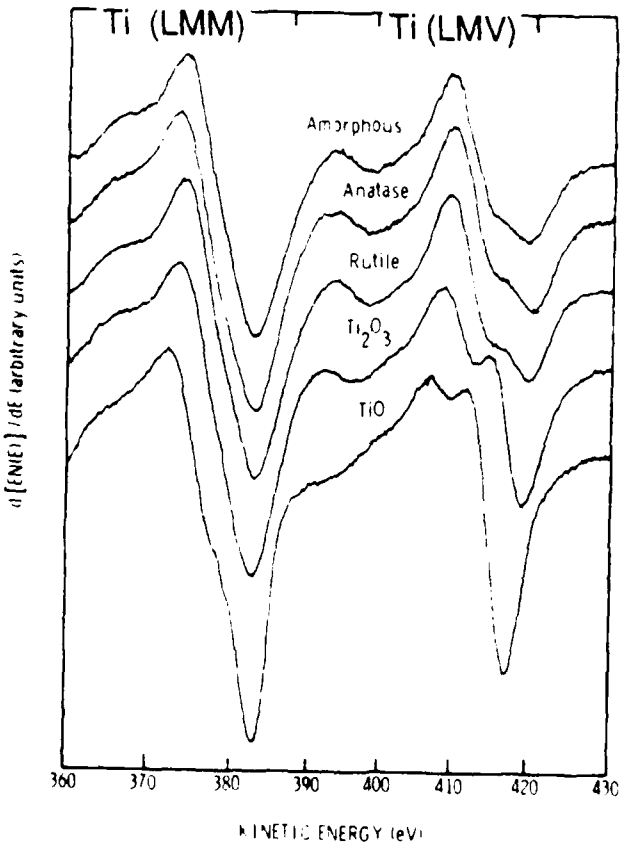

Figure 7. Ti $L_{2,3}$,$M_{2,3}$,$M_{2,3}$ and $L_{2,3}$,$M_{2,3}$,V Auger line shapes for TiO, Ti_2O_3, and TiO_2 [33].

impractical [36].

Solomon and Baun [34] use Fischer's [35] molecular orbital, M.O., models to interpret the undifferentiated titanium oxide Auger LMV spectra of Ti, TiO, and TiO_2. Titanium was assumed to be octahedrally coordinated to oxygen. The difference between the TiO and TiO_2 was explained by the $2t_{2g}$ M.O. level where TiO has two electrons in this level and TiO_2 has none. Figure 8 [35] is a qualitative molecular orbital energy diagram for titanium octahedrally coordinated to oxygen. The A - G designations correspond to the labeled spectra in Figure 9 [34]. Comparing the spectra for TiO and TiO_2, it can be seen that the B component in TiO corresponds to the $2t_{2g}$ -> $2p_{3/2}$ transition while the A component in TiO_2 corresponds to the $2e_g$ -> $2p_{3/2}$ transition. Solomon and Baun [34] report the Ti_{LMM} and Ti_{LMV} N(E) spectra for Ti, TiO, and TiO_2. A shoulder on the high energy side of the $L_{1}L_{1}M_{2,3}M_{2,3}$ peak at 382 eV is present only in the metal spectrum. The TiO and TiO_2 spectra show differences in the $L_{1}L_{1}M_{2,3}N_{1}$ and $L_{1}L_{1}M_{2,3}M_{4,5}$ peak shapes with TiO showing an asymmetry to the low energy side and TiO_2 to the high energy side.

While Auger line shapes theoretically yield oxidation state information, stoichiometry conclusions from experimental results may be difficult to make due to the possibility of electron or ion beam reduction during

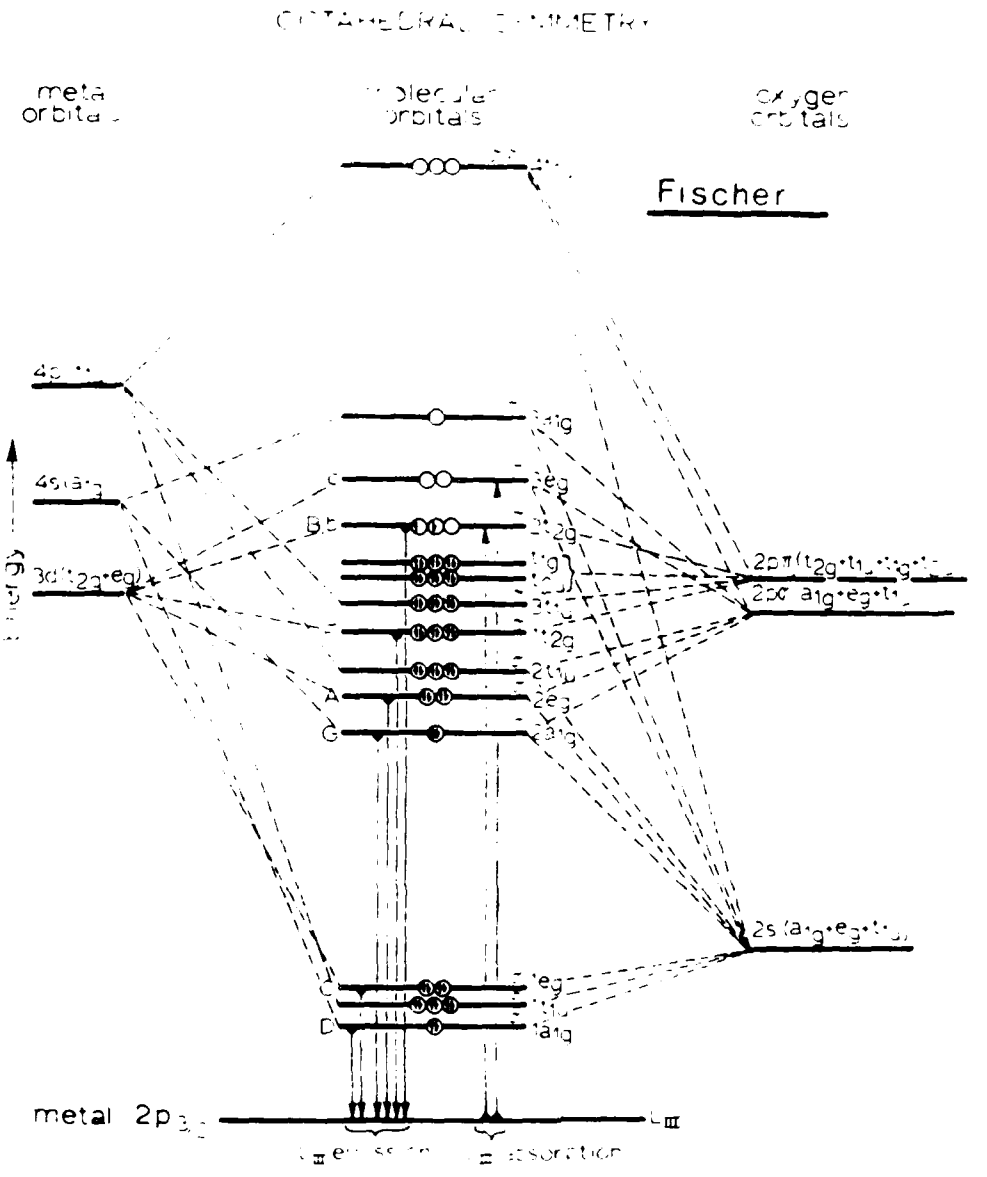

Figure 8. Molecular orbital energy diagram for titanium octahedrally coordinated to oxygen [35].

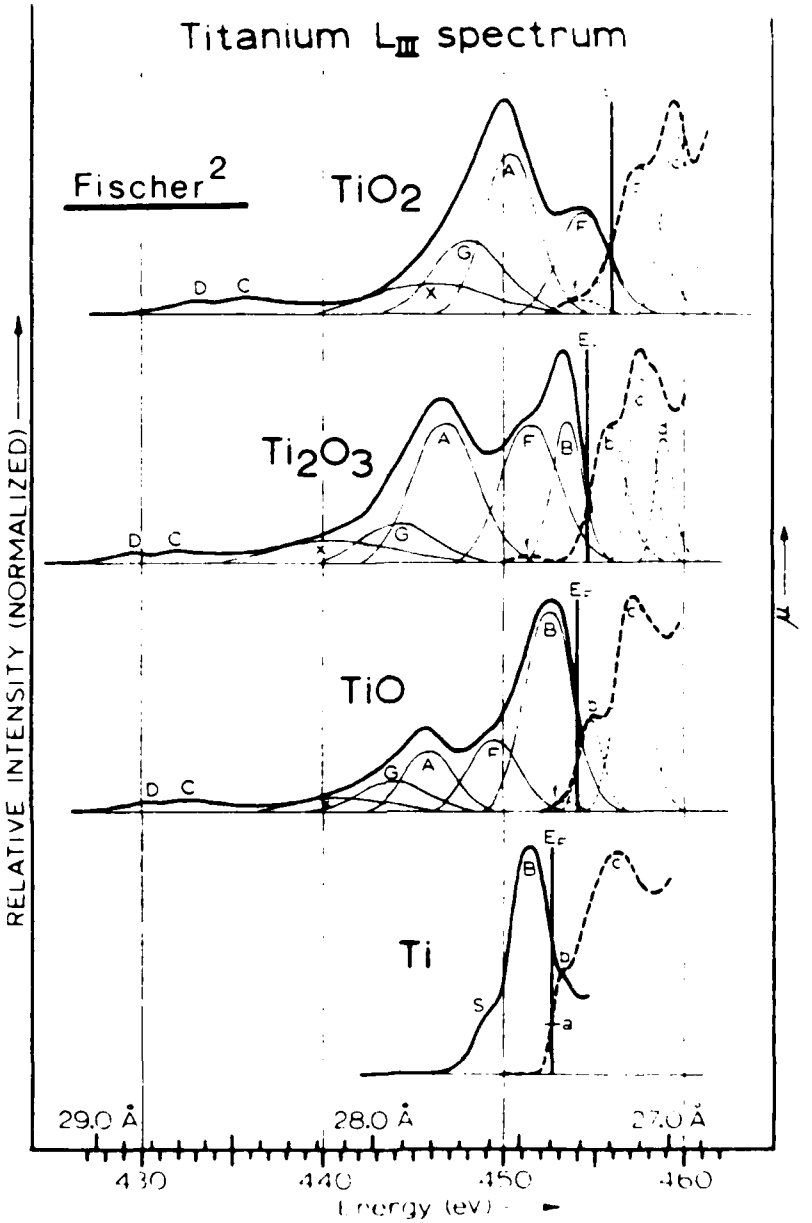

Figure 9. Titanium L_3 emission (solid lines) and absorption (dotted lines) spectra for Ti, TiO, Ti_2O_3, and TiO_2 with peak labels corresponding to Figure 8 [34].

analysis.

Auger peaks can also be observed in an XPS spectrum. The Auger series typically observed in XPS spectra are KLL for boron to sodium, LMM for sulfur to germanium, and MNN for molybdenum to neodymium. The presence of Auger peaks can aid in identification of the elements present, particularly if two x-ray sources are available. The kinetic energy of Auger electrons is independent of the x-ray energy, while the kinetic energy of photoelectrons is dependent on the x-ray energy. Therefore, by changing the x-ray, the photoelectron peaks will move when plotted on a K.E. scale, while the Auger peaks will remain at the same energy.

Depth profiling is commonly used to ascertain the relative oxide thickness of an oxide layer on a metal. Here, the signal of selected elements is followed versus sputter time to attain a "profile" of the composition of a particular depth into the sample.

d. Quantitative analysis

Quantitative analysis by XPS has received a lot of attention in the literature due to the complexity of what influences the intensity and shape of a peak. There are three basic routes to quantitation: a) calculate relevant terms from first principles, b) use published data bases of

correction factors, or c) use locally produced standards. A combination of these three techniques usually proves most effective [29]. The following discussion briefly reviews some authors' approaches to quantitative analysis by XPS, followed by the justification for the methods chosen in this work.

Fadley et al. [37] present a detailed theoretical discussion on quantitative XPS, taking into account x-ray reflection and refraction, surface roughness, instrumental parameters such as x-ray flux and acceptance functions, and patchy overlayers. Only a small portion of their theory will be presented here. The number of photoelectrons, dN, which is emitted per second from a given subshell, nl, of atoms in a differential volume element with a thickness, dz, at a distance z below the surface of the sample can be calculated. These photoelectrons enter the spectrometer with velocity vectors within the geometric acceptance solid angle, Ω_o, from an effective area, A_o, which is a projection of the spectrometer entrance aperture. Figure 10, taken from reference [37], is a schematic representation of the spectrometer geometry. The x-rays impinge on the sample at an angle, ϕ, and photoelectrons leave the surface at an angle, θ. The kinetic energy of the photoelectron upon leaving the sample surface is E and the kinetic energy at the analyzer is E_o where $E \geq E_o$. Some basic assumptions are

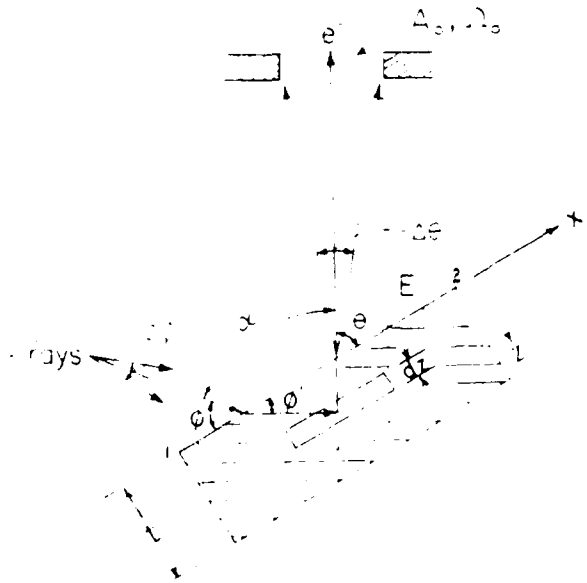

Figure 10. Schematic diagram of XPS spectrometer geometry used in angle dependent studies [37].

listed below:

1) the sample is perfectly smooth and amorphous;

2) the x-ray flux is uniform;

3) x-ray, ℓ_x, and photoelectron, $\ell_E(E)$, attenuation lengths, or mean free paths, follow an exponential decay;

4) the x-ray attenuation length is independent of ϕ; and,

5) the photoelectron attenuation length is independent of θ.

Fadley et al. [37] present a general expression for the number of photoelectrons:

$$dN(\theta) = \left[\begin{array}{c}\text{X-ray flux}\\ \text{at depth z}\end{array}\right] * \left[\begin{array}{c}\text{number of atoms}\\ \text{in volume element}\end{array}\right] *$$

$$\left[\begin{array}{c}\text{probability for nl}\\ \text{emission into } \Omega_o\end{array}\right] * \left[\begin{array}{c}\text{fraction escaping}\\ \text{in no-loss peak}\end{array}\right]$$

$$\left[\begin{array}{c}\text{intensity loss factor}\\ \text{due to retardation}\end{array}\right] * \left[\begin{array}{c}\text{detection}\\ \text{efficiency}\end{array}\right] \qquad (4)$$

$$dN(\theta) = \left[I_o(1 - R)\,\frac{\sin\phi}{\sin\phi}\,\exp\left(-\frac{z}{\ell_x \sin\phi}\right)\right] * \left[p\,\frac{A_o}{\sin\theta}\,dz\right]$$

$$\left[\frac{d\Omega_{nl}}{d\Omega}\,\Omega_o\right] * \left[\exp\left(-\frac{z}{\ell_E(E)\sin\theta}\right)\right] *$$

$$\left[F\,\frac{E_o}{E}\right] * \left[D_o\right]$$

where, I_o is the x-ray flux, R is the x-ray reflection coefficient, p is the number density of atoms, $d\Omega_{nl}/d\Omega$ is the differential photoelectron cross section for nl sub-shell, $z/\sin\phi'$ and $z/\sin\theta$ are the path lengths for x-rays and photoelectrons, respectively, in the sample, $F(E_o/E)$ is the intensity loss due to retardation and D_o is the detector efficiency. This equation can be rewritten and integrated for a sample with constant atomic density, p, and thickness, t, to yield the total number of photoelectrons:

$$N_t(\theta) = C_o \frac{E_o}{E} (1 - R)\, p \frac{d\sigma_{nl}}{d\Omega} \pounds_E(E) \sin\phi \; x \qquad (5)$$

$$\frac{[1 - \exp\{-t\,[(1/\pounds_x \sin\phi') + (1/\pounds_E(E) \sin\theta)]\}}{\sin\phi' + (\pounds_E(E)/\pounds_x) \sin\theta}$$

where C_o is an inclusive term for I_o, A_o, Ω_o, and D_o. This detailed equation can be simplified by making some further assumptions. In order to obtain an atomic fraction or concentration, the number of photoelectrons for a particular element is ratioed to the total number of photoelectrons from all contributing elements. Therefore, instrumental parameters such as I_o, A_o, Ω_o, and D_o will cancel when the atomic concentrations are calculated. It is assumed that x-ray reflection and refraction can be neglected; therefore, $R = 0$, $\phi = \phi'$, and because $\pounds_x >> \pounds_E$, $\sin\phi'$ will be much greater than $\pounds_E/\pounds_x \sin\theta$. This allows the equation to be

simplified to:

$$N_t(\theta) = C_o \frac{E_o}{E} p \frac{d\sigma_{nl}}{d\Omega} \mathcal{E}_E(E) \left[1 - \exp\left(- \frac{t}{\mathcal{E}_E(E) \sin\theta}\right)\right] \quad (6)$$

or, for a sample of infinite thickness, that is with no overlayer, equation (6) reduces to:

$$N_\infty(\theta) = C_o \frac{E_o}{E} p \frac{d\sigma_{nl}}{d\Omega} \mathcal{E}_E(E) \equiv N_o \quad (7)$$

The number of photoelectrons ejected is a function of instrumental parameters, the energy analyzer, the density of the sample, the cross-section, and the mean free path.

Powell and Larson [38] present a similar model for quantitative XPS with a modification of the cross-section term to include Reilman's asymmetry parameter [39].

There has been much discussion in the literature about calculation of the mean free path or photoelectron attenuation length, $\mathcal{E}(E)$. The following discussion summarizes some of the approaches.

Penn [40] calculated values for mean free paths for elemental solids and compounds using the following equation for kinetic energies falling in the range of 200 eV $\leq$ E $\leq$ 2400 eV:

$$\mathcal{E}_t(E) = \frac{E}{[a\ (\ln E + b)]} \quad (8)$$

where a and b are functions of electron concentration.

Seah and Dench [41] compiled published results and found a relationship between the mean free path and the kinetic energy for elements, inorganic compounds, and organic compounds for energies greater than 150 eV. For a single element,

$$\ell_m = \frac{538}{E^2} + 0.41\,(aE)^{\frac{1}{2}} \text{ [monolayers]} \tag{9}$$

For inorganic materials

$$\ell_m = \frac{2170}{E^2} + 0.72\,(aE)^{\frac{1}{2}} \text{ [monolayers]} \tag{10}$$

For organic materials,

$$\ell_d = \frac{49}{E^2} + 0.11\,(E)^{\frac{1}{2}} \text{ [mg/m}^2\text{]} \tag{11}$$

where a is the monolayer thickness defined by

$$a^3 = A/(pnN) \times 10^{24} \tag{12}$$

where p is the bulk density in kg/m^3, N is Avogadro's number, and n is the number of atoms per molecule and A is the atomic or molecular weight. Note that for kinetic energies in the range used with a Mg anode in XPS, the first part of equations (9) to (11) are negligible, yielding a basic relationship of

$$\ell \propto E^m \qquad \text{where } m = \tfrac{1}{2} \tag{13}$$

Wagner et al. [42] used a multipoint analysis on electron mean free paths of pure materials to find that m ranged

between 0.65 and 0.75. They found that Penn's relationship, equation (8) could be approximated by $\pounds \alpha E^m$, where m = 0.77. Their experimental data in comparison with the theoretical calculations indicated that m is not likely to be as low as 0.5, as found by Seah [41], nor likely to exceed 0.75, with an average value of 0.66. Ashley and Tung [43] predicted the value for m theoretically and also found m to be between 0.65 and 0.80. In contrast to Ashley [43] and Wagner's [42] findings, Tokutaka et al. [44] propose yet another method to calculate the mean free path with results agreeing more closely to Seah & Dench's [41] than to Penn's [40]. For electron energies greater than 350 eV, the mean free path for elements of atomic numbers, Z, less than 24 or greater than 74,

$$\ln \pounds(E) = \frac{\ln [Q(Z)/3.32]}{\ln (7.74/3.32)} (1.6551 - 0.2890 \ln E) + (-3.2563 + 0.9395 \ln E) \quad (14)$$

with similar equations for the other atomic numbers, where $Q(Z) = Zp_x/M_x$ with p_x as the bulk density in g/cm^3 and M_x as the atomic weight in g/mol. Battistoni et al.[45] compare different quantitative approaches classifying them as first principle methods [38] or sensitivity factor methods [46]. They give the familiar equation for the current of photoelectrons, I_A, as:

$$I_A = N_A\sigma \left[1 + \frac{\beta}{2} \left(\frac{3}{2} \sin^2 \theta - 1 \right) \right] \pounds(KE) \exp(-t/\pounds) \quad (15)$$
$$F(KE,E_A)\ T(KE,E_A)\ D$$

where N_A is the number of atoms per unit volume, σ is the photoionization cross-section, β is the asymmetry parameter, θ is the take off angle, t is the overlayer thickness, $\pounds$ is the inelastic mean free path, $F(KE,E_A)$ is the electron-optical factor, $T(KE,E_A)$ is the transmission function, $\exp(-d/\pounds)$ is the attenuation due to overlayer, and D is the detector efficiency. They used Scofield's cross sections [47], Reilman's β [39], and Wagner's [42] expression for mean free path with the exponential relationship of $\pounds \alpha KE^{0.7}$. The accuracy of their results using the first principle method was explained by the factors, F x T and $\exp(-d/\pounds)$ compensating for each other. As the kinetic energy decreases, the transmission function, T, should increase the photoelectron number due to the dependence $T \alpha KE^{-1}$ using the FAT mode. The overlayer contamination, represented by $\exp(-d/\pounds)$ should attenuate the photoelectron intensity, causing a decrease in peak intensity with decreasing KE. The authors concluded that both methods yielded a 10% average relative error in atomic ratios compared to the calculated atomic ratios.

The method chosen in this work for atomic fraction calculation is as follows. The corrected area for the

element, CA_i, is equal to the area for ith element, A_i, divided by the cross-section, σ_i, calculated by Scofield [47], and the mean free path, ℓ_i, taken as $(KE)^{.75}$. If the analysis was done in the FRR mode, the above number was divided by the KE as shown in equation (16), but multiplied by the KE in the FAT mode as shown in equation (17).

$$CA_i = \frac{A_i}{\ell_i \sigma_i KE_i} \tag{16}$$

$$CA_i = \frac{A_i \quad KE_i}{\ell_i \sigma_i} \tag{17}$$

The above method was applied to each element detected on the sample. These were then summed and the atomic fraction obtained by ratioing the corrected area to the sum of the corrected areas for all elements detected. The ratio technique allows instrumental factors to be canceled.

e. Curve fitting

The peak width, ΔE, of an XPS photopeak is dependent on the natural line width of the core level, ΔE_n, the photon source width, ΔE_p, and the analyzer resolution, ΔE_A as shown below:

$$\Delta E = (\Delta E_n^2 + \Delta E_p^2 + \Delta E_A^2)^{\frac{1}{2}} \tag{18}$$

This assumes Gaussian line shapes for the photoelectron

peaks [29].

The peak width, ΔE, is also termed the full width at half maximum or FWHM. When curve fitting XPS peaks using software provided with the instrument, care must be taken to obtain useful information. The variable parameters are FWHM, peak position and peak height. By obtaining spectra of standards, the FWHM can be approximated. The peak positions can be chosen with some prior chemical knowledge of the sample composition. Although curve fitting can provide useful additional information pertaining to the bonding states in the sample, over- or mis- interpretation by curve fitting must be avoided.

f. Angle dependent XPS

By obtaining XPS spectra of a substrate with a thin overlayer at a series of take-off angles, θ, the thickness and patchiness of the overlayer can be calculated from the atomic fractions of a component in the overlayer and of a component in the substrate. The intensity of a photopeak from the overlayer of thickness, t, has been given in equation (6).

The intensity of the photopeak from the bulk is given by equation (19).

$$N_{\infty,t}(\theta) = C_o E_o/E \; p \; d\sigma/d\Omega \; \pounds(E) \; \{ \exp (-t/\pounds(E) \sin \theta)\} \quad (19)$$

Ratioing equation (19) to equation (6), results in equation (20):

$$\frac{\text{Bulk}}{\text{Surface}} \quad \frac{N_{\infty,t}(\theta)}{N_t(\theta)} = \frac{C_o \frac{E_o}{E} p \frac{d\sigma}{d\Omega} \pounds(E) \left[\exp(-\frac{t}{\pounds(E)\sin\theta})\right]}{C_o \frac{E_o'}{E} p' \frac{d\sigma}{d\Omega}' \pounds'(E) \left[1 - \exp(-\frac{t}{\pounds(E)\sin\theta})\right]} \quad (20)$$

Equation (20) can be simplified further by making a few assumptions. First, because of the ratio, the instrumental parameters, C_o, will cancel. By taking $N(\theta)$ as the area of the photopeak, E_o/E as the energy correction which is related to $(KE)^{-1}$ in the FAT mode, and p as the concentration, equation (20) reduces to equation (21), with an aluminum overlayer on a chromium substrate.

$$\frac{\left[\frac{A_{Cr}\ KE_{Cr}}{\pounds_{Cr}\ \Phi_{Cr}}\right]\cdot\frac{1}{C_{Cr}}}{\left[\frac{A_{Al}\ KE_{Al}}{\pounds_{Al}\ \Phi_{Al}}\right]\cdot\frac{1}{C_{Al}}} = \frac{\exp\left[-\pounds_{Al}\frac{t}{\sin\theta}\right]}{1 - \exp\left[-\pounds_{Al}\frac{t}{\sin\theta}\right]} \quad (21)$$

With the quantity in brackets on the left hand side corresponding to the atomic percent, equation (21) can be rearranged to equation (22),

$$\text{Log}\left[\frac{AP_{Al}\ C_{Cr}}{AP_{Cr}\ C_{Al}} + 1\right] = \frac{t}{\pounds_{Al}}\cdot\frac{1}{\sin\theta} \quad (22)$$

The left side of this equation can be plotted versus $1/\sin\theta$ yielding a slope of $t/\pounds_{Al}$. The above treatment assumes a

continuous film.

For a patchy overlayer, the following refinements are made:

$$\text{Surface} \quad N_t(\theta) = \gamma N_t(\theta) \tag{24}$$

$$\text{Bulk} \quad N_{\infty,t}(\theta) = N_o\left[(1-\gamma) + \gamma \exp\left(-\frac{t}{\ell_{Al}\sin\theta}\right)\right] \tag{25}$$

where γ is the fraction of the bulk covered by the surface. Combining equations as before, yields equation (26),

$$\frac{AP_{Cr}\, C_{Al}}{AP_{Al}\, C_{Cr}} = \frac{(1-\gamma) + \gamma \exp\left(-\frac{t}{\ell_{Al}\sin\theta}\right)}{\gamma\left[1 - \gamma \exp\left(-\frac{t}{\ell_{Al}\sin\theta}\right)\right]} \tag{26}$$

which can be rearranged to yield equation (27),

$$\text{Log}\left[\frac{\frac{AP_{Cr}\, C_{Al}}{AP_{Al}\, C_{Cr}} + 1}{\frac{AP_{Cr}\, C_{Al}}{AP_{Al}\, C_{Cr}} - \frac{1}{\gamma} + 1}\right] = \frac{t}{\ell_{Al}} \cdot \frac{1}{\sin\theta} \tag{27}$$

By matching a theoretical plot of AP_{Al}/AP_{Cr} versus θ, with the actual data, the thickness and patchiness can be determined.

3. Secondary ion mass spectrometry, SIMS

When an energetic beam of ions, typically 1 - 4 KeV, impinges on a solid sample, neutral atoms, positive and

negative ions are sputtered from the surface [48]. Figure 11 illustrates the processes occurring when the primary ion beam interacts with the surface [49]. The primary ions implant into the solid surface and the energy dissipated causes secondary particles to be emitted. These particles can be atoms or clusters of atoms, which are neutral, positively or negatively charged [49]. Usually, only a small fraction, 0.01 - 1 %, of the sputtered particles are emitted as charged secondary ions [50]. The ions are then analyzed by a mass spectrometer, yielding a mass spectrum. Thus SIMS is simply another method for mass spectrometry, where the solid surface is of interest.

Depending upon the current density of the primary beam, SIMS can be static, sputtering fractions of monolayers with monolayer lifetimes of several hours, or dynamic, where several monolayers are sputtered per second [48,51]. Static SIMS requires primary beam currents less than 10 nA/cm^2, preferably less than 1 nA/cm^2. [51] Special ion guns and detection systems are required. The discussion here will be limited to dynamic SIMS.

With its high sputter rate, dynamic SIMS causes atomic mixing, thus sharp interfacial boundaries are lost. The primary purpose of dynamic SIMS is therefore elemental and isotopic identification [48,51,52]. Qualitative analysis requires proper assignment of the ion species to the

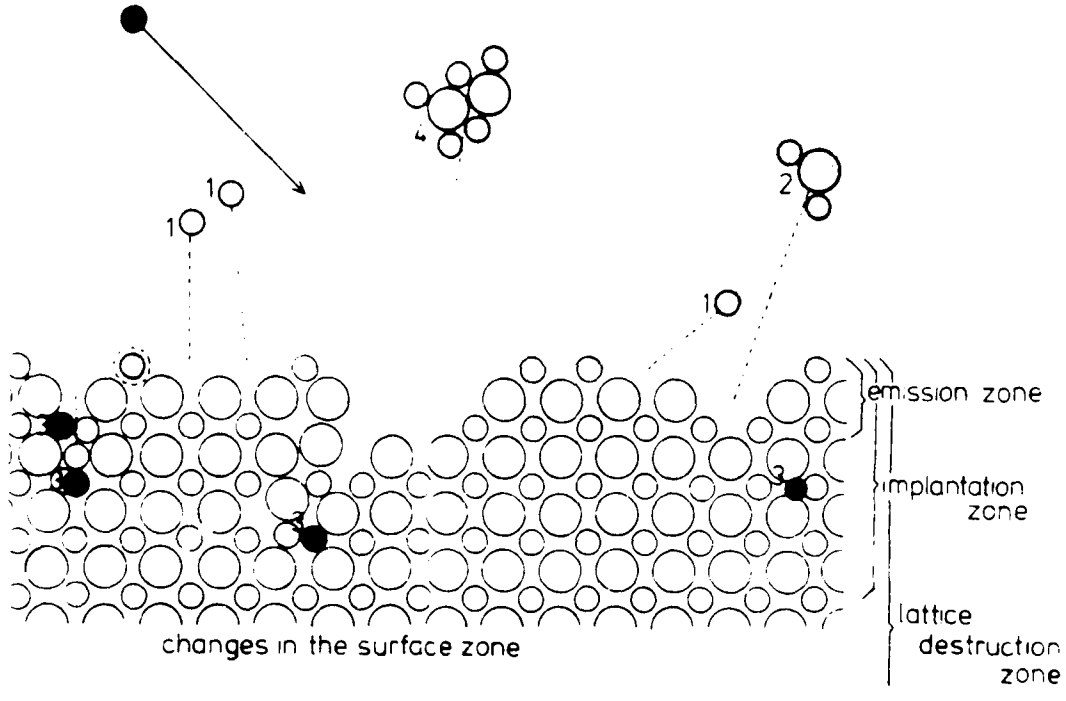

Figure 11. Ion bombardment-induced changes in the surface zone of the solid [49].

observed peaks, thus some prior knowledge of the sample composition is extremely helpful.

While the ultimate sensitivity in XPS and AES is approximately 10^{-3} atomic percent, SIMS is sensitive to 10^{-6} atomic percent [53]. Depending on the element being detected and the matrix, SIMS can be sensitive to the ppb level [51]. The limit of detection of silicon, for example, is one part in 10^{8} [54]. Unfortunately, while sensitivity variation in AES can be one order of magnitude from least to most sensitive, SIMS sensitivity can vary four to five orders of magnitude, making quantitative SIMS difficult [54].

Quantitatively, the current detected, I_x, is a function of the concentration of atom X, C_x, the sputter yield, S_x, the probability of ionization, P_x, the primary ion beam density, N_i, and an instrumental constant, k, as shown below: [48,55]

$$I_X = k\, C_X\, S_X\, P_X\, N_i \qquad (28)$$

It is primarily the probability of ionization that causes the sensitivity to vary four to five orders of magnitude.

The presence of oxygen enhances the secondary ion yield, and the probability of ionization due to the fractional oxygen coverage on the sample's surface [55]. Therefore, it is sometimes in-bled during sputtering to

enhance sensitivity. However, when studying oxidized samples, in-bleeding oxygen may cause difficulty in data interpretation.

Hayes and Evans [13] have analyzed titanium oxide films with static SIMS. Predominant peaks were observed at 46 to 50 m/z for Ti^+ isotopes and 62 to 66 m/z for TiO^+. The isotopic abundance was 8%, 7.3%, 74%, 5.5%, and 5.2% for masses 46 to 50, respectively. Peaks due to ion impact-induced fragmentation of adsorbed hydrocarbon contamination were observed at 27, 29, 43, 55, and 57 m/z for $C_2H_3^+$, $C_2H_5^+$, $C_3H_7^+$, $C_4H_7^+$, and $C_4H_9^+$, respectively. Other peaks observed were 15 m/z for CH_3^+, 39 m/z for K^+ and 18 m/z for adsorbed H_2O^+. TiH^+ and $TiOH^+$ at 49 and 65 m/z were also observed as these peaks exceeded the expected isotopic ratios.

4. Fourier transform infrared spectrometry, FTIR

a. Infrared phenomenon

Molecules undergo translational, rotational and vibrational transitions. The frequency of vibrational transitions is in the infrared range between wavelengths of 15.4 to 2.5 μm or wavenumbers of 650 to 4000 cm^{-1} [56]. The wavelength, λ, is inversely proportional to the absorbed energy, E, as shown in equation (29) [57],

$$\lambda = hc/E \qquad (29)$$

where h is Planck's constant and c is the speed of light.

The wavenumber, K, is proportional to the absorbed energy as shown in equation (30) [57].

$$K = E/hc \tag{30}$$

When infrared radiation impinges on a sample, the groups of atoms absorb energy at particular frequencies, v, depending upon the masses of the atoms, M_x and M_y, and the force constant, k, as shown by equation (31) [57].

$$v = \frac{1}{2\pi c} \left[\frac{k}{M_x M_y / (M_x + M_y)} \right]^{\frac{1}{2}} \tag{31}$$

For the vibrational transitions to absorb infrared energy, the vibration must cause a change in the dipole moment of the molecule.

Stretching and bending vibrations are observed in infrared spectroscopy. Stretching vibrations occur when the interatomic distance increases and decreases along the bond axis. Bending vibrations involve either a change in bond angle between bonds with a common atom or movement of a group of atoms with respect to the remainder of the molecule without the atoms in the group moving with respect to each other [56,57]. Figure 12 schematically shows the stretching and bending modes.

b. Dispersive versus Fourier transform infrared

In a dispersive instrument, infrared radiation travels

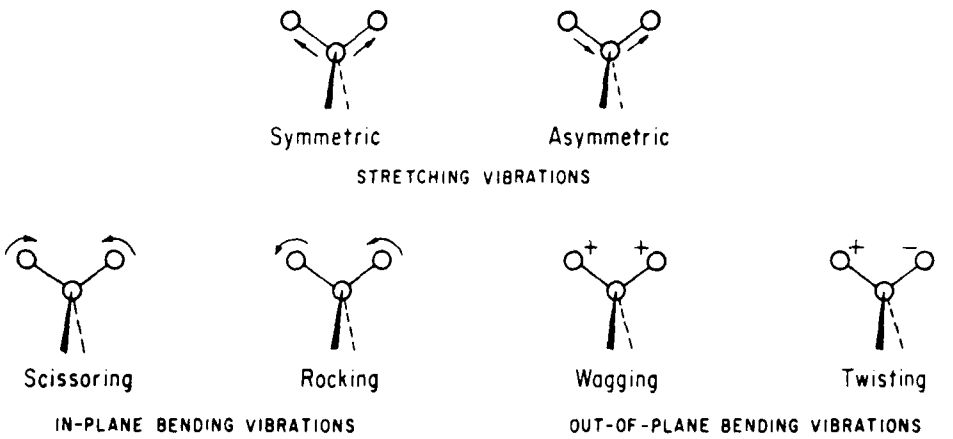

Figure 12. Stretch and bending modes of molecules interacting with infrared radiation [57].

through a prism or grating yielding near monochromatic light which then travels through a slit to the sample. The grating or prism moves allowing light of all infrared frequencies to sequentially radiate the sample. In a Fourier transform instrument, all of the infrared radiation travels through a series of mirrors in a Michelson interferometer to the sample. The Michelson interferometer contains a fixed and a movable mirror with a beam splitter which transmits 50% of the light to one mirror and reflects 50% of the light to the other mirror. As the movable mirror traverses up and back, the light interferes constructively and destructively with the light reflecting from the fixed mirror to form a complex summation of cosine waves or an interferogram [56,58]. This interferogram of light impinges on the sample which will absorb frequencies depending upon the molecules and the amount present and is detected. The interferogram, in the time domain, is then transformed to the frequency domain and displayed as an intensity vs. wavenumber spectrum.

There are well known advantages to Fourier transform infrared over the dispersive instruments. Because only a portion of the total available light hits the sample in the dispersive instruments, the throughput is reduced over the Fourier transform instruments where all of the light contacts the sample. This "throughput advantage" allows 80

to 200 times more light to reach the sample than in dispersive instruments. A second advantage is the "multiplex advantage". Because information over the entire spectrum is obtained with each scan of the Fourier transform instrument instead of one frequency at a time with the dispersive instrument, a much higher signal to noise ratio is obtained for the same number of times scanned [58]. Wavenumber accuracy is also assured with a Fourier transform instrument due to self-calibration with a He-Ne laser. This enables the spectra to be coadded and subtracted will little loss of resolution [59].

There are two types of infrared detectors commonly used - thermal and quantum and the infrared energy is detected by two different mechanisms. A thermal detector detects a change in temperature of the absorbing material, whereas with quantum detectors, the infrared energy interacts with the electrons in the solid, exciting them to a higher state such that the signal is proportional to the energy absorbed. The most commonly used thermal detector is a pyroelectric bolometer, DTGS or a deuterated triglycine sulfate detector. The pyroelectric bolometer is a ferroelectric heat sensing material which changes its degree of electrical polarization when the temperature changes. The resulting electrical signal is proportional to the infrared energy. Quantum detectors have a higher sensitivity and are best used for

low signal samples. They are made of semiconductor materials such as mercury-telluride and cadmium telluride in a MCT detector. Because of the semiconductor material, these detectors must be cooled to liquid nitrogen temperatures so that the electrons can be excited to the conduction band and become current carriers when infrared radiation strikes the detector [60].

c. Techniques in infrared - transmission, diffuse reflectance infrared Fourier transform, DRIFT, photoacoustic spectrometry, PAS, attenuated total reflectance, ATR, and external reflectance, ER

Five basic types of infrared sampling for solids will be briefly discussed: transmission, internal reflection, diffuse reflection, external reflection and photoacoustic spectroscopy. The infrared beam travels through the sample in transmission IR. Free standing films, films coated onto salt plates or pressed pellets are common sample types for surface studies. The sample preparation and measurement can be relatively easy. The sample must allow the beam to pass through it without too much loss of intensity. In some cases, the path length of the sample is difficult to determine, making quantitation impossible.

The internal reflection technique commonly used is attenuated total reflectance or ATR. Samples such as

polymer films, oils, or gels are coated onto a crystal of high refractive index such as germanium or thallium bromide-thallium iodide. When the angle of incidence of the light is higher than the critical angle for the crystal, internal reflection occurs through the crystal [59]. Because the sample is coated on the outside of the crystal, the radiation is attenuated by the absorption of radiation by the coating. The sample must be in intimate contact with the crystal for good quality spectra to be obtained.

When the particle size of the sample is comparable to the wavelength of radiation, the incident light is absorbed, refracted and diffusely reflected [59]. The diffuse reflectance technique, DRIFT, uses externally reflected light which is scattered by the sample, collimated and detected. Powders and non-reflective, scattering samples are best analyzed by this technique. The sample preparation is usually simple and samples can be diluted with KBr to obtain the desired signal intensities. The spectra are, however, difficult to quantify.

Although the detector is different in photoacoustic spectroscopy, or PAS, the sample types and resulting spectra are often similar to DRIFT. When infrared radiation impinges upon a sample, the samples are heated. The thermal expansion of the surrounding gas from this heating can be detected with a microphone and is related to the atomic

vibrations. Sample types are typically powders or samples too reflective for DRIFT and not reflective enough for external reflection infrared.

Specular reflectance spectroscopy is used to study thin films on reflective metal substrates and monolayer and sub-monolayer coverages can be detected. The principles of this particular technique are the subject of the next section.

d. External reflection infrared

Specular reflectance is used to study near monolayer to submonolayer films on reflective metal surfaces [59]. At non-normal angles of incidence, a phase change in the light occurs upon reflection depending on the angle of incidence and the state of polarization, thus changing the sensitivity [61,62]. When the angle of incidence is nearly normal to the reflective surface, close to 0°, the incident and reflective waves recombine to form a standing wave. This standing wave will have an electric field with a node at the surface. Therefore, there will be no interaction of the incident radiation with the film on the surface [61]. Thus, large angles of incidence, nearly grazing the sample, yield the best results [62].

The state of polarization also affects the resulting signal. When light is polarized perpendicular to the plane of incidence, there is a 180° phase shift in the incident

light. This occurs at nearly all angles of incidence [61]. Because the phase change is 180°, the interaction of the incident and reflected light causes a standing wave with a node at the surface. Thus, no spectral information about the surface can be obtained [62,63]. In contrast, when the light is polarized parallel to the plane of incidence, the phase shift changes rapidly at high angles of incidence [61]. An elliptical standing wave results with an electric vector perpendicular to the metal surface [61,63]. This can improve sensitivity up to 25 times [64]. The absorbance varies linearly with thickness, d, up to a d/λ of 0.0004 where λ is the wavelength of light. The absorbance, A, depends upon the refractive index and the extinction coefficient of both the metal and the film, and will decrease with increasing refractive index of the film, n_2 and increase with increasing extinction coefficient of the film, k_2. The absorbance will also increase with increasing extinction coefficient of the metal, k_3, and is not sensitive to the refractive index of the metal, n_3 [61].

Problems exist in the quantitation and peak identification in specular reflectance due to peak distortions and peak shifts [62,65]. Because the electric fields at the surface differ for different frequencies, the reflection bands will be asymmetric [65]. For thin films, less than 100 nm, the peak maxima will shift to a higher frequency

compared to a transmission spectrum [65]. This occurs for bands with $\nu^{\frac{1}{2}} \approx 20$ cm^{-1} and for $k_2 > 0.1$. For sharp bands, $\nu^{\frac{1}{2}} < 5$ cm^{-1}, less shift will occur. For absorption bands where $k_2 << 0.1$, the spectrum will be nearly identical to the transmission spectrum; however, the intensities may differ. For monolayer or very thin films, the peak maximum will always be shifted to higher frequencies. Finally, as the thickness of the band increases, the distortion effects will change more rapidly for higher frequency bands [65].

e. Peak identification

In order to interpret the interactions occurring at an interface, the infrared absorbance peaks must be correctly identified. The following is a compilation of peak positions reported in the literature for the functional groups of interest in the study of alkoxides and a diglycidal ether of bisphenol A, or a DGEBA based epoxy.

There are some general rules in peak assignment. Stretching vibrations require more energy and are therefore observed at shorter wavelengths or higher wavenumbers than bending vibrations. Triple bonds are stronger than double bonds which are stronger than single bonds for C-C, C-N, and C-O with peaks occurring between 2300 - 2000 cm^{-1}; 1900 - 1500 cm^{-1}; and 1300 - 800 cm^{-1}, respectively [57].

One of the most readily identifiable regions is the C-H

stretching vibration region in the 2975 to 2840 cm^{-1} range. The CH_3 asymmetric stretching vibration occurs at 2975 - 2950 cm^{-1}, resolved from the CH_2 asymmetric stretching vibration at 2930 cm^{-1}. The CH_3 symmetric stretching region occurs at 2885 - 2865 cm^{-1} with the CH_2 symmetric stretching region at 2870 - 2840 cm^{-1} [66]. In addition to the CH_3 and CH_2 stretching vibrations, $-CH_2-$ wagging, twisting and rocking vibrations are observed at 1150 - 1450 cm^{-1} [67].

Water and CO_2 can be observed on samples, usually with incomplete purging of the sample chamber. CO_2 can be identified by a doublet occurring at 2363 and 2334 cm^{-1}. Water absorbs, in addition to the -OH stretch at 3710 cm^{-1}, at 1600 - 1650 cm^{-1} from the scissors deformation vibrations [57,68,69].

The -OH stretch frequency occurring in the 3800 - 3300 cm^{-1} region depends upon the association of the hydroxyls. Free, unassociated alcoholic -OH groups absorb as sharp bands at 3610 cm^{-1} whereas polymeric -OH groups absorb as broad bands around 3300 cm^{-1} [57]. Surface hydroxyls on TiO_2 show stretching frequencies at 3730 - 3715, 3660 - 3650, and 3420 - 3410 cm^{-1} [70,71]. The stretching frequency of hydroxyl groups on alumina surfaces is related to the net charge on the -OH group. Hydroxyl groups in a coordination sphere of tetrahedrally coordinated Al^{3+} will absorb at 3760 - 3800 cm^{-1} while -OH groups shared

by octahedrally and tetrahedrally coordinated Al^{+3} will absorb at 3700 - 3750 cm^{-1} [72].

Library spectra provide a beginning for peak identification in that they allow one to compare peak positions of the library spectrum to the actual data obtained in the lab. Once agreement is attained, peak identification follows.

Library spectra of tetra iso-propyl titanate, TIPT, and tetra n-butyl titanate, TNBT, have been published by Sadtler [73,74], and are shown in Figure 13. Peak positions, as read from the spectra, are listed in Table III, along with other series of peaks reported for TIPT [75,76]. The isopropoxy groups in TIPT have characteristic bands at 1160 - 1175 cm^{-1}, 1120 - 1140 cm^{-1}, and 1110 cm^{-1} [75-77]. These bands have been attributed to isobranching, alkyl absorption induced by the oxygen and O-C stretch, respectively [76]. A doublet is observed at 1375 and 1365 cm^{-1} due to the gem-dimethyl structure of the isopropoxide [75,77]. N-butyl groups in TNBT have been observed at 1150, 1125, and 1075 cm^{-1} [75,76], attributed to normal paraffinic absorption, induced alkyl absorption and C-O stretch, respectively [76]. Bands have also been reported at 1190 and 1025 cm^{-1} [77]. The (C-O)M stretch is observed at 900 - 1150 cm^{-1} [75,77,78]. In correlating the C-O stretching frequency of an alcohol and its corresponding alkoxide, the frequency

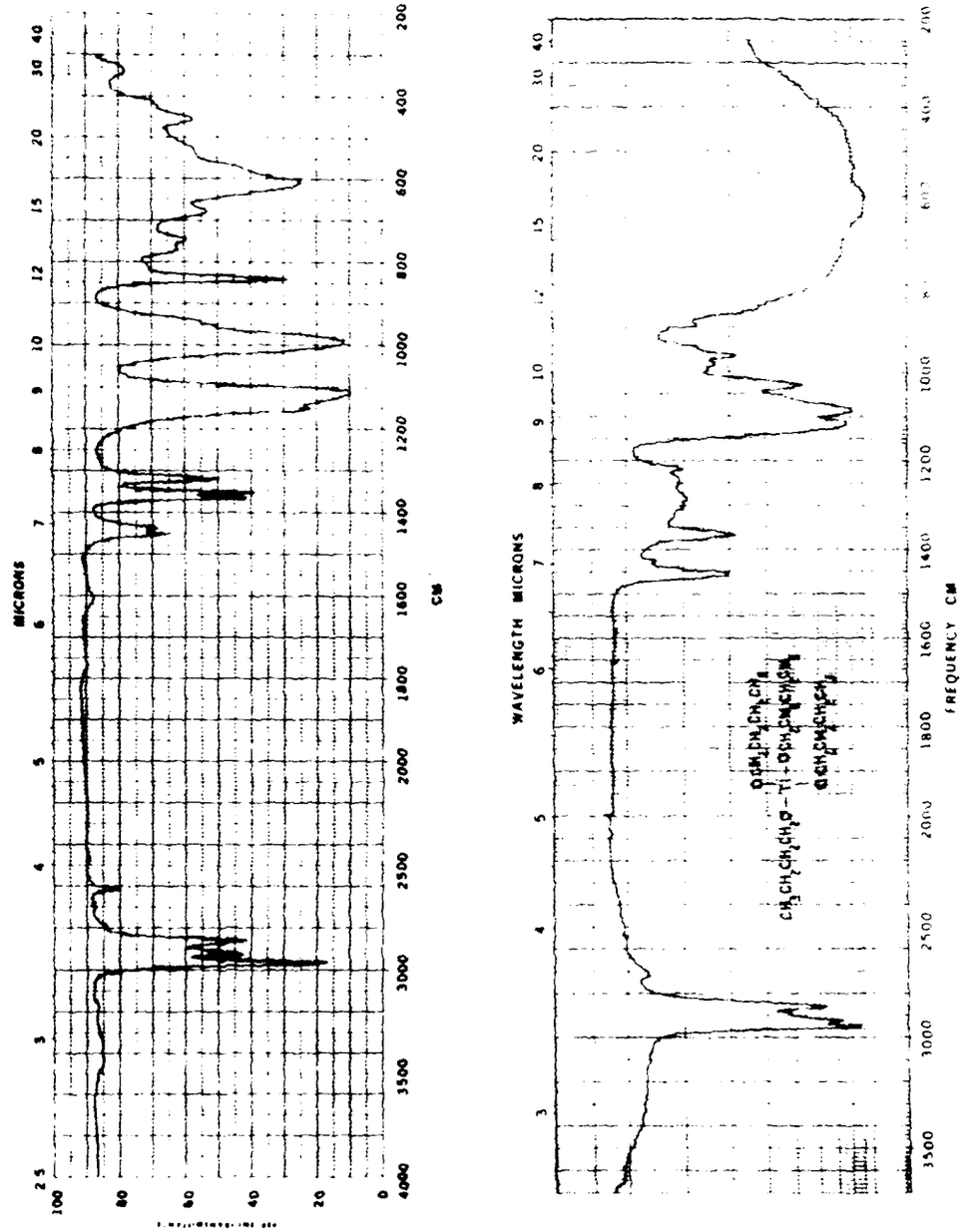

Figure 13. Sadtler IR spectra of isopropyl alcohol, Titanium (4˙) salt, TIPT, (33830K), and of butyl titanate, TNBT, (15547K) [73,74].

TABLE III

IR Peak Positions in TIPT and TNBT Spectra [73-76]

TIPT [75] cm^{-1}	TIPT [73] cm^{-1}	TIPT [76] cm^{-1}	TNBT [74] cm^{-1}
2959	2960	2958	2950
2924	2920	2924	2920
2857	2860	2857	2880
	2620		
2604			
1462		1462	1460
1451	1450	1451	
	1435		
1425		1424	1420
1391		1391	
1381		1381	
1370	1365	1370	1370
	1350		
1328	1320	1328	
			1280
1248		1248	
			1220
1159		1159	
	1150		
		1136	
1124		1123	
	1115		1115
			1085
			1030
1000		1000	
	990		985
			960
950		954	
			890
		872	
852			
	840		
	740		
	675		
619			
	610		
535			
474			
	460		
402			

will be lower in the alkoxide [78]. The degree of shift of the (C-O)M peak has been attributed to the nature of the alkoxide group, but no relation to the mass of the metal atom has been observed [75,77]. Both secondary propyl and secondary butyl C-O stretches absorb at 1105 cm^{-1} and the n-butyl C-O stretch absorbs at 1075 cm^{-1} [79].

The Ti-O stretch in TIPT is reported at 619 cm^{-1} [78], while in TiO_2 the band is reported at 840 cm^{-1} [64]. For anatase TiO_2, the Ti-O stretch is reported at 811 cm^{-1} and at 603 cm^{-1} for rutile TiO_2 [80].

A library spectrum for sec-butyl aluminum alkoxide, designated as E-8385, is also available [81] as seen in Figure 14, with the peak positions read from the spectrum listed in Table IV. Less peak identification information is available for the aluminum alkoxide. Barraclough [78] reports bands above 1000 cm^{-1} due to the (C-O)M stretch and five bands from 539 - 699 cm^{-1} due to (Al-O) stretch, while Wilhoit reports an Al-O-Al stretch at 935 cm^{-1} [77]. Two Al-OAl stretch absorptions can occur depending upon their orientation. If the transition moment is normal to the surface, the Al-OAl stretch will occur at 960 cm^{-1}, whereas, when the transition moment is parallel to the surface, the Al-OAl stretch will absorb at 650 cm^{-1} [82].

Information from the infrared spectra of aluminum oxides can also prove useful in peak identification.

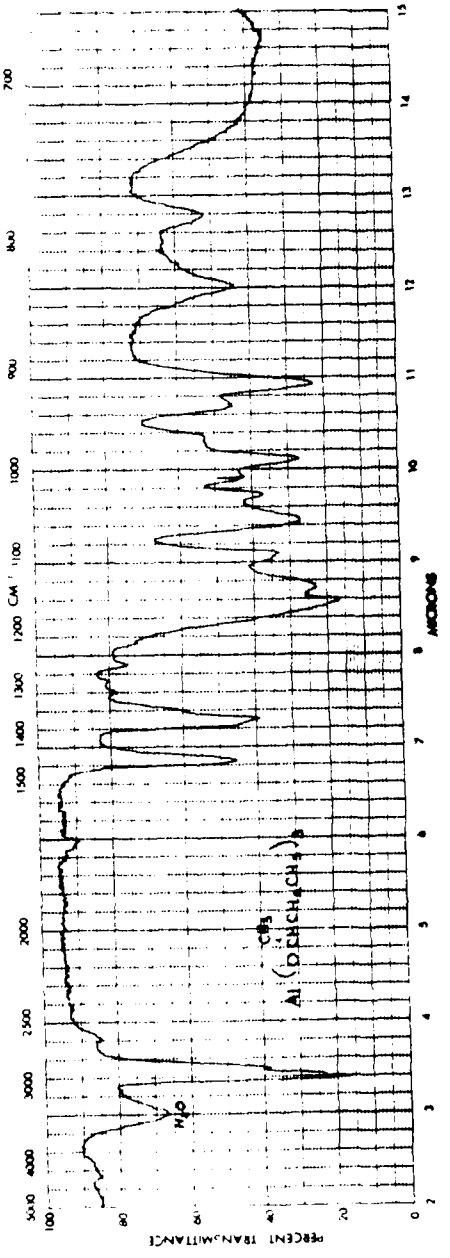

Figure 14. Sadtler IR spectrum of 47948P, sec-butyl alcohol, aluminum salt, E-8385, [81].

TABLE IV

IR Peak Positions in E-8385 Spectrum [81]

E-8385 cm^{-1}
3300
2960
2900
2850
1460
1380
1370
1350
1270
1165
1140
1100
1060
1030
1010
990
970
920
835
775

α-Al_2O_3 shows well defined bands between 740 and 541 cm^{-1} characteristic of 6-coordinated Al while diffuse bands between 1000 and 500 cm^{-1} result from disordered alumina tetragonally coordinated [83]. The Al-O-Al stretch has also been reported at 800 cm^{-1} [84].

In addition to studying the infrared bands on alkoxide surfaces, the infrared bands from an epoxy surface are also of interest. To gain a better understanding of the epoxy/ alkoxide interactions, EPON 828 with an aromatic amine curing agent was used. DGEBA epoxy resin has been well characterized by IR in the literature. A compiled list of the identified peaks found in the literature for the resin is in Table V [85-87]. Bands have been reported for EPON 828, a DGEBA resin, at 1608, 1510, 1250, 1184, 1035, and 832 cm^{-1}, as well as the epoxy band at 915 cm^{-1} [87].

The cross-linking agent used with EPON 828 is diamino diphenyl sulfone, DDS, whose structure is given in Section II.G. As this primary aromatic amine becomes a secondary or tertiary amine upon cure of the DGEBA epoxy, peaks corresponding to primary, secondary and tertiary aromatic amines, and secondary and tertiary aliphatic amines must be followed. Usually, the C-N stretch of primary and secondary amines absorbs at 1090 - 1020 cm^{-1}, and 1190 - 1170, 1175 - 1130 cm^{-1}, respectively. However, because the electron pair on the nitrogen conjugates with the aromatic ring, the C-N

TABLE V

IR Peak Positions and Assignments for DGEBA

DEGBA (cm^{-1})	Peak Assignment
3603	-OH str.
3077	C-H asym. str. CH_3
2963	C-H asym. str. $-CH_2$
2909	C-H sym. str. CH_3
2857	C-H sym. str. $-CH_2$
1613	substituted aromatics
1587	substituted aromatics
1515	substituted aromatics benzene ring str. [86]*
1370	methyl gp CH_3 bend of gem-dimethyl [86]
1250	aryl-O str. C-O-C asym. str. [87]
1184	C-H inplane def. [87] C-C of isopropylidene gp [86]
1103	phenyl ether
1076	substituted aromatics C-O str. [86]
1031	substituted aromatics C-O str. [86] C-O-C sym. str. [87]
1013	substituted aromatics
917	epoxy gp
865	epoxy gp
833	out of plane bending of p-disubstituted benzene ring [86,87]

* Others not labeled are [85]

bond develops double bond character, thus increasing the frequency of absorption. The C-N stretch of primary and secondary aromatic amines occurs in two bands at 1360 - 1250 and 1280 - 1180 cm^{-1}. Tertiary aromatic amines absorb at 1380 - 1330 cm^{-1}. [66]

The N-H stretch vibration will occur in two bands for primary amines at 3520 - 3450 and 3420 - 3350 cm^{-1}. Secondary amines show one band at 3400 - 3300 cm^{-1}. The N-H deformation vibration will absorb at 1615 - 1580 cm^{-1} for primary aromatic amines. For primary aliphatic amines, the deformation band occurs at 1650 - 1580 cm^{-1} and secondary amines absorb with a weaker band at 1580 to 1490 cm^{-1}. Care must be taken in peak assignment in this region as aromatic ring absorption also occurs in this region.

For organic sulfones, the O=S=O asymmetric stretch occurs at 1360 - 1290 cm^{-1} and 10 - 20 cm^{-1} lower in the solid phase, often in more than one peak. The symmetric stretch occurs at 1170 - 1120 cm^{-1} or at 1180 - 1145 cm^{-1} in the solid phase. The sulfone scissors deformation vibration occurs at 610 - 545 cm^{-1}.

C. Surface Energy of High Energy Surfaces

In a liquid, the molecules in bulk are equally attracted to one another in all directions. At the surface of the liquid, however, there is an unequal force of

attraction causing the liquid molecules to pull inward towards the bulk liquid. This phenomenon gives rise to a drop's spherical shape. The surface free energy of the liquid is the energy required to reversibly and isothermally increase a unit area of surface. When a liquid drop contacts a solid surface, the drop will assume a particular shape due to the interaction of the liquid with the surface. This balance of forces is shown schematically in Figure 15 and is explained by Young's equation below.

$$\gamma_{SV} = \gamma_{SL} + \gamma_{LV} \cos \theta \qquad (32)$$

where γ_{sv} is the surface free energy of the solid in equilibrium with the vapor; γ_{sL} is the interfacial energy of the liquid/solid interface; γ_{Lv} is the surface energy of the liquid/vapor interface; and θ is the contact angle of the liquid on the solid. The air interface can be replaced by a liquid interface to yield an interfacial contact angle measurement. This liquid/liquid/solid contact angle approach, used by Peper and Berch, Tamai et al., and Hamilton, [88-90], was the basis for the determination of the surface free energy of high energy surfaces such as mica and aluminum by Schultz and coworkers [88,91,92]. Here, a high energy solid was immersed in an alkane and the contact angle of a water drop on the immersed surface was measured. In this case, Young's equation becomes

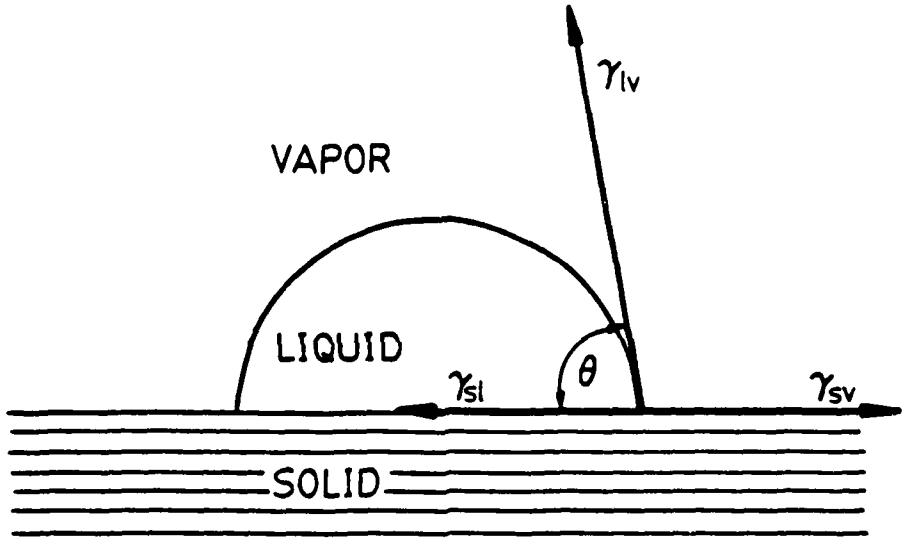

Figure 15. Schematic diagram of the balance of forces when a liquid contacts a solid surface [128].

$$\gamma_{SH} = \gamma_{SW} + \gamma_{HW} \cos \theta_{SW/H} \quad (33)$$

where γ_{SH} is the solid/hydrocarbon interfacial energy; γ_{SW} is the solid/water interfacial energy; γ_{HW} is the water/hydrocarbon interfacial energy; and $\theta_{SW/H}$ is the interfacial contact angle. The solid/liquid interfacial energies can be defined as

$$\gamma_{SH} = \gamma_S + \gamma_H - 2(\gamma_S^D \gamma_H)^{\frac{1}{2}} \quad (34)$$

$$\gamma_{SW} = \gamma_S + \gamma_W - 2(\gamma_S^D \gamma_W^D)^{\frac{1}{2}} - I_{SW}^P \quad (35)$$

where γ_S is the surface energy of the solid; γ_H is the surface energy of the hydrocarbon; γ^D_S is the dispersive component of the surface energy of the solid; γ_W is the surface energy of water; γ^D_W is the dispersive component of the surface energy of water; and I^P_{SW} is the polar interaction parameter.

For "real" surfaces such as pretreated Ti-6-4, corrections for roughness and porosity must be made on the measured contact angles. A roughness coefficient, r, can be obtained by first coating the pretreated surfaces and a smooth glass surface with gold. The contact angle of formamide can be measured on both surfaces. By ratioing the cosine of the contact angle on titanium, θ_{Ti}, to the cosine of the contact angle on glass, θ_g, the roughness coefficient

can be calculated as shown in equation (36).

$$\frac{\cos \theta_{Ti}}{\cos \theta_{g}} = r \qquad (36)$$

The contact angles of water drops on pretreated Ti-6-4 obtained using the interfacial technique, θ_r, can also be corrected for roughness by equation (37) yielding a contact angle, θ_s, for a smooth surface.

$$\frac{\cos \theta_{r}}{r} = \cos \theta_{s} \qquad (37)$$

The correction for a contact angle measured on a porous surface, θ_p, requires a measure of the area of the surface covered with oxide and the area covered with pores, h. Equations (38) and (39) show the correction for the contact angles measured on a porous surface where N is the number of pores per square centimeter and R is the average radius of the pores.

$$\cos \theta_{s} = \frac{\frac{\cos \theta_{p}}{r} + h}{1 - h} \qquad (38)$$

$$h = N(\pi R^2) \qquad (39)$$

By equating equations (33) and (34) and then substituting equation (35) for γ_{sw} the following relation develops

$$[\gamma_W - \gamma_H + \gamma_{HW}\cos\theta_S] = 2(\gamma_S^D)\ [(\gamma_W^D) - (\gamma_H)] + I_{SW}^P \quad (40)$$

By measuring the contact angle of water on the desired solid surface, immersed in a series of alkanes, the dispersive and polar component of that solid surface can be obtained graphically. A plot of the left side of equation (40) versus the bracketed part of the right hand side yields a slope of $2\gamma^p{}_s$ and an intercept of $I^p{}_{sw}$. This approach is based on the assumption that the water drop will displace the hydrocarbon from the solid surface [88]. A prediction for displacement can be calculated by equation (41) where displacement occurs if the inequality holds [93].

$$I_{SW}^P > 2[(\gamma_S^D)^{\frac{1}{2}} - (\gamma_H)^{\frac{1}{2}}]\ [(\gamma_H)^{\frac{1}{2}} - (\gamma_W^D)^{\frac{1}{2}}] \quad (41)$$

The polar component can then be determined by using either the geometric mean, equation (42) or the harmonic or reciprocal mean, equation (43)

$$I_{SW}^P = 2(\gamma_W^P \gamma_S^P)^{\frac{1}{2}} \quad (42)$$

$$I_{SW}^P = \frac{4(\gamma_W^P \gamma_S^P)}{\gamma_W^P + \gamma_S^P} \quad (43)$$

The use of the geometric mean for the dispersive component has been a point of continuing discussion in the literature since Fowkes first proposed it [94]. Others have

also chosen to use the geometric mean and empirically showed its validity with polymer surfaces. Wu [96] has shown that while the geometric mean empirically works for nonpolar polymer systems, it is not applicable to polar/polar systems. He proposes the "reciprocal mean" or the harmonic mean, for the dispersive interfacial energy and for the polar interfacial energies. For the polar or non-dispersive interfacial energies, the geometric mean did not give accurate results. Although Wu uses the reciprocal mean, Schultz et al. [89] showed the geometric mean for polar components of the surface energy of mica empirically fits the data, while the harmonic or reciprocal mean does not.

Once the dispersive and polar components are obtained, where $\gamma = \gamma^P + \gamma^D$, the surface energies can be used to calculate the thermodynamic work of adhesion between x and y using the Dupre equation:

$$W_A = \gamma_x + \gamma_y - \gamma_{xy} \tag{44}$$

The work of adhesion of an epoxy/Ti-6-4 bond in air and water can be calculated by equations (45a) and (45b), assuming values of 37.2 and 8.3 for $\gamma^D{}_E$ and $\gamma^P{}_E$ of the epoxy, respectively [97].

$$W_A = 2[(\gamma^D_{Ti}\gamma^D_E)^{\frac{1}{2}} + (\gamma^P_{Ti}\gamma^P_E)^{\frac{1}{2}}] \tag{45a}$$

$$W_A = 2[\gamma_W - (\gamma_{Ti}^D \gamma_W^D)^{1/2} - (\gamma_{Ti}^P \gamma_W^P)^{1/2} - (\gamma_E^D \gamma_W^D)^{1/2} - (\gamma_E^P \gamma_W^P)^{1/2} + (\gamma_{Ti}^D \gamma_E^D)^{1/2} + (\gamma_{Ti}^P \gamma_E^P)^{1/2}] \quad (45b)$$

D. Acidity/Basicity of Solid Surfaces

Two important intermolecular interactions are London dispersion forces and electron donor-acceptor or acid-base interactions with H-bonding falling into the acid base category [98-100]. In adhesion science, understanding the acid-base interactions between metal oxides and primers or polymer adhesives, will aid significantly in first explaining existing data and secondly in designing better bonds.

A metal oxide surface is covered with hydroxyl groups and molecular water as depicted in Figure 16 [99]. How the hydroxyls are bound to the metal oxide, will determine their acidity (see Section A.2) and thus how the oxide surface interacts with the polymer. In hydrothermal durability studies, a third issue comes to play, namely the mechanism of water displacement. Here, water reaches the interface and disrupts the bonds between the polymer, HXR or XR, and the oxide, MOH, as shown below [99]:

$$\begin{matrix} H \\ M\text{-}O - - - HXR \end{matrix} + 2H_2O \quad <-> \quad \begin{matrix} H \\ M\text{-}O - - - HOH \end{matrix} + H_2O - - - HXR \quad (46)$$

$$M\text{-}O\text{-}H - - - XR + 2H_2O \quad <-> \quad M\text{-}O\text{-}H - - - OH_2 + HOH - - XR \quad (47)$$

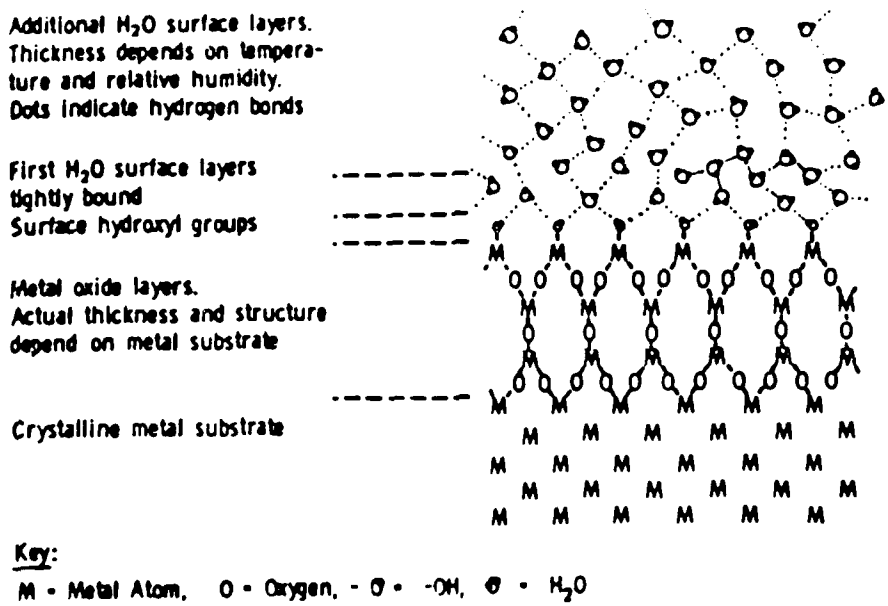

Figure 16. Schematic representation of water and oxide layers on a metal surface [99].

where X would typically be O, S, or N. Bolger [99] suggests that there is an optimum concentration of polar groups on the polymer so that an equal match occurs between the acid-base groups of the oxide and the polymer.

Indicator dyes can be used to determine the relative acidity/basicity of a surface. First a brief introduction to solid acids and bases will be given, followed by a description of a common chemical group of indicators.

The acid strength of a solid is its ability to convert an absorbed neutral base to its conjugate acid. If this reaction takes place via proton transfer (BrÖnsted acidity), the acid strength can be described by the Hammett acidity function, H_o:

$$H_o \equiv -\log a_{H^+} \frac{f_B}{f_{BH^+}} \qquad (48)$$

or

$$H_o = pK_A + \log [B]/[BH^+] \qquad (49)$$

where a_{H^+} is the proton activity, f is the activity coefficient, [B] is the neutral base concentration and [BH] is the conjugate acid concentration [101,102]. If the reaction occurs by transfer of an electron pair (Lewis acidity) from the adsorbate to the surface, H_o is defined as follows [101,102]:

$$H_o \equiv -\log a_A \frac{f_B}{f_{BA}}$$

or

$$H_o = pK_A + \log$$

AD-A189 503 AN INTERDISCIPLINARY APPROACH TO PREDICTIVE MODELING OF STRUCTURAL ADHESI.. (U) VIRGINIA TECH CENTER FOR ADHESION SCIENCE BLACKSBURG J A FILBEY ET AL. OCT 87 2/4

UNCLASSIFIED CAS/CHEM-87-7 N00014-82-K-0185 F/G 11/1 NL

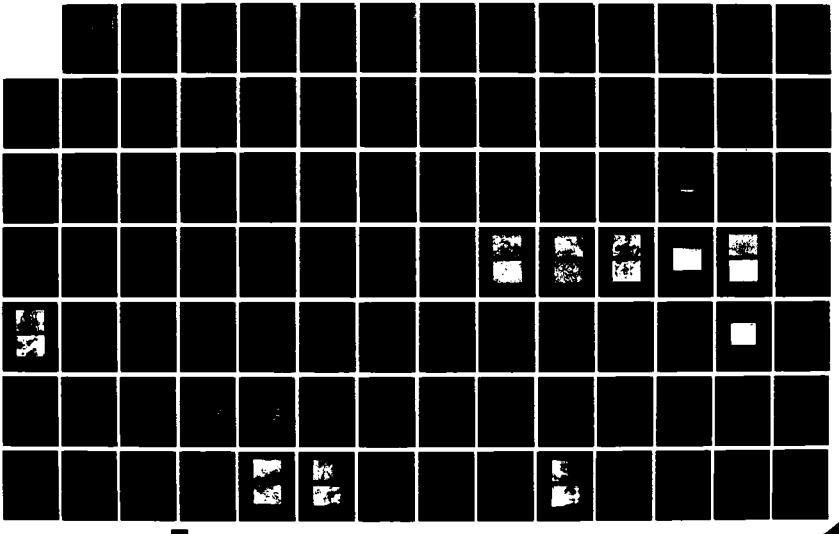

The basic strength of a solid surface is the ability to convert an adsorbed electronically neutral acid to its conjugate base, or the ability to donate an electron pair to the adsorbed acid. When the adsorbed acid is an indicator dye, a reaction such as:

$$AH + B \leftrightarrow A^- + BH^+ \qquad (52)$$

where AH is the indicator dye and B is the solid base. The basic strength of B can be defined by:

$$H_o = pK_A + \log [A^-]/[AH] \qquad (53)$$

where $[A^-]$ is the basic form and [AH] is the acidic form of the indicator [101].

The color of the indicator dye is an indication of the acidity/basicity of the surface. If the indicator dye is the color of the acid form, H_o is equal to or less than the pK_A of the indicator. The lower the pK_A and the lower the H_o, the more acidic the surface [101]. By selecting a series of indicators, preferably from analogous chemical groups so that the mechanism of color change is the same, the acidity/basicity of the surface can be bracketed.

To assign a number to the acidity/basicity of a surface, several assumptions need to be made. For example, the first change in color is perceived when 10% of the indicator is in its basic form,

$$[A^-]/[AH] = 0.1/0.9 \approx 0.1 \qquad (54)$$

A further increase in intensity is only perceived after 90% of the indicator is in its basic form or,

$$[A^-]/[AH] \approx 10. \quad (55)$$

H_o, for the initial change, is equal to $pK_A - 1$ and for the final change is equal to $pK_A + 1$. The assumption, then, is that the intermediate color change occurs when 50% of the indicator dye is in the basic form, or

$$[A^-]/[AH] \approx 1 \quad (56)$$

so that $H_o = pK_A$, and the value of the basic strength of the surface is the pK_A. This assumption will be used in this study. Another assumption will be that the indicators do not distinguish between Brönsted and Lewis acidity and the measured acidity will be the sum of both types.

One chemical group of indicator dyes is the sulphonephthaleins which are often used because of their sharp color changes and good intensities [103]. Figure 17 shows a series of sulphonephthalein indicator dyes with the pK_A values listed below each structure. As compared to the parent compound of this group, phenol red, whose forms are shown in Figure 18 [103], these are in their acid form. The ease in which they convert to the base form is controlled by the substituents on the phenyl rings. Halogens, such as bromine, are electron withdrawing groups, whereas $-CH_3$ groups are electron donating. For example, on bromophenol blue, the bromines withdraw electron density from the -OH

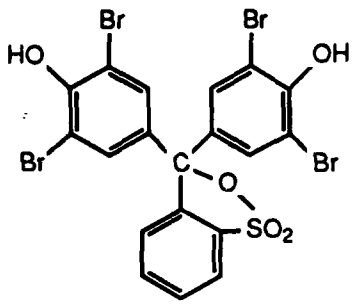

Bromophenol Blue
3.0 - 4.6

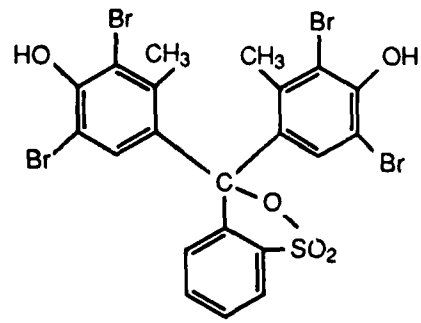

Bromocresol Green
3.8 - 5.4

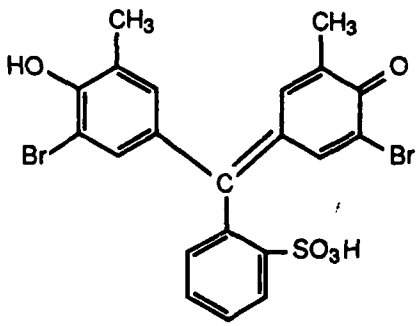

Bromocresol Purple
5.2 - 6.8

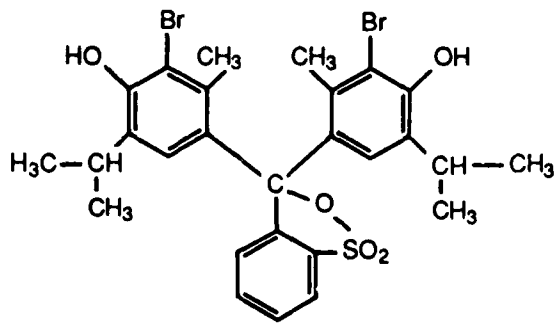

Bromothymol Blue
6.0 - 7.6

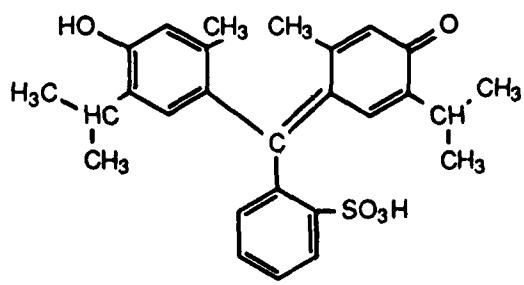

Thymol Blue
1.2 - 2.8 , 8.0 - 9.6

Figure 17. Series of sulphonephthalein indicator dyes [103].

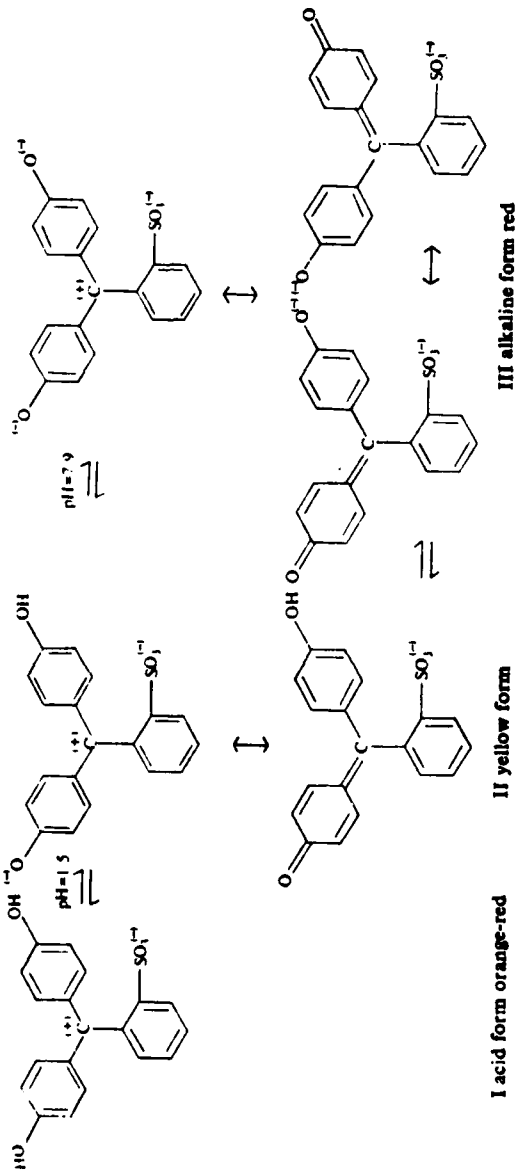

Figure 18. Structural changes causing color changes in phenol red [103].

groups, making it easy for the proton to be donated, changing to its basic form. Thus, bromophenol blue has a lower pK_a than bromocresol purple where one bromine has been replaced by an electron donating group, $-CH_3$.

E. Adhesive Bonding

1. General discussion

Adhesive bonding offers advantages over conventional means of fastening, such as welding or riveting, due to the better strength to weight ratio, uniform stress distribution along the bond line, and corrosion resistance. While adhesives are now being used to join materials in load bearing structures, the problem of bond durability in hot, wet environments still exists. Water in the glue line may change the properties of the adhesive, as water plasticizes the adhesive, causing a decrease in strength [104]. The adhesive/adherend interface is also affected by water. Sargent and Ashbee [105] used an interference technique to measure the swelling of an epoxy/titanium bond. As water enters the bond line, water solubles in the adhesive can collect in areas of delamination at the interface. Because the chemical potential of water in the pockets is lower than the surrounding water medium, the pressure of the interfacial liquid increases causing expansion of the delamination zone and ultimately failure.

The deleterious effect of water on an adhesive bond can also be explained by water hydrolyzing physical interactions and/or chemical bonds between the adhesive and adherend, decreasing joint strength [106]. Natan and Venables [107] believe that the oxide layer on an adherend, such as aluminum or titanium, undergoes a transformation in the bond line which causes destruction of the adhesive/adherend interface while Kinloch and others [108] suggest the oxide transformation occurs after delamination of the adhesive from the adherend. Gledhill and Kinloch [108] measured both the fraction of interfacial failure and the fraction of corrosion with time in different water temperatures for steel/epoxy bonds. They found that the activation energy for interfacial failure was similar to that of diffusion of water into the epoxy, while the activation energy of corrosion was much higher. Thus, the debonding was caused by the water at the interface not by corrosion of the steel.

The "weak boundary layer" argument has also been used as the scapegoat for poor bond durability. At the interface, the adhesive may undergo a cross-linking different than in the bulk, causing a layer with weaker mechanical properties. Brockmann and coworkers [109] show, by TEM of microtomed aluminum/epoxy sections, bright areas at the interface indicating a lower density material. The adhesive at the interface has a lower density because it is

not as highly cross-linked.

Poor hydrothermal durability has thus been attributed to osmotic pressure of water in delamination zones, to hydrolysis of physical and chemical bonds between the adhesive and metal oxide, to transformation of metal oxide, to diffusion of water into the adhesive, and to weak boundary layers formed between metal oxide and adhesive.

Structural adhesives are usually highly cross-linked, high modulus, low creep, but brittle materials [108,110]. The adhesives are, therefore, modified or "toughened" with elastomers which phase separate upon cure. This phase separation allows the adhesive matrix to maintain its high modulus, while the elastomer toughens the "composite" material. The toughening mechanism is thought to occur because of the larger crack-tip deformation zone in toughened adhesives compared to brittle ones. The crack-tip is blunted, decreasing the local stress concentration at the crack tip, thus requiring higher loads to fail the material [110]. Because of the rubber modification to the brittle adhesive, the fracture energy of the adhesive bond now depends on the bond line thickness. The amount of adhesive used to join two materials will affect the strength of the bond. Bascom shows the effect of bond line thickness on fracture energy in Figure 19. For bond lines thinner than the optimum, the size of the crack-tip deformation zone is

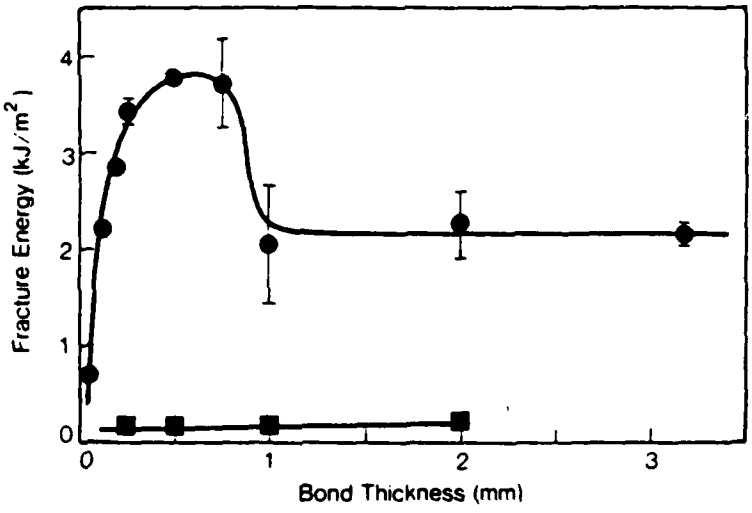

Figure 19. Adhesive fracture energy vs. bond line thickness for epoxy and rubber modified epoxy [110].

restricted, thus limiting the toughening mechanism of crack-tip blunting. When the bond line is thicker than the optimum, high stress fields can form well ahead of the crack tip and extend down the bond line, yielding a lower fracture energy [110].

2. Roughness and pore penetration

Fowkes [94] has shown, using a simple interparticle interaction calculation that by van der Waals forces alone, the ideal bond strength for a given area of a polyethylene/iron interface far exceeds any measured tensile bond strength. While theoretically a rough adherend surface may not be necessary, other considerations in addition to adhesive/adherend interactions, such as van der Waals, must be taken into account. For example, the moduli of the adherend and adhesive may be different, causing stress concentration at the interface. If the adherend is roughened, the stress may be better transferred from adherend to adhesive [111,112]. Roughening the adherend surface can provide a surface with contaminants removed, increased surface area, miniature scarf-like geometries and enhanced spreading of the adhesive. Undesirable features such as abrasive particles remaining on the surface and incomplete wetting of the surface by the adhesive may also occur with roughening the adherend surface [112]. Incomplete wetting

can cause air to be trapped between the adhesive and the adherend, providing stress concentrations at the interface.

The penetration of adhesives into crevices and pores on an adherend surface has been a concern of many adhesion scientists. Brockmann and coworkers [113a] showed using TEM and EELS that the primer penetrated the aluminum oxide pores. However, if only the smaller molecules enter the pores, a different cross-link density will occur perhaps causing a weak boundary layer. In addition to experimental techniques such as microtomy with TEM, fracture analysis by STEM, XPS, and AES with depth profiling, the depth of penetration of an adhesive into a porous structure can be calculated. The epoxy will penetrate a cylindrical pore until the back pressure of trapped air in the pore equals the capillary driving force of filling the pore. The distance of penetration, x, will depend upon the length of the pore, L, the radius of the pore, r, the surface energy of the epoxy, γ_{LV}, the contact angle of the adhesive in the pore, θ, and the atmospheric pressure, P_A, as shown below [113]:

$$x = L \left[1 - \frac{P_A r}{2 \gamma_{LV} \cos\theta + P_A r} \right] \quad (57)$$

3. Wedge test

In adhesively bonded structures, there are three basic

modes of failure as illustrated in Figure 20. Mode I is opening or cleavage, Mode II is forward shear, and Mode III is sidewise shear or torsion. A Mode I environmental test is capable of distinguishing between adequate, marginal and poor pretreatments. Marceau and coworkers proposed a variation of the uniform double cantilever beam test - the wedge test [114]. Instead of a constant load, being applied to the double cantilever beam sample, a constant displacement, namely the wedge, is applied to the wedge sample. G_1, the strain energy release rate, takes on a different meaning. For the constant load, double cantilever beam test, G_1 is the energy required for crack propagation; whereas, for the constant displacement or wedge test, G_1 is the energy for crack arrest. As the crack length increases, the strain energy release rate or G_1 decreases, thus yielding a potential for defining "threshold values" for G_1 [114]. G_1 is calculated for the wedge test as shown below [114-116]:

$$G_1 = \frac{y^2 M h^3 (3 (a + 0.6h)^2 + h^2)}{16 ((a + 0.6h)^3 + ah^2)^2} \qquad (58)$$

where y is the displacement at load point or the wedge thickness, a is the distance from load point to crack tip, h is the height or thickness of the adherend beam, and M is the modulus of the adherend beam. The terms 'h²' and 'ah²' serve as the shear contribution to the elastic energy of the adherend. An empirical average correction for the rotation

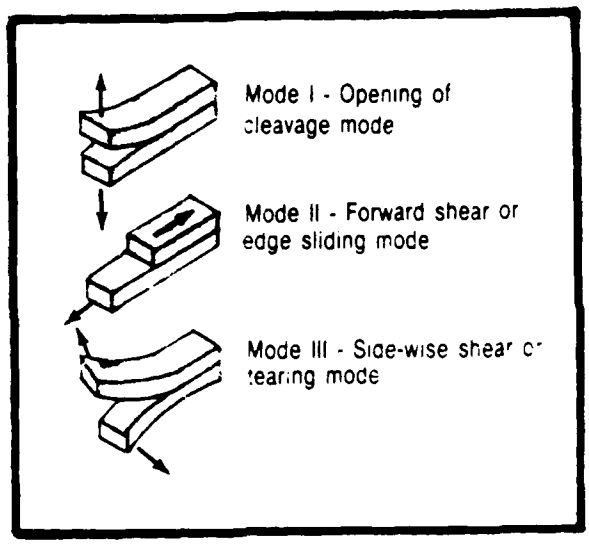

Figure 20. Basic loading modes [114].

of the adherends ahead of the crack tip is made by the 0.6h term [116]. Equation 58 is valid only if the adherends deform elastically. If the adherend surface strain, ε, is given by:

$$\varepsilon = \left[\frac{3\,G}{M\,h}\right]^{\frac{1}{2}} \qquad (59)$$

then, the adherend bending will be elastic only if :

$$G \leq \frac{M\,h\,\varepsilon_y^2}{3} \qquad (60)$$

where $\varepsilon^2{}_y$ is the adherend yield strain [116].

Results of the wedge test have correlated with in-service experience. Marceau et al. [114], cut wedge, lap shear, and climbing drum samples from aircraft panels which had both failed and remained intact in-service. While neither the lapshear test or the climbing drum test samples correlated with the inservice performance, the wedge test showed similar trends to inservice failures.

4. Lap shear test

Shear properties of adhesives are tested by tension loading in the lap shear test. ASTM-D1002-72 describes the requirements for the test [117]. In reality, the lap shear geometry tests by both Mode I and Mode II, due to the stress

concentration at the edges of the overlap [114]. Figure 21 shows the deformation of the lap shear joint when a load is applied. The shear stresses in the joint are shown in Figure 22 [118].

5. Stress durability test

As the purpose of test specimens is to predict service failures, the lap shear test alone is not adequate. If a lap shear bond is loaded and then placed in a hot-wet environment, the fractures can be characteristic of in-service failures. Marceau et al. [114], showed that unstressed lapshear joints maintained their original strength when exposed to aqueous environments, whereas the stressed lapshear joints failed much more rapidly.

F. Metal Alkoxides

1. Introduction

Metal alkoxides have been used in sol/gel chemistry and in the formation of glasses for many years [77,123-126]. A new found application of these alkoxides is to use them as primers on adherend surfaces to enhance bond durability [119-122]. The primer use is a new area, with little study and understanding, thus an open field for investigating both adhesion and chemical properties of the alkoxide coatings.

Figure 21. Deformation of a lap shear joint when load is applied [118].

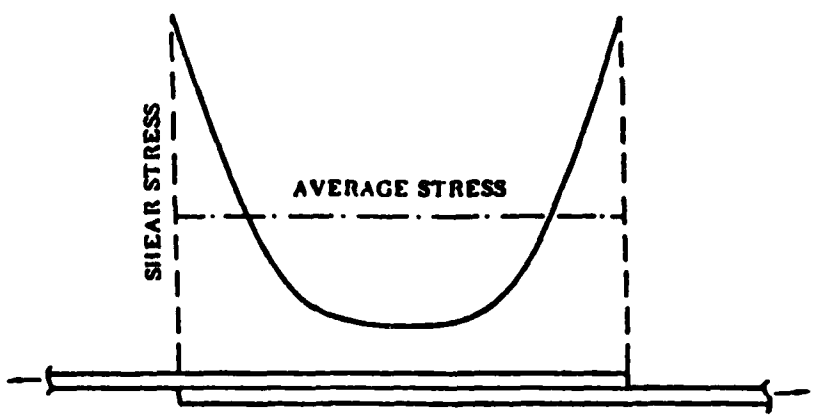

Figure 22. Shear stress in a lap shear joint [118].

2. Alkoxides in adhesive bonding

Organic primers are often applied to metal adherends following chemical pretreatment to protect the surface prior to adhesive bonding and to enhance bond durability. Pike found that inorganic primers, such as metal alkoxides, improved the durability of aluminum/epoxy bonds. Sec-butyl aluminum alkoxide, applied to both porous and non-porous aluminum oxide surfaces, improved the durability of bonds made with a 177° C cure epoxy four to ten times over organic primers [119-121]. Enhanced durability was also observed for 121° C cure epoxy systems [120]. The sec-butyl aluminum alkoxide was applied from a 1% solution in toluene creating a smooth primer layer masking the original adherend aluminum oxide topography. The bond durability depended upon the thickness of the alkoxide primer layer. Bonds made with alkoxide primer layers of 450 nm or greater showed improved durability over thinner alkoxide primer layers [119,121]. The primer layers were cured at temperatures between 25° and 325° C. The durability of the bonds was not affected by the cure temperature of the primer [119-121].

The reason for this enhanced durability of aluminum/ epoxy bonds using an inorganic or alkoxide primer in place of the conventional organic primer is not clear. Pike postulates that the mechanism for this improvement is the formation of a stable amorphous boehmite, AlO(OH) layer upon

hydrolysis of the alkoxide primer. The hydrolysis may occur by water of hydration on the oxide of the adherend, by water in the solvent or by atmospheric moisture. The hydrolysis would yield not only the oxide, but also the alcohol which would evaporate with the application solvent [119,120]. Because the resulting primer layer is smooth, mechanical interlocking arguments commonly used for porous and rough surfaces to explain good durability cannot be used. An alternate explanation for the improved durability would be a chemical interaction between the alkoxide primer and the epoxy [120,122]. Another possibility would be that the primer reduces the chances for weak boundary layer formation [122] because the surface is no longer rough or porous where it is believed segregation of an adhesive can occur [109]. Thus, the phenomenon of inorganic primers enhancing bond durability has been observed; however, understanding the nature of the alkoxide interaction with the adherend surface and the adhesive is still an open question.

3. Chemistry of alkoxides

Although new to adhesive bonding, metal alkoxides are not new to chemistry. Sol/gel studies involving metal alkoxides have received much attention in the formation of glasses. To better understand the chemistry of these metal alkoxides primers, a look into the solution chemistry of

metal alkoxides may provide insight.

Metal alkoxides hydrolyze to form metal hydroxides or metal oxides and alcohol as shown by the following generalized reactions:

$$M(OR)_v + vH_2O \rightarrow M(OH)_v + vROH \quad (61)$$

$$M(OH)_v \rightarrow MO_{v/2} + (v/2)H_2O \quad (62)$$

where M is the metal, R is the alkyl group, and v is the valence of the metal [123]. Usually, the hydrolysis of metal alkoxides is not as straight forward as the above reactions indicate. A hydrolysis and a polymerization reaction occur simultaneously as shown below for a metal with a valence of four, such as titanium,

$$\equiv M\text{-}OR + HOH \rightarrow \equiv M\text{-}OH + ROH \quad (63)$$

$$\equiv M\text{=}OH + RO\text{-}M\equiv \rightarrow \equiv M\text{-}O\text{-}M\equiv + ROH \quad (64)$$

Here, both reactions occur between the OR and the OH groups with the polymerization reaction forming bridging oxygens. Note that if complete hydrolysis occurred, polymerization would be impossible, thus no bridging oxygens would be present. Many parameters affect the rates of hydrolysis and polymerization: the type of alkoxide, the availability of water and hence the alkoxide/water ratio, the dilution of the system, the type of solvent, and the reaction temperature [123-125].

Aluminum alkoxides hydrolyze vigorously to form monohydroxides initially which later convert to trihydrox-

ides as shown below [123,125].

$$Al(OR)_3 + 2H_2O \rightarrow AlOOH + ROH \quad (65)$$

$$AlOOH + H_2O \rightarrow Al(OH)_3 \quad (66)$$

The hydrolysis product of sec-butyl aluminum alkoxide depends upon the reaction temperature and medium. Non-liquid hydrolysis by atmospheric moisture produces an amorphous monohydroxide, while hot water hydrolysis creates a crystalline monohydroxide or boehmite. A trihydroxide, or bayerite, forms when the alkoxide is hydrolyzed in cold water [123,126]. When the amorphous boehmite is heated to 300° C, amorphous γ-alumina can form [127].

Titanium alkoxide hydrolysis is very complex [124]. The hydrolysis and polymerization reactions are similar to equations (63) and (64). Titanium differs from aluminum in that it doesn't have multiple forms of hydroxides [123]. The oxide content of the final reaction product or oxide polymer depends upon the amount of water initially present. The variability of oxide content in the polymerized alkoxide is described by the following [124]:

$$nTi(OR)_4 + (4n + x - y)H_2O \rightarrow \quad (67)$$

$$Ti_nO_{(2n-(x+y)/2)}(OH)_x(OR)_y + (4n - y)R(OH)$$

where n is the number of polymerized titanium ions, x is the number of OH groups and y is the number of OR groups in the molecule.

G. EPON 828/ DDS

EPON 828 (Shell) is a diglycidal ether of bisphenol A or DGEBA, epoxy resin with a repeat unit, n, between 0 and 1. EPON 828 is viscous, 10,000 to 16,000 cp, with a molecular weight of approximately 380 g/mol and the following structure [85]:

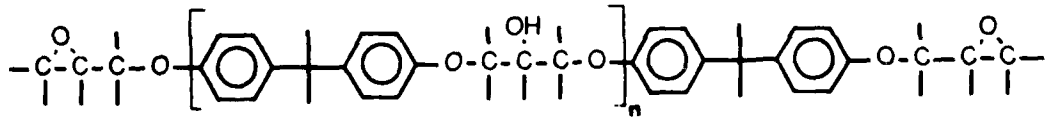

(68)

4-aminophenyl sulfone (Aldrich), or DDS, with a molecular weight of 248.3 g/mol, is an amine curing agent with the following structure:

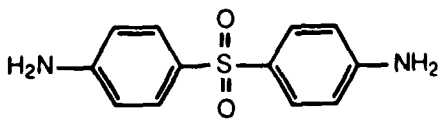

(69)

The mole ratio for the cross-linking reaction to occur as:

(70)

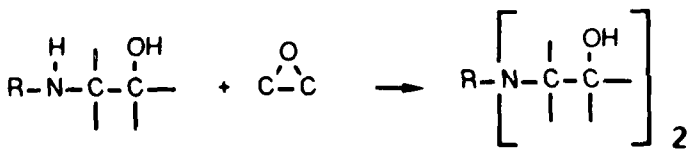

is 2 mol EPON 828 to 1 mol DDS. This mole ratio equals a weight ratio of 75 wt% EPON 828 to 25 wt% DDS.

The EPON 828/DDS system was chosen as a model because DGEBA is well characterized in the literature and DDS is an amine curing agent. Although FM-300 composition is proprietary, it is thought to contain a bisphenol based epoxy with an amine-type curing agent.

III. EXPERIMENTAL

A. Materials

Ti-6Al-4V was the only alloy used in this study. Three forms were used - lap shear coupons supplied by NASA Langley, 2.54 x 12.7 x 0.13 cm; wedge coupons supplied by RMI Titanium, 2.54 x 15.24 x 0.38 cm; and foil purchased from Arnold Subsidiary Magnetics and Electronics, Inc., 0.0038 cm thick. Table VI lists the specifications of the wedge material obtained from RMI Titanium.

Ferrotype plates (Thompson Photo Products) provided a reflective substrate for reflectance infrared spectroscopy. The steel plates, 10.51 cm thick, were coated with nickel and an 80 nm chromium overlayer.

A 175° C cure rubber-modified structural epoxy unscrimmed film adhesive, FM-300U (American Cyanamid) was used for all adhesive bonding. It was stored at -18° C.

Tetra-iso-propyl titanate, TIPT, tetra-n-butyl titanate, TNBT, and sec-butyl aluminum alkoxide, E-8385, were obtained from Stauffer Chemical Company. All three alkoxides are lightly colored viscous liquids which hydrolyze vigorously with water and therefore must be stored in a desiccator.

EPON 828, (Shell), a viscous, lightly colored liquid was used as received. The cross-linking agent, diaminodiphenyl sulfone, DDS, a white powder (Aldrich) was

TABLE VI

Specifications for Ti-6Al-4V

Element	%
C	0.01
N	0.014
Fe	0.15
Al	5.9
V	3.8
O	0.117
Ti	Remainder

recrystallized in methanol and water before use.

All chemicals unless otherwise indicated were obtained from Fisher Scientific Company.

B. Sample Preparation

1. Pretreatments of Ti-6-4

The Ti-6-4 adherends were pretreated by four methods prior to analysis or adhesive bonding - chromic acid anodization, CAA; sodium hydroxide anodization, SHA; phosphate/fluoride acidic etch, P/F; or TURCO basic etch, TURCO. Details of the pretreatment procedures are listed in Appendix A. The designation PSHA indicates a pickling step preceded anodization in SHA treatment.

2. Ferrotype plates

Ferrotype plates were cut as disks (2.54 cm in diameter) for substrates in the XPS analysis of films or as 2.54 cm square plates for substrates in FTIR analysis. They were cleaned with acetone, soap and water and dried prior to plasma cleaning. An oxygen plasma was generated in a Plasmod TM dry asher using 50 to 70 watts of radio frequency power. The Plasmod was run for 20 min prior to use. The cleaned samples were then placed in the Plasmod for 20 min. Upon removal, the samples were rinsed with deionized water and dried with prepurified nitrogen immediately before use.

3. Polished Ti-6-4

Ti-6-4 disks (2.54 cm in diameter) were cut from lap shear coupons and polished for infrared reflectance studies. Hand held brass pieces were constructed to hold the disks for the polishing wheels. A series of fixed diamond or silicon carbide polishing wheels were used from 168 to 600 mesh, stepping to the next finer wheel only when the titanium disk was covered with uniform scratches. A felt wheel was then used with 0.3 μm α-alumina slurry. The polished disks were finally placed in a vibrating bath containing either Buehler Mastermet colloidal silica or 0.05 μm ß-alumina deionized water slurry overnight for the final polish. The disks could not stay in the vibrating bath longer or corrosion of the polished surfaces would occur. Once a visibly scratch free-surface was obtained, the polished Ti-6-4 disks were plasma cleaned as described above.

4. Aluminum oxide preparation

Three model aluminum oxides were prepared to determine the XPS binding energies and atomic percents for each oxide. $Al(OH)_3$ was prepared by placing commercially pure aluminum foil (CP Al foil from ALCOA) in boiling water for four h. Al_2O_3 was prepared by heating CP Al foil in air at 525° C for six h in a type 1550 Thermolyne furnace. The sample was

cooled in a desiccator before analysis. Amorphous hydroxide, AlOOH, was prepared by first placing the CP Al foil in boiling water containing triethanol amine (TEA) (approximately 0.15 ml TEA to 500 ml water; pH = 8.5) for 3 to 4 h and then heating the sample in air at 325° C for 2 h. All samples were analyzed by XPS within 15 min of removal from treatment conditions.

5. Metal alkoxides

Three metal alkoxides were studied as adhesion promoters - tetra n-butyltitanate, TNBT, tetra iso-propyltitanate, TIPT, and sec-butyl aluminum alkoxide, E-8385. Weight/weight percent solutions were prepared in a glove bag under a dry nitrogen atmosphere to prevent atmospheric hydrolysis of the alkoxides. Typically, 1 wt% solutions were prepared in dry toluene. The toluene was dried by stirring it over calcium hydride overnight and distilling it into a dry flask containing activated 4 Å molecular sieves.

The alkoxide solutions were applied to the polished Ti-6-4 or the ferrotype plates by spin coating or by brush coating. The ferrotype or Ti-6-4 plates were attached to the spin coater plate with double stick tape. The plates were then flooded with solution and spun at approximately 1500 to 1600 rpm for 5 to 10 sec in laboratory atmosphere. Solutions were brush coated in one or five coats on the

ferrotype or Ti-6-4 plates in a glove bag purged with dry N_2, allowing each coat to visibly dry before the next was applied. The alkoxide coatings were then cured at either room temperature under vacuum or at 300° C for 2 to 24 h. Transfer of the samples from glove bag to vacuum or oven was made in normal laboratory atmosphere.

6. EPON 828 / DDS

Model epoxy films on aluminum alkoxide substrates were studied to better understand the interaction of the FM-300 with the alkoxide primed adherends. Neat films of EPON/DDS were made for transmission infrared as well as dilute solutions in methylene chloride for reflectance infrared and XPS analysis. The EPON 828 was first heated in an oven at approximately 70° C to decrease the viscosity for ease in handling. 7.5 g of the resin was weighed on a top load balance into a 50 ml Erlenmeyer flask with a stir bar large enough to completely sweep the bottom of the flask. The flask was then placed under vacuum with a cold trap, heated and stirred in an oil bath at 65° to 75° C for at least one h to remove any moisture or dissolved volatiles. The temperature was then increased to 140° C, the vacuum removed for the addition of 2.5 g of DDS, and replaced. The mixture was allowed to stir until the DDS had completely dissolved, usually 15 to 25 min. Upon dissolution of the DDS, films

were cast onto aluminum foil and allowed to sit overnight. They were then cured in air at 160° C for 1 h and at 210° for 1 h.

Weight/weight percent solutions of EPON 828/DDS were made in methylene chloride using a 75% EPON 828 to 25% DDS ratio and shaken overnight. The solutions were then spun coat onto uncoated or alkoxide coated reflective metal substrates for reflectance infrared analysis. The films were cured in air at 160° C for 1 h and at 210° C for 1 h.

C. Instrumental Techniques

1. Scanning electron microscopy, SEM, and scanning transmission electron microscopy, STEM

The surface topography of pretreated Ti-6-4 surfaces was studied using SEM and STEM. SEM was done on a JEOL JSM-35-c electron microscope. Pretreated samples were punched as 0.95 cm disks and sputter coated with 20 nm of gold. This coating reduced the effect of charging of the sample by the electron beam. Stereophotomicrographs were also taken. At 200 x and at the tilt of interest, the sample was focussed. A spot on the sample was aligned with a center point marked on the screen. The z-axis was adjusted so that the spot chosen on the sample remained in line with the center point on the screen when the tilt axis was rotated +/- a few degrees. Next, the sample was photo-

graphed at the desired magnification. The sample was then tilted +/- 7 degrees while keeping the spot on the sample aligned with the center spot of the screen using the x- and y- axis controls and a second picture taken. By placing the higher angle photograph on the left side, the pictures were aligned so a stereo image could be viewed through stereo glasses.

STEM pictures were taken on a Philips EM-420T electron microscope. Ti-6-4 foil was pretreated and cut to 3 by 8 mm pieces. The samples were conductive, so coating the samples to prevent charging was not necessary.

2. XPS

XPS is a powerful tool which was used in all phases of the study. Chemical composition and reproducibility of surface pretreatments was determined. After adhesive bonds had been tested, the failure surfaces were analyzed by XPS to determine the locus of failure. The composition, thickness and patchiness of alkoxide coatings on ferrotype plates was also studied by XPS.

Three XPS instruments were used in these investigations. Spectra were obtained from a Physical Electronics SAM 550 spectrometer at Polyscientific using a double pass CMA. Both the KRATOS XSAM 800 and the PHI 5300 ESCA system used a hemispherical analyzer. The KRATOS analyzer was run

in the FRR mode, while the PHI 5300 analyzer was run in the FAT mode. A magnesium x-ray anode was used in all instruments at a power of 250 W. Sample sizes of the pretreated and failure surfaces were 0.95 cm diameter disks. Ferrotype plates were 2.54 cm diameter disks. Samples were usually scanned over a binding energy range of 0 to 1000 eV. Narrow scans were done on any significant peaks noted in the wide scan spectrum.

On the PHI 5300 ESCA system, angle dependent studies were done to change the analysis depth. In addition to the usual 90° take-off angle, take-off angles of 60°, 45°, 30°, 15°, and 10° were used in the analysis of alkoxide films.

The effect of temperature on the pretreated oxides was studied in the KRATOS spectrometer. Coupon and foil samples were mounted with screws to the probe and placed into the vacuum chamber of the spectrometer. The samples were then heated by conduction to 350° and 450° C, held at that temperature for 10 min, and cooled back to room temperature quickly by liquid N_2 running through the probe. Spectra were collected before and after heating to determine if any chemical change occurred in the oxide after heating. Upon removal from the XPS, the foil samples were immediately placed in the STEM for observation of possible topographical changes.

In some cases, spectra from the KRATOS and PHI instru-

ments were curve fit. Because the energy resolution of the KRATOS is lower than the PHI, the full width at half maximum, FWHM, of the photoelectron peaks will be larger. To determine the correct FWHM to use, standards such as polydimethyl siloxane, PDS, and TiO_2 powder were analyzed and the C 1s, O 1s, Si 2p, and Ti 2p peaks curve fit. With these "models", real sample spectra were curve fit using an appropriate FWHM.

An XPS standard sample of PDS, whose C:O:Si ratio is 2:1:1 was analyzed on the PHI instrument to assure proper calculation methods were being used to obtain the atomic percents, as well as to determine a FWHM. Table VII lists the XPS analysis. The ratio of 2.2:1.0:1.1 closely agrees with the expected ratio, thus assuring that proper procedures are used for atomic percent calculations. The FWHM for the oxygen and carbon peaks was 1.4 eV.

Spectra of TiO_2 powder were collected on the KRATOS and the PHI instruments and the FWHM of the O 1s and the Ti 2p3 obtained. Table VIII lists the XPS analysis. The FWHM on the KRATOS for the O 1s and the Ti 2p3 peaks is 1.6 eV and 1.4 eV, respectively. The TiO_2 spectra from the PHI instrument shows an O 1s curve fit FWHM of 1.4 eV and 1.3 eV for Ti 2p3. The O/Ti ratio from the curve fit oxygen peak is 2.3, slightly higher than the expected 2.0.

TABLE VII

XPS Analysis of Polydimethyl Siloxane Standard

ELEMENT	B.E.	A.P.	C : O : Si	FWHM
C 1s	285.	50	2.2	1.4
O 1s	532.6	23	1	1.4
Si 2p	102.4	27	1.1	

TABLE VIII

XPS Analysis of TiO_2 Powder

SPECTROMETER	ELEMENT	B.E.	A.P.	FWHM
KRATOS	C	285.	42.	
	O	529.7	44.	1.6
	Ti	458.5	14.	1.4
PHI	C	285.	40.	
	O	529.9	44.	1.4
			34.*	
	Ti	458.7	15.	1.6

* Curve fit A.P. of O 1s contribution to O-Ti bond

3. AES

AES was used to determine the chemical composition of pretreated Ti-6-4 oxides by taking wide scans. Narrow scans were collected between 300 eV and 600 eV to study the titanium line shapes for insight into the stoichiometry of the oxides. Relative oxide thickness and changes in the chemistry of the oxides with depth were studied by depth profiling with Ar^+ ions. Some initial AES wide scans were collected on a Physical Electronics SAM 500 spectrometer. The other wide scans, narrow scans, and the depth profiles were collected on a Perkin-Elmer PHI 610 scanning Auger microprobe with an electron beam voltage of 3 to 5 kV and a beam current of 0.05 μA. Samples were depth profiled by argon ion sputtering with an ion beam current of 0.2 μA.

4. SIMS

Dynamic SIMS spectra were collected on a Perkin-Elmer PHI 610 scanning Auger microprobe from the pretreated Ti-6-4 surfaces to gain insight into the chemical composition of the surface oxide. Mass to charge ratios ranged from 1 to 200 AMU. Spectra were taken with and without an in-bleed of oxygen. Peak heights were measured with a ruler on the log scale and converted to an equivalent linear length to calculate the atomic abundance.

5. FTIR

Grazing angle reflectance Fourier transform infrared spectrometry was used to study thin alkoxide and epoxy films on reflective ferrotype plates and polished Ti-6-4 surfaces. A grazing angle reflectance attachment, shown in Figure 23, [129] was used in either Nicolet 5DX or 5DXB spectrometers. The sample chamber was purged with nitrogen for 30 to 60 min before a spectrum from 4600 to 400 cm^{-1} was obtained.

Two detectors, a deuterated triglycine sulfate or DTGS detector and a high sensitivity liquid nitrogen cooled mercury cadmium telluride or MCT detector, were used. Peak positions were determined using cursor selected data points on the computer.

D. Roughness

The micrometer roughness of pretreated Ti-6-4 coupons and foils was determined using a Taylor-Hobson Talysurf 4 Profilometer. A diamond stylus measured the average peak to valley distance as well as giving a record of the profile. Ten tracings were made on each surface and the roughnesses were averaged and the standard deviation calculated.

E. Contamination

Pretreated Ti-6-4 coupons were pretreated, dried and

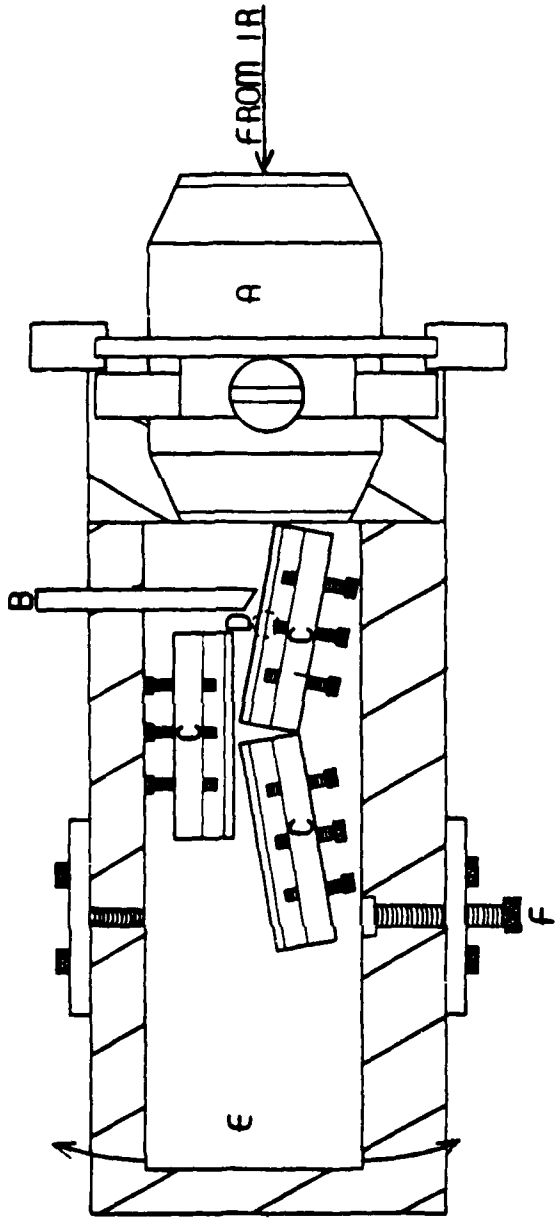

Figure 23. Schematic diagram of grazing angle reflectance attachment used in all FTIR studies. [129]

hung in air in the laboratory environment. The contact angle of water on the surfaces were measured over time. The time for appearance of a contact angle greater than 10 degrees was chosen for comparison.

F. Surface Energy Determination

The surface energy of pretreated Ti-6-4 samples was determined by interfacial contact angle measurements. Ti-6-4 coupons, pretreated by one of three pretreatments - CAA, P/F, or TURCO - were placed in a hot plate oven at 110° C for at least 48 h immediately following pretreatment. The oven was then turned off and the coupons allowed to cool to room temperature. The room temperature coupon was then immersed in hexane, octane, decane or hexadecane in a glass container at room temperature. A 8 µl water drop was placed on the immersed Ti-6-4 surface by a syringe needle held approximately 3 mm above the surface. The contact angle of the water drop on the immersed Ti-6-4 sample was measured by a goniometer telescope through the glass container 15 seconds after the drop had been applied to the surface. Figure 24 shows the experimental set-up. Four measurements were recorded for each side of the drop and for each coupon, four drops were measured. This procedure was repeated three times for the TURCO and P/F pretreatments and twice for the CAA pretreatment. The contact angles were statistically

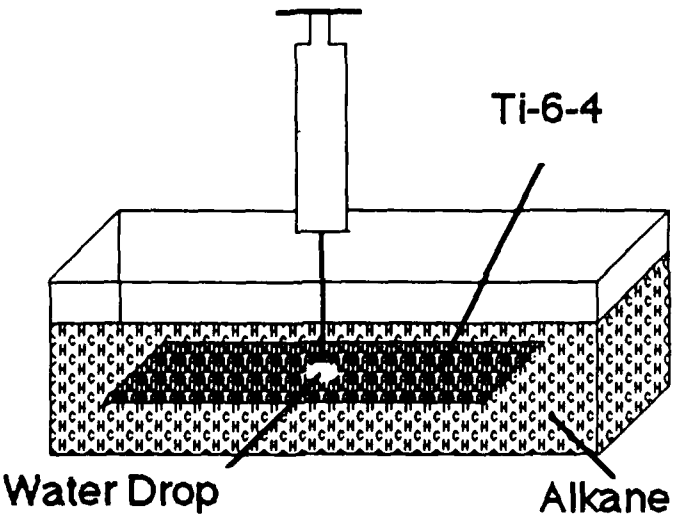

Figure 24. Schematic diagram of experimental set-up for interfacial contact angle measurements.

treated to obtain an average value. Before using these averaged contact angles to calculate the dispersive and polar components of the surface energy, corrections for roughness and porosity were made using equations 37 and 38 in Section II.C. The pretreated surfaces and acid cleaned glass were coated with 100 nm of gold using an SPI sputter coater. The contact angle of a drop of formamide on each surface was measured. The area covered by pores on the CAA surface was determined from STEM photomicrographs by counting the number of pores per unit area using an average pore diameter of 40 nm.

G. Indicator Dye Test

Indicator dyes were used to determine the surface acidity/basicity of pretreated Ti-6-4 adherends [130]. Bromothymol blue solution (LaMotte Chemical Products) was used as received. 0.01 g of the following dyes were each dissolved in 25 ml of deionized water: Orange 1, Thymol blue (both Pfaltz and Bauer, Inc.), and Bromophenol blue (Arthur H. Thomas Co.). 0.1 g of Bromocresol purple (Chemical Dynamics Corporation) was dissolved in 9.25 ml of 0.02N NaOH and diluted to 250 ml with deionized water. Ti-6-4 coupons were pretreated, dried under a flowing stream of dry nitrogen and immediately tested by placing two drops of dye on the dried pretreated surfaces and observing the color of the wet dye and after the dye had dried on the pretreated surface.

H. Adhesive Bonding

1. FM-300 characterization

FM-300 uncured epoxy film was analyzed by XPS. A piece was cut to fit on the XPS probe 2.54 cm in diameter.

Dynamic mechanical thermal analysis, DMTA, was used to study cured FM-300 films before and after 30 day exposure to 80° water. A Polylab DMTA analyzer was used at 1 Hz from 0° to 200° C, thus monitoring the alpha transition. The DMTA samples were made by outgassing the uncured epoxy in a vacuum oven at room temperature for at least 24 h. Four layers of the outgassed epoxy film were cured under 1.72 MPa pressure at 175° C for 1.5 h from a room temperature start in plates separated by 0.038 cm shims. One film was then placed in 80° C water for 30 days before analysis.

2. Pore penetration study

To determine if the epoxy penetrated the CAA porous oxide, a piece of Ti-6-4 foil was anodized by the CAA pretreatment. FM-300 film was placed on top of the CAA foil, covered with a Teflon sheet and bonded at 175° C for 1.5 h. Because of the foil flexibility, the epoxy/foil laminate could be peeled apart by hand, creating a metal failure surface, MFS, and an adhesive failure surface, AFS. These surfaces were studied by STEM, XPS, and AES with depth profiling.

3. Lap shear test

Lap shear coupons (2.54 x 12.7 x 0.13 cm) were pre-treated and bonded with four layers of FM-300U epoxy. The pretreated surfaces were not primed with an organic primer. The lap shear coupons were placed in a jig set for 1.27 x 2.54 cm overlap. The FM-300 film was cut as 1.9 x 2.54 cm pieces to provide adhesive fillets, thus reducing stress concentration at the ends of the coupons. The jig was placed in a Pasadena Hydraulics platen press and heated from room temperature to 175° C at 13.8 MPa bonding pressure for 1.5 h. The heat was turned off and the joints allowed to cool to room temperature under pressure. All lap shear joints were aged for at least 10 days before testing. Lap shear bonds were pulled to break at room temperature on an Instron at a crosshead rate of 0.127 cm per min. The breaking strength was obtained from measuring the peak strength from the strip chart recorder output. The lap shear strengths were averaged and the standard deviation calculated. The failure surfaces were studied by XPS and SEM to determine the locus of failure.

4. Stress durability test

Lap shear joints, as described above, were also loaded to 40% of the average breaking strength by a spring of known force constant. The loaded joints were placed in a 3M stress durability tester at 80° C, 95% r.h. and the time for

the joint to fail was measured. Some pretreated surfaces were also brush coated with aluminum alkoxide in a N_2 atmosphere prior to bonding and testing. The failure surfaces were studied by XPS to determine the locus of failure.

5. **Wedge test**

Wedge coupons, 2.54 x 15.24 x 0.38 cm, were pretreated and bonded with two layers of FM-300U cut to the same dimensions as the wedge coupons leaving 0.5 cm clear at each end. The pretreated surfaces were not primed with an organic primer; however, some were primed with titanium and aluminum alkoxides in a N_2 atmosphere prior to bonding. The thickness of the bond line was controlled using Teflon film spacers yielding a bond line thickness of 0.0381 cm. No jig was used to prepare the wedge joints which were placed in a platen press and heated from room temperature to 175° C at 1.72 MPa bonding pressure for 1.5 h. The heat was turned off and the joints allowed to cool to room temperature under pressure. A Ti-6-4 wedge was driven into one end of the wedge joint with a hammer causing an initial crack to propagate. The position of the initial crack was measured with a ruler to the nearest 1 mm and the joint placed in an environment. The crack propagation with time was then monitored periodically by removing the joint from the environment to measure the crack. G_1 values were calculated

using equation 58 where y = 0.38 cm and M = 1.14×10^{11} Pa. The environments included: 80° C, 95% r.h.; 80° C or 95° C, water immersion; and immersion in 80° C buffer solution. The 0.5M basic phosphate buffer solution at pH = 11.0 - 11.5 was made of 268.07 g of $Na_2HPO_4 \cdot 7H_2O$ and 380.12 g of $Na_3HPO_4 \cdot 12H_2O$ (Fisher Scientific) per 2 liters of solution in deionized water and heated slowly to 80° C for complete dissolution. The acidic phosphate buffer solution at pH of 1.8 to 2 contained 22.90 g H_3PO_4 and 6.68 g NaH_2PO_4 per 2 liters of solution in deionized water.

I. Statistical Analysis

Data from roughness, contact angle, XPS and lap shear strength measurements were analyzed statistically to determine the variability in measurement, the reproducibility of pretreatments, and the statistical similarity in lap shear strengths. Because the measurements are an attempt to define systems as a whole, or "populations" in statistical terms, the "estimate of the population standard deviation", s_x, was used as calculated by:

$$s_x = \left[\frac{\sum_i (x_i - \bar{x})^2}{n - 1} \right] \qquad (71)$$

where x_i is the specific measurement, x is the mean value and n is the number of measurements.

To calculate a confidence limit, for the above example,

the student's t value is needed for samples of less than 30 measurements:

$$m = x \pm t_{f,\alpha}\, s_x\, n^{-\frac{1}{2}} \qquad (72)$$

where m is the population mean which equals the calculated mean, x, ± a value which includes the student t value, $t_{f,\alpha}$, from a table depending upon the degrees of freedom, f, and the confidence limit of 68.26, 95, or 99%; the estimated population standard deviation, s_x, and the number of samples, n. [131]

The contact angles were statistically treated to obtain an average value. For each alkane, the measured angles were averaged, the standard deviation calculated and a 95% confidence limit determined. Any angle lying outside the 95% confidence limit was then discarded and a new mean calculated.

IV. Results and Discussion

A. Part I - Physical and Chemical Properties of Ti-6-4 Oxides

1. Topography

a. Profilometry

Micrometer roughness of pretreated Ti-6-4 was determined by profilometry. Figure 25 shows the tracings from the profilometer for the CAA, P/F, TURCO pretreated coupon surfaces as well as for a smooth glass slide reference. Table IX lists the average peak to valley height with the standard deviation for both the pretreated coupon surfaces and the pretreated foil surfaces. The coupon surfaces were an order of magnitude rougher than the foil surfaces which were an order of magnitude rougher than the glass slide reference. The TURCO coupon surface was the roughest coupon surface, while the P/F foil surface was the roughest foil surface. Ditchek et al. [16a], using SEM photomicrographs as a basis, rated the roughness of pretreated Ti-6-4 with P/F as a smooth surface, TURCO as macrorough on the micrometer level and CAA as porous, qualitatively agreeing with the profilometry results obtained here for the coupon surfaces.

b. SEM/STEM

The surface topography of the CAA, SHA, P/F, and TURCO

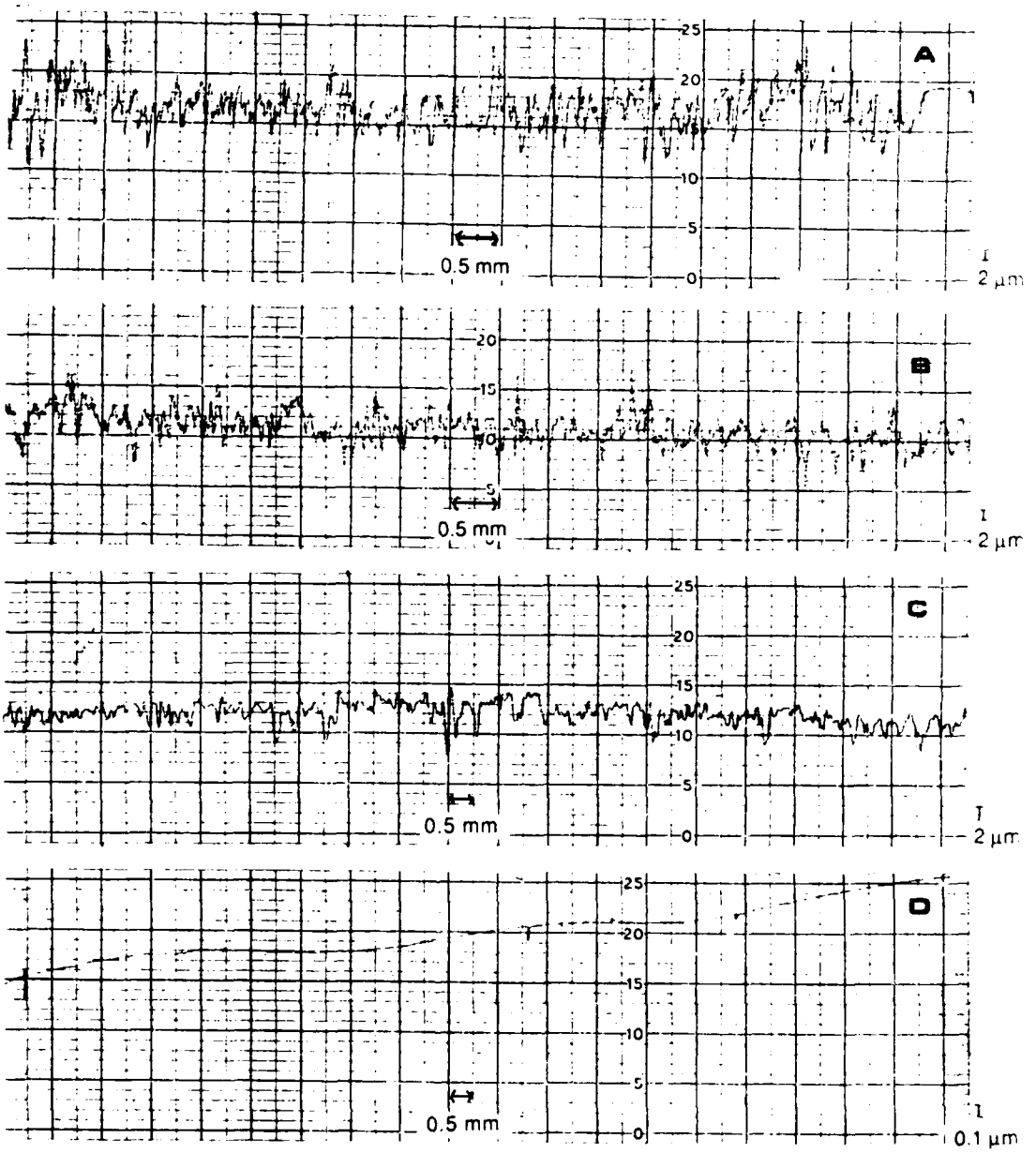

Figure 25. Profilometer tracings of (A) TURCO, (B) P/F, and (C) CAA pretreated Ti-6-4 coupons and (D) acid-cleaned glass slide.

TABLE IX

Roughness measurement by profilometry of Ti-6-4 foil and lap shear coupon surfaces

Ti-6-4 Foil

Pretreatment	Average peak to valley (μm)	Standard Deviation
CAA	0.33	0.041
P/F	0.45	0.11
TURCO	0.35	0.084
Untreated	0.24	0.050

Ti-6-4 Coupons

Pretreatment	Average peak to valley (μm)	Standard Deviation
CAA	2.13	0.26
P/F	2.84	0.28
TURCO	3.36	0.034
Glass	0.029	0.008

oxides was studied by both SEM and STEM. Figures 26 to 29 show SEM photomicrographs at 2000 x magnification of the four pretreatments. All four surfaces appeared different from each other. The two pretreatments using acidic solutions possess predominantly more gray features than the surfaces from basic solutions. The difference in the white and gray areas arises from the alpha-beta phase nature of the Ti-6-4 oxide with the white beta phase being preferentially etched by the acidic solution.

Figures 30 and 31 show SEM stereophotomicrographs of SHA and PSHA surfaces. The pickling step, prior to the anodization in PSHA notably affects the final topography causing less nodular features to be present. The high density of nodular features is thought to affect the AES depth profile results reported in section 4d. Kennedy et al. [19] report SEM photomicrographs different than the ones shown in Figures 30 and 31. The previously reported SHA surface are even more densely packed with sharply pointed nodular features.

When these oxides were observed at higher magnifications by STEM, not previously reported for the SHA surfaces, macro-porosity was observed in the anodized surfaces but not with the etched surfaces. Figures 32 to 34 show the STEM photomicrographs of CAA, SHA, and PSHA oxides. The porosity in the PSHA surface appeared to be similar to the CAA

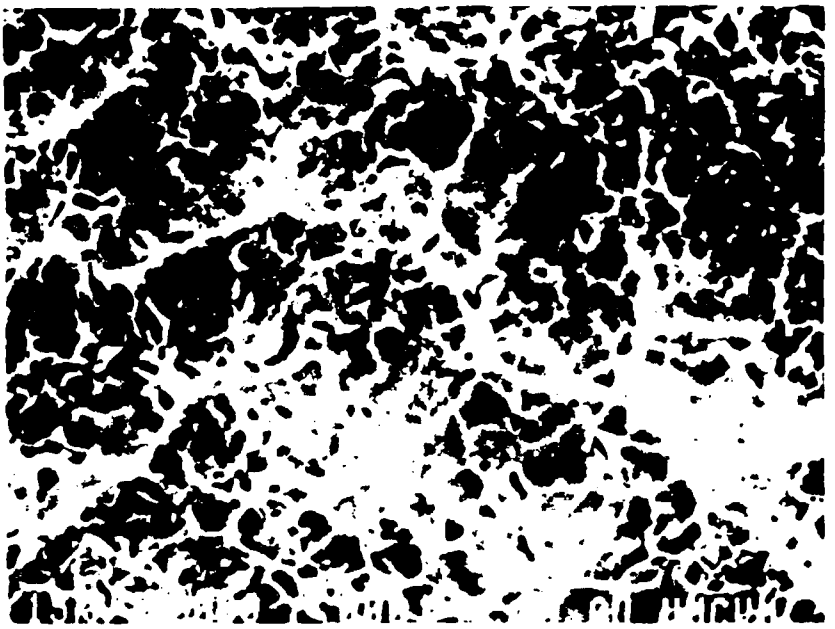

Figure 26. SEM photomicrographs at 2000 x of CAA pretreated Ti-6-4.

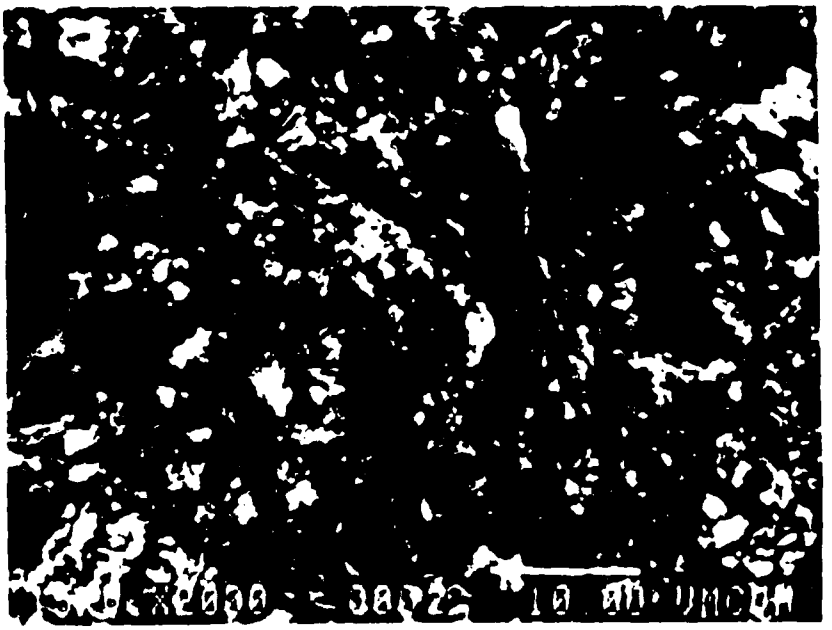

Figure 27. SEM photomicrographs at 2000 x of SHA pretreated Ti-6-4.

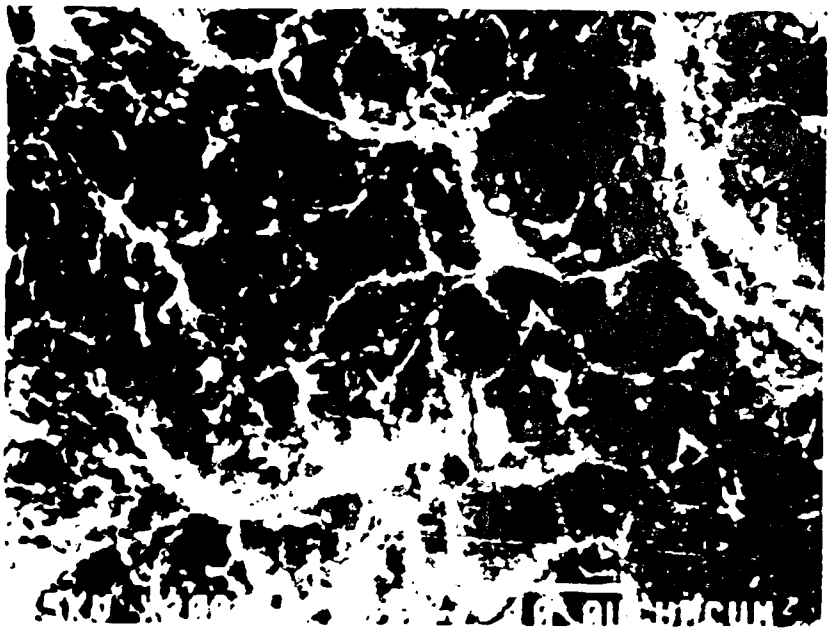

Figure 28. SEM photomicrographs at 2000 x of P/F pretreated Ti-6-4.

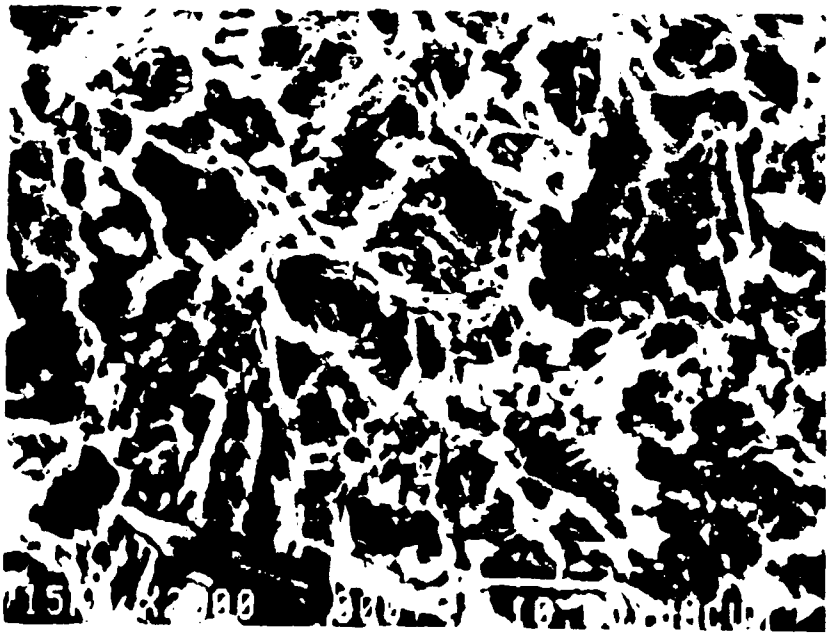

Figure 29. SEM photomicrographs at 2000 x of TURCO pretreated Ti-6-4.

Figure 30. SEM stereophotomicrograph at 7800 x of SHA pretreated Ti-6-4.

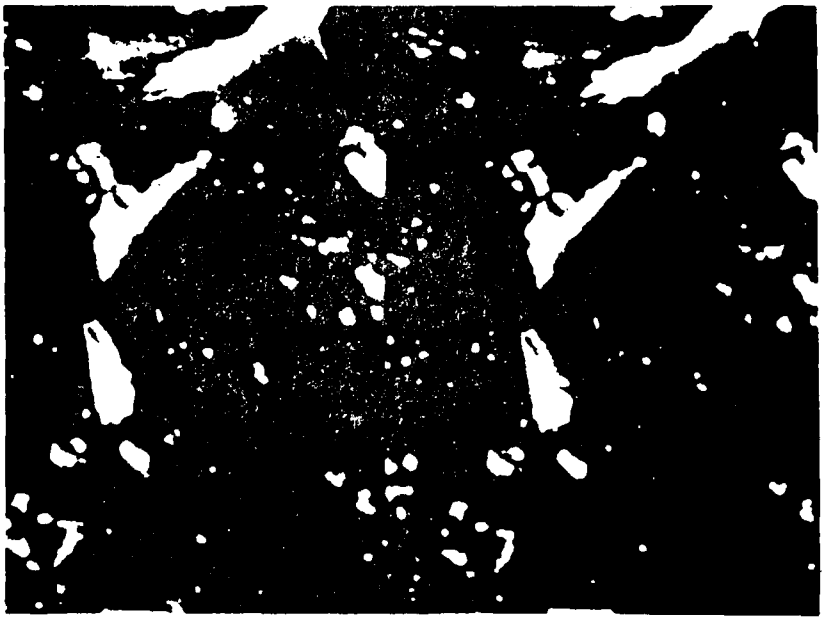

Figure 31. SEM stereophotomicrograph at 7800 x of PSHA pretreated Ti-6-4.

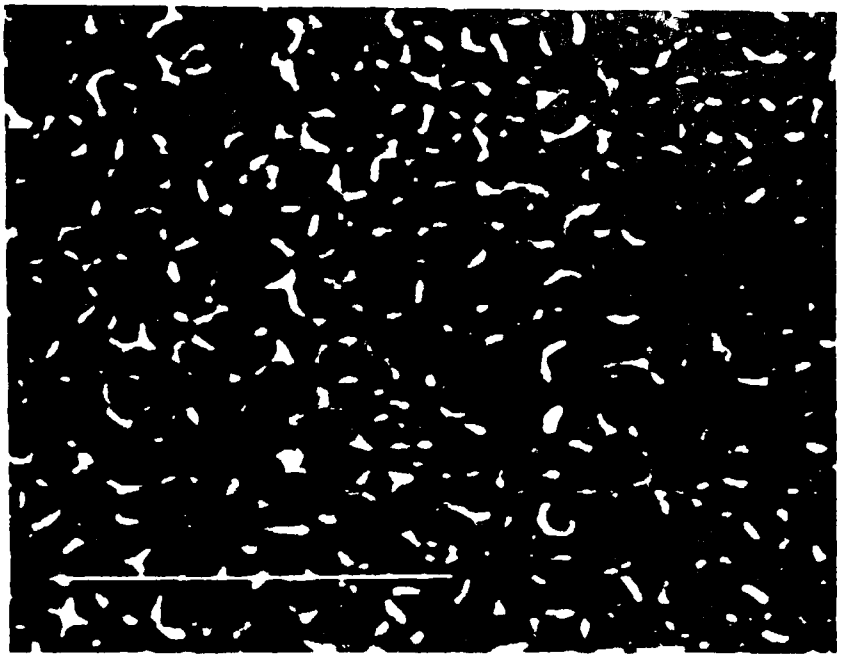

Figure 32. STEM photomicrograph at 100,000 x of CAA pretreated Ti-6-4 surface.

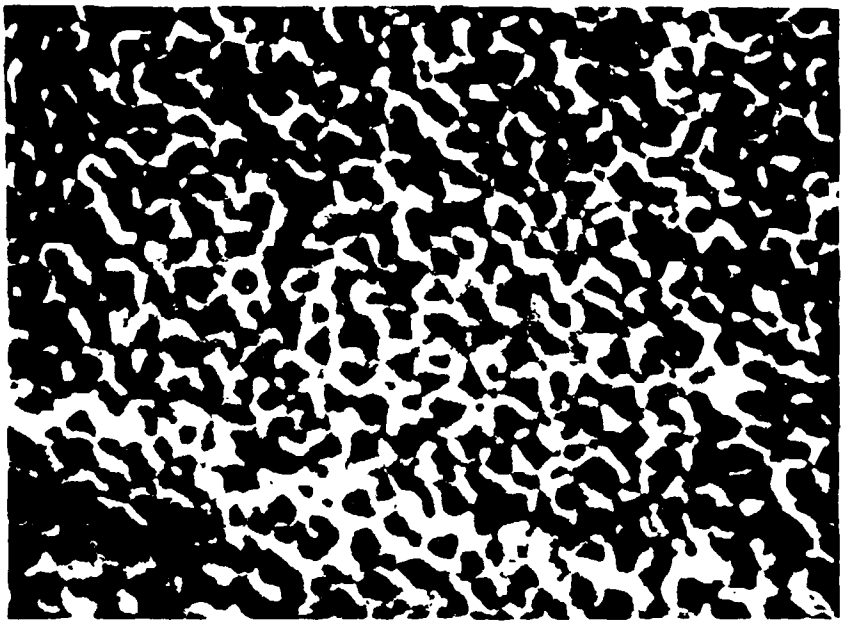

Figure 33. STEM photomicrograph at 100,000 x of PSHA pretreated Ti-6-4 surface.

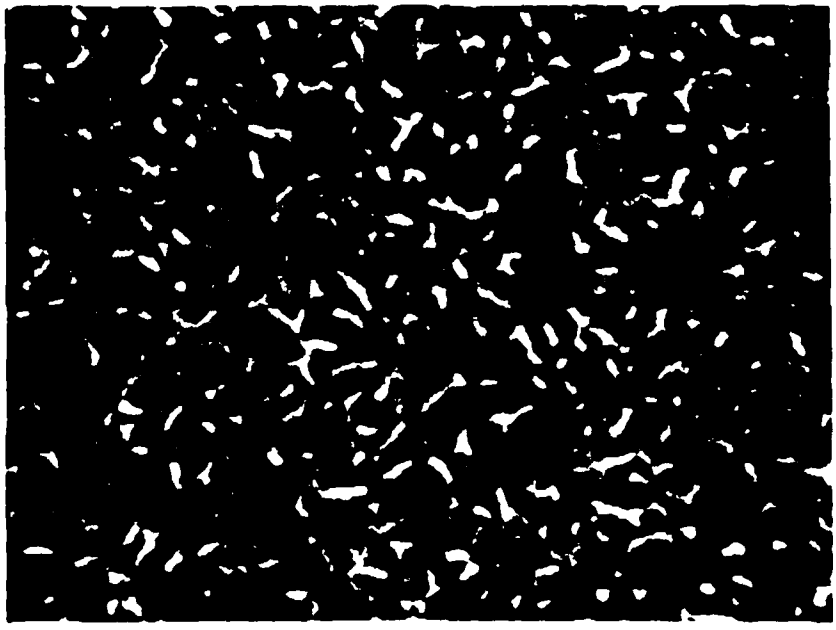

Figure 34. STEM photomicrograph at 100,000 x of SHA pretreated Ti-6-4 surface.

surface with pore diameters of approximately 40 nm, while the SHA surface did not show as clear a porosity.

As discussed in section II.A.3, the mechanism of pore formation is believed to be due to fluorine initiating dissolution followed by localized heating. Both CAA and PSHA surfaces are pickled prior to anodization. XPS analysis of pickled Ti-6-4 indicates a high concentration of fluorine on the surface, thus allowing for the initiation of well defined pores. Complementing the presence or absence of fluorine is the difference in current densities between the CAA and SHA procedures. In the CAA process, the current density was controlled; whereas it was not controlled in the SHA or PSHA treatments. Because the pickling step removed most of the barrier oxide layer, the PSHA surface showed less resistance to the current initially. Thus, the effect of localized heating may be more pronounced in the pickled samples than the non-pickled SHA samples.

Figures 35 and 36 show STEM photomicrographs of the P/F and TURCO surfaces. No porosity, as in the anodized surfaces, is observed on the etched surfaces. Porosity was also reported by Ditchek et al. [16] for the CAA pretreated Ti-6-4 surfaces but not for the P/F or TURCO pretreated Ti-6-4 surfaces.

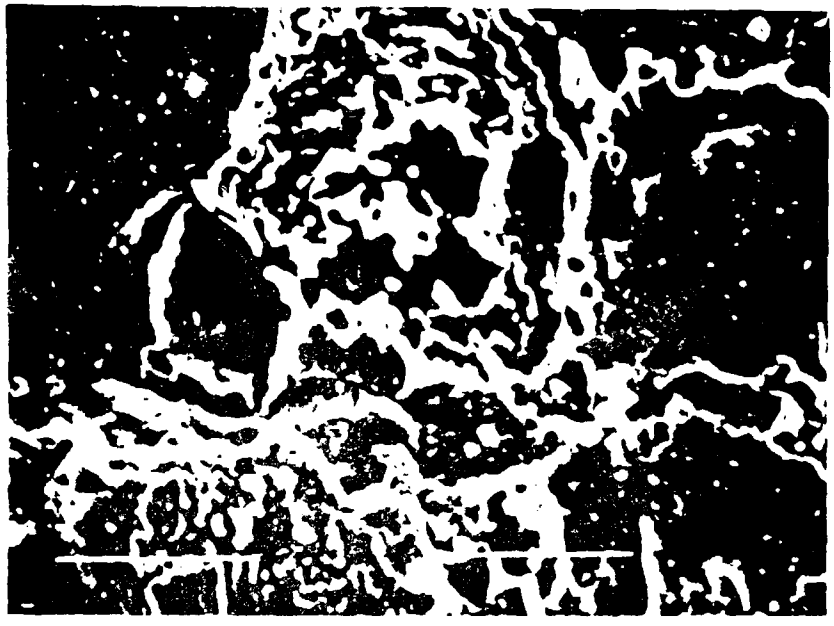

Figure 35. STEM photomicrograph at 50,000 x of P/F pretreated Ti-6-4 surface.

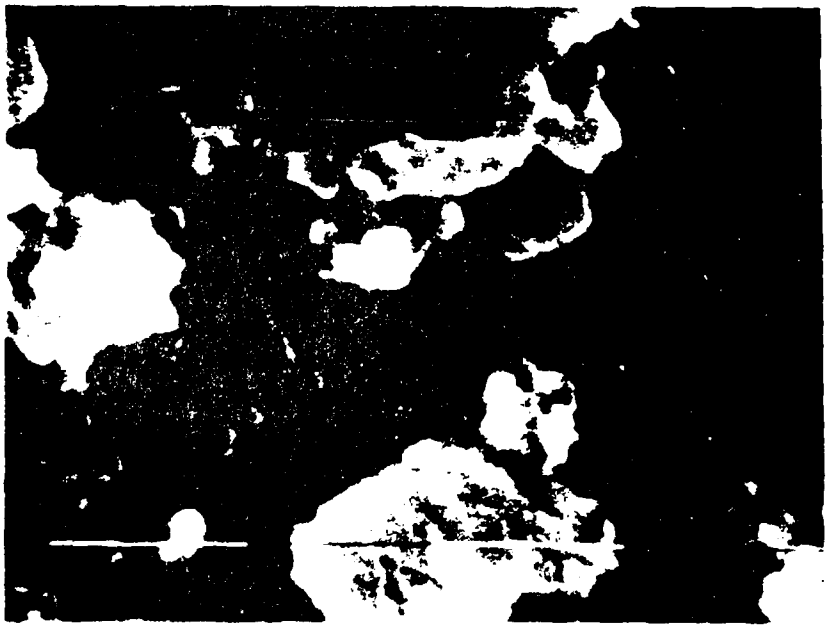

Figure 36. STEM photomicrograph at 50,000 x of TURCO pretreated Ti-6-4 surface.

c. Contamination

Atmospheric contamination readily occurs on high energy surfaces. Contamination was evaluated by the time for a water contact angle of 10 degrees to form on the Ti-6-4 surface. These times were characteristic for each pretreatment: 12 h for P/F, 31 h for TURCO, and 72 h for CAA. The order of increasing time for contamination was found to be P/F > TURCO > CAA. The explanation of this contamination rate is related to the surface topography. The P/F surface is smoother than the TURCO surface as measured by SEM and profilometry. The CAA surface is also smoother than the TURCO surface; however, porosity is present in the CAA surface. It appears that the time for contamination to occur is directly related to the surface area of the Ti-6-4 oxide surface, with the order of surface area being P/F < TURCO < CAA.

2. Surface energy

The polar and dispersive components of the surface free energy were determined for CAA, P/F, and TURCO surfaces from interfacial contact angle measurements. The assumption that the water drop completely displaces the alkane was proven by calculation using equation 41 and finding the inequality to hold in each case. The dispersive component of the surface energy of the pretreated surfaces and a polar interaction

term were graphically determined using equation 40. Because the pretreated surfaces were not homogeneous and smooth, scattering in the contact angle measurements was present. To reduce the effects of this scatter, multiple contact angle measurements were made and statistically treated as described previously. While excellent reproducibility of the contact angles was difficult, relative values between the pretreatments can still be compared. Table X lists the values of the dispersive and polar components of the surface energy using both a geometric mean (gm) and a harmonic mean (hm) to calculate the polar component from equations 42 and 43. The numbers in parentheses are the values obtained when no correction for roughness or porosity is made. Particularly for the porous surface of CAA, there is a significant difference in the γ^p and γ^d values when no correction is made for porosity and roughness. While values of γ^p calculated using the geometric mean are slightly lower than using the harmonic mean, no major difference is observed. Carre and Schultz [91] found for sulfuric acid anodized, SAA, 5052 aluminum, dispersive and polar components of the surface energy were 125 and 44 mJ/m^2, respectively. For a sealed anodized surface, where the pores have been filled, the dispersive and polar components of the surface energy were 41 and 15 mJ/m^2, respectively. The values obtained for the anodized titanium, while lower, agree qualitatively with

TABLE X

Dispersive and polar components of the surface energy of pretreated Ti-6-4, using the geometric mean (GM) and the harmonic mean (HM). γ in mJ m^{-2}

Pretreatment	γ^D_s	γ^P_s(GM)	γ^P_s(HM)
CAA	87 (4.0)	30 (1.9)	32
P/F	64 (40)	14 (14)	18
TURCO	52 (31)	16 (17)	20

TABLE XI

Work of adhesion in air and in water. W in mJ m^{-2}

Pretreatment	W_A Ti/epoxy	W_A Ti/water	W_{AW} Ti/epoxy
CAA (GM)	146	165	26.6
CAA (HM)	140	167	33.8
P/F (GM)	119	128	37.7
P/F (HM)	120	135	51.1
TURCO (GM)	112	124	32.8
TURCO (HM)	112	131	45.2

those of Carre and Schultz. Likewise, the slightly lower values for the etched titanium surfaces compare to their sealed anodized surfaces [91].

From the polar and dispersive components of the surface energy, the work of adhesion for the epoxy/Ti-6-4 and for the water/Ti-6-4 interfaces in air was calculated using equation 45a and the calculated values are listed in Table XI. The work of adhesion in air for the CAA pretreated Ti-6-4/epoxy compares well with that of 176 mJ/m^2 for SAA aluminum and the TURCO and P/F pretreated Ti-6-4/epoxy compare well with 101 mJ/m^2 for sealed SAA aluminum [91]. The work of adhesion for the Ti-6-4/water interface was higher than for the Ti-6-4/epoxy interface. A similar trend was observed in the aluminum system. Thus, titanium has a higher affinity for water than for the epoxy. This affinity can be illustrated by calculation of the work of adhesion of a Ti-6-4/epoxy interface in a water environment using equation 45b. Table XI also lists the work of adhesion for the Ti-6-4/epoxy bond in water, W_{Aw}. The calculated work of adhesion was seriously reduced for bonds in a water environment. Thus, thermodynamics predicts a weaker bond between the titanium and epoxy in water than in air.

3. Acidity/basicity

The sulphonephthalein indicator dyes change color

between their acid and base form depending upon their pK_A. The acidity/basicity of a pretreated Ti-6-4 surface was determined by observing the colors of a series of sulphonephthalein indicator dyes and two azo-type indicator dyes. Table XII lists the colors observed for each dye on the pretreated surfaces when the dyes were liquid on the surface and after drying. The pH of the surface was determined by observing the color change and assuming the surface pH was equal to the pK_A of the dye.

The CAA surface, particularly after the dyes dried, was clearly acidic with a pH between 1.2 and 3.4. In contrast, the SHA surface was basic, with a pH between 8.0 and 9.6. The acidity/basicity of the P/F and TURCO surfaces was not as clearly defined. The P/F surface appeared to be in the acidic range with a pH of 3.4 - 3.8. The TURCO surface, while indicating in the 5.2 - 6.8 range with bromocresol purple, also indicated in the 8.0 - 9.6 pH range with Thymol blue. With diffuse reflectance visible spectroscopy, Mason et al. [130] found the P/F surface to be acidic with the pH between 4.9 and 7.3, and the TURCO surface basic with the pH between 7.3 and 9.2. The difference between the present and reported results is most likely due to the difference between the naked eye versus a spectroscopic technique in determining the "color" of the dye.

TABLE XII

Results of Indicator Dye Test

Indicator	Indicator pH Change Range	CAA^w	CAA^d	P/F	TURCO	SHA
Benzeneazo-diphenyl amine	1.2 - 2.1 r y	y	y	y	y	y
Bromophenol Blue	3.4 - 3.6 y b	g	y	g	b	b
Bromocresol Green	3.8 - 5.4 y b	y		y	g-b	b
Bromocresol Purple	5.2 - 6.8 y b	y	y	y	g-y	p-b
Bromothymol Blue	6.0 - 7.6 y b	b	o	g	b	b
Orange 1	7.6 - 8.9 o p	o	o	o	o	dk-o
Thymol Blue	8.0 - 9.6 y b	y	o	y	g-y	dk-g

w - wet d - dry r - red o - orange y - yellow

g - green b - blue p - purple dk - dark

4. Chemical composition

a. Oxide composition by XPS, AES, SIMS

The chemical composition of the pretreated oxides was determined by XPS. Tables B-I to B-V in Appendix B list the elements detected, the binding energies (B.E. in eV), and the atomic percents (A.P.) for the CAA, P/F, TURCO, SHA, and PSHA pretreatments. The elements detected on all pretreated surfaces by XPS were carbon, oxygen and titanium. Figures C1 to C5 in Appendix C show the high resolution XPS spectra of these peaks for each pretreatment.

CAA surfaces contained a small percentage of fluorine, present as an inorganic fluoride from the electrolyte, HF. Chromium, contained in the anodizing bath, was not detected. The P/F surfaces contained a small percentage of phosphorus from the etch solution. Fluorine was not usually detected.

TURCO surfaces contained both silicon and iron. Ditchek et al. [16] detect iron particles on the TURCO pretreated surface. When the surface was pickled after gritblasting but before the TURCO treatment, no silicon or iron was detected. XPS did not detect silicon or iron in the TURCO 5578 mixture. Iron and silicon, therefore, resulted from the gritblast step, and the pickling step removed this iron and silicon contamination.

The SHA pretreatment for Ti-6-4 is reported by Kennedy et al. [19]. Their optimum pretreatment conditions were

chosen for this study. Silicon, calcium, phosphorus, and fluorine were detected on the SHA surface; however, no sodium from the anodization bath was detected. The silicon was from the gritblasting step; calcium and fluorine resulted from the tap water rinse. The tap water rinse was used to duplicate the procedure of Kennedy et al. so that direct comparison of the SEM photomicrographs could be made. The PSHA surface contained less silicon and more fluorine due to the pickling step [16].

In addition to XPS, AES yields compositional information of the surface region. Wide scan spectra were collected for CAA, SHA, PSHA, P/F, and TURCO pretreated surfaces. The elements detected and their kinetic energies are listed in Table XIII. The elements detected on the pretreated surfaces using AES agree with those detected using XPS.

The oxygen to titanium ratio was calculated from ratioing the peak intensities of the oxygen KLL transition at 512 ev and the titanium LMM transition at 382 ev. Table XIV lists peak ratios for TiO_2 powder used as a standard and for five pretreatments: CAA, P/F, TURCO, SHA, and PSHA. The average O/Ti ratio for the TiO_2 powder was 2.1 with 95% confidence limit of ± 0.22. The O/Ti ratio of the surface by relative peak height for CAA, P/F and TURCO is the same as TiO_2, with the SHA and PSHA showing slightly higher O/Ti

TABLE XIII

AES Wide Scan Elements and Kinetic Energies (K.E.) for CAA, P/F, TURCO, SHA and PSHA Pretreated Surfaces

Pretreatment	Element	K.E.
CAA	C	266
	O	512,486
	Ti	414,382
	F	658,632
P/F	C	272
	O	512,494
	Ti	412,382
	F	112
TURCO	C	272
	O	512,494
	Ti	418,382
	Fe	702,648
	Si	94
SHA	C	272
	O	512,494
	Ti	418,386
	Ca	294
	Si	80
	P	120
PSHA	C	272
	O	512,494
	Ti	418,384
	Ca	294
	P	120

TABLE XIV

Oxygen to Titanium ratios from peak heights at 512 ev and 382 ev

Surface	O/Ti
TiO_2	2.1
	2.3
	1.9
	2.1
CAA	2.1
	2.4
P/F	2.2
	2.1
TURCO	2.0
	1.8
SHA	2.4
PSHA	2.5

ratios. The higher value of the O/Ti ratio is consistent with a higher O/Ti ratio observed by XPS.

AES can also be used to make elemental maps of a surface by searching an area for a particular element. The TURCO pretreated surface was mapped for iron, as it had been reported that micron sized iron particles existed on the surface [16]. Iron is detected on the surface, primarily in clusters as evidenced by the white regions in Figure 37 showing the iron map at 7000x magnification. It is believed the iron results from the gritblast step and is removed by the pickling step present in the pretreatments other than TURCO.

Dynamic SIMS spectra were collected for TiO_2 powder and the pretreated Ti-6-4 surfaces. Tables B-VI to B-XI in Appendix B list the mass/charge ratios and the peak assignments of all peaks at a specified level or higher with the $^{48}Ti^+$ peak set to 100%. As these spectra are from a dynamic SIMS experiment with a high sputter rate, specific conclusions about the top monolayers on the surface cannot be made as in the static SIMS experiment. The assignment of peaks was primarily based on prior knowledge of the surface composition by XPS and AES. Because the sensitivity of ions such as $^{23}Na^+$ and $^{40}K^+$ is high, these elements are also detected on the pretreated surfaces. Typical peaks detected were the titanium isotopes from 46 to 50 m/z and their corresponding

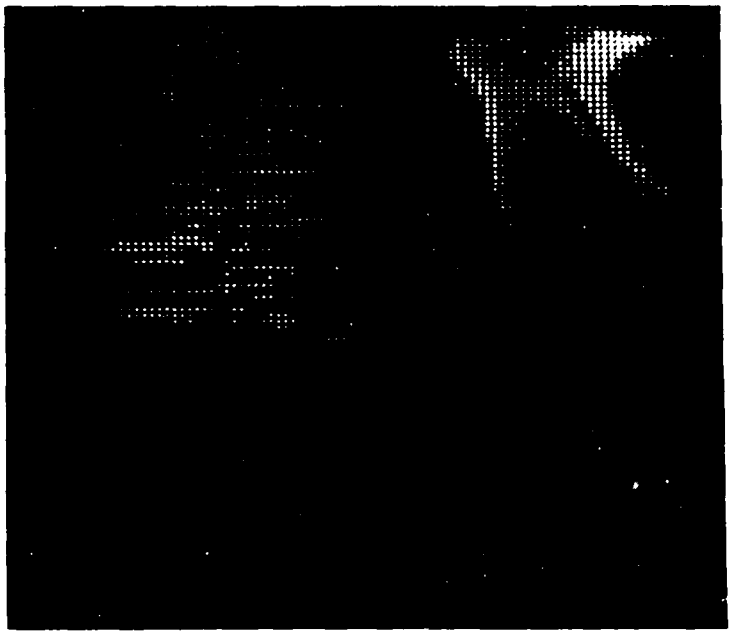

Figure 37. AES elemental map of iron on a TURCO pretreated Ti-6-4 surface.

peaks when bonded to oxygen, for example TiO^+ from 62 to 66 m/z. Al^+ at 27 m/z and V^+ at 51 m/z are also detected from the Ti-6-4 alloy, while XPS and AES do not usually detect these alloying elements. Elements characteristic of the pretreatments detected were F^+ at 19 m/z in CAA and P/F; SiO^+ at 44 m/z in TURCO, SHA and PSHA; and a larger calcium contribution in SHA and PSHA at 40, 56, 72, and 88 m/z for Ca^+, CaO^+, CaO_2^+, and CaO_3^+, respectively. Negative ion spectra were also collected for CAA and P/F pretreated Ti-6-4 surfaces showing two peaks at 16 and 19 m/z for O^- and F^-, respectively.

The titanium isotopic abundances reported by Hayes and Evans for a static SIMS study on titanium electrodes were 8.0, 7.3, 74, 5.5, and 5.2 % for 46 to 50 m/z, respectively [13]. The natural isotopic abundances for titanium are 7.93, 7.28, 73.94, 5.51, and 5.34 % for 46 to 50 m/z, respectively [132]. The isotopic abundances for titanium in the CAA, TURCO, and P/F pretreated surfaces were analyzed for the Ti^+ and TiO^+ peaks. The isotopic abundances, listed in Table XV, match the literature values within the experimental error of measuring the peak heights. Figure 38 graphically illustrates the similarity of the isotopic abundances for Ti^+ and TiO^+ on the CAA pretreated surfaces.

The SIMS spectra can be taken with or without an in-bleed of oxygen. As an adsorbed layer of oxygen increases

TABLE XV

Isotopic Abundance of Titanium from Dynamic SIMS Spectra for CAA, TURCO and P/F Pretreated Surfaces

	Ti^+				
Mass/ Charge	CAA	TURCO	P/F	[13]	[131]
46	8.94	9.02	9.05	8.0	7.95
47	8.01	7.24	8.11	7.3	7.75
48	71.82	72.42	72.66	74.	73.45
49	5.77	5.51	5.23	5.5	5.51
50	5.46	5.82	4.95	5.2	5.34

	TiO^+				
Mass/ Charge	CAA	TURCO	P/F	[13]	[131]
62	7.93	8.33	8.04	8.0	7.95
63	7.51	7.88	7.62	7.3	7.75
64	71.08	70.65	72.09	74.	73.45
65	7.11	7.46	6.46	5.5	5.51
66	6.37	5.67	5.79	5.2	5.34

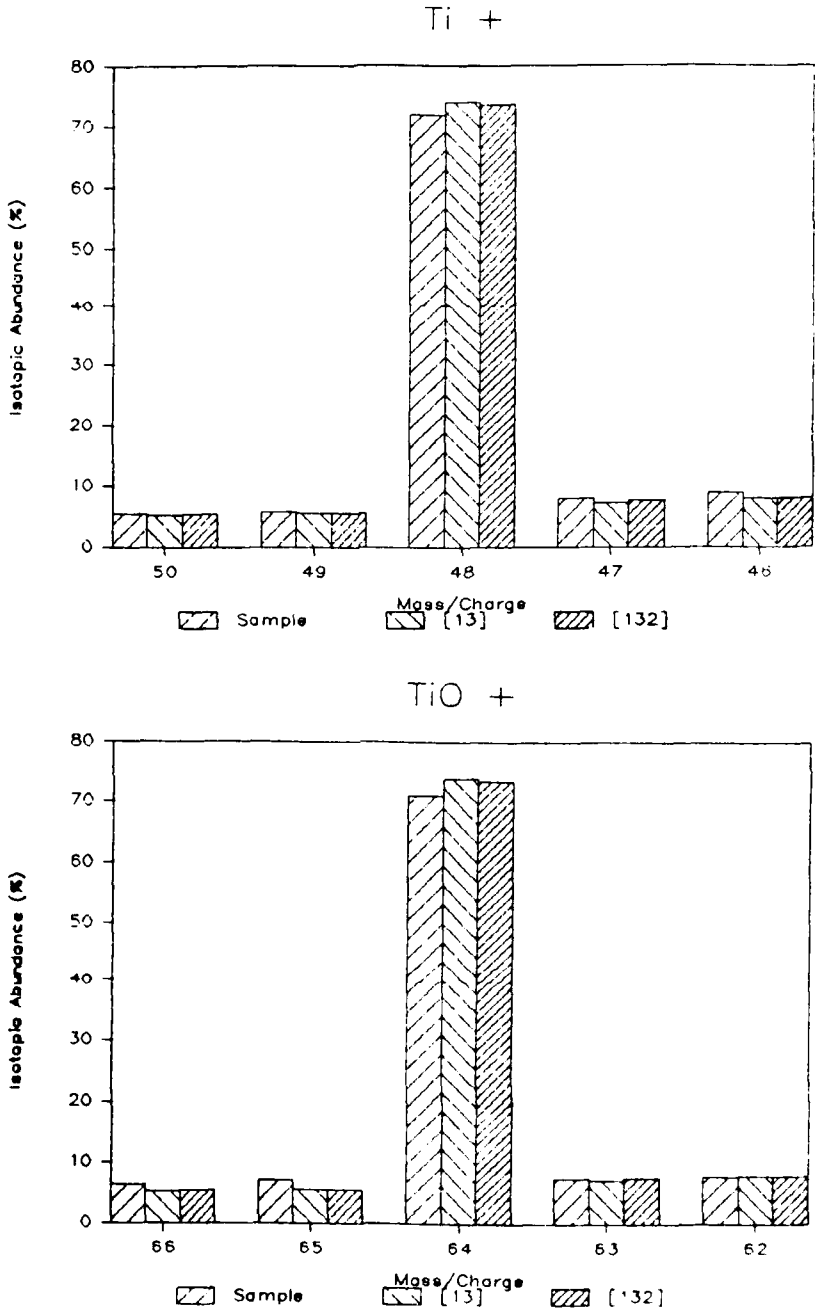

Figure 38. Graphical comparison of the titanium isotopic abundances of CAA pretreated Ti-6-4 sample for Ti^{+} and TiO^{+}.

the ionization efficiency [55], more ions are detected as seen by comparing Figures 39 and 40 for the CAA surface with and without an in-bleed of oxygen. While more ions are detected, care must be taken in drawing conclusions. SIMS has primarily shown to detect similar elements on the surface as XPS and AES, but provided no further insight into the chemical composition of the pretreated oxide surfaces.

b. Reproducibility of pretreatment

While good chemical reproducibility of surface preparation is imperative in the study of the durability of various pretreatments, studies such as these have not been reported in the literature. The chemical reproducibility of the pretreatments was investigated by XPS for the CAA, P/F, and TURCO pretreatments. The atomic percents and binding energies were averaged and statistically analyzed. Table XVI lists for each pretreatment, the elements detected, the average binding energy and the average atomic percent with the 95% confidence limits. The binding energies had confidence limits with narrow ranges. Since the binding energy indicates the chemical bonding state of an element, a small confidence limit shows the pretreated surfaces were chemically reproducible. The confidence limits for the average atomic percents were wide, presumably due to variability of the surface contamination layers.

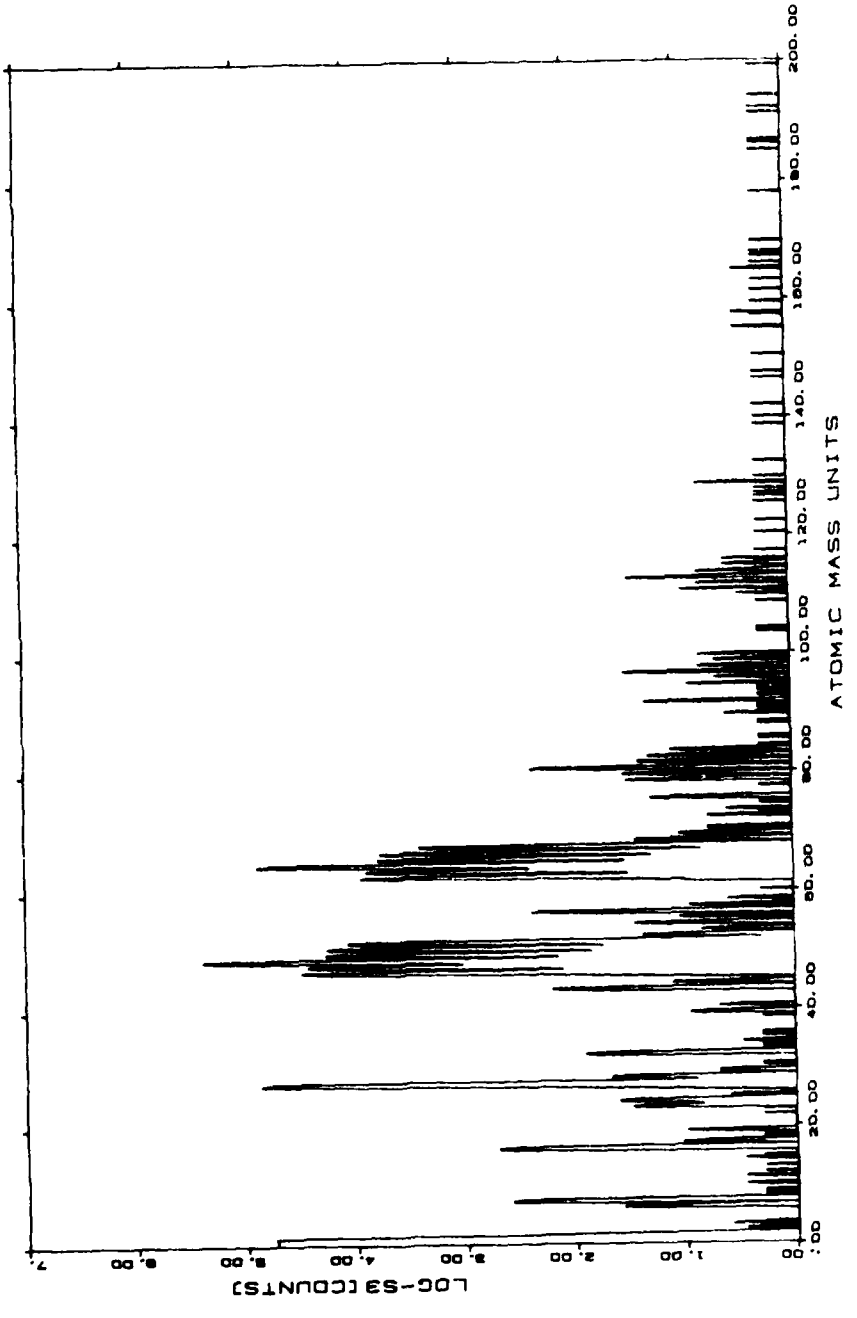

Figure 39. CAA pretreated Ti-6-4 SIMS spectrum with an in-bleed of O_2.

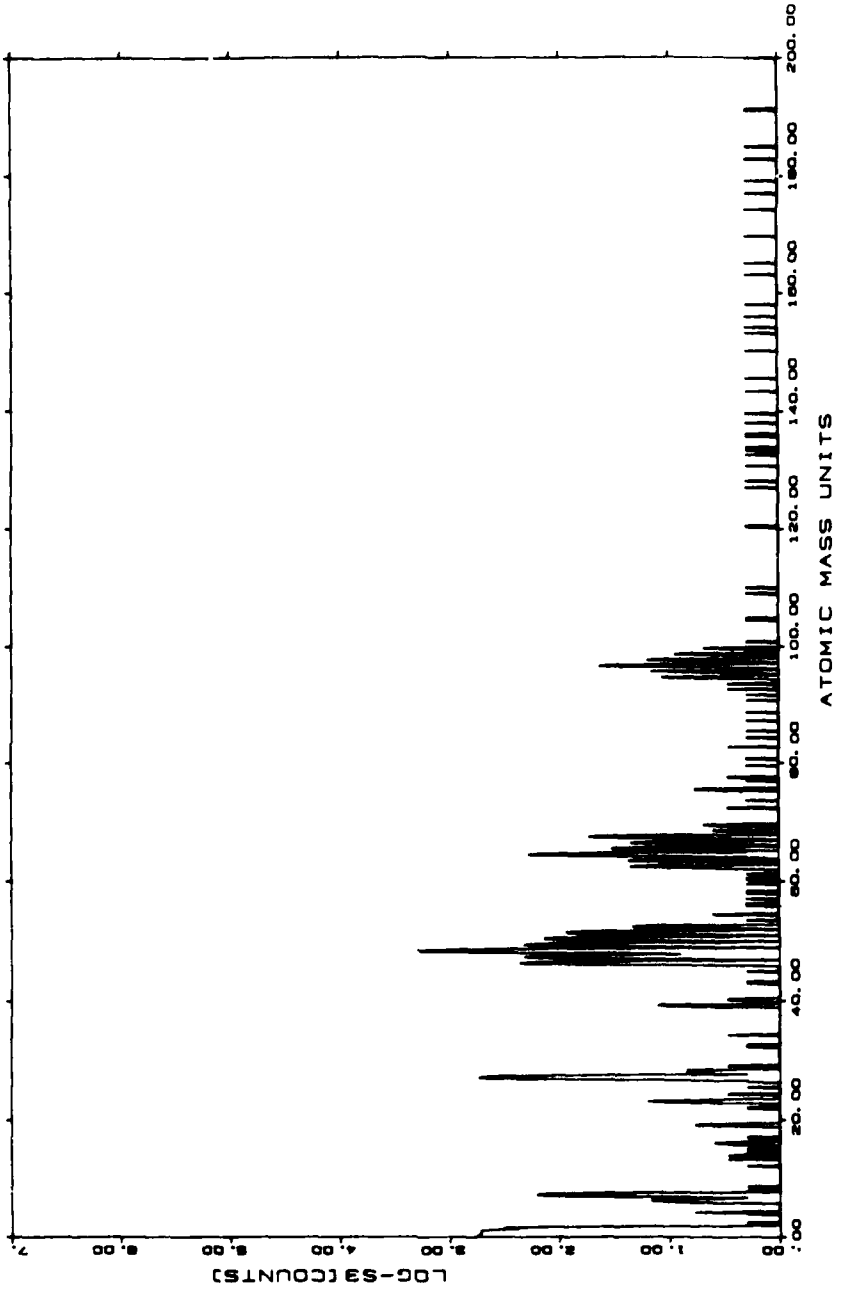

Figure 40. CAA pretreated Ti-6-4 SIMS spectrum without an in-bleed of O_2.

TABLE XVI

Chemical Reproducibility of CAA, P/F and TURCO Pretreated Ti-6-4

Pretreatment	Element	B.E. (ev)	± 95%	A.F.	± 95%
CAA	C	285.0	--	49	7.3
	O	530.4	0.1	37	4.3
	Ti	458.8	0.1	11	2.4
	F	685.0	0.2	2.7	0.9
P/F	C	285.0	--	46	10.8
	O	530.4	0.3	41	8.3
	Ti	458.6	0.2	10	2.6
	P	133.1	0.3	2.1	0.6
TURCO	C	285.0	--	52	9.2
	O	530.0	0.5	36	8.0
	Ti	458.5	0.3	5.6	1.9
	Si	104.2	0.7	6.2	6.4
	Fe	712.2	2.7	1.1	0.9

c. **Stoichiometry by AES line shapes**

The answer to the question of the stoichiometry of the pretreated Ti-6-4 oxides has remained elusive. One method used to determine oxide stoichiometry is by Auger line shapes from narrow scan spectra. Figure 41 shows a narrow scan dN(E)/dE spectra from the Perkin Elmer PHI 610 for the CAA surface with the Ti and O regions labeled. The P/F, TURCO, and SHA spectra are similar and thus are not shown. dN(E)/dE spectra were also obtained on the Physical Electronics SAM 500 between 360 to 430 ev for CAA, P/F, and TURCO surfaces and are in agreement with the spectrum shown in Figure 41. These spectra agree in peak position and shape to those reported by Roman et al. [133] for O_2 gas oxidized titanium, which they attributed to TiO. The spectra also agree with those reported by Solomon and Baun for TiO as shown in Figure 42 [34].

The N(E) spectra also elucidates stoichiometry of titanium oxides. Figure 43 shows the narrow scan spectra for a CAA pretreated surface; the P/F, TURCO, and SHA pretreated surfaces appeared identical. The region between 400 and 433 ev can be compared to Figure 9 in Section II.B.2.c. The shape of the doublet appears to match that of the TiO peak, not the TiO_2 peak. TiO_2 powder was also analyzed and is shown in Figure 44 and here, the spectra does match that of TiO_2. Thus it would appear for Auger line shapes that the

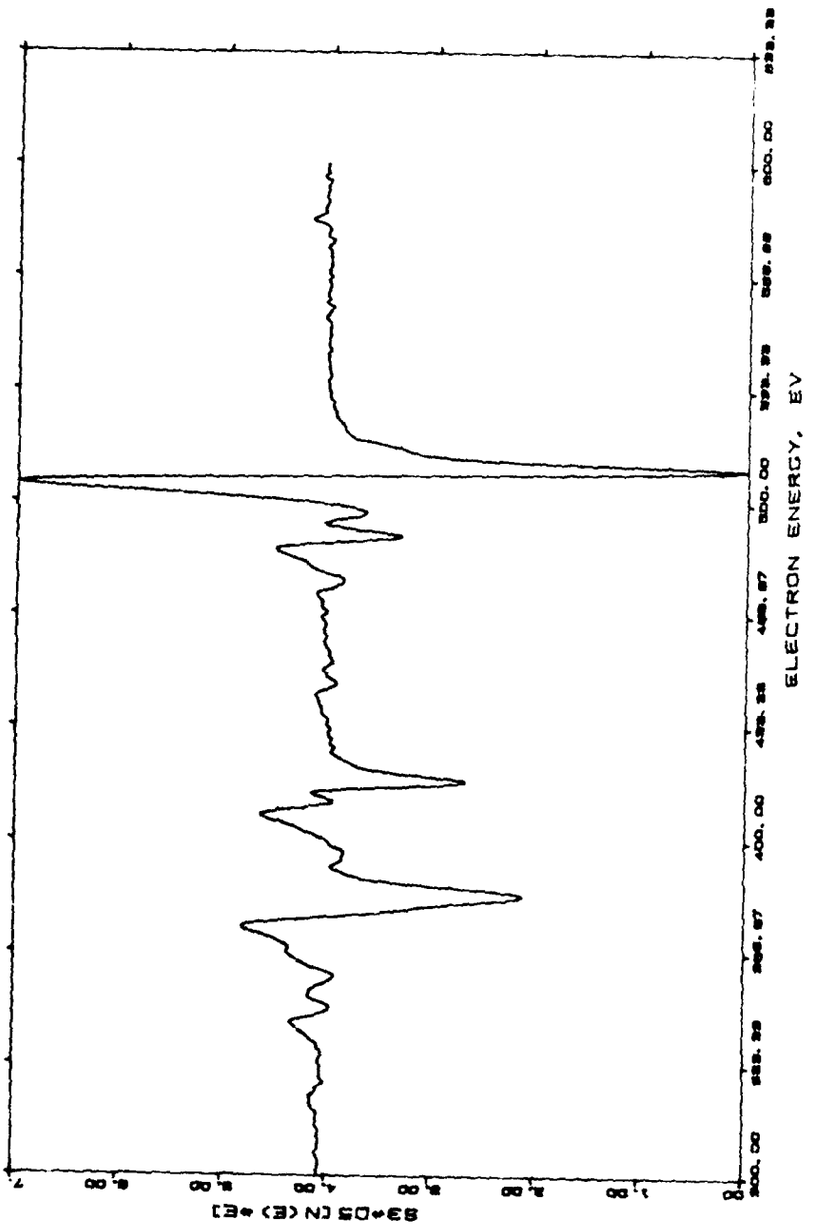

Figure 41. AES narrow scan dN(E)/dE spectrum of the CAA pretreated Ti-6-4 surface.

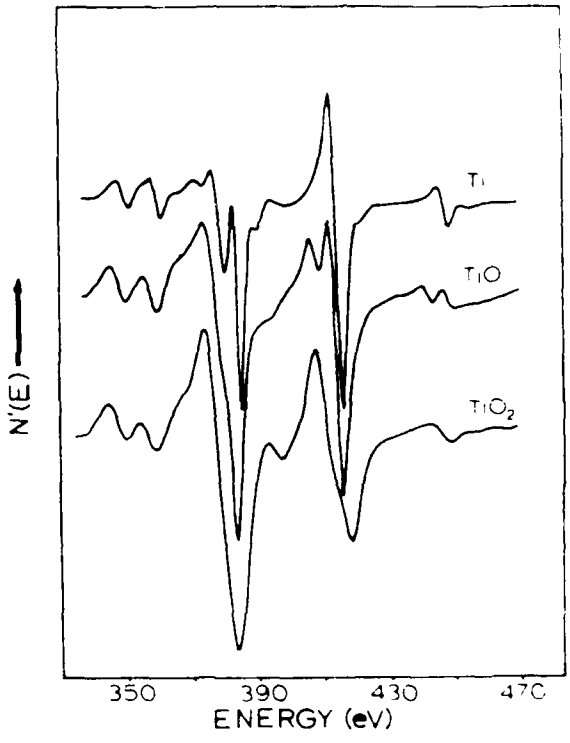

Figure 42. Ti(LMM) and Ti (LMV) dN(E)/dE Auger spectra of Ti, TiO, and TiO_2 [34].

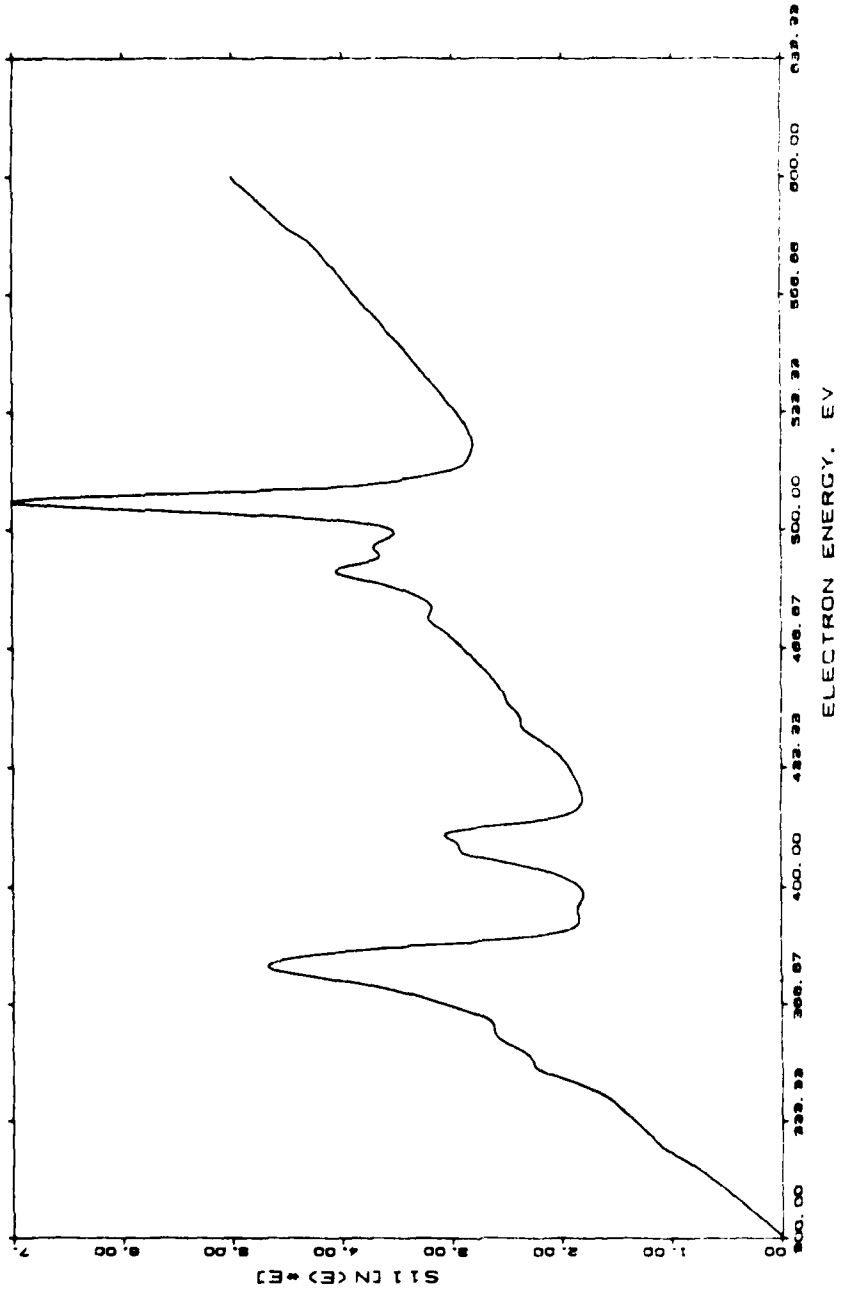

Figure 43. Narrow AES scan of CAA pretreated Ti-6-4.

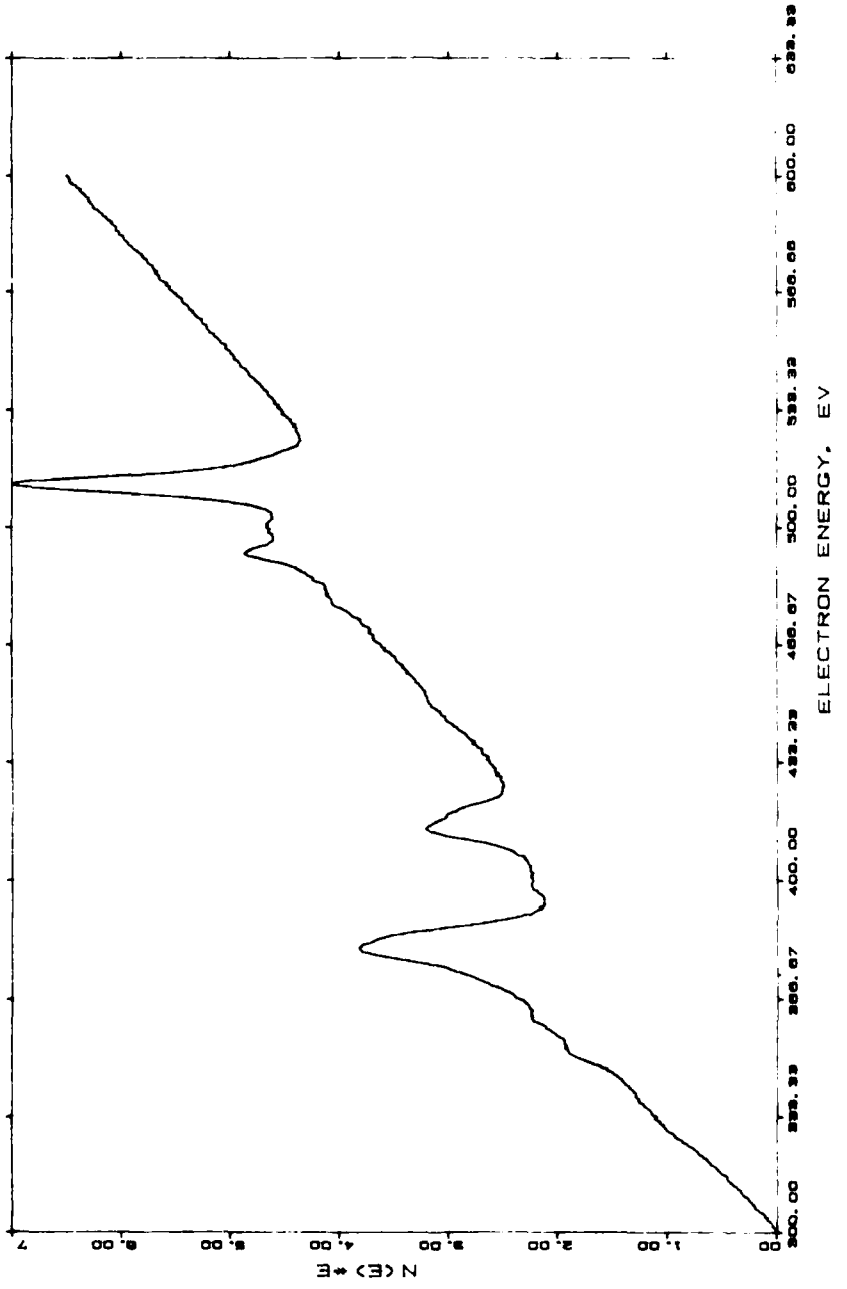

Figure 44. Narrow AES scan of TiO_2 powder.

stoichiometry of the pretreated titanium oxides is TiO. However, as discussed in section II.B.2.c, Davis et al. [33] found the titanium oxide films could be reduced under electron beam bombardment. Thus the question of oxide stoichiometry remains unanswered by AES.

d. Relative oxide thickness

Relative oxide thickness was determined by AES with depth profiling by Ar^+ ion sputtering. Figure 45 shows an example of a depth profile of a CAA surface. The point of intersection of the oxygen and titanium signals is compared with the other pretreated Ti-6-4 surfaces. Table XVII lists the average time for the oxygen and titanium signals to intersect for each pretreatment. These results obtained with the PHI 610 compare qualitatively with those from the SAM 500 with the order of decreasing thickness CAA > TURCO > P/F. The PSHA and SHA pretreated surfaces require a strikingly longer time to reach the signal intersection, which may not be due simply to the increase in oxide thickness, but to the time required to sputter through the nodular overlayer seen in Figure 30 [134]. The PSHA is covered to a lesser degree with the nodular overlayer and sputters to the Ti-O intersection faster than the SHA.

Assuming the CAA oxide is 140 nm thick [135], the sputter rate would be 42.4 nm/min, giving TURCO a thickness of

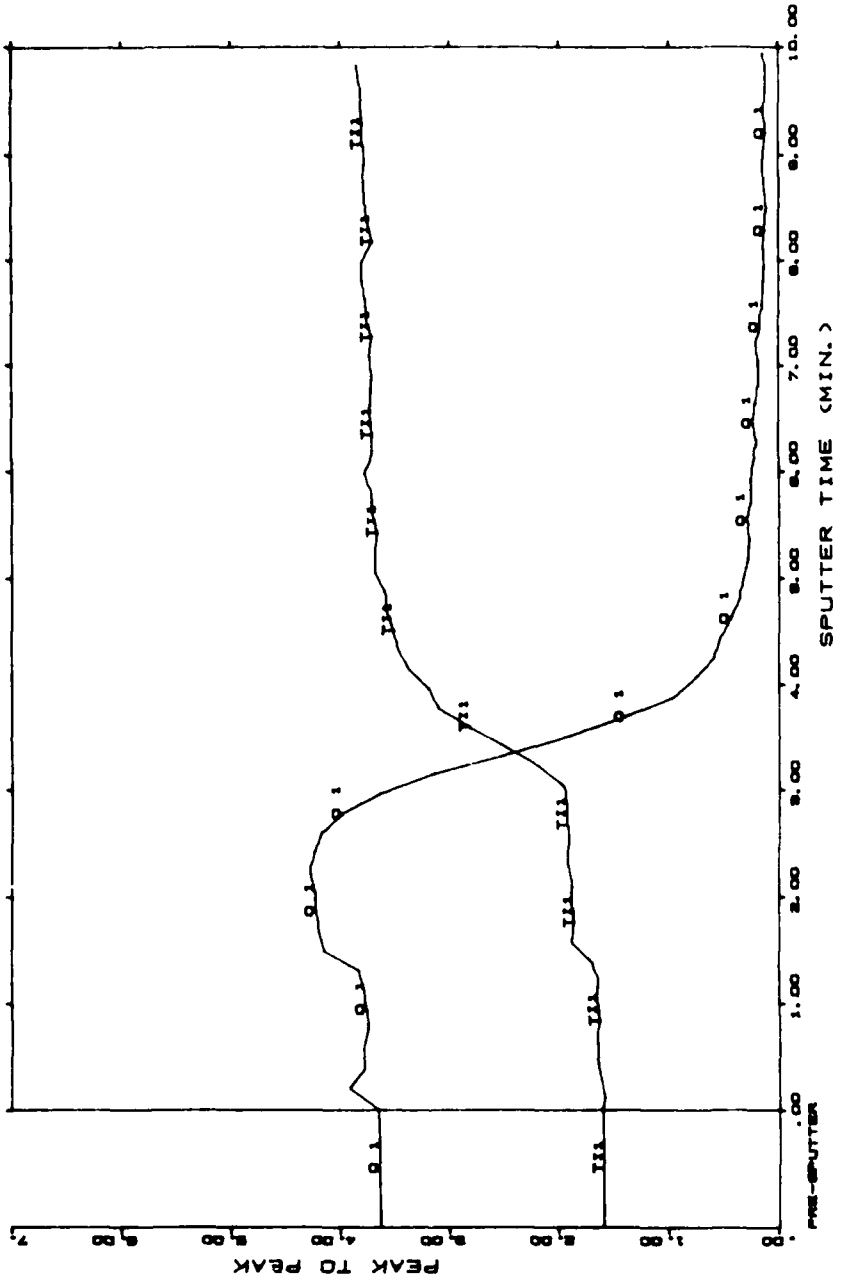

Figure 45. AES depth profile of CAA pretreated Ti-6-4 surface.

TABLE XVII

AES Depth Profile
Average Time to Reach Ti-O Signal Intersection

Pretreatment	Ave. Time
CAA	3.3 min
P/F	0.5 min
TURCO	1.2 min
SHA	64 min
PSHA	9.5 min

51 nm and P/F, 21 nm. Because of the nodular overlayer on the SHA and PSHA pretreated Ti-6-4 surfaces, the thickness was not approximated.

5. Oxide thermal stability

The effects of heating five pretreated Ti-6-4 coupons and foils on chemical and topographical stability of the oxides was studied by XPS. Two anodized samples, CAA and PSHA, and two etched samples, P/F and TURCO, were studied. Both coupon and foil CAA surfaces typically contained carbon, oxygen, titanium and fluorine with the foil surfaces also containing aluminum. The aluminum may be from the XPS probe or the sample itself. Table B-XII in Appendix B lists the elements detected, the binding energies, atomic percents, and the titanium FWHM for the CAA surfaces. There was little difference in chemical composition between the heated and unheated samples. The high binding energy side of the C 1s peak decreased after heating - a phenomenon seen for all pretreated surfaces. The titanium full width at half maximum (FWHM) remained relatively constant, broadening slightly for the heated coupon surface; however, the peak shape did not change.

Only foil samples were studied for the PSHA samples, with Table B-XIII in Appendix B listing the XPS analysis. Carbon, oxygen, titanium, calcium and silicon were detected

on all samples, with reproducible binding energies and atomic percents. Aluminum was sometimes detected and magnesium and phosphorus were single occurrence contaminants. The titanium FWHM was constant for room temperature and heated samples with no change in peak shape. PSHA samples showed no effect of heat on chemical composition.

Differences did occur, however, in the chemically etched samples. The P/F samples typically contained carbon, oxygen, titanium and phosphorus. All but one of the foil samples contained aluminum. Nitrogen was present on one sample, as was sodium present as an obvious contaminant. Table B-XIV in Appendix B lists the XPS analysis for the P/F surfaces. In all cases, the elevated temperature spectra showed broader titanium 2p peaks than the room temperature spectra. The degree of broadening did vary with drastic broadening in three of the four cases. The reason for broadening is discussed below.

Table B-XV in Appendix B lists the XPS analysis for the TURCO samples which typically contained carbon, oxygen, titanium and iron. Aluminum was present on all but one foil sample and silicon, believed to originate from the grit-blasting step, was present only on the coupon samples as the foil samples were not gritblasted. Lead is believed to be a contaminant from the spectrometer and the sulfur was of unknown origin. In all cases, the TURCO samples showed some

degree of Ti 2p peak broadening with elevated temperature. Two foil samples, actually showed the presence of elemental titanium in contrast to strictly titanium oxide observed in all other cases.

The anodized samples were chemically stable at the elevated temperatures showing no change in chemical composition or in Ti 2p peak shapes. The P/F and TURCO samples, however, showed significant Ti 2p peak broadening at elevated temperatures with a typical example shown in Figure 46. This broadening indicates a reduction of the TiO_2 oxide to oxides of lower titanium oxidation state such as Ti_2O_3 and TiO. The reduction of TiO_2 powder at temperatures greater than 250° C under vacuum has been documented [13,136]. The reduction of the Ti^{4+} surface ions is believed to be caused by the contamination of the surface by adsorbed organic compounds [7].

STEM was used to investigate any structural changes that may have occurred upon exposing the samples to elevated temperatures. Figures 47 to 50 show the CAA, PSHA, TURCO, and P/F pretreated foil samples after heating as compared to before heating seen in Figures 32, 33, 35 and 36. No clear differences, such as oxide cracking or peeling, are observed in the oxides after heating. The anodized surfaces maintain their porous integrity and the etched surfaces, while showing Ti 2p peak broadening by XPS, show no structural

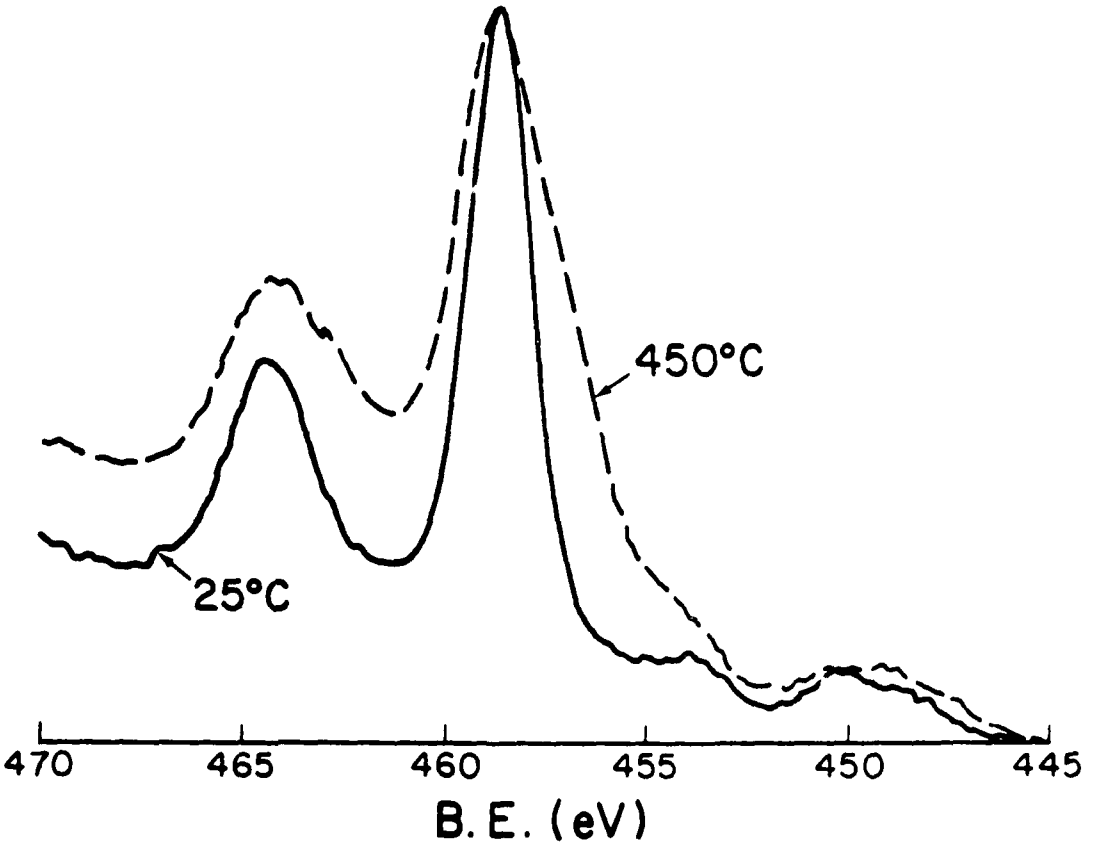

Figure 46. Ti 2p peak before and after heating P/F and TURCO pretreated Ti-6-4 surfaces.

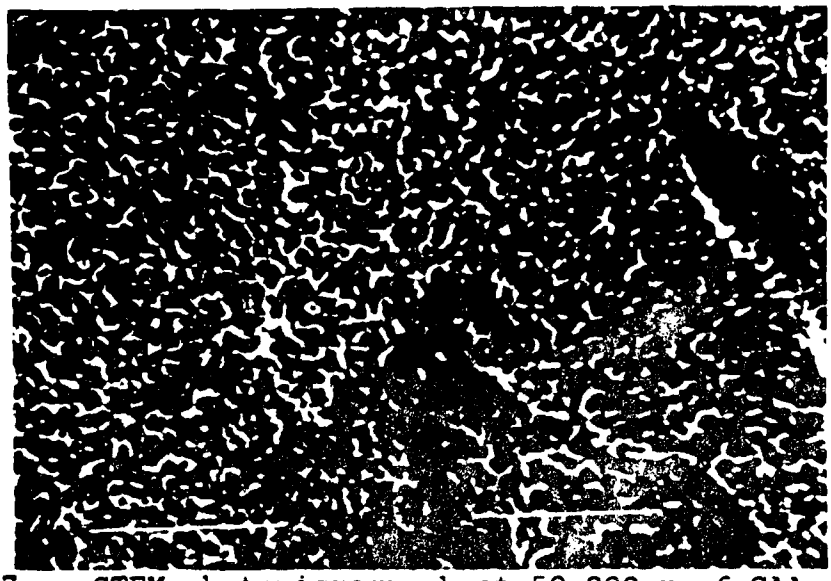

Figure 47. STEM photomicrograph at 50,000 x of CAA pretreated Ti-6-4 after heating to 350° C for 10 min.

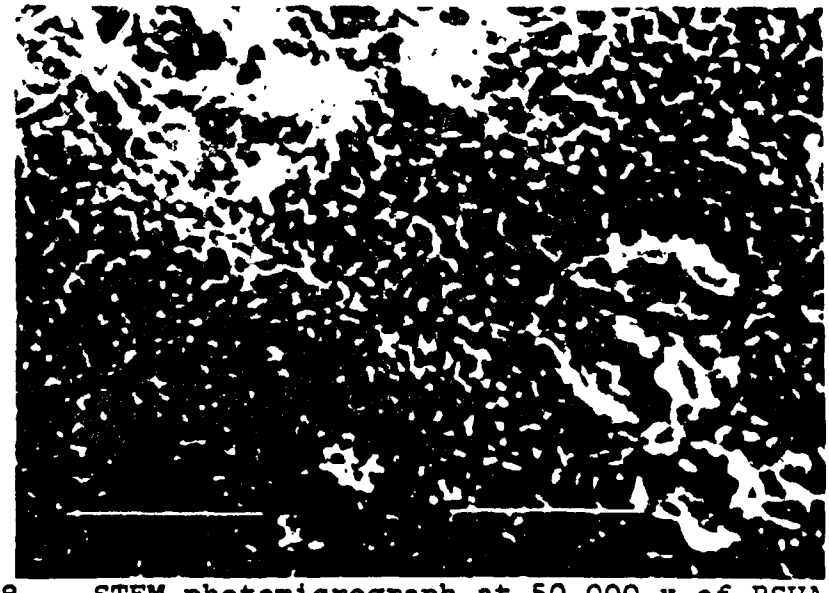

Figure 48. STEM photomicrograph at 50,000 x of PSHA pretreated Ti-6-4 after heating to 350° C for 10 min.

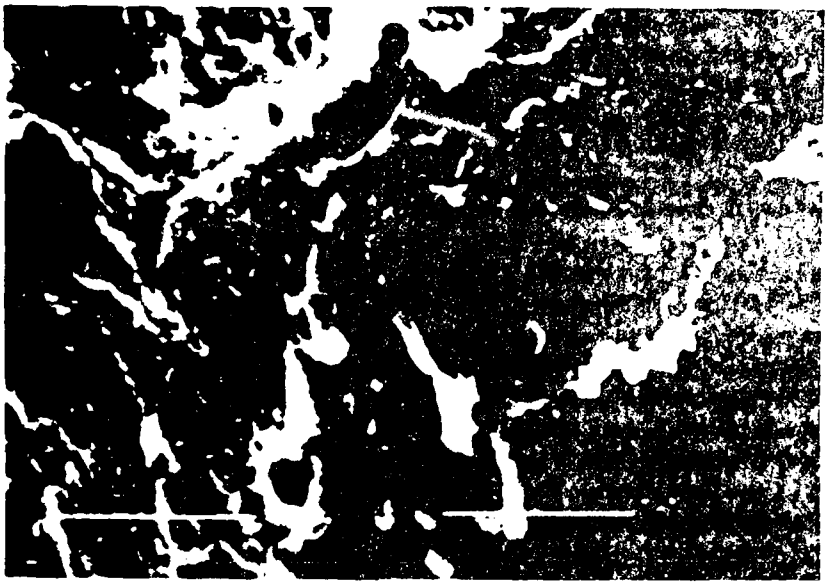

Figure 49. STEM photomicrograph at 50,000 x of P/F pretreated Ti-6-4 after heating to 350° C for 10 min.

Figure 50. STEM photomicrograph at 50,000 x of TURCO pretreated Ti-6-4 after heating to 350° C for 10 min.

changes in the surface oxide at the nanometer level as observed with STEM. Natan and Venables [137,107] heated CAA in vacuum to 250° C and found no change in the oxide thickness with the amorphous structure maintained, in agreement with the present results. Shaffer et al. [138] also found the structural integrity to be visibly maintained at temperatures of 370° C; however, there was a major decrease in bond strength of tensile buttons after heating.

B. Part II - Strength and Durability of Ti-6-4 Epoxy Bonds

1. FM-300 characterization

Three batches of the FM-300 epoxy were studied by XPS to aid in the interpretation of post-failure surface analysis by XPS. Table XVIII lists the XPS analysis for the FM-300 and for the protective sheets covering the Batch I epoxy. Bromine was not detected in Batch I epoxy, while Batch II and Batch III did contain bromine. The bromine serves as an XPS tag for the presence of epoxy on a failure surface. Other tags are the binding energy of the oxygen at 532.8 eV, as titanium oxide oxygen falls at 530.2 eV, and a small atomic percent of nitrogen. The cover sheets showed a small amount of silicon, a contaminant often seen on failure surfaces. Batch I and II were analyzed on the KRATOS instrument and Batch III was analyzed on the PHI instrument.

Because the FM-300 epoxy is exposed to hydrothermal

TABLE XVIII

XPS Analysis of FM-300U Epoxy Film
and Protective Cover Sheets

SAMPLE	ELEMENT	BINDING ENERGY	ATOMIC PERCENT
FM-300	C	285.	89.
Batch II	O	529.4	6.8
KRATOS	Br	70.4	1.2
	N	399.5	1.0
	Si	102.4	2.3
FM-300	C	285.	72.
Batch III	O	532.9	23.
PHI	Br	71.1	1.3
	N	400.1	4.1
FM-300	C	285.	85.
Batch I	O	532.6	10.
	Si	102.2	4.8
FM-300	C	285.	97.
Cover sheet	O	532.1	1.9
	Si	101.5	0.7
Epoxy liner	C	285.	97.
Interfacial	O	532.2	1.8
	Si	101.5	0.7
Epoxy liner	C	285.	97.
Top side	O	532.1	1.9
	Si	101.8	0.9

conditions in the bond line, it was of interest to determine the effects of an 80° C water soak on the epoxy. The alpha transition of an epoxy film, before and after exposure to 80° C water for one month was studied by DMTA. No significant difference in the epoxy film was exhibited before and after water exposure, therefore indicating that the wedge and stress durability test results were not due to adhesive property degradation.

2. Pore penetration study

The presence of a porous structure in the Ti-6-4 surface created by anodization creates an excellent opportunity for increased surface area for adhesive/oxide interaction. The penetration of epoxy into the porous oxide is a fundamental question needing to be answered for surface area of contact arguments to be valid.

FM-300 was cured on CAA pretreated Ti-6-4 foil and peeled apart. Both the metal failure surface, MFS, and the adhesive failure surface, AFS, were examined by STEM. Figures 51 and 52 show the photomicrographs at 50,000x of the two surfaces. The metal failure side showed a faint evidence of porosity, however, it was unclear as to whether the surface was covered by a thin layer of adhesive or if the majority of the porous structure had been removed. The adhesive failure side appeared as if the epoxy had been

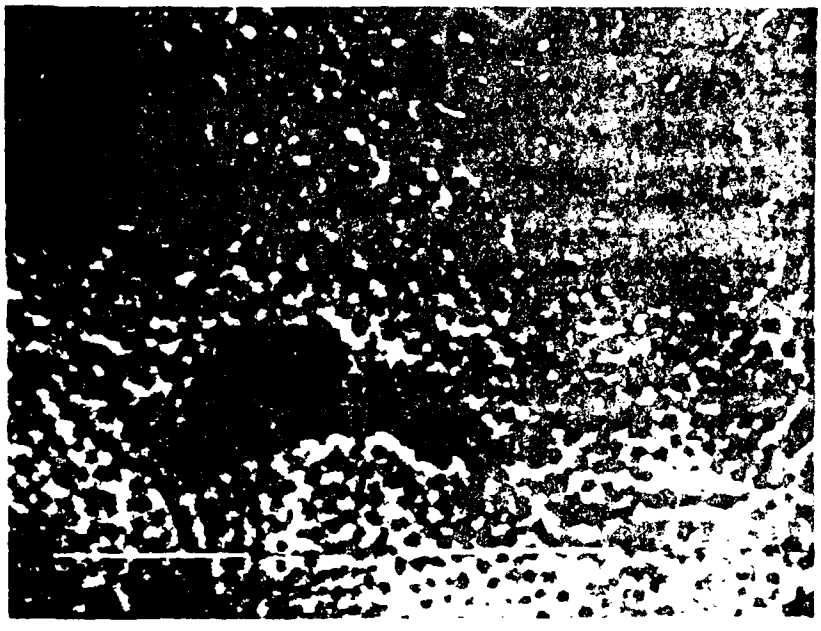

Figure 51. STEM photomicrograph at 50,000 x of MFS of CAA pretreated Ti-6-4 foil peeled from FM-300.

Figure 52. STEM photomicrograph at 50,000 x of AFS of FM-300 peeled from CAA pretreated Ti-6-4 foil.

pulled out of the porous structure. The surface chemical composition was therefore studied by XPS with results listed in Table XIX. Only titanium oxide was present on both surfaces with a high percentage of fluorine. No bromine was detected and the oxygen was indicative of Ti-O bonds. Natan and Venables [137] showed, by AES depth profiling, an increase in fluorine concentration at the oxide/metal interface. The high fluorine concentration indicated that failure had occurred at the base of the porous structure; however, the extent of penetration of the epoxy into the pores was still unclear. The adhesive failure side was then depth profiled with AES. Figure 53 shows the atomic concentration with sputter time. The presence of the carbon signal simultaneously with the titanium and oxygen signals indicated that the epoxy did indeed penetrate the porous structure. This pore penetration is a significant finding because it shows the surface area of interaction between the adhesive and oxide is greatly enhanced by the presence of pores.

The penetration of a fluid into a porous structure can also be calculated for a given porous structure and fluid by equation 57. For a titanium oxide with a pore length of 100 nm and a radius of 20 nm, assuming atmospheric pressure, a surface energy of the epoxy of 45 mJ/m^2 and a zero contact angle, the epoxy will fill the pore to 98 nm or 98% of the pore will be filled. Thus, theoretically and experimentally

TABLE XIX

XPS analysis of MFS and AFS
from pore penetration [illegible]

Surface	Element	B.E (eV)	At. %
MFS	C	285.0	31
	O	530.4	48
	Ti	459.1	20
	F	685.3	11
AFS	C	285.0	22
	O	530.6	26
	Ti	459.1	7.2
	F	683.5	43
	N	402.2	1.3

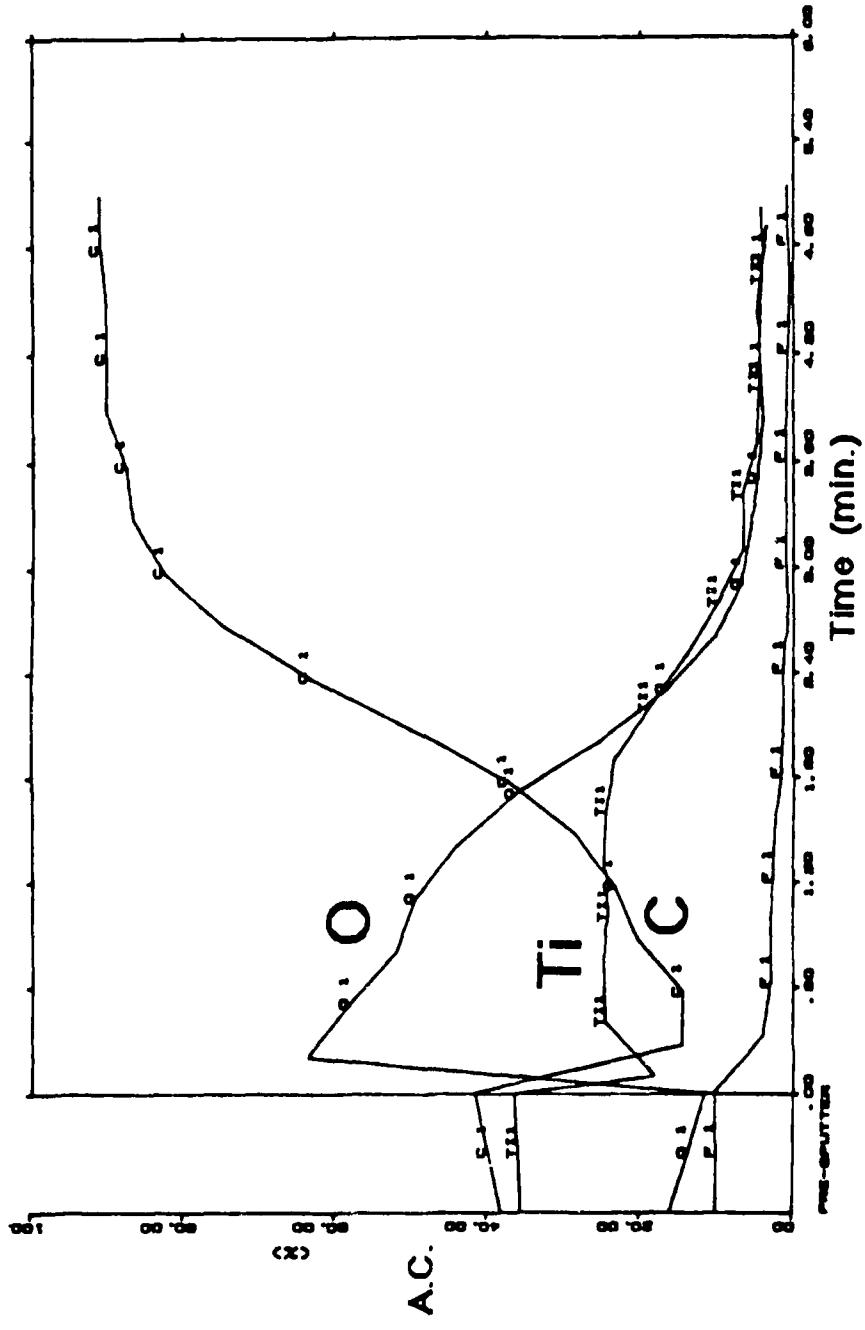

Figure 53. AES depth profile of AFS of FM-300 peeled from CAA pretreated Ti-6-4 foil.

the epoxy has been shown to penetrate the porous structure of the CAA and SHA surfaces.

A limited number of pore penetration studies have been reported. Packham [113] reports molten polyethylene penetrates 98% of 10 nm radius pores. In cross-section TEM photomicrographs, Brockmann et al. [113a] have shown that primer penetrates phosphoric acid anodized aluminum pores.

3. Lap shear test

a. Lap shear strength

Strength to break measurements were done on lap shear joints made from CAA, P/F, and TURCO pretreated Ti-6-4. The average breaking strengths with the 95% confidence limits for CAA, P/F, and TURCO were 26 ± 4.5, 25 ± 5.6, and 28 ± 6.2 MPa, respectively. The CAA showed the smallest variability in lap shear strength with the breaking strengths of CAA, P/F and TURCO not showing a significant difference.

The similarity in bond strength of the CAA, P/F and TURCO bonds could imply that the bond performance of the three pretreated surfaces is similar. The similarity could also imply that the lap shear test is not able to differentiate between pretreated surfaces. As will be shown in the following section, the durability of bonds made with the three pretreatments varies dramatically. Thus, the inability of the lap shear test to distinguish between

AD-A189 503 AN INTERDISCIPLINARY APPROACH TO PREDICTIVE MODELING OF 3/4
STRUCTURAL ADHESI.. (U) VIRGINIA TECH CENTER FOR
ADHESION SCIENCE BLACKSBURG J A FILBEY ET AL. OCT 87
UNCLASSIFIED CAS/CHEM-87-7 N00014-82-K-0185 F/G 11/1 NL

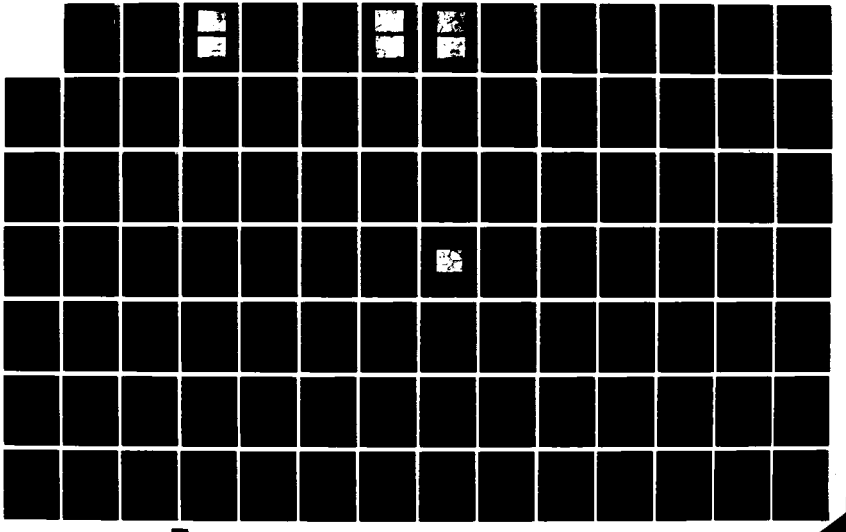

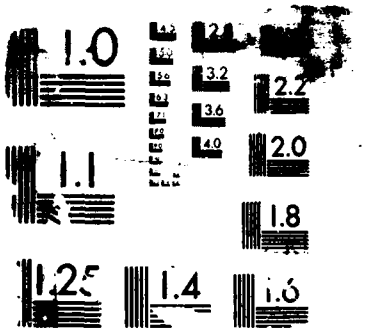

poor surface treatments is documented here for the first time. The lap shear test should not be used to evaluate surfaces for bonding, but rather simply to evaluate adhesive performance. Unfortunately, the use of the lap shear test for just this bonding information continues to be reported in the literature.

b. Locus of failure

Although the lap shear strengths did not differ, the locus of failure changed depending on the pretreatment. For all pretreatments, the failure surfaces appeared to result in a metal failure side (MFS) and an adhesive failure side (AFS). The failure surfaces were then studied by XPS. Table B-XVI in Appendix B lists the XPS analysis for CAA, P/F, and TURCO. For the CAA pretreated coupons, both the MFS and the AFS showed titanium oxide. A titanium metal peak, as well as an oxide peak, was also seen on the MFS showing that the remaining oxide layer was thinner than approximately 5 nm. The oxygen peak occurred at 530.6 eV, indicative of a titanium oxide. The AFS contained a high percentage of fluorine and no bromine was detected. Figures 54 and 55 show SEM photomicrographs of the MFS and AFS failed CAA lap shear samples. The AFS clearly appears to match the MFS and no epoxy is visible on either side. Thus, the bonds failed within the oxide layer, close to the base

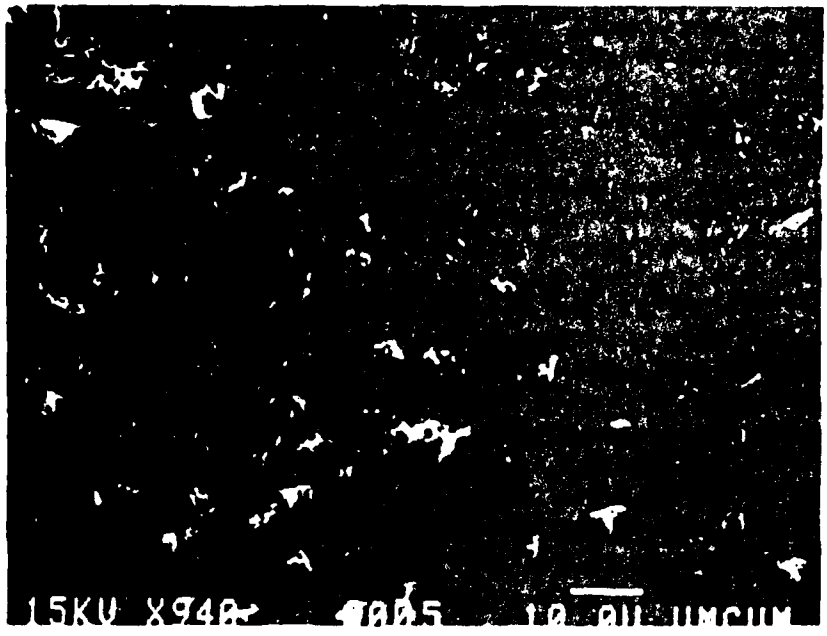

Figure 54. SEM photomicrograph at 940 x of AFS from CAA pretreated Ti-6-4 lap shear bond.

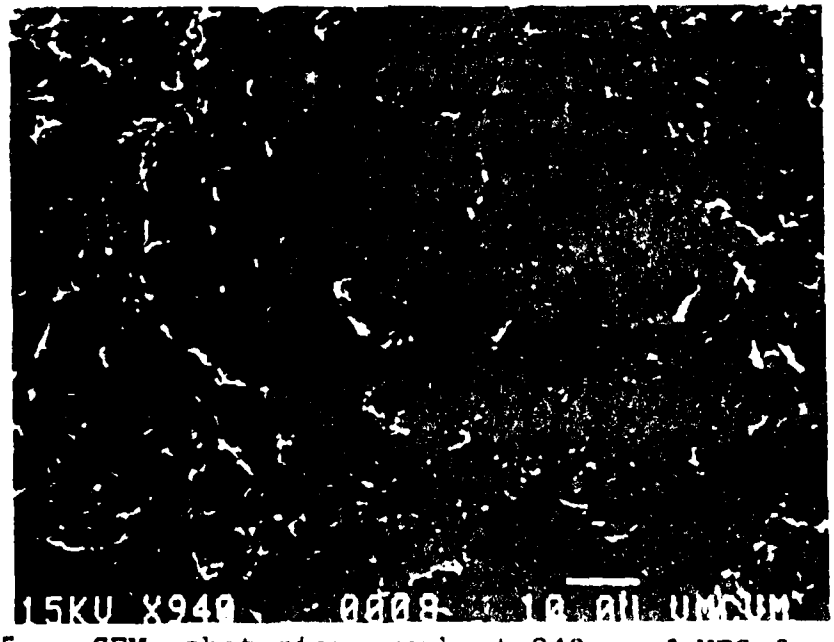

Figure 55. SEM photomicrograph at 940 x of MFS from CAA pretreated Ti-6-4 lap shear bond.

of the pores, a similar failure to the pore penetration experiment. Figure 56 shows schematically the locus of failure for the CAA samples.

The P/F and TURCO pretreated bonds showed a locus of failure different from the CAA bonds. Although the failure appeared to be interfacial, no titanium was detected on either the AFS or the MFS. The oxygen peak at approximately 533 ev indicated carbon-oxygen bonds in the epoxy. Bromine, present in the epoxy, was detected on both the AFS and the MFS and nitrogen was detected in some cases. Epoxy is seen on both MFS and AFS of the TURCO and P/F failure surfaces in the SEM photomicrographs in Figures 57 to 60. Thus, the P/F and TURCO pretreated samples failed within the adhesive, close to the metal oxide, as shown schematically in Figure 61. CAA pretreated surfaces were soaked in boiling water to destroy to porous structure prior to bonding. The failure surfaces were analyzed by XPS with results listed in Table B-XVI. Failure is not within the oxide as in CAA, but in the adhesive as in the etched P/F and TURCO surfaces, indicating porosity must be present to cause oxide failure.

In summary, the lap shear strengths of bonds made with CAA pretreated Ti-6-4 were similar to those made from TURCO and P/F pretreated Ti-6-4, and the locus of failure visually appeared to be similar. However, results from XPS and SEM analysis showed that the locus of failure differed between

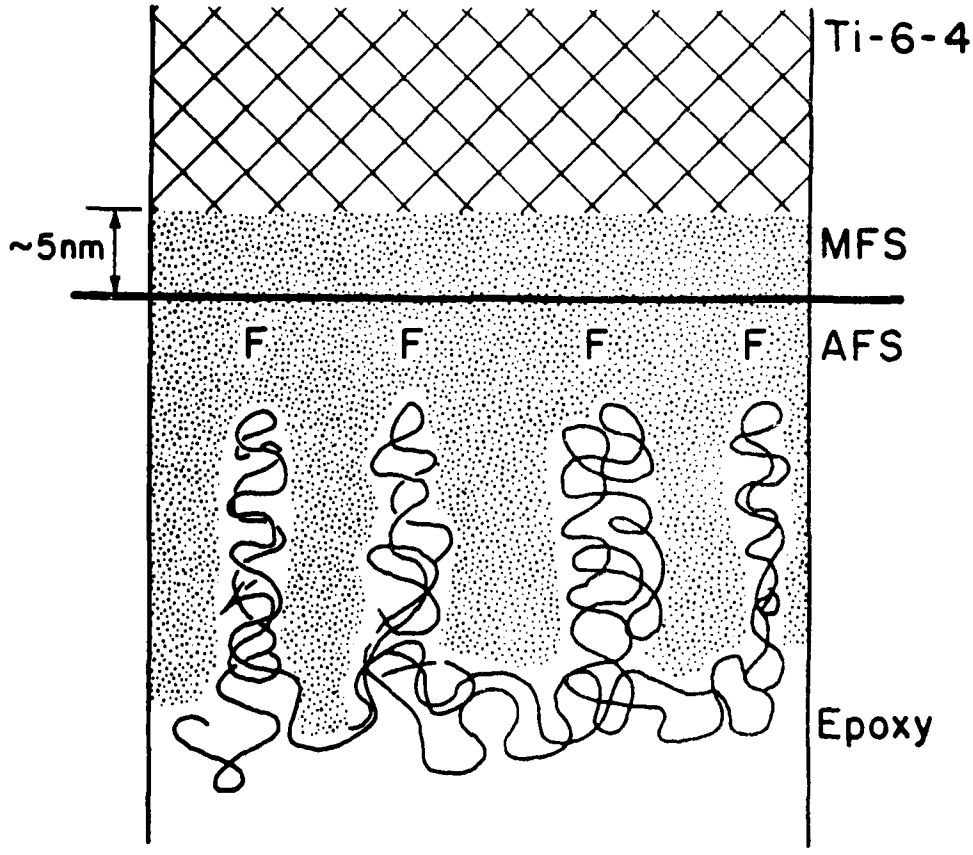

Figure 56. Schematic representation of locus of failure for CAA pretreated Ti-6-4 lap shear bonded with FM-300.

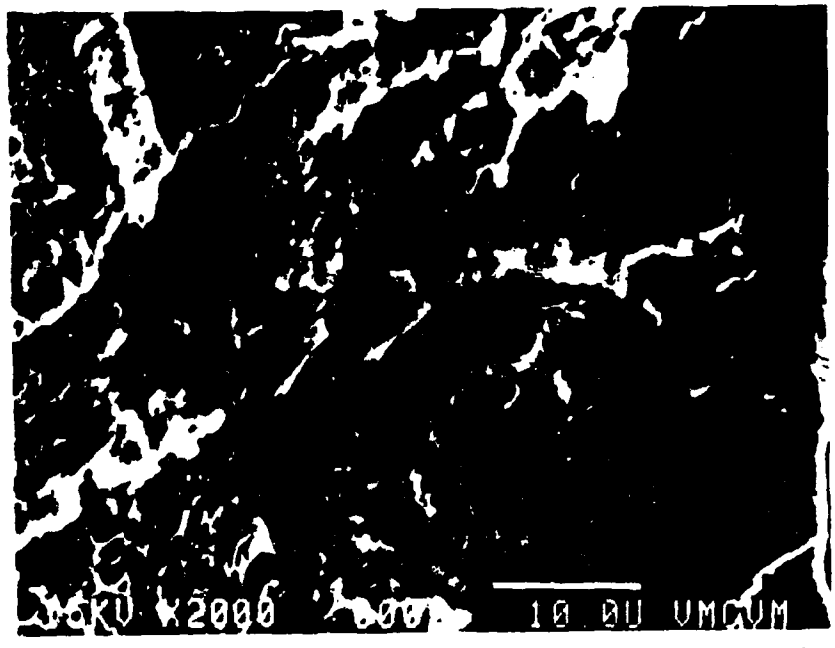

Figure 57. SEM photomicrograph at 1000 x of AFS from P/F pretreated Ti-6-4 lap shear bond.

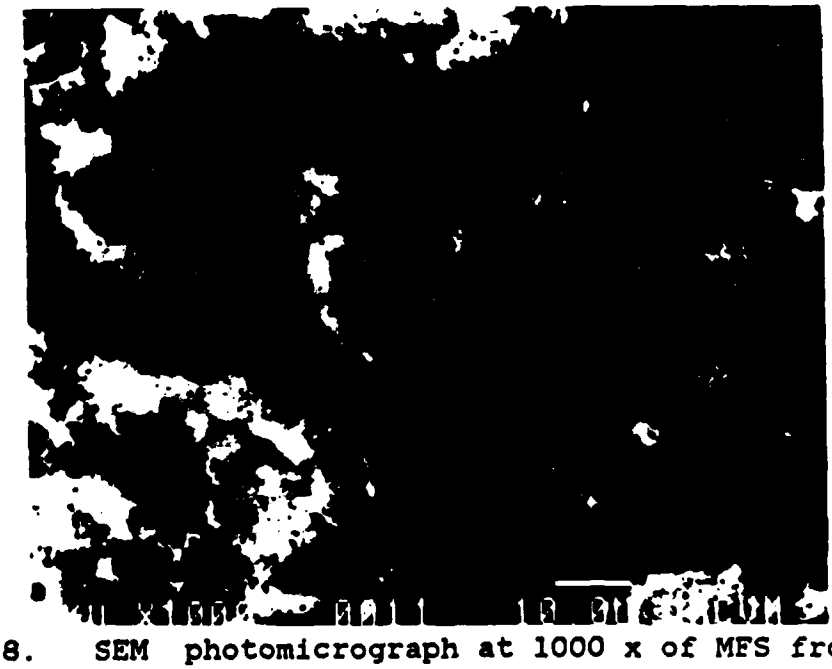

Figure 58. SEM photomicrograph at 1000 x of MFS from P/F pretreated Ti-6-4 lap shear bond.

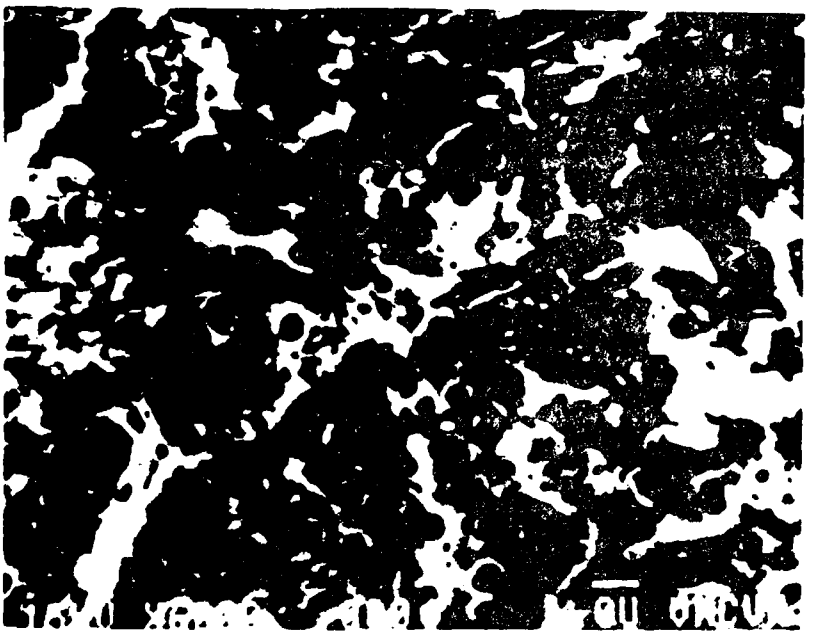

Figure 59. SEM photomicrograph at 3200 x of AFS from TURCO pretreated Ti-6-4 lap shear bond.

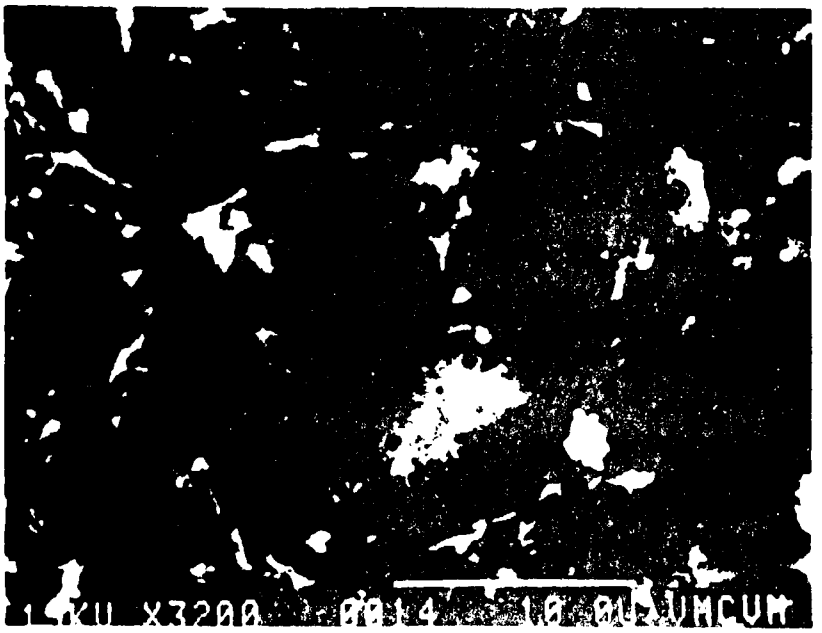

Figure 60. SEM photomicrograph at 3200 x of MFS from TURCO pretreated Ti-6-4 lap shear bond.

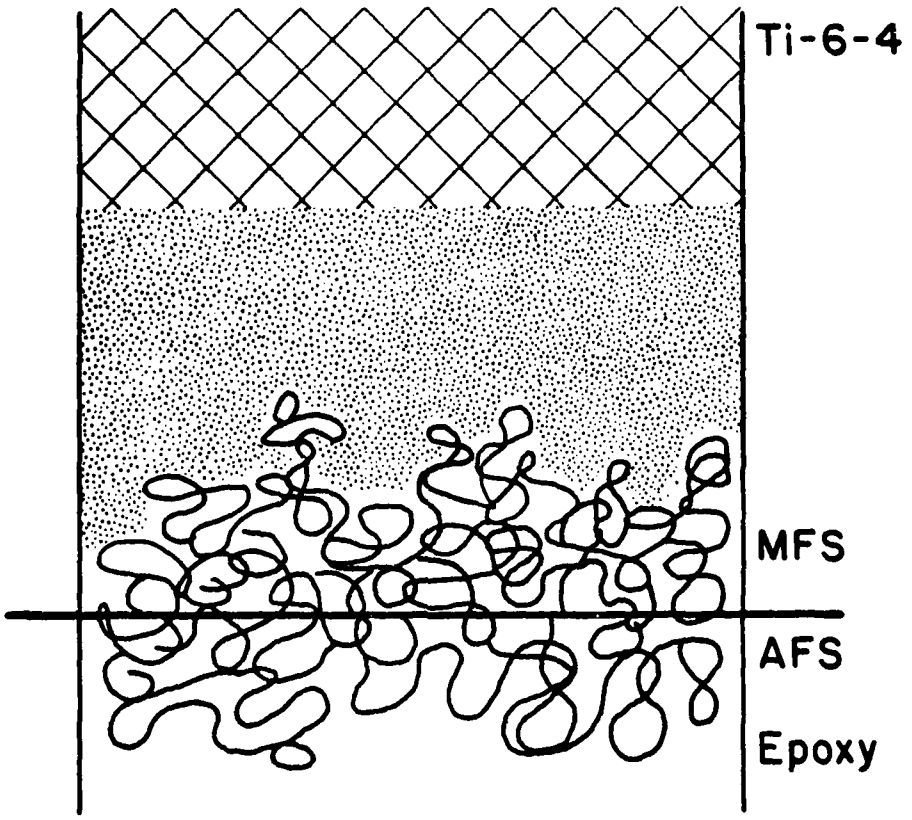

Figure 61. Schematic representation of locus of failure for P/F and TURCO pretreated Ti-6-4 lap shear samples bonded with FM-300.

the anodized and etched surfaces with oxide failure occurring for the CAA and cohesive failure in the adhesive occurring in the etched surfaces.

4. Stress durability test

a. Time to failure

Although the lap shear test was unable to differentiate between good and poor surface pretreatments, the stress durability test allowed the hydrolytic stability of the lap shear bonds to be tested while under a load of 40% of ambient temperature breaking strength. A notable difference was seen for the three pretreatments in the stress durability test as shown by the time to failure windows in Figure 62. The P/F surface showed poor durability with all bonds breaking in less than one day, while the TURCO and CAA surfaces showed better durability with the CAA being the most durable. Stress durability results of CAA, TURCO and P/F pretreated Ti-6-4 bonds from Wegman and Levi [17] agree qualitatively with the present results.

The stress durability test used lap shear bonds which possessed similar ultimate breaking strengths in ambient conditions as reported in the previous section, but when exposed to hot, wet conditions showed large differences in durability.

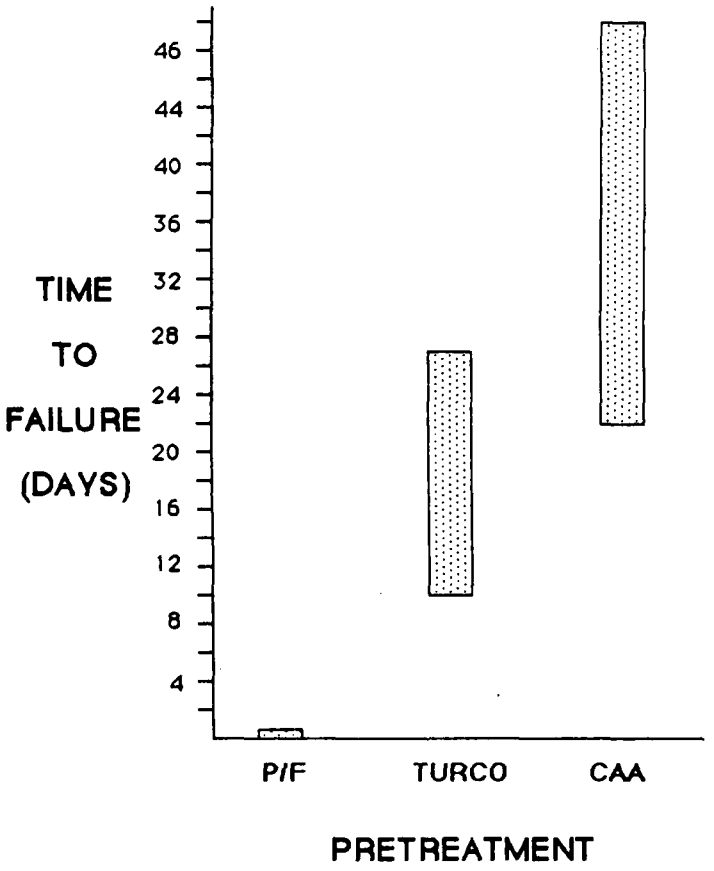

Figure 62. Time to failure windows from the stress-durability test at 80° C, 95% r.h.

b. Locus of failure

The locus of failure for the P/F and TURCO stress durability samples was determined using XPS with results listed in Tables XX and XXI. The MFS for both samples showed the presence of titanium oxide. No bromine was detected on these surfaces. The AFS showed the presence of bromine with the O 1s peak indicative of the epoxy. Thus, failure occurred at the interface between the epoxy and the pretreated titanium surface. These results are in contrast with the locus of failure results obtained for the unexposed lap shear samples, where failure occurred within the epoxy.

The CAA stress durability failure surfaces showed different failure on the edges than in the center. XPS analysis indicated interfacial failure around the edges of the failure surface and oxide failure in the center of the failed surface. These results are not unexpected as once approximately 60% of the bond integrity has been destroyed by moisture around the edges, the remaining center bonded portion can no longer withstand the applied load and rapid deformation occurs similar to the lap shear test, thus similar failure in the center of the bond.

The presence of moisture weakens the titanium oxide/epoxy interface causing it to be the "weakest link" in the system, as predicted from the work of adhesion calculations reported previously in section IV.A.2.

TABLE XX

XPS Analysis of Stress Durability Failure Surfaces of P/F Bonded with FM-300U.

SAMPLE	ELEMENT	BINDING ENERGY	ATOMIC PERCENT
P/F - MFS	C	285.	73.
	O	529.8	21.
	Ti	458.5	4.3
	Ca	348.5	1.7
	P		TRACE
P/F - AFS	C	285.	85.
	O	532.1	13.
	Br	71.6	0.7
	N	399.6	1.4

TABLE XXI

XPS Analysis of Stress Durability Failure Surfaces of TURCO Bonded with FM-300U.

SAMPLE	ELEMENT	BINDING ENERGY	ATOMIC PERCENT
TURCO - MFS	C	285.	62.
	O	531.9,529.8	33.
	Ti	458.4	2.4
	Ca	347.7	1.5
	Na	1071.8	0.5
	Fe		TRACE
TURCO - AFS	C	285.	78.
	O	532.7	17.
	Br	70.9	0.6
	N	400.1	2.2
	Al	120.2	2.7

5. Wedge test

a. Crack extension tests

The wedge test was also shown to be sensitive to surface pretreatment. Ditchek et al. [16a] reported the durability of CAA, P/F, and TURCO pretreated Ti-6-4 which had been primed with an organic primer and exposed to 60° C, 95% r.h. The CAA was found most durable and the P/F the least durable with TURCO showing intermediate durability. It was of interest, therefore, to look at the performance of the same pretreatments under more severe environments, with no primer, which has not been reported previously.

CAA, SHA, TURCO, and P/F samples were exposed in a 80° C, 95% r.h. environment. The CAA, SHA and TURCO samples showed no crack propagation for 14, 26 and 14 day test periods, respectively. Cracks did propagate, however, in the P/F samples which showed rapid crack propagation to failure in less than 24 h.

Three of the pretreatments, CAA, TURCO, and P/F were tested in 80° C water immersion. The P/F samples were again not durable to the environment, while the CAA and TURCO samples showed no crack propagation in the test period of 49 days and 26 days, respectively. Upon breaking open the joints, an area of 0.5 to 1 cm below the initial crack showed apparent interfacial failure, in contrast to the cohesive failure of the remainder of the joint. This

indicated that although crack growth was not exhibited, bond degradation was occurring.

To further accelerate the wedge test, CAA, SHA, TURCO, and P/F surfaces were immersed in 95° C water. After 16 days, the TURCO samples showed the initiation of crack growth, with the crack propagating 0.1 cm, but the CAA and SHA samples showed no propagation. However, for longer exposure times, cracks began to propagate in the CAA and SHA samples. Thus, results from the stress durability test qualitatively agreed with results from the wedge test with the anodized surfaces being the most durable, followed by TURCO, and finally with the P/F showing poor durability similar to that in 80° C.

The rate of crack growth versus time for P/F samples immersed in 95° C water is shown in Figure 63. There is an initial decrease in the rate of crack growth due to the joint geometry. Because the wedge test is a constant displacement test, as the crack length increases, the load at the crack tip decreases, thus a decreasing rate is expected. After approximately 1.5 h, however, the rate begins to increase and continues to increase until failure. This increase can be explained by the dominant influence of the environment on the adhesive bond.

A basic buffer solution was also used as an immersional environment for some wedge samples. TURCO and P/F samples

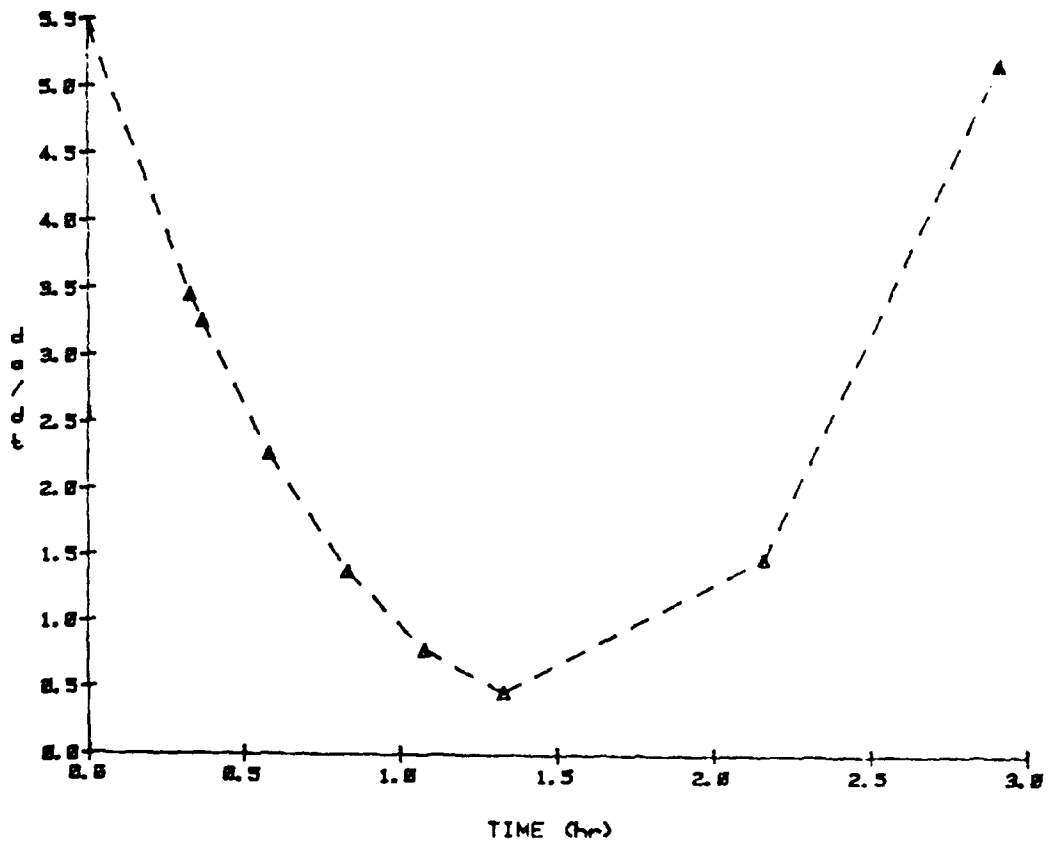

Figure 63. Rate of crack extension vs. time for P/F samples in 95° C.

were placed in a basic buffer at 80° C. After 17 days, the TURCO samples showed little, if any crack growth - only 0.3 cm in one sample. The crack growth with time for the P/F samples is shown in Figure 64 with the 80° C, 95% r.h. as a reference. The rate of crack growth for the P/F sample is slower in the basic buffer than in relative humidity. Slower than expected crack propagation has also been observed by Matz and LeFebvre [139]. If the degradation of the epoxy/ titanium oxide interface by hydrolysis of interfacial bonds, is catalyzed by hydrogen ions, then the rate of crack growth should be lower where the concentration of hydrogen ions is lower.

An acidic buffer at pH=2 was also used as an immersional environment. However, the Ti-6-4 coupons showed visible dissolution in the acidic environment. Still, the TURCO and CAA pretreated samples showed reasonable durability, as shown in Figure 65.

b. Strain energy release rate, G_1

As discussed in section II.E.3., the strain energy release rate, or G_1, for the wedge test is the energy for crack arrest and can, therefore, give an indication of how much energy the bond can withstand. Initial crack lengths were averaged and the 95% confidence limit found to be 6.0 ± 0.4 cm for CAA, 6.3 ± 0.3 cm for P/F and TURCO. Calculating

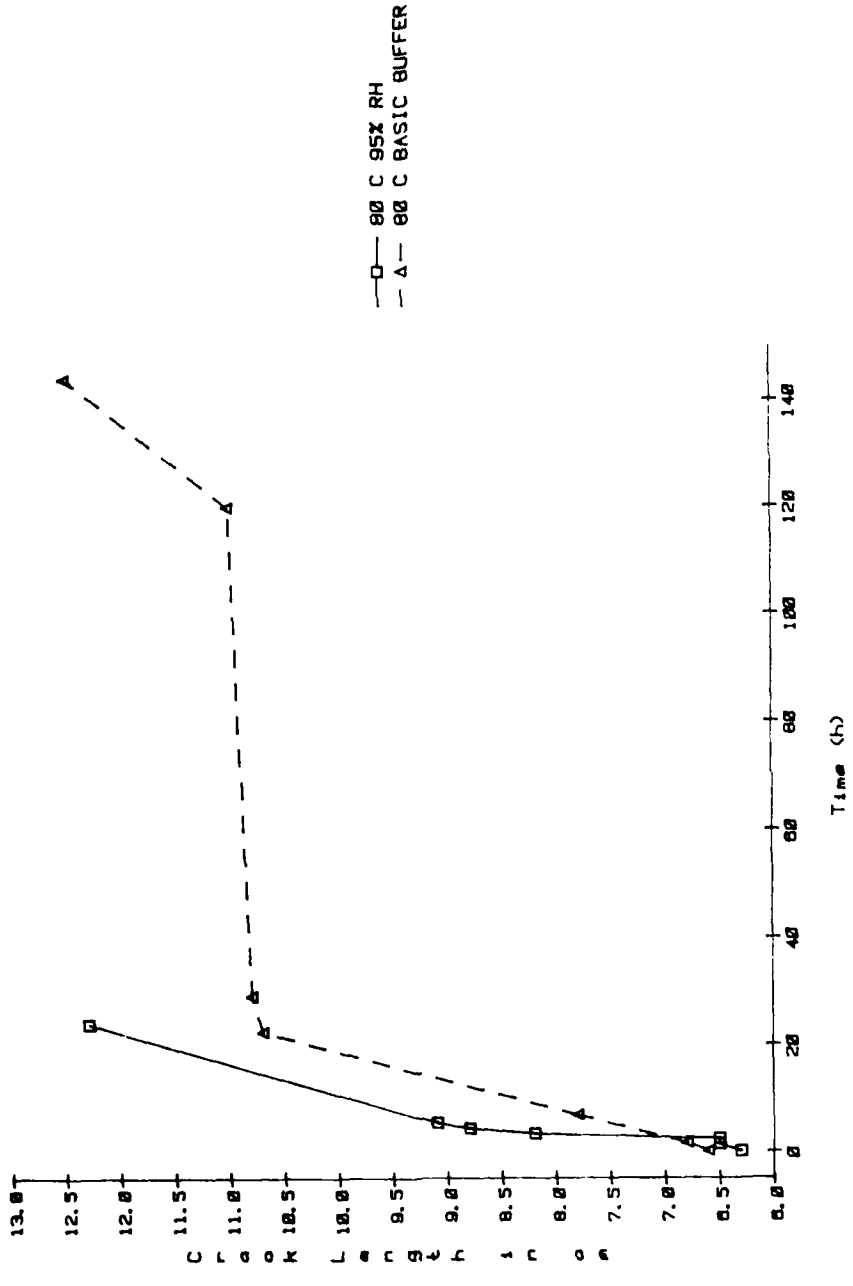

Figure 64. Crack extension vs. time for P/F pretreated wedge samples bonded with FM-300 and immersed in basic buffer at pH = 11.8, and 80° C.

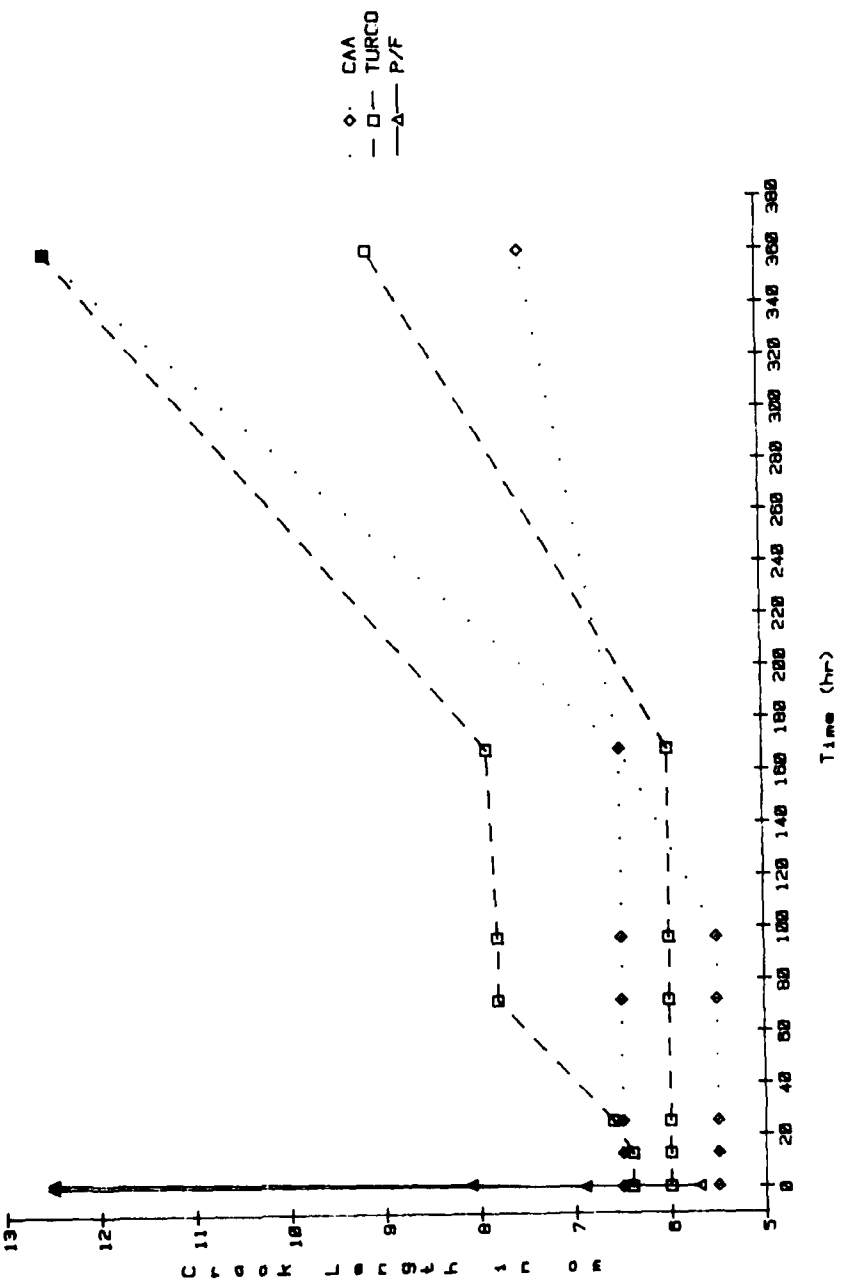

Figure 65. Crack extension vs. time for CAA and TURCO pretreated wedge samples bonded with FM-300 and immersed in acidic buffer at pH = 2, and 80° C.

the corresponding G_1 values with 95% confidence limit yields 1200 ± 340, 940 ± 180 and 960 ± 160 Pa m for CAA, P/F, and TURCO, respectively. While the CAA pretreated samples have a higher average G_1, there is no statistical difference between the initial energy each bond can withstand for the various pretreated samples.

The difference occurs, then, when the bonds are exposed to the environment. A similar trend was observed for the lap shear test. No statistical difference in lap shear strength exists, however, upon exposure to humidity under load, there is a drastic change in durability between pretreatments.

In the 80° C, 95% r.h. environment, the CAA and TURCO pretreated samples showed no crack propagation. Therefore, the energy for crack arrest was greater or equal to approximately 1000 Pa m. On the other hand, for the P/F samples, the crack never arrested for the entire bond length of 12 cm tested. Thus, the P/F treated samples could not even withstand 76 Pa m - the energy at the end of the bond. In cases where the crack arrests after some initial crack growth, a threshold G_1 can be calculated, as will be seen in a later section.

c. Locus of failure

The locus of failure for the P/F wedge samples was

determined using XPS with results listed in Table XXII. The MFS showed no epoxy; titanium, oxygen and carbon were detected with the oxygen binding energy indicative of titanium oxide. The AFS showed only carbon, oxygen, nitrogen and bromine, with binding energies corresponding to that of the neat epoxy. The bonds failed at the epoxy/metal oxide interface, as was seen for the locus of failure in the stress durability test results.

With either test, the stress-durability test using the lap shear geometry or the wedge test, the locus of failure for environmentally exposed bonds is the same. These results are a significant finding showing that the failure is a function of the interfacial degradation and is independent of the test geometry.

6. Summary

Some key issues in adhesive bond testing and failure analysis have been addressed. First, the lap shear test was unable to differentiate between the different pretreatments; however, the locus of failure differed between the etched and anodized surfaces. The ability to detect differences in locus of failure in the lap shear test indicates the failure surfaces are not destroyed in the test itself. Secondly, when hot, wet conditions are introduced to a stressed sample, either stress durability or wedge, significant

TABLE XXII

XPS Analysis of P/F Pretreated Wedge Test Failure Surfaces Bonded with FM-300U

SAMPLE	ELEMENT	BINDING ENERGY	ATOMIC PERCENT
P/F - MFS	C	285.	43.
	O	529.4	36.
	Ti	458.1	9.1
	N	399.6	9.8
	Ca	347.0	1.5
P/F - AFS	C	285.	91.
	O	532.4	8.2
	Br	71.7	0.5
	N		TRACE

differences in the durability of pretreatments is observed, with the locus of failure now occurring at the epoxy/Ti-6-4 oxide interface in all cases. These results lead to a third extremely important issue. For each set of tests reported here, the adhesive, adherend, and environmental conditions remained constant, with the only difference being the surface preparation of the adherend. Predictive modeling of durability, using only bulk properties of adherend and adhesive is, therefore, not sufficient. Interfacial properties must be included to provide an adequate predictive model.

C. Part III - Metal Alkoxides as Adhesion Promoters

1. Adhesive Bonding

The P/F pretreated Ti-6-4 showed poor durability compared to the CAA, SHA, and TURCO pretreatments. Because of its poor durability, it was chosen as the substrate to test metal alkoxide primers for the enhancement of durability. Alkoxides as adhesion promoters have showed varied success and the mechanisms by which they operate are not yet understood. Thus, both adhesive testing of alkoxide primed bonds and characterization of the metal alkoxides was warranted.

Two alkoxides, TNBT and E-8385, were tested on P/F pretreated samples using the wedge test in 95° C water. Three alkoxides, TNBT, TIPT, and E-8385 were tested on P/F pretreated samples using the wedge test in 80° C, 95% r.h.

Using the stress-durability test, E-8385 was tested on both P/F and CAA pretreated Ti-6-4.

a. Wedge test

The effect of primer thickness was studied by applying one and five coats to the adherend surface prior to bonding. Figure 66 compares the durability of the bonds made with one and five coats of E-8385 and TNBT. Five coats of the primer showed better durability than one coat for both alkoxides, consistent with results reported by Pike [121] for aluminum adherends coated with E-8385 and bonded with epoxy. The initial slopes of the curves in Figure 66 show that the E-8385 improved the durability of the P/F pretreatment over the TNBT. The rate of crack growth was determined from the slope of a line fit to the data. Figure 67 shows the rate of crack growth versus time for the E-8385 coated P/F samples. At 95° C water immersion, an increase in the rate of crack propagation follows an initial decrease in rate. This result implies the joint design dominates the initial crack growth. Because of the constant displacement, the load decreases with increasing crack length, thus a decrease in the rate would be expected. The environmental effects then dominate causing an increase in the rate of crack propagation. Note that the turning point for the increase in rate of crack growth occurs after 12 h, in contrast to the P/F sam-

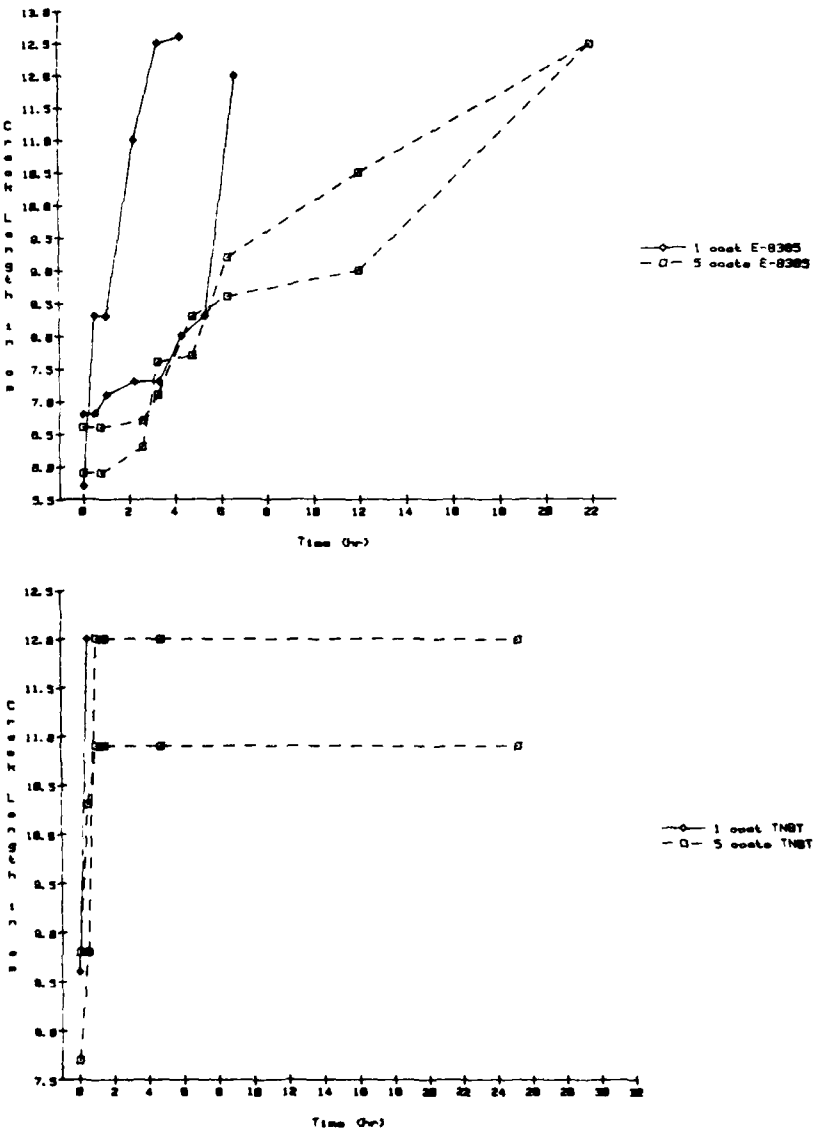

Figure 66. Crack extension vs. time for P/F pretreated wedge samples coated with one and five coats of TNBT or E-8385, bonded with FM-300 and immersed in 95° C water.

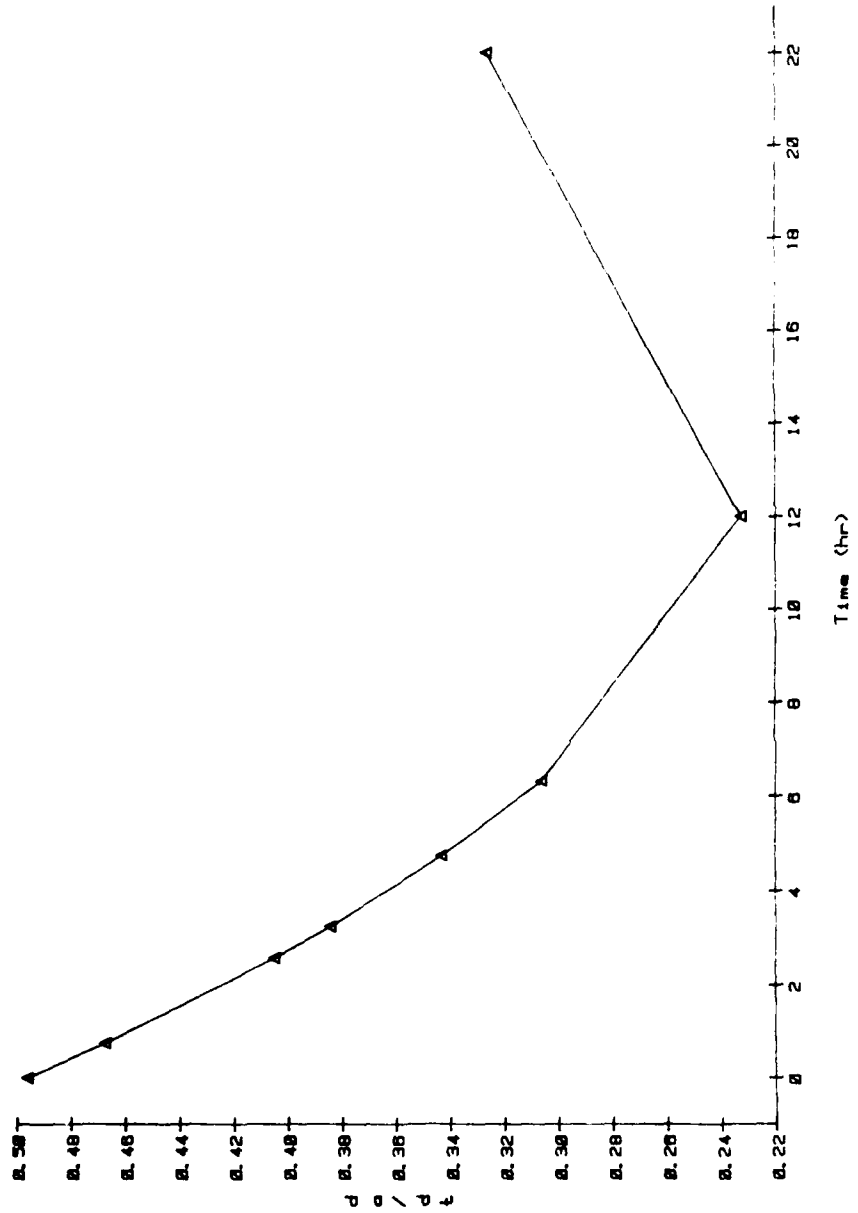

Figure 67. Rate of crack growth vs. time for P/F pretreated wedge samples coated with five coats of E-8385, bonded with FM-300 and immersed in 95° C water.

ples in Figure 63 which change direction in less than 1.5 h.

The locus of failure for the P/F with alkoxide exposed to 95° C water immersion was investigated using XPS and Table XXIII lists the XPS analysis. As discussed previously, the locus of failure in the unprimed P/F bonds occurs at the epoxy/titanium oxide interface. The failure surfaces of the TNBT coated P/F bonds also show titanium oxide on the MFS, with no evidence of epoxy, while the AFS shows bromine, nitrogen and high binding energy oxygen, but no titanium. Thus, failure appears to be interfacial in the titanium alkoxide case as well.

The E-8385 primed failure surfaces tell a different story. Titanium is present on the MFS, but at a lower atomic percent than on the MFS of unprimed P/F. The striking difference is the presence of aluminum from the primer and nitrogen, presumably from the epoxy, although no bromine was detected. The AFS also shows the presence of aluminum and nitrogen, as well as bromine, with no indication of titanium. The failure seemed to occur, therefore, in the aluminum oxide primer layer which must be discontinuous to allow bromine on the AFS and titanium on the MFS to be detected. An intriguing feature on the MFS is the presence of nitrogen, which indicates a preferential adsorption of the amine curing agent in the epoxy on the aluminum alkoxide/oxide surface.

TABLE XXIII

XPS analysis of wedge test failure surfaces
of P/F pretreated Ti-6-4 coated with alkoxides

SAMPLE	ELEMENT	BINDING ENERGY	ATOMIC PERCENT
E-8385 on	C	285.	26.
P/F - MFS	O	530.8	47.
	Ti	458.8	2.2
	Si	102.7	7.3
	N	400.1	2.3
	Al	74.4	15.
E-8385 on	C	285.	45.
P/F - AFS	O	532.6	37.
	Br	70.7	0.4
	Si	103.2	6.5
	N	400.2	2.4
	Al	74.7	8.6
TNBT on	C	285.	43.
P/F - MFS	O	530.7	41.
	Ti	459.0	5.1
	Si	102.8	10.
	Ca	348.0	1.4
	Al	TRACE	
TNBT on	C	285.	74.
P/F - AFS	O	533.1	21.
	Si	TRACE	
	N	400.0	3.4
	Br	70.8	1.1

Three alkoxide primers were tested in 80° C, 95% r.h. The TNBT and the TIPT were coated on P/F pretreated wedge samples and cured at 25° or 300° C prior to adhesive bonding. The E-8385 was coated on the P/F wedge samples and cured at 25° C.

The 25° C cured TNBT wedge samples failed upon wedge insertion and the 300° C cured TNBT wedge samples showed crack propagation to failure within 2.5 hours. The TIPT also showed rapid crack propagation with the 25° C cured film samples failing slightly faster than the 300° C cured film samples. Figure 68 shows the crack length versus time for the titanate primers with an unprimed P/F control. The initial rates (slopes in Fig. 68) for the first 24 h of crack propagation, show that the slowest crack propagation is with the P/F control. The TIPT primed samples show a slower rate of crack propagation than the TNBT primed sample, but both TIPT and TNBT show no enhancement in bond durability of P/F pretreated bonds exposed to 80° C, 95% r.h.

For the TIPT samples, however, the crack appears to arrest at rather long crack lengths of 11 and 10.5 cm for the 25° and 300° C cure samples respectively. A threshold value for G_1 can then be calculated. The energy for crack arrest for the 25° C cure TIPT primed P/F samples is 110 Pa m and 130 Pa m for the 300° C cured TIPT primed P/F samples, whereas the energy for crack arrest in the TNBT bonds is

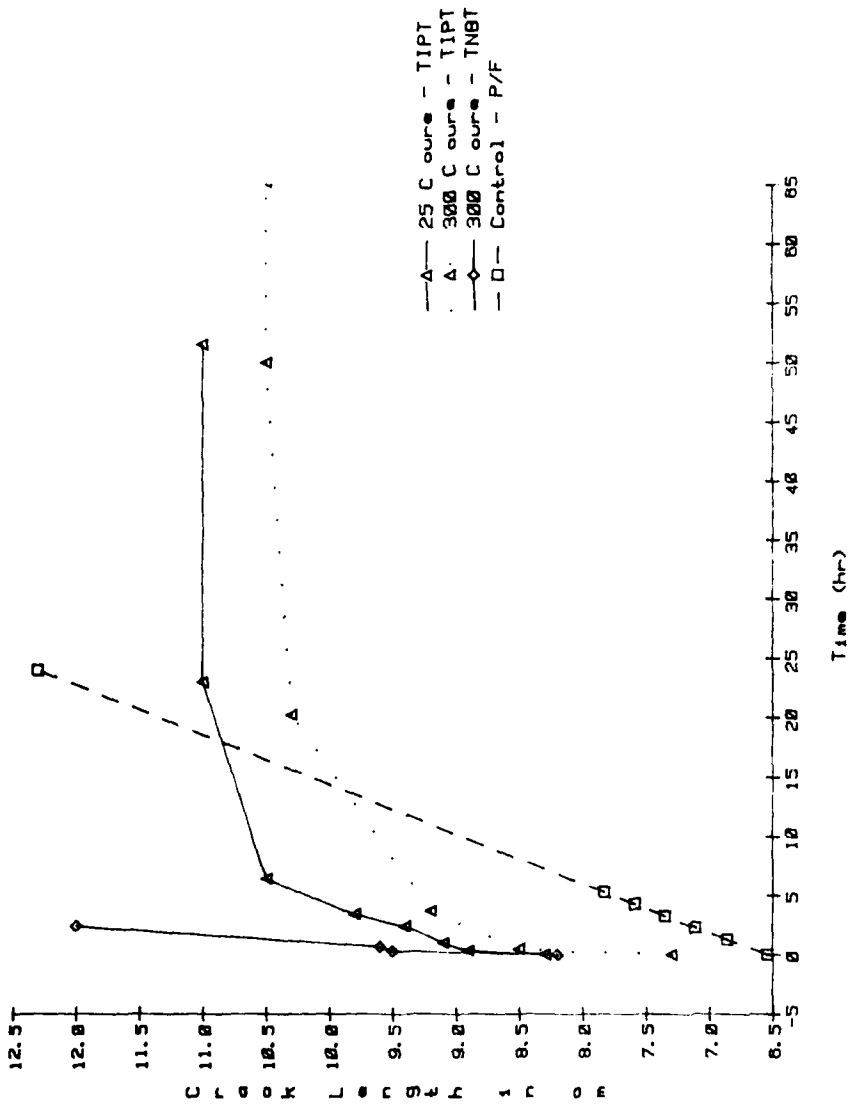

Figure 68. Crack extension vs. time for P/F pretreated wedge samples coated with five coats of TNBT and TIPT, bonded with FM-300 and exposed to 80° C, 95% r.h.

less than 76 Pa m.

The failure surfaces of the TNBT 25°C cure sample, which broke upon wedge insertion were analyzed by XPS with results listed in Table XXIV. Neither the MFS nor the AFS showed the presence of titanium. Bromine and oxygen at 533 eV were detected on both the AFS and MFS. While failure visually appeared to be interfacial, XPS results indicate failure occurred within the epoxy. This last conclusion demonstrates that state-of-the-art surface analysis must be used in determining the locus of failure.

In contrast to the titanate primers, the aluminum alkoxide primers, E-8385, showed a profound enhancement of the P/F durability when bonded and tested via the wedge test. No crack propagation was observed for two days and in 14 days, the crack still had not propagated to failure as shown in Figure 69 contrasting the unprimed P/F samples where the crack usually propagated to failure within 24 hours.

b. Stress durability test

The stress durability test results for P/F and E-8385 primed P/F qualitatively agree with the wedge test results. The E-8385 primed P/F bonds lasted 10 to 20 times longer than the unprimed P/F bonds. When the CAA surface was primed with E-8385, the durability was similar to the E-8385 primed P/F bonds as shown in Figure 70 with a much narrower

TABLE XXIV

XPS Analysis for Locus of Failure of
P/F Wedge Sample Coated with 25° C Cured TNBT

SAMPLE	ELEMENT	B.E.(ev)	A.P.
TNBT on	C	285.	92.
P/F - MFS	O	530.0	5.9
	Ti	NONE	
	Br	70.9	0.3
	Si	102.2	1.3
	N	TRACE	
P/F - AFS	C	285.	89.
	O	533.1	8.8
	Br	71.0	0.8
	N	400.1	0.9
	Si	102.3	0.5

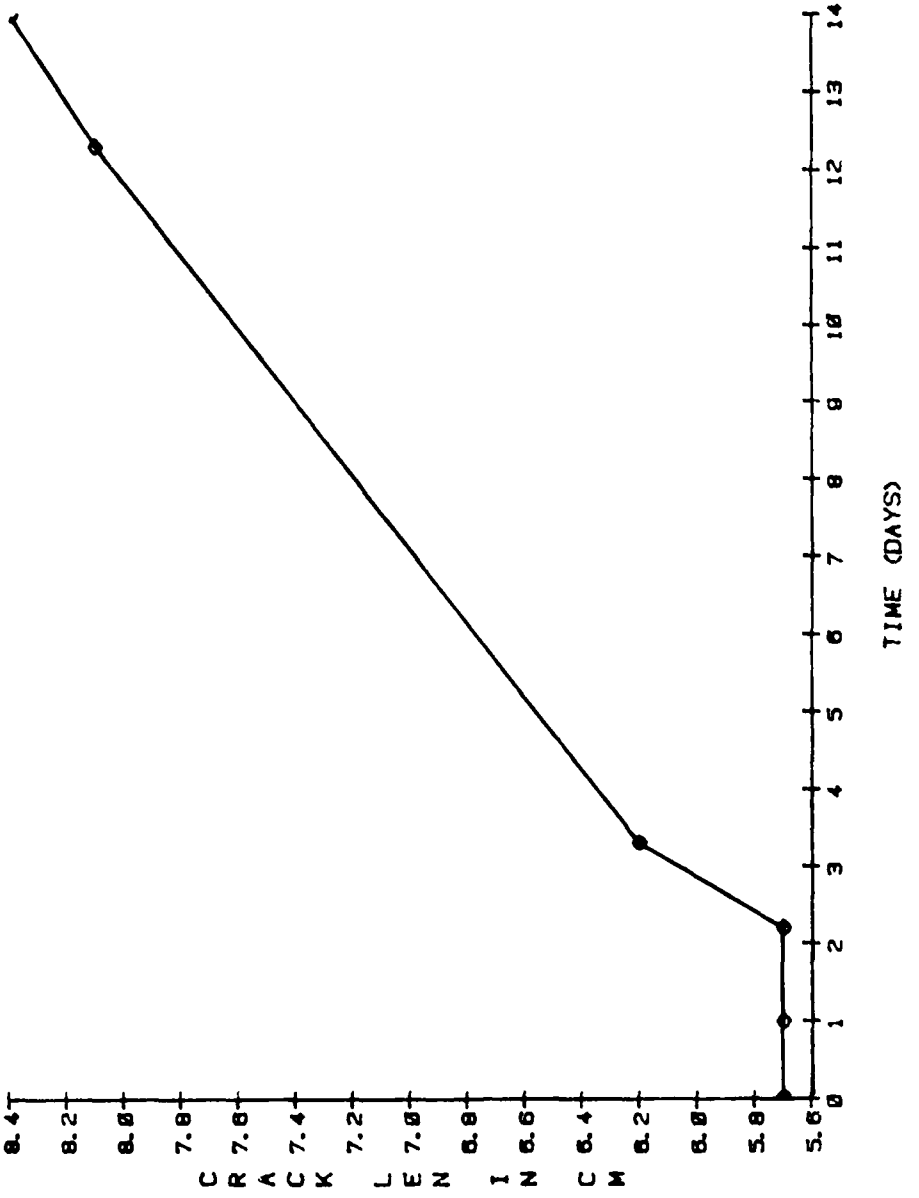

Figure 69. Crack extension vs. time for P/F pretreated wedge samples coated with five coats of E-8385, bonded with FM-300 and exposed to 80° C, 95% r.h.

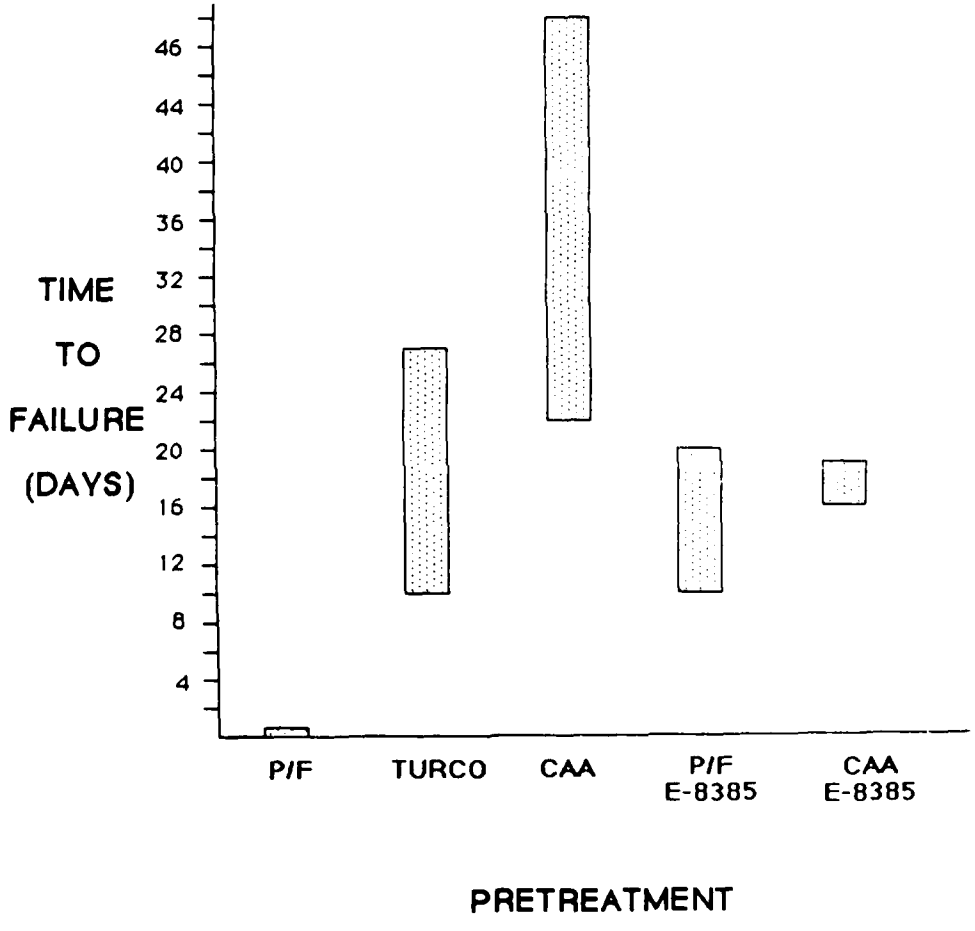

Figure 70. Time to failure windows for stress-durability test at 80° C, 95% r.h.

distribution of time to failure. However, the CAA primed bonds were less durable than the unprimed CAA bonds, indicating that the increased surface area of the pores in the CAA surface provides a better interface with the epoxy than the flat, non-porous aluminum alkoxide coating surface. The locus of failure for the E-8385 primed P/F stress durability bonds was investigated with XPS and Table XXV lists the XPS results for the MFS and AFS. The MFS contains titanium, oxygen, aluminum and nitrogen in significant levels, with a trace of bromine detected as well. The AFS contains bromine, nitrogen, high binding energy oxygen, and aluminum, but no titanium. Therefore, the locus of failure was similar to that seen in the wedge test. The presence of the bromine on the MFS can also be explained. In the stress durability test, the bonds were loaded to 40% of the breaking strength. When the bond has degraded to 40% of its original strength, it will fail catastrophically. As discussed in section B3, the locus of failure in the P/F pretreated lap shear bonds was within the epoxy. Since some of the original bond integrity is maintained at 40% load, the part of the bond intact prior to failure will exhibit a failure more similar to that of ambient lap shear than the wedge test, thus the trace quantities of bromine.

TABLE XXV

XPS Analysis for Locus of Failure of P/F Coated with E-8385 and Exposed to 80° C, 95% r.h.

SAMPLE	ELEMENT	B.E.(ev)	A.P.
E-8385 on	C	285.	46.
P/F - MFS	O	530.6,533.0	73.
	Br	TRACE	
	N	400.3	5.8
	Al	74.7	1.3
	Ti	459.0	4.7
P/F - AFS	C	285.	75.
	O	532.7	20.
	Br	70.7	0.4
	N	399.7	1.7
	Al	75.0	3.4
	Ti	NONE	

2. Physical and chemical properties of alkoxides

a. XPS

The chemical composition of three alkoxide films, TNBT, TIPT, and E-8385 was studied by XPS.

i. TNBT

The cure temperature affected the surface composition of TNBT films brush coated from dry toluene onto ferrotype plates. Table XXVI lists the elements detected, the binding energies, atomic percents and atomic percent ratios. As indicated by the C/Ti ratios, significantly less carbon was detected on the 300° C cured film than on the 25° C cured film. While the decrease in carbon could be due to less contamination, it is more likely due to a more complete reaction of the alkoxide to oxide and alcohol with subsequent release of alcohol. The FWHM of the Ti 2p3 peak remained constant at 1.4 eV for 25° and 300° C cured films.

No chromium from the substrate was detected in the 25° C cured film indicating a film thicker than 5 nm. In contrast to the 25° C cured film, chromium was detected on the 300° C cured film, indicating a film less than 5 nm thick or a discontinuous film.

Because chromium was detected on the 300° C cured film, the film was analyzed at take-off angles of 30° and 10° to probe regions closer to the surface. The Si/Ti ratio increased with decreasing take-off angle indicating the

TABLE XXVI

XPS Analysis of TNBT Film on Ferrotype Plates

CURE TEMP	TAKE-OFF ANGLE	ELEMENT	B.E. (ev)	A.P.	RATIO TO Ti
25° C	90°	C	285.	35.	2.3
		O	531.2	46.	2.4 *
		Ti	459.6	15.	-
		Cr	-	0	0
		Si	102.0	3.6	0.24
300° C	90°	C	285.	10.	0.63
		O	530.8	62.	2.6 *
		Ti	459.4	16.	-
		Cr	577.7	2.8	0.18
		Si	102.7	8.6	0.54
	30°	C	285.	13.	0.93
		O	530.9	62.	2.5 *
		Ti	459.3	14.	-
		Cr	577.9	1.5	0.11
		Si	102.7	10.	0.71
	10°	C	285.	28.	3.5
		O	532.4, 530.8	52.	2.6 *
		Ti	459.2	8.0	-
		Cr	577.3	1.3	0.18
		Si	102.6	11.	1.4

* O 1s curve fit A.P. used.

silicon was a surface contaminant. The source of the contamination will be discussed in section a.3. The oxygen 1s photopeak had a shoulder on the high binding energy side primarily due to the O-Si bond which also increased as the take-off angle decreased. The C/Ti ratio also increased with decreasing take-off angle indicating that the remaining carbon was primarily contamination. The atomic percent (AP) of the curve fit O 1s peak corresponding to the Ti-O bond ratioed to the AP of the Ti 2p3 peak was found to be constant at 90°, 30°, and 10° for the 300° C cure.

ii. TIPT

The cure temperature also affected the surface composition of the TIPT film. Table XXVII lists the elements detected, the binding energies, the atomic percents and the atomic percent ratios. Again, less carbon was detected on the 300° C cured film than on the 25° C cured film. The FWHM for the Ti 2p3 peak was 1.4 eV for all samples as in the TNBT samples. The silicon contamination was also present on these films and the Si/Ti ratio increased with decreasing take-off angle, as did the C/Ti ratio. Similar to the TNBT films, the 25° C cured TIPT film showed no chromium where the 300° C cured film did.

TABLE XXVII

XPS Analysis of TIPT Film on Ferrotype Plates

CURE TEMP	TAKE-OFF ANGLE	ELEMENT	B.E. (ev)	A.P.	RATIO TO Ti
25° C	90°	C	285.	31.	2.1
		O	531.1	47.	2.4 *
		Ti	459.5	15.	-
		Cr	-	0	0
		Si	101.9	6.6	0.44
300° C	90°	C	285.	8.4	0.49
		O	530.9	64.	2.7 *
		Ti	459.3	17.	-
		Cr	577.8	2.0	0.12
		Si	102.6	8.4	0.49
	30°	C	285.	10.	0.59
		O	530.9	65.	3.8
		Ti	459.4	17.	-
		Cr	578.3	0.9	0.05
		Si	102.7	6.4	0.38
	10°	C	285.	20.	1.7
		O	531.4	60.	5.0
		Ti	459.6	12.	-
		Cr	577.8	0.6	0.01
		Si	103.0	7.3	0.61

* O 1s peak curve fit A.P. used.

iii. E-8385

The effect of cure temperature, solvent moisture and film application method was studied with E-8385 films. Tables XXVIII and XXIX list the elements detected, the binding energies, the atomic percents, and the atomic percent ratios. In contrast to the titanate films, chromium was detected on both the 25° C and the 300° C cured films.

For both the 25° and 300° C cured films, the Cr/Al ratio was higher in the wet toluene films than the dry toluene films. The difference in the Cr/Al ratio indicated that the films formed from the wet toluene were thinner or less continuous than those formed from dry toluene. If the water in the toluene reacted with the aluminum alkoxide in the solution, before being deposited on the ferrotype plate, less alkoxide was in the solution when it was applied, thus a thinner or less continuous film resulted.

The samples coated from dry toluene showed the C/Al ratio decreased after the 300° C cure films. The FWHM values for O and Al were slightly larger in the 300° C cured films at 3.0 and 2.3 eV than the 25° C cured films, at 2.9 and 2.1 eV, respectively. Samples coated from wet toluene also showed a decrease in the C/Al ratio for the 300° C cure films. The values for the FWHM of the O and Al peaks, 4.2 and 3.7 eV, respectively, were larger than for the dry toluene samples and decreased in the 300° C cure samples to

TABLE XXVIII

XPS Analysis of E-8385 on Ferrotype Plates

Dry Toluene

CURE TEMP	TAKE-OFF ANGLE	ELEMENT	B.E. (ev)	A.P.	RATIO TO Al
25° C	90°	C	285.	21.	0.88
		O	532.5	47.	2.0
		Al	75.0	24.	-
		Cr	577.8	1.8	0.88
		Si	102.2	6.3	0.26
	30°	C	285.	23.	0.96
		O	532.5	45.	1.9
		Al	75.4	24.	-
		Cr	577.3	0.5	0.02
		Si	102.3	7.9	1.9
	10°	C	285.	36.	2.6
		O	532.3	45.	3.2
		Al	74.9	14.	-
		Cr	-	0	0
		Si	101.9	4.8	0.34
300° C	90°	C	285.	11.	0.40
		O	532.0	53.	1.8
		Al	74.6	29.	-
		Cr	577.4	2.1	0.07
		Si	102.4	4.2	0.14
	30°	C	285.	13.	0.45
		O	532.1	52.	1.8
		Al	74.6	29.	-
		Cr	577.6	1.2	0.04
		Si	102.4	4.5	0.16
	10°	C	285.	16.	0.57
		O	530.2	53.	1.9
		Al	74.6	28.	-
		Cr	578.0	0.4	0.01
		Si	102.4	3.2	1.1

TABLE XXIX

XPS Analysis of E-8385 on Ferrotype Plates

Wet Toluene

CURE TEMP	TAKE-OFF ANGLE	ELEMENT	B.E. (ev)	A.P.	RATIO TO Al
25° C	90°	C	285.	20.	1.0
		O	532.2	47.	2.4
		Al	75.8,74.8	20.	-
		Cr	577.3	7.3	0.37
		Si	102.5	6.0	0.30
	30°	C	285.	25.	1.3
		O	532.7	46.	2.3
		Al	76.2	20.	-
		Cr	577.3	3.1	0.16
		Si	102.8	6.9	0.35
	10°	C	285.	31.	2.1
		O	532.7	47.	3.1
		Al	75.4	15.	-
		Cr	576.6	1.5	0.1
		Si	102.5	5.8	0.39
300° C	90°	C	285.	7.9	0.40
		O	532.1	57.	2.9
		Al	74.8	20.	-
		Cr	577.4	6.9	0.35
		Si	102.9	6.9	0.35
		S	169.8	2.2	
	30°	C	285.	10.	0.53
		O	532.3	58.	3.1
		Al	74.9	19.	-
		Cr	577.3	4.1	0.22
		Si	102.8	8.1	0.43
		S	169.3	2.6	
	10°	C	285.	7.8	0.49
		O	532.3	66.	3.9
		Al	74.7	17.	-
		Cr	577.5	2.7	0.16
		Si	102.7	4.7	0.28
		S	169.6	2.0	

3.3 and 2.1 eV. No marked change of silicon concentration with take off angle was observed.

The origin of the silicon observed in the TNBT, TIPT, and the E-8385 films was not immediately evident. One possible source of the silicon was from the brushes used to apply the films. Therefore, E-8385 films were spun coat onto ferrotype plates from wet toluene solutions. Table XXX lists the XPS analysis. The Si/Al ratios were five times less than the brush coated films, while the Cr/Al ratios were comparable. Thus, the observed silicon was primarily from the brush used to apply the alkoxide films.

iv. Model aluminum oxides

To better assign the binding energies of the aluminum alkoxide XPS peaks, model aluminum oxides, prepared as described in Section III.B.4, were analyzed by XPS. Table XXXI lists the elements detected, the binding energies and atomic percents for Al_2O_3, $Al(OH)_3$, and AlOOH.

The aluminum binding energy of the E-8385 films brush coated from both the wet and dry toluene and cured at 300° C best match the aluminum binding energy of AlOOH. In contrast, the films cured at 25° C possess an aluminum binding energy closer to that of $Al(OH)_3$. The oxygen binding energies match the binding energies of O 1s in the $Al(OH)_3$ or

TABLE XXX

XPS Analysis of E-8385 on Ferrotype Plates

Wet Toluene Spun Coat

CURE TEMP	TAKE-OFF ANGLE	ELEMENT	B.E. (ev)	A.P.	RATIO TO Al
25° C	90°	C	285.	28.	1.6
		O	531.9	48.	2.8
		Al	74.4	17.	-
		Cr	577.2	6.5	0.38
		Si	TRACE		0
	30°	C	285.	35.	2.1
		O	532.1	43.	2.5
		Al	74.3	17.	-
		Cr	577.4	2.7	0.16
		Si	101.9	1.1	0.07
	10°	C	285.	39.	2.3
		O	532.0	41.	2.4
		Al	74.2	17.	-
		Cr	577.6	1.7	0.10
		Si	102.0	1.1	0.07
300° C	90°	C	285.	12.	2.0
		O	531.3	53.	2.2
		Al	74.8	24.	-
		Cr	577.3	8.7	0.36
		Si	102.2	1.6	0.07
	30°	C	285.	15.	0.63
		O	531.9	53.	2.2
		Al	74.7	24.	-
		Cr	577.3	6.2	0.26
		Si	102.7	1.8	0.08
	10°	C	285.	23.	1.4
		O	532.1	54.	3.2
		Al	74.7	17.	-
		Cr	577.4	4.8	0.28
		Si	102.4	1.7	0.10

TABLE XXXI

XPS Analysis of Aluminum Oxides

Surface	Element	B.E.	A.P.	O/Al
$Al(OH)_3$	C	285	17	
	O	532.5	55	2.3
	Al	75.5	24	
	Si	102.6	5.0	
AlOOH	C	285	14	
	O	532.4	53	2.2
	Al	74.8	24	
	Si	102.6	9.0	
Al_2O_3	C	285	11	
	O	531.7	50	1.3
	Al	74.2	40	

AlOOH samples.

v. Angle dependent XPS studies - alkoxides

Angle dependent XPS studies of thin alkoxide films on a substrate of different composition can allow one to calculate the thickness of an overlayer or thin film. Using equation (22) the thickness of the overlayer is calculated from the atomic percents of aluminum (in the thin film) and chromium (in the substrate); the concentrations of aluminum and chromium ; and the mean free path for aluminum. The concentrations of chromium and aluminum were calculated as density/molecular weight, assuming a stoichiometry of Cr_2O_3 and AlOOH. With a density of 5.21 g/cc and a molecular weight of 152 g/mol [132], the concentration of Cr_2O_3 is 0.0343 mol/cc. The aluminum oxide concentration is 0.55 mol/cc using a density of 3.3 g/cc and a molecular weight of 60 g/mol [132].

By plotting the left side of equation (22) versus $1/\sin\theta$, the slope of the resulting curve yields the thickness of the uniform overlayer. The thicknesses resulting from the calculations of a continuous overlayer are listed in Table XXXII. Results from the continuous overlayer calculation indicated the 300° C cure films were thinner than the 25° C cure films which can be due to the fact that the films at 25° C cure still contain the alcohol group of the

TABLE XXXII

Results of Angle Dependent XPS Studies

Coating Technique	wt % in Toluene	Cure Temp	Continuous Thickness	% Patchy	Patchy Layer Thickness
Brush	1% wet	300°C	75 Å	80	135 Å
Brush	1% dry	300°C	110 Å	100	65 Å
Brush	1% wet	25°C	140 Å		
Spin Coat	1% wet	25°C	150 Å	85	145 Å
Spin Coat	1% wet	300°C	50 Å	70	240 Å
Spin Coat	1% dry	25°C		90	115 Å
Spin Coat	1% dry	25°C		85	100 Å
Spin Coat	2% dry	25°C		85	260 Å

alkoxide, where the 300° C cure films do not.

However, assuming the typical escape depth of a photoelectron is 5 nm, calculated overlayer thicknesses of 15 nm while still detecting the substrate are not reasonable. Therefore, a patchy overlayer model was considered.

SEM photomicrographs indicated that the overlayer was indeed patchy. Figure 71 shows a 2 wt% E-8385 film spun coat onto a ferrotype plate. Using this picture as a guide, the percent patchiness was estimated with 100% being full coverage and 0% being no overlayer.

Using the patchy overlayer model, theoretical curves were then calculated for AP_{Al}/AP_{Cr} plotted versus θ with patchiness ranging from 0.8 to 1 and for thicknesses of 5 to 20 nm. Figure 72 shows a theoretical curve with data plotted for an E-8385 film spuncoat from a 1 wt % solution in toluene. The patchiness and thickness of the sample is determined by matching the data points with the theoretical curve. To better match the theoretical curves to the data, a program was written, listed in Appendix D [140], to determine the optimum patchiness and thickness for each sample. These optimized numbers were then checked by the appropriate plot to assure the data matched the theoretical curves. Table XXXII lists the percent patchiness and film thickness for E-8385 films cured at 25° and 300° C.

In general, the patchiness is between 80% and 90% with

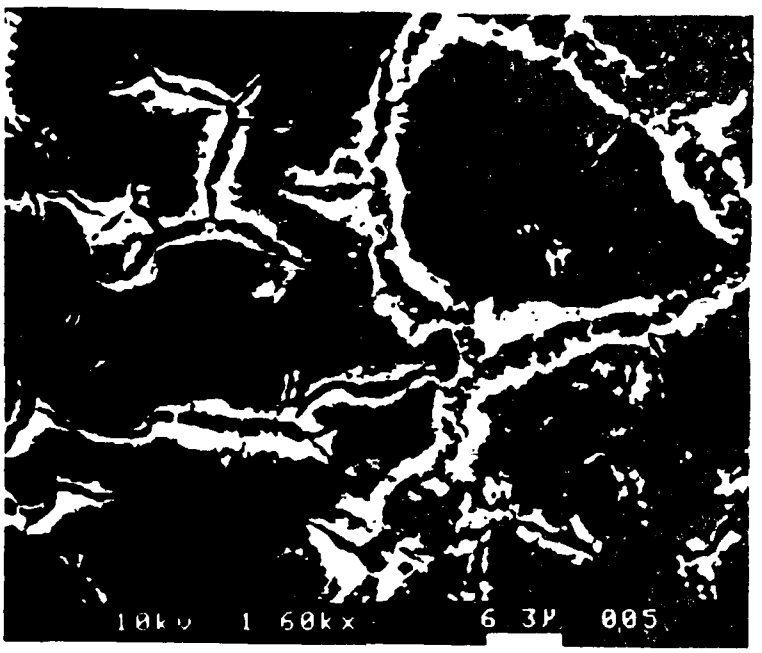

Figure 71. SEM photomicrograph at 1600 x of E-8385 film spun coat from a 2 wt% solution onto a ferrotype plate.

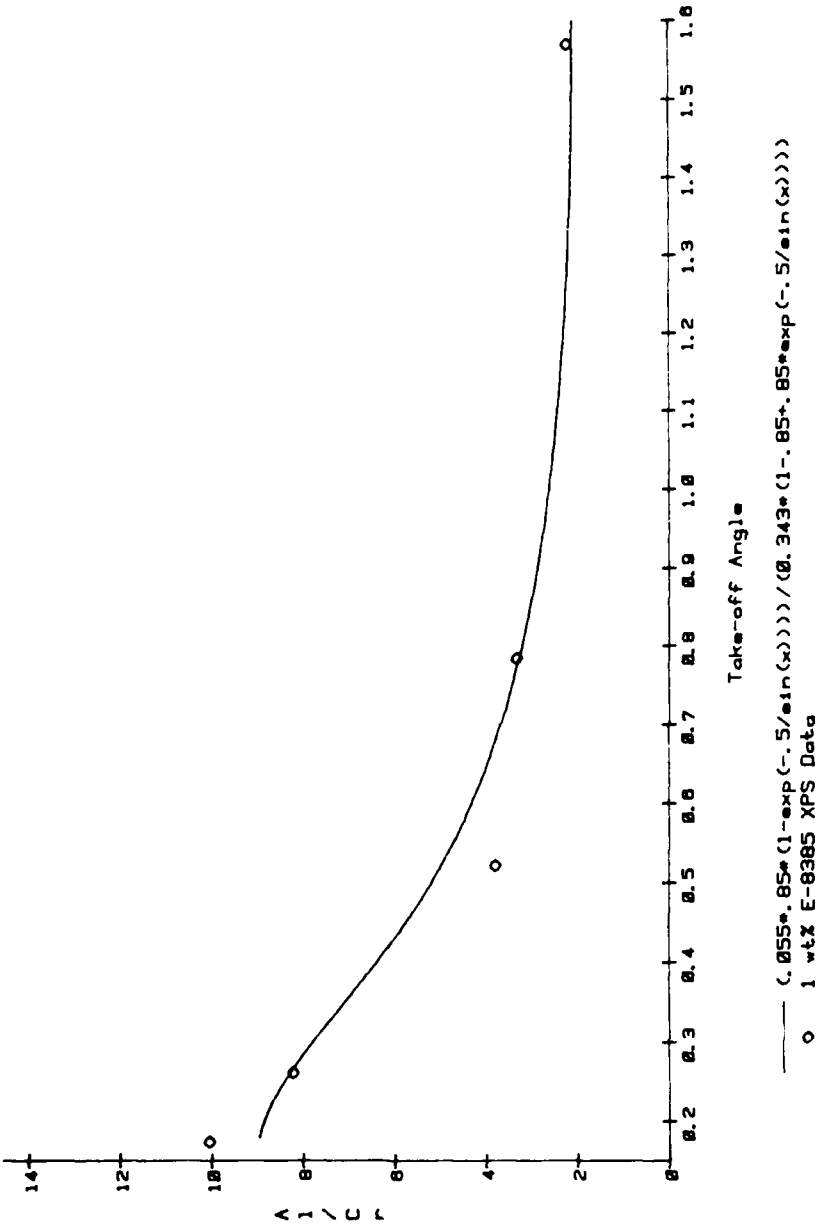

Figure 72. Theoretical curve with data from angle dependent XPS study on E-8385 film spun coat from a 1 wt% solution in toluene.

the thickness of the patches over 10 nm thick. The two films spun coat from 1 wt% dry toluene solution were similar in thickness, 10 - 11.5 nm, and patchiness, 85 - 90%. The 1 wt% samples were then studied by grazing angle reflectance FTIR.

b. FTIR

i. TIPT

A 1 wt% solution of TIPT in toluene was brush coated onto ferrotype plates in five coats. The film was then cured at 25° C under vacuum or at 300° C in air, before reflectance spectra collected as shown in Figures 73 and 74. Table XXXIII lists the peak positions and the peak assignments.

The 25° C cure shows a broad -OH absorbance with the C-H stretch region, 2959 - 2857 cm^{-1}, clearly resolved. Correspondingly, the -CH- deformation vibration region at 1445 cm^{-1}, the gem-dimethyl absorbance at 1377 cm^{-1}, and the (C-O)Ti stretch at 1052 cm^{-1} are clearly present. In contrast, the C-H stretch region is absent in the 300° C cure film and only a small (C-O)Ti stretch is observed at 1049 cm^{-1} indicating that the alcohol portion of the alkoxide is removed at the 300° C cure. These results are in agreement with the XPS results showing a notably lower C/Ti ratio at the 300° C cure compared to the 25° C cure. The Ti-O

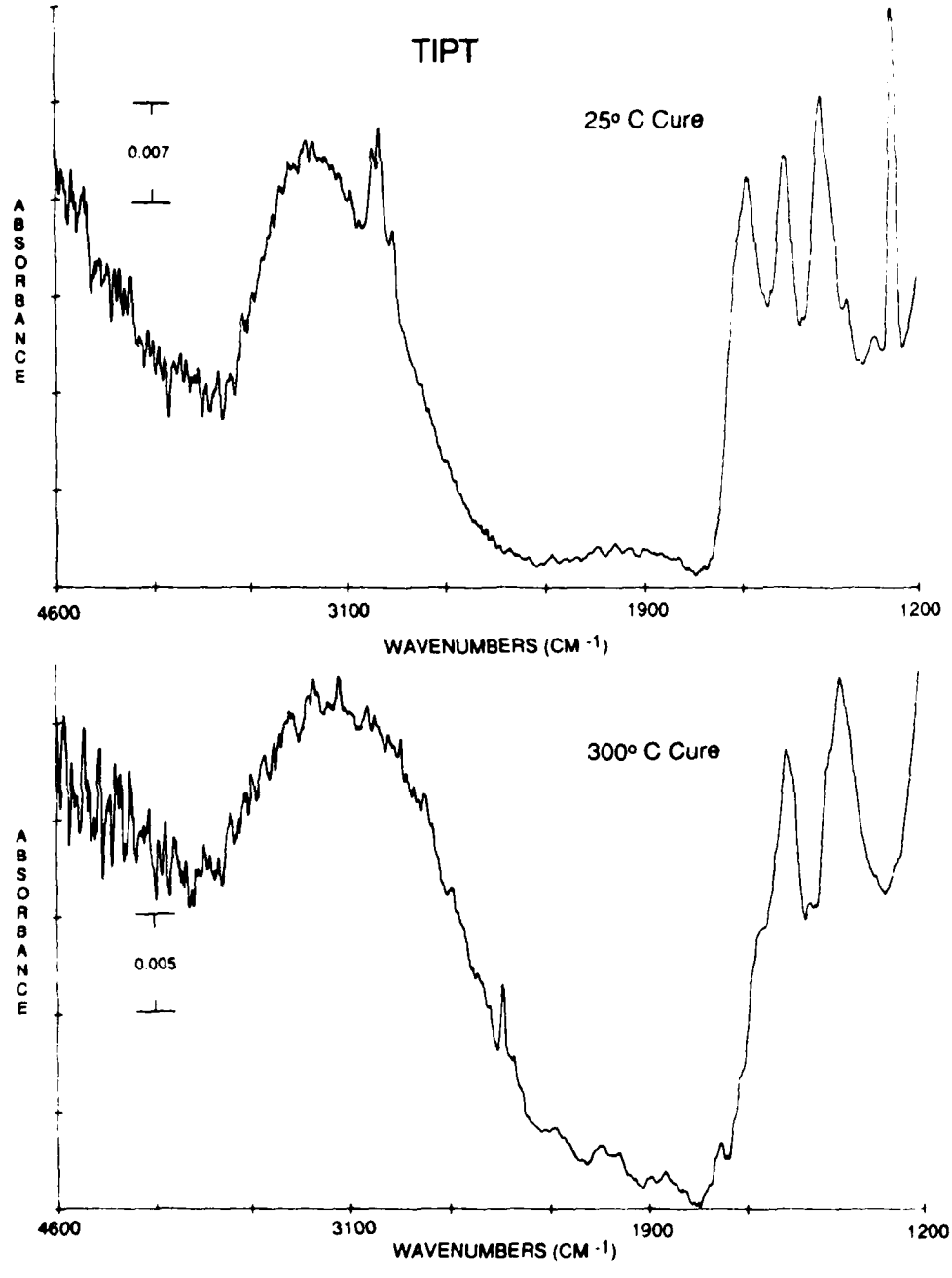

Figure 73. Grazing angle FTIR spectra from 4600 to 1200 cm^{-1} of TIPT on ferrotype plates, cured at 25° and 300° C.

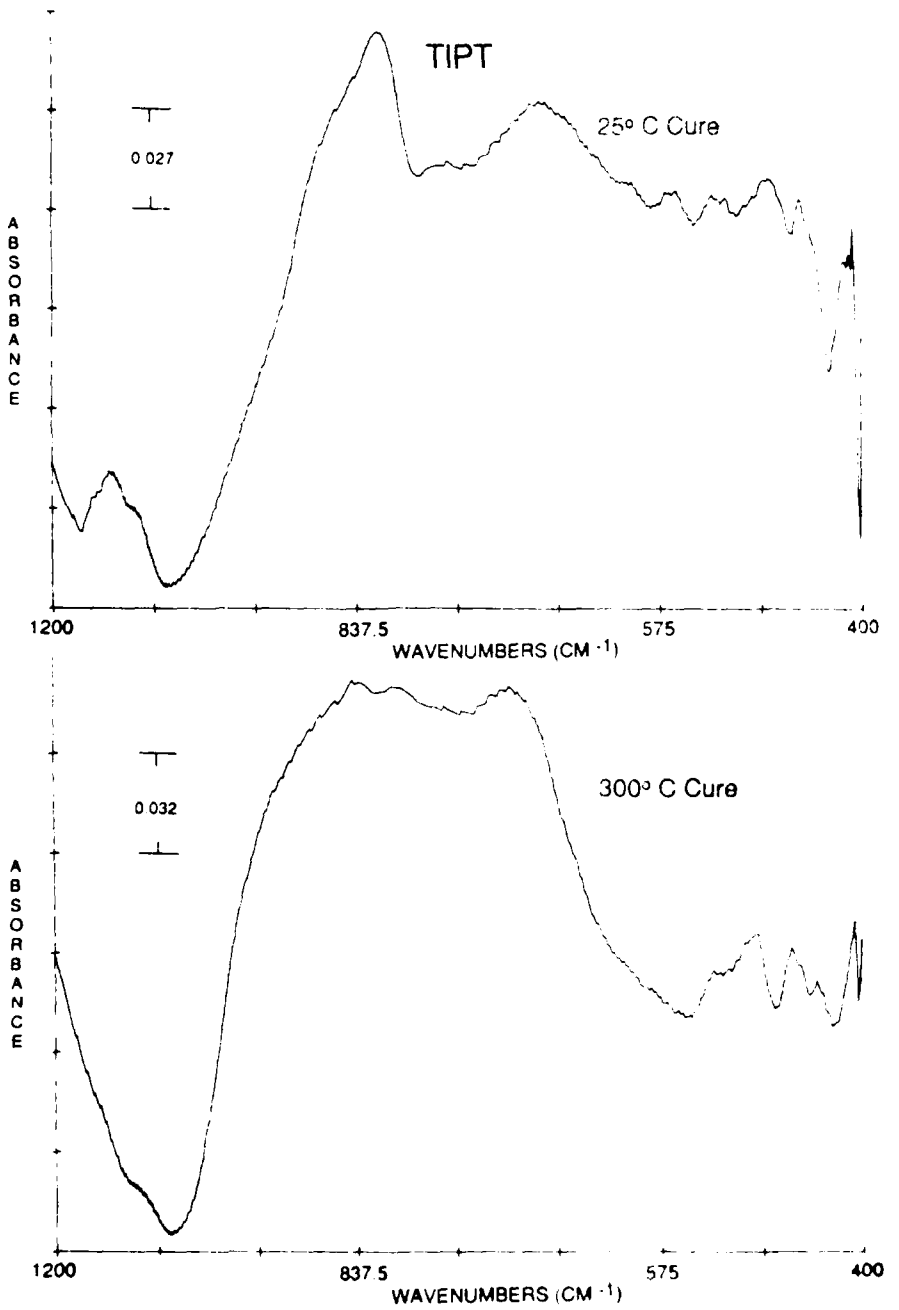

Figure 74. Grazing angle FTIR spectra from 1200 to 400 cm^{-1} of TIPT on ferrotype plates, cured at 25° and 300° C.

TABLE XXXIII

Grazing angle FTIR peak positions and assignments for TIPT films on ferrotype plates

TIPT 25° C (cm^{-1})	TIPT 300° C (cm^{-1})	Peak Assignment
3300		-OH str.
	3140	-OH str.
2959		C-H asym. str. CH_3
2926		C-H asym. str.-CH_2 alkanes
2857		C-H sym. str. -CH_2-
	2336	
	1719	
1636		OH water of cryst.
	1616	OH water of cryst.
	1543	
1539		
1445		-CH_2 scissors vib.
		CH_3 asym. def. vib.
	1404	
1377		sym. C-$(CH_3)_2$ def. vib.
1310		
1261		inplane O-H def. vib.
1098		iso-branching vib.
1053		
	1049	(C-O)M str.
	837	Ti-O
820		Ti-O
	800	
766		
	704	OH out of plane vib.
679		
563		
527	530	
	492	
482		
	461	
453	453	
	440	
	406	

stretch region appears to broaden greatly after the 300° C cure indicating a titanium oxide layer is formed.

ii. TNBT

TNBT films were prepared similarly to the TIPT films and the spectra are shown in Figures 75 and 76. A spectrum of neat TNBT is also shown in Figure 77. The peak positions and assignments are listed in Table XXXIV. The series of peaks at 1126, 1098, and 1042 cm^{-1} are present in the literature spectrum, the neat compound spectrum and the film spectrum with relative peak intensities also in agreement. The absorption of n-butyl groups and the (C-O)Ti stretch contribute to these three bands.

Using the TIPT spectra of the 25° and 300° C cure films as a guide, the 1045 cm^{-1} band is likely due to the (C-O)Ti stretch because it is the only remaining peak of the three after the 300° C cure. Other similar observations can be made between the 25° and 300° C cured films. The C-H stretch region, 2957 - 2859 cm^{-1}, disappears after the 300° C cure again agreeing with the XPS data which shows a decrease in the C/Ti ratio after the 300° C. The broad Ti-O stretch at 875 cm^{-1} is also present in the TNBT film as in the TIPT film.

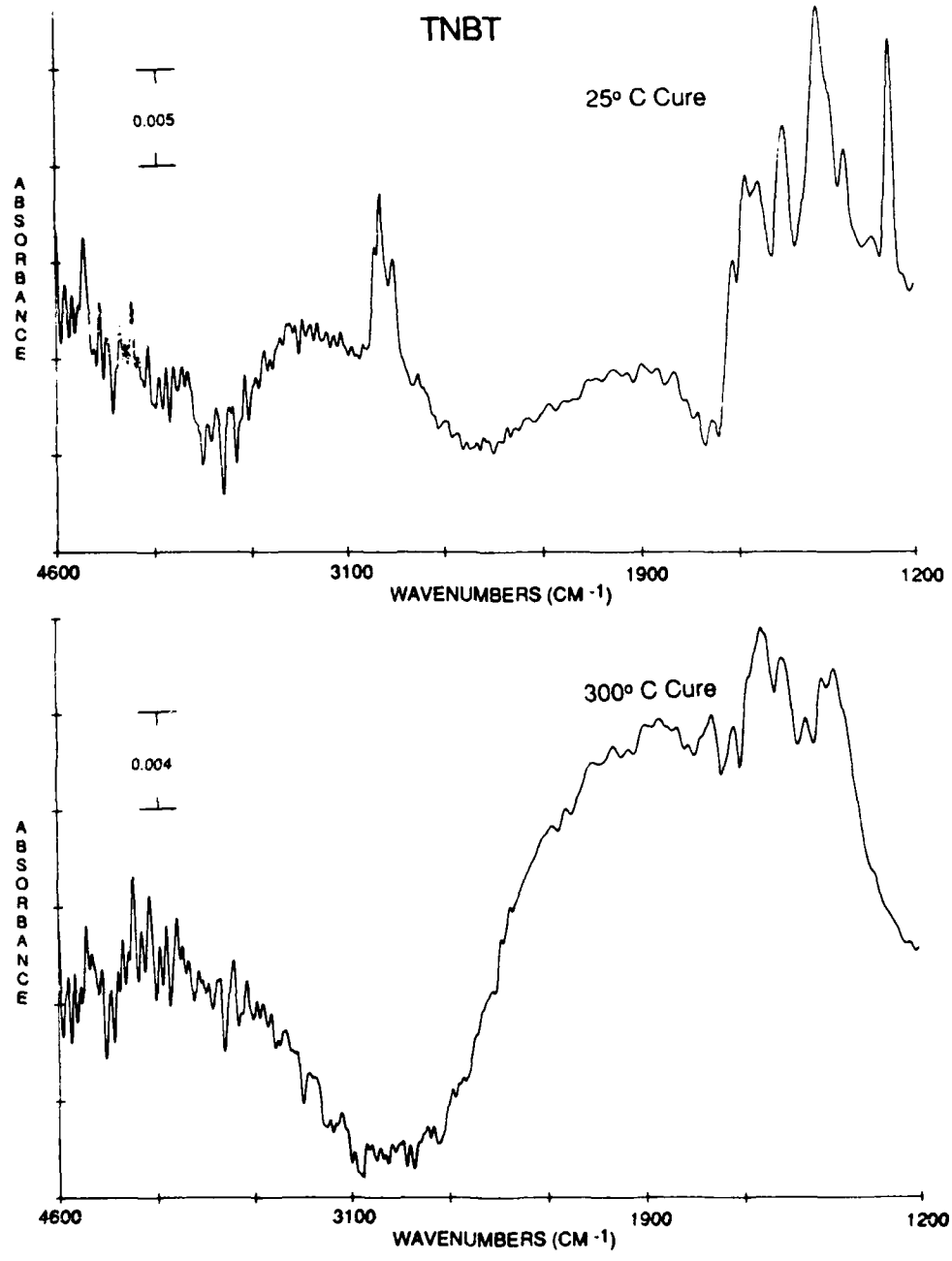

Figure 75. Grazing angle FTIR spectra from 4600 to 1200 cm^{-1} of TNBT on ferrotype plates, cured at 25° and 300° C

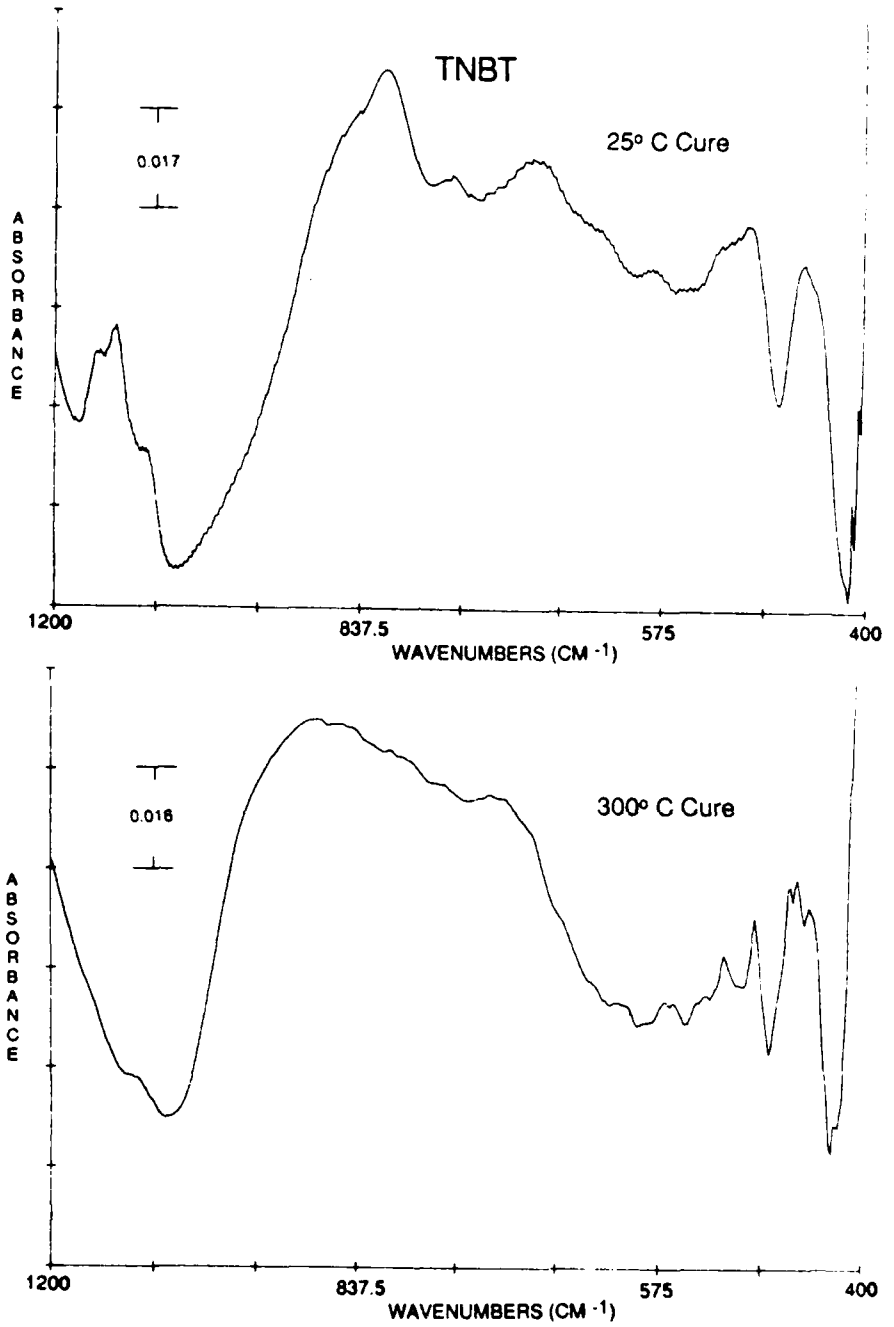

Figure 76. Grazing angle FTIR spectra from 1200 to 400 cm^{-1} of TNBT on ferrotype plates, cured at 25° and 300° C.

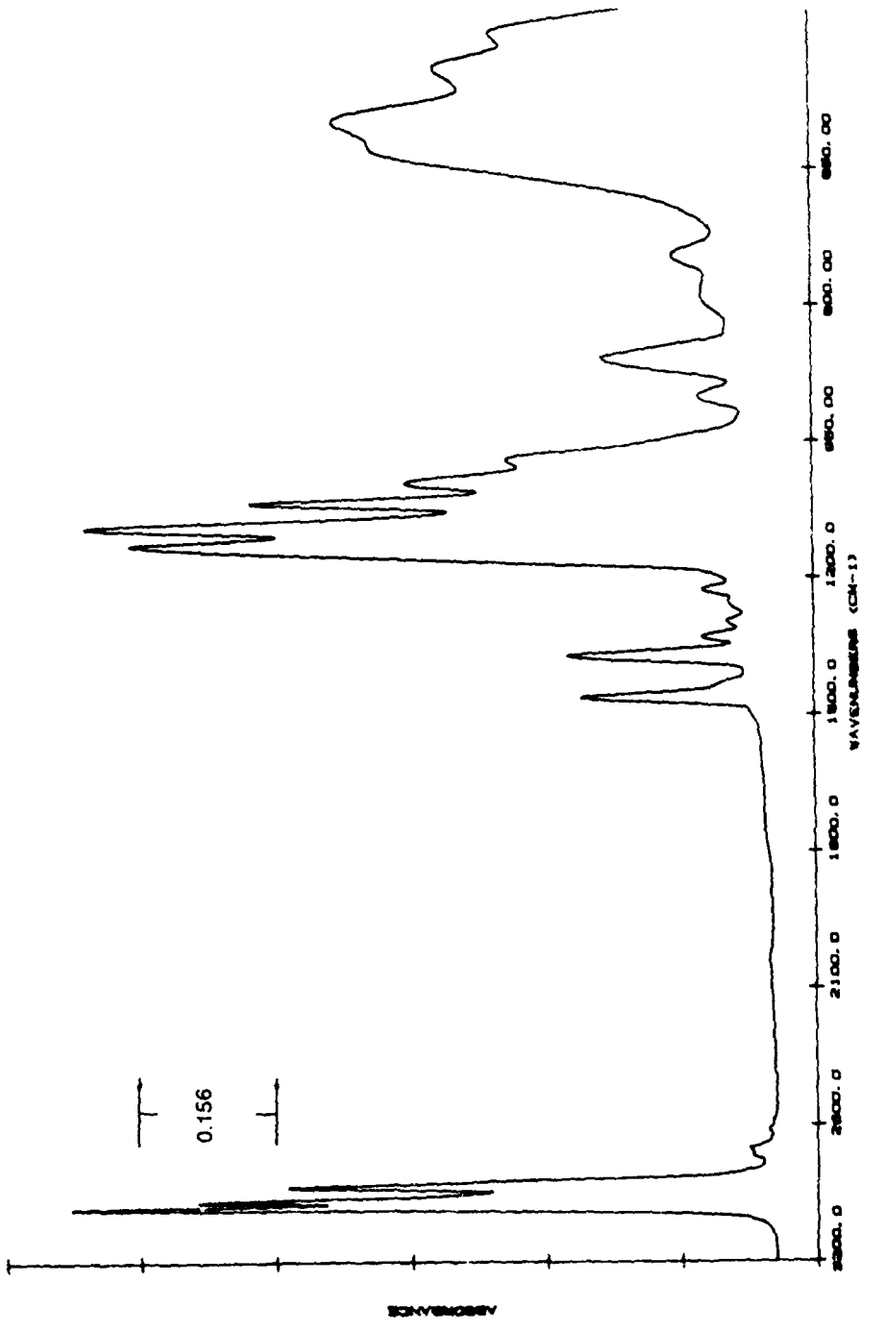

Figure 77. Transmission FTIR spectrum of neat TNBT between KBr crystals.

TABLE XXXIV

Grazing Angle and Transmission FTIR Peak Positions and Assignments for TNBT Films on Ferrotype Plates and Neat TNBT between KBr Crystals

Neat TNBT KBr (cm^{-1})	1 wt% Brushed 25° C (cm^{-1})	1 wt% Brushed 300° C	Peak Assignment
	3370		-OH str.
2959	2957		C-H asym. str. CH_3
2930	2924		C-H asym. str.-CH_2 alkanes
2870	2859		C-H sym. str. -CH_2-
		1724	
	1665	1669	-OH water of cryst.
	1632		-OH water of cryst.
	1600	1597	-OH water of cryst.
	1535	1541	
		1485	-CH_2- scissors vib.
1462	1447	1441	-CH_3 asym def. vib.
	1414	1408	
1371	1377		
1329			
1298	1307		
	1250		
1227			
1126	1126		induced alkyl absorp
1088	1098		C-O str
1036	1042	1045	
995			
970			
903			
860	816	876	Ti-O
746	760		
	683	710	
631			
600		608	
	582	569	
540			straight chain alkanes
		517	
501	500	490	straight chain alkanes
	451	453	

iii. E-8385

A neat sample of E-8385, primarily unhydrolyzed sec-butyl aluminum alkoxide, was analyzed by transmission infrared. The spectrum, which agrees well with the Sadtler index spectrum shown previously in Figure 14 for sec-butyl aluminum alkoxide, is shown in Figure 78 with the peak positions and assignments listed in Table XXXV.

One wt% solutions of E-8385 were brush coated from wet and dry toluene onto ferrotype plates and cured at 25° and 300° C. The spectra are shown in Figures 79 to 82 with the peak positions and assignments listed in Table XXXVI. The 25° C cure spectra of the E-8385 from the wet and dry toluene are similar with additional water peaks in the wet toluene spectrum. Characteristic peaks fall at 1094, 1053, and 856 cm^{-1} which are likely due to (C-O)Al stretching and Al-O stretching vibrations. Upon 300° C cure, the methyl stretch region at 2961 cm^{-1} disappears for both wet and dry toluene samples; however, the water peaks remain present in the sample coated from wet toluene, even after the 300° C cure. In both cases, a broad peak appears at 1144 and 883 cm^{-1} after 300° C cure.

A large -OH stretch absorbance is present in all samples. The E-8385 films differ from the titanate films in the area of the OH stretching region. The area of the -OH band is greater for the E-8385 films, than in the TIPT

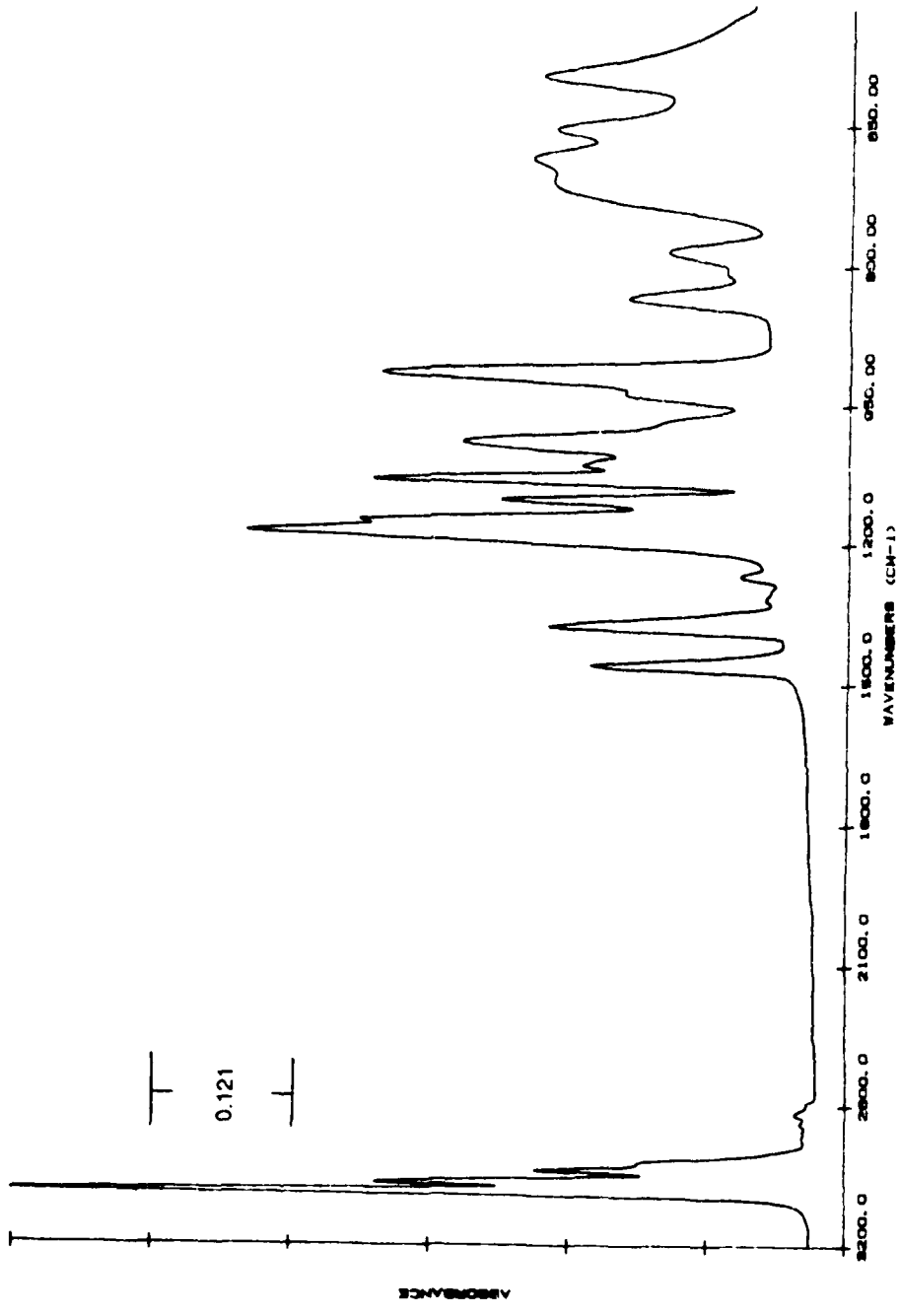

Figure 78. Transmission FTIR spectrum of neat E-8385 between KBr crystals.

TABLE XXXV

Transmission FTIR Peak Positions and Assignments for Neat E-8385 Between KBr Crystals

Neat E-8385	Peak Assignment
2967	C-H asym. str. CH_3
2928	C-H asym. str.-CH_2alkanes
2876	C-H sym. str. CH_3
2843	C-H sym. str. -CH_2-
2633	
1460	-CH_2 scissoring, alkanes CH_3 asym. def. vib.
1377	sym. (C-CH_3) def. vib.
1269	inplane O-H def. vib.
1173 1148 1103 1059 1032	C-O str.
991	
968,sh	Al-O-Al trans. mom. perp. to surf.
941,sh 916	Al-O-Al
835 785 687 654	Al-O-Al trans. mom. par. to surf.
598	

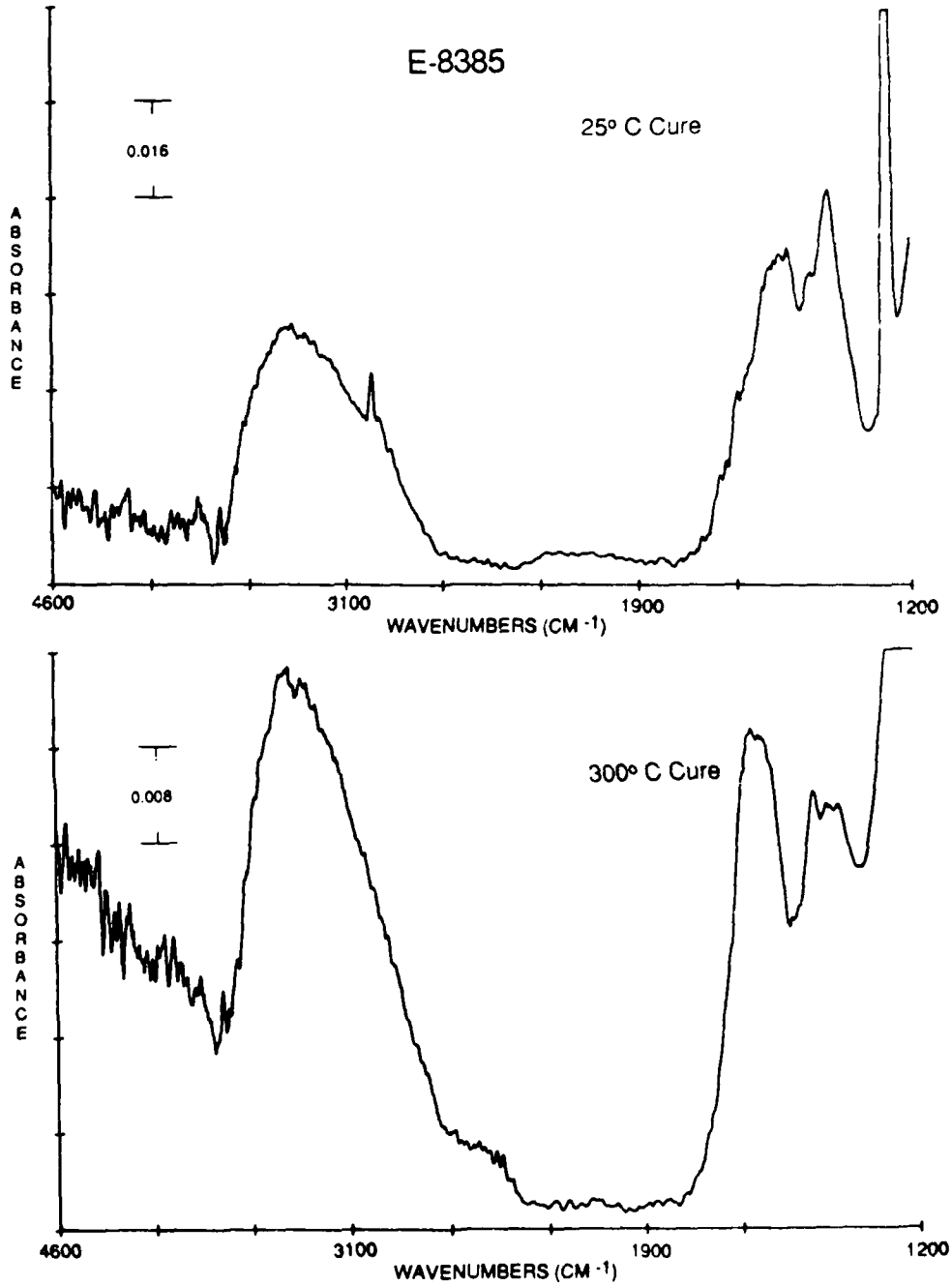

Figure 79. Grazing angle FTIR spectra from 4600 to 1200 cm^{-1} of E-8385 from dry toluene on ferrotype plates, cured at 25° and 300° C.

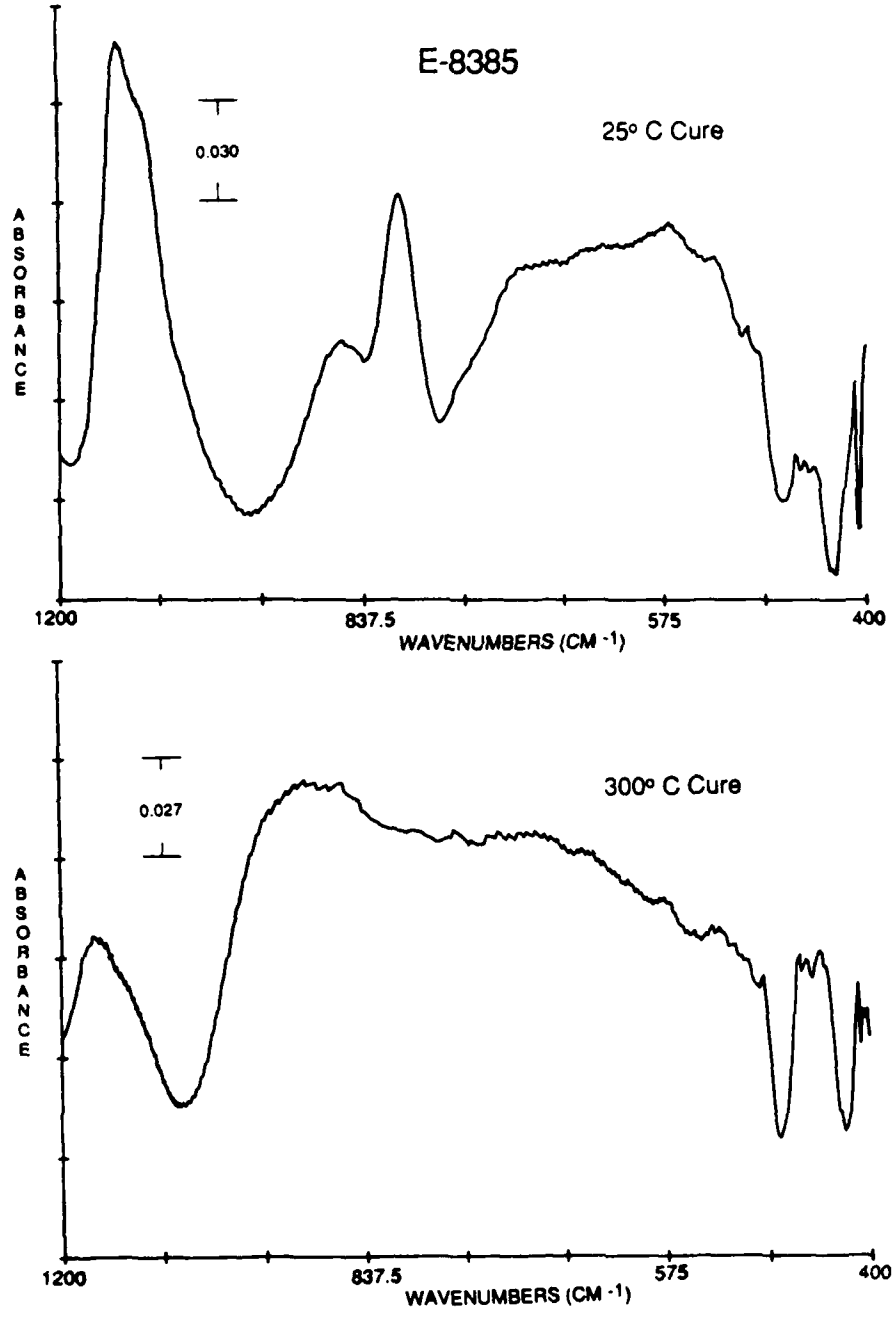

Figure 80. Grazing angle FTIR spectra from 1200 to 400 cm^{-1} of E-8385 from dry toluene on ferrotype plates, cured at 25° and 300° C.

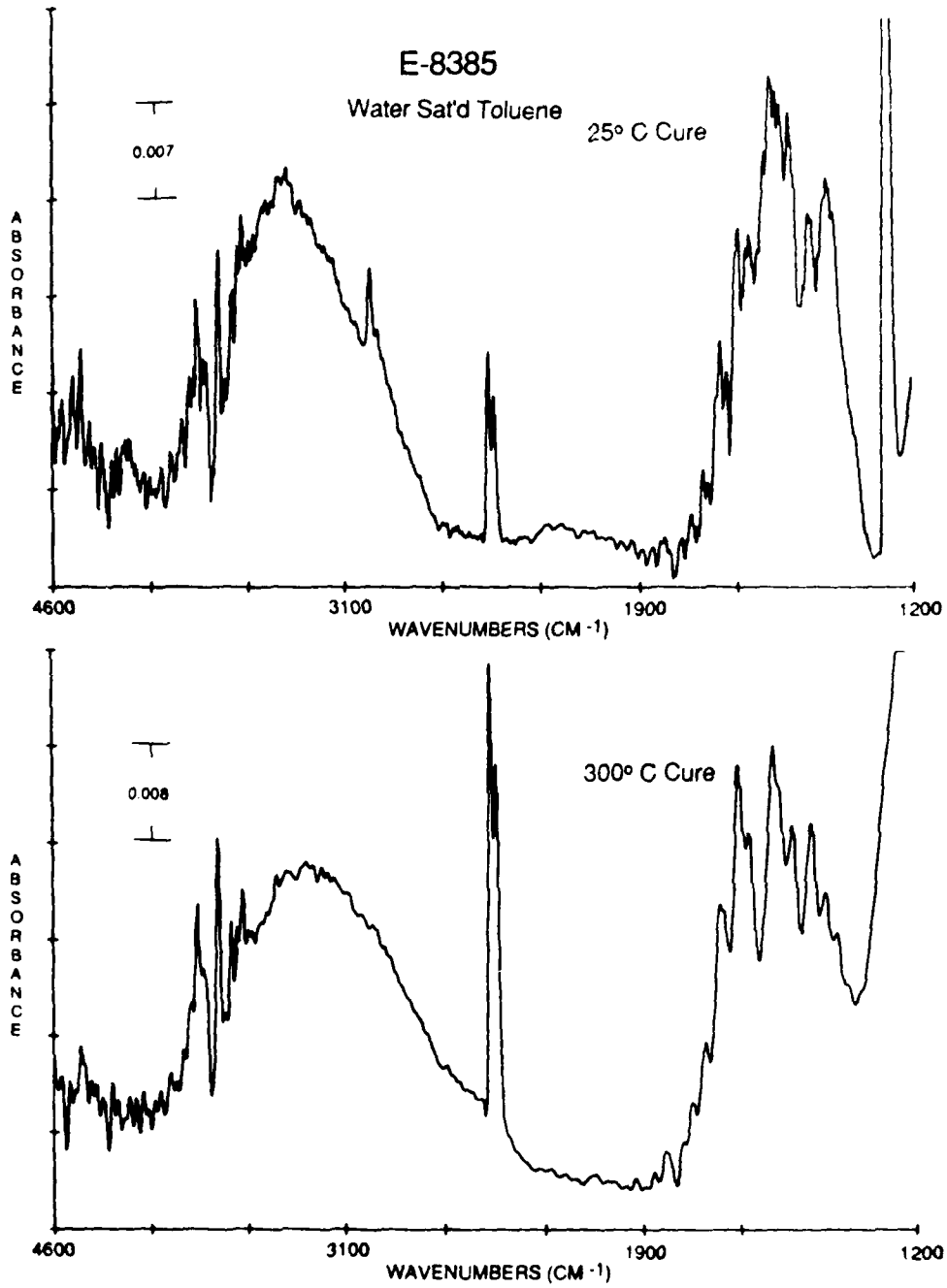

Figure 81. Grazing angle FTIR spectra from 4600 to 1200 cm^{-1} of E-8385 from wet toluene on ferrotype plates, cured at 25° and 300° C.

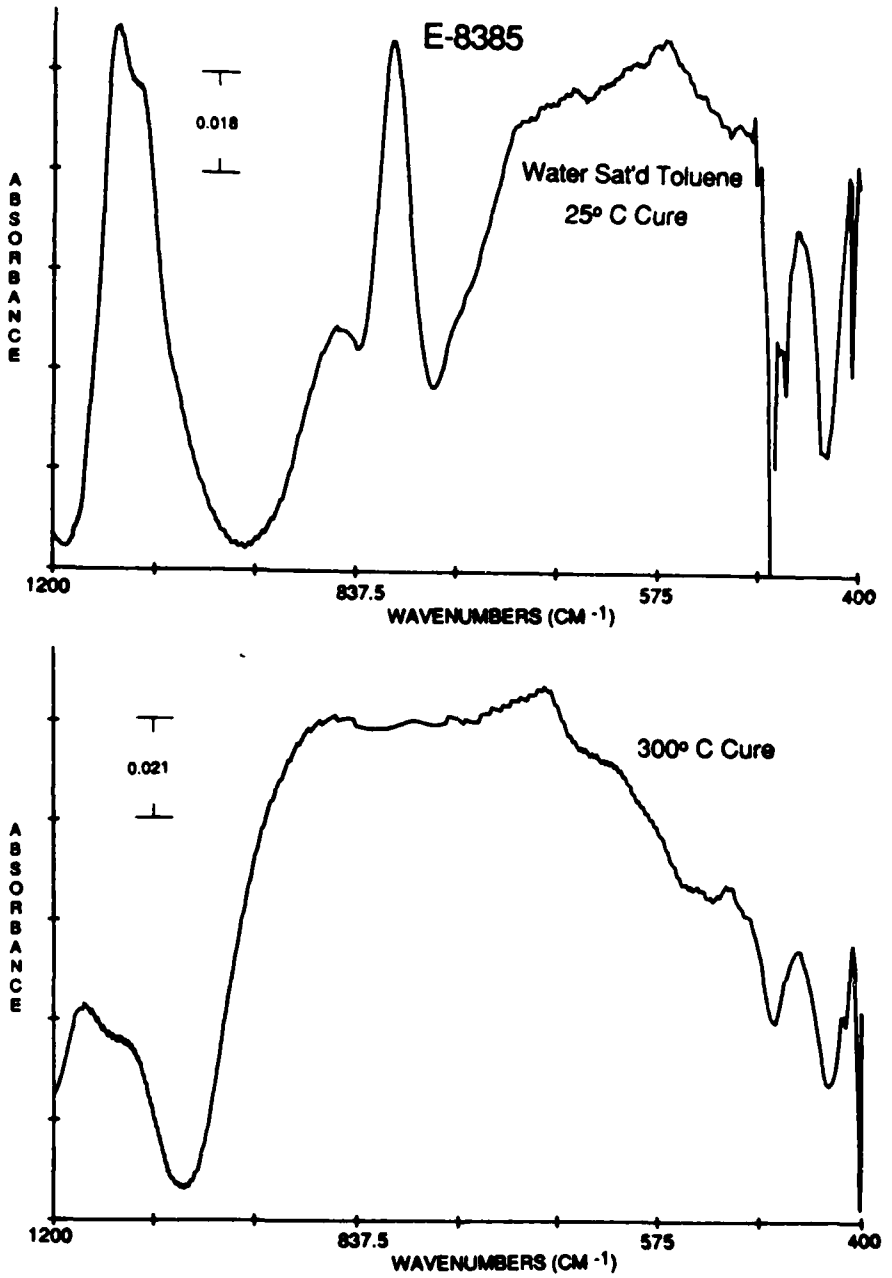

Figure 82. Grazing angle FTIR spectra from 1200 to 400 cm^{-1} of E-8385 from wet toluene on ferrotype plates, cured at 25° and 300° C.

TABLE XXXVI

Grazing Angle FTIR Peak Positions and Assignments for E-8385 Films on Ferrotype Plates

E-8385 25° C (cm^{-1})	E-8385 300° C (cm^{-1})	Peak Assignment
3856	3856	
3748	3746	-OH str.
3676	3621	
3395	3223	
2963		C-H asym. str. CH_3
2926		C-H asym. str. $-CH_2$ alkanes
1694	1692	
1649		-OH water of cryst.
1620	1622	
1559	1559	
1543		
1512	1510	
1462	1462	$-CH_2$ scissoring, alkanes CH_3 asym. def. vib.
1418	1423	
1261		-OH in plane def. vib.
	1147	
1090		
1051	1062	C-O str.
855	870	
806		
698		
	672	
571		
492	513	

film which is significantly greater than the TNBT film, indicating the highest concentration of hydroxyl groups on the E-8385 surface. The presence of a higher concentration of hydroxyl groups may indicate a more chemically active surface for forming hydrogen bonds with the epoxy, thus more durable bonds. The E-8385 primed P/F bonds were clearly more durable than the TIPT or the TNBT primed bonds. The TIPT samples showed slightly better durability and also a higher concentration of -OH groups than on TNBT.

As evidenced by the locus of failure results, discussed previously, aluminum alkoxide primer is found on both sides of the failed joint, whereas in the titanium alkoxide primed joints, the failure is interfacial between the primer and the epoxy. This failure locus indicates less or weaker interactions between the titanium alkoxide and the epoxy than the aluminum alkoxide and epoxy.

c. Acidity/basicity

E-8385 films were spun coat onto ferrotype plates and cured at 25° or 300° C prior to indicator dye tests. Table XXXVII lists the results from the dye tests. Both the 25° and 300° C cure films lie between a pH of 6.8 and 7.6. In addition, another phenomenon was noted, namely, the dye spread on the heat cured films. The contact angle of water on the 25° C films was 73° ± 6°, and 0° on the 300° C cured

TABLE XXXVII

Results of Indicator Dye Test on E-8385 Films

Indicator	Indicator pH Change Range	E-8385 Cure Temperature 25°C	300°C
Bromophenol Blue	3.4 - 3.6	Blue	Purple
Bromocresol Green	3.8 - 5.4	Blue	Blue
Bromocresol Purple	5.2 - 6.8	Purple	Purple
Orange 1	7.6 - 8.9	Orange	Orange
Thymol Blue	8.0 - 9.6	Yellow	Yellow

films. The spreading of a water drop indicates the 300° C cure films have a higher surface energy than the 25° C cure films, probably due to the loss of hydrophobic alcohol carbon chains and subsequent formation of aluminum oxide/hydroxide.

3. Interaction of aluminum alkoxide with model epoxy by FTIR

Grazing angle FTIR is an optimum method for studying the chemistry of interfaces. Because bonds made with aluminum alkoxide primed P/F Ti-6-4 and FM-300 commercial epoxy showed enhanced durability over unprimed bonds, it was of interest to probe an epoxy/aluminum alkoxide interface to determine if chemical reactions between the epoxy and alkoxide had occurred.

a. EPON 828/DDS

In order to properly identify the peaks in EPON 828/DDS films, each component was first analyzed separately. A 1 wt% solution of EPON 828 in methylene chloride was spun coat onto a ferrotype plate and outgassed in a vacuum oven at 25° C for 1 h. Figure 83 shows the spectrum and Table XXXVIII lists the peak positions and assignments [66,86,87, 141,142]. DDS was dissolved in methylene chloride, spun coat onto a ferrotype plate and outgassed in a vacuum oven at 25° C for 1.5 h. Figure 84 shows the resulting spectrum

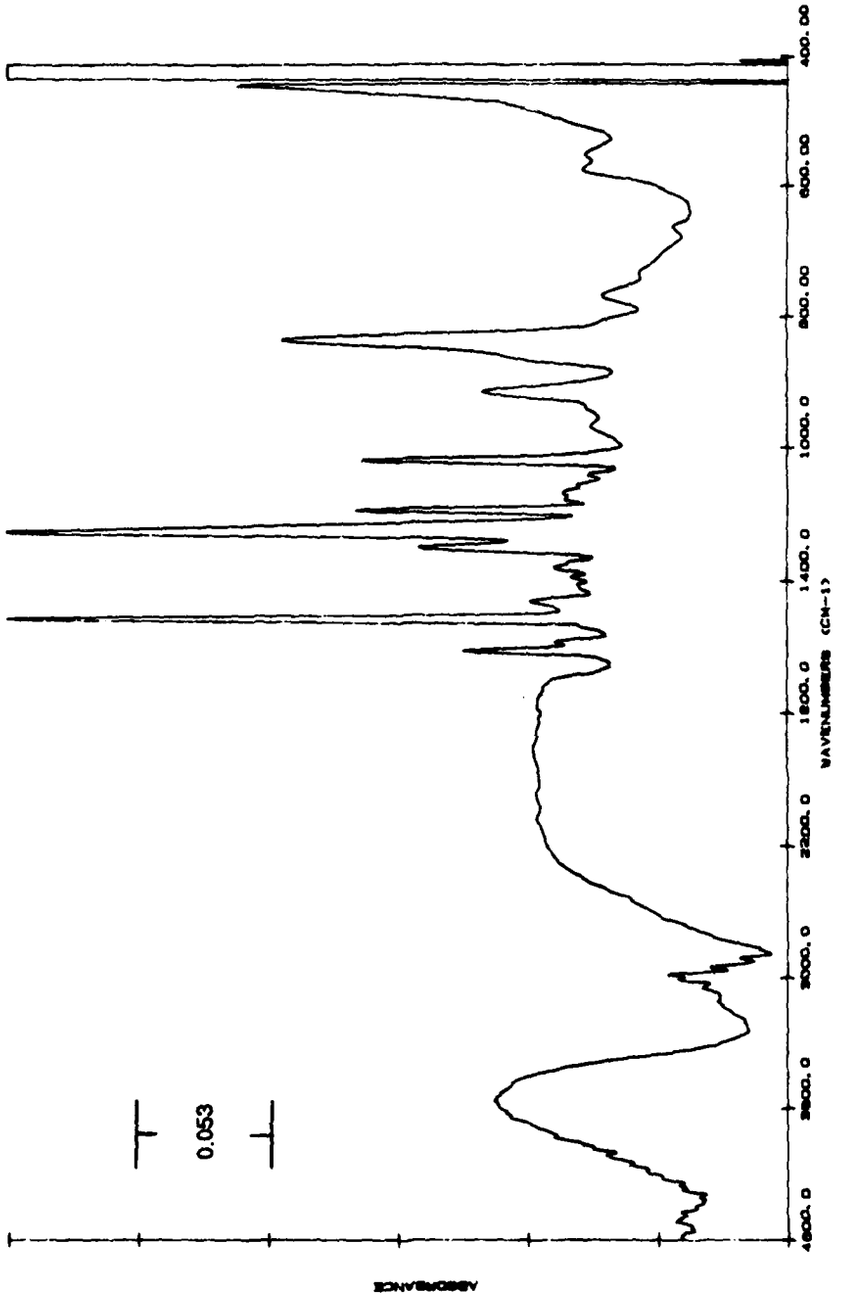

Figure 83. Grazing angle FTIR spectrum of EPON 828 film on ferrotype plates.

TABLE XXXVIII

Grazing Angle FTIR Peak Positions and Assignments for EPON828 Films on Ferrotype Plates

EPON828 (cm^{-1})	Peak Assignment
3732	-OH str.
3005	C-H asym. str. epoxide
2974	C-H asym. str. CH_3
2930	C-H asym. str. $-CH_2$
2876	C-H sym. str. CH_3
1609	aromatic C-C str. quadrant str. benzene ring
1584	aromatic C-C str. quadrant str. benzene ring
1512	semicircle str. benzene ring C=C str. benzene ring
1462	aliphatic C-H bend
1298	-OH in-plane def. $-CH_2-$ twisting
1251	aryl-O str. C-O-C asym. str.
1186	C-H inplane def. C-C str. of Ar-C-Ar
1038	C-O str. C-O-C sym. str.
916	asym. epoxy ring vib.
837	out of plane bending of p-disubstituted benzene ring

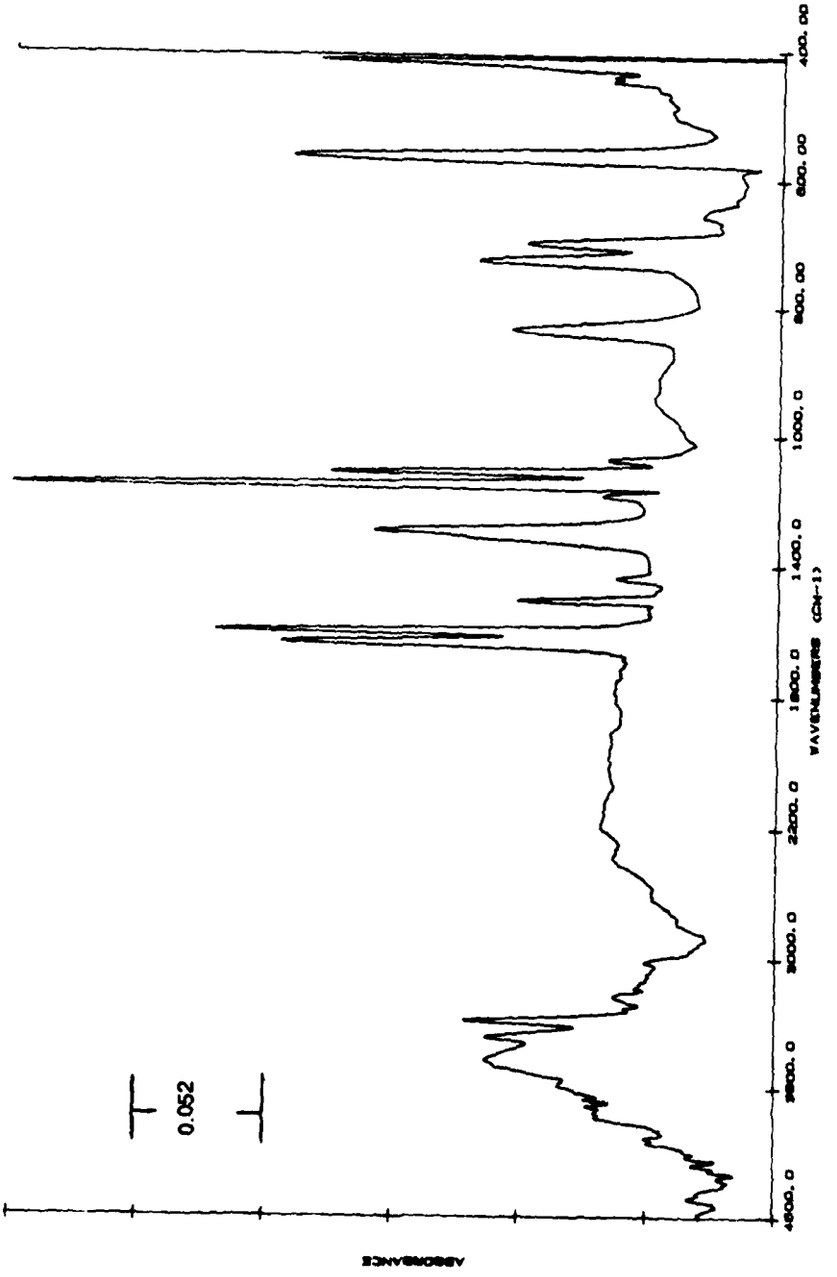

Figure 84. Grazing angle FTIR spectrum of DDS film on ferrotype plates.

with peak positions and assignments listed in Table XXXIX [66,87,128,141,142].

A 0.15 wt% solution of EPON 828/DDS was made in methylene chloride, spun coat onto ferrotype plates and outgassed in a vacuum oven at 25° C for 30 min. Figure 85 is the uncured film with peak positions and assignments listed in Table XL. The epoxy peak at 914 cm^{-1} is clearly present. After the film was cured for one h at 150° C and one h at 210° C another spectrum was attained, as shown in Figure 86. Table XLI lists the peak positions and assignments. The shape of the peak in the epoxide region changed with the peak at 914 cm^{-1} no longer prominent. The peak at 1036 cm^{-1} in the uncured film is diminished in the cured film. The peak at 1630 cm^{-1}, present in the DDS film and in the uncured EPON 828/DDS film disappears after cure, indicating the primary aromatic amine in the DDS has reacted to become a secondary or tertiary aromatic/aliphatic amine.

Figure 87 shows the transmission FTIR spectrum of an EPON 828/DDS film. Table XLII lists the peak positions and assignments. The peak positions match those of the EPON 828/DDS film on ferrotype plate closely, except for the C-O stretch at 1246 cm^{-1} in the neat sample falls at 1258 cm^{-1} in the film. This shift in peak position could indicate an interaction of the epoxy film with the surface, however, the shift may also be due to optical effects.

TABLE XXXIX

Grazing Angle FTIR Peak Positions and Assignments for DDS Films on Ferrotype Plates

DDS (cm^{-1})	Peak Assignment
3626	
3840	N-H asym. str. aromatic
3376	N-H sym. str. aromatic
3235	
3016	aromatic C-H str.
1631	N-H def. prim. aromatic amine
1597	aromatic C-C str.
1503	C-C str. of phenyl ring
1437	
1288	O=S=O asym. str.
1184	
1148	O=S=O sym. str.
1108	
1074	
834	C-H out of plane def.
725	
698	C-H out of plane def.
654	
562	sulfone scissors vib.

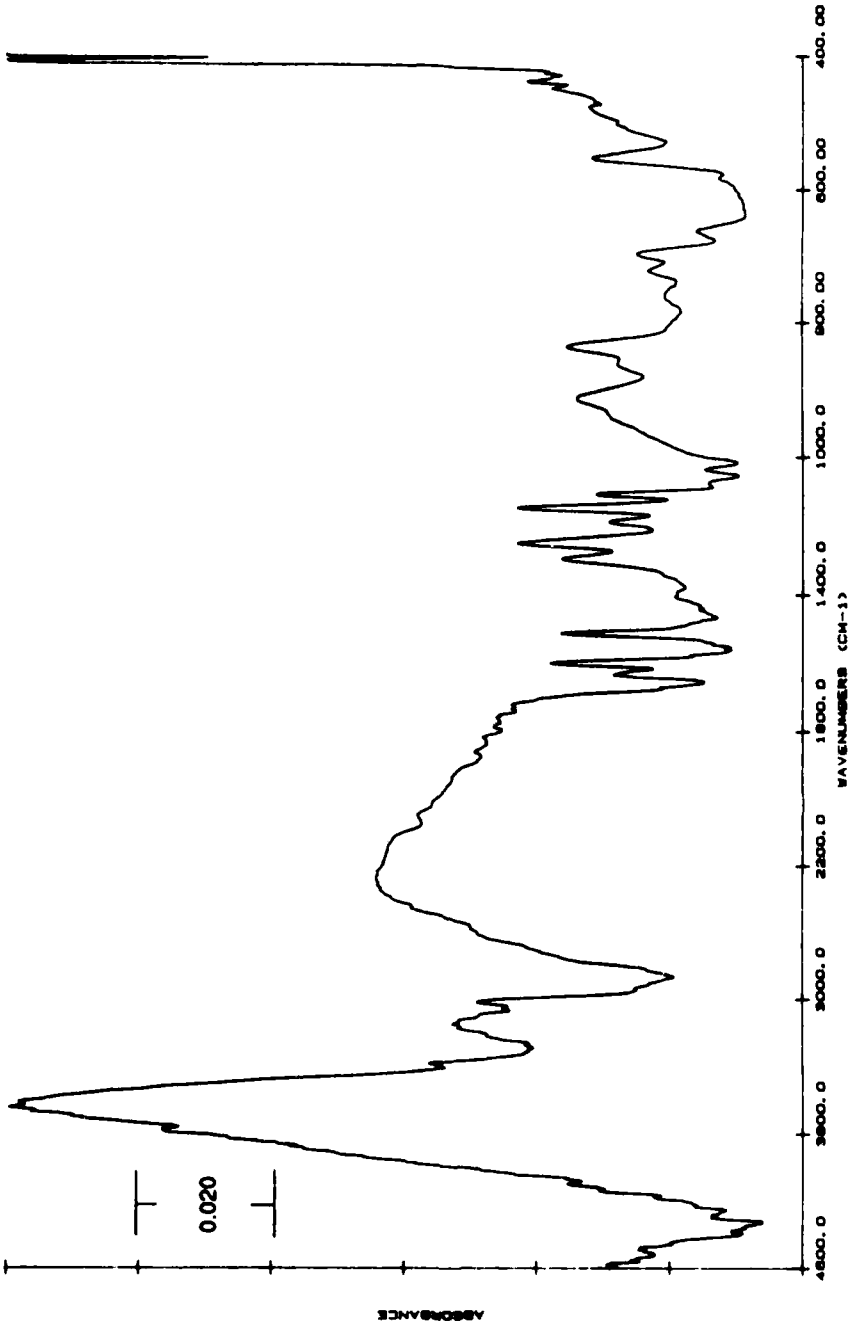

Figure 85. Grazing angle FTIR spectrum of uncured EPON 828/DDS film on ferrotype plates.

TABLE XL

Grazing Angle FTIR Peak Positions and Assignments for Uncured EPON 828/DDS Films on Ferrotype Plates

Uncured EPON828/DDS (cm^{-1})	Peak Assignment
3777	-OH str.
3628	
3381	
3146	
3031	
1630	N-H def. prim. amine, water
1597	aromatic C-C str.
	quadrant str. benzene ring
1508	semicircle str. benzene ring
	C=C str. benzene ring
1398	
1296	-OH in-plane def.
	$-CH_2-$ twisting
	O=S=O asym. str.
1250	aryl-O str.
	C-O-C asym. str.
1188	C-H inplane def.
	C-C str. of Ar-C-Ar
1148	O-S-O sym. str.
1107	
1036	C-O str.
	C-O-C sym. str.
945	
914	asym. epoxy ring vib.
868	
837	out of plane bending of
	p-disubstituted benzene ring
762	
723	
698	C-H out of plane bending
664	
554	sulfone scissors vib.

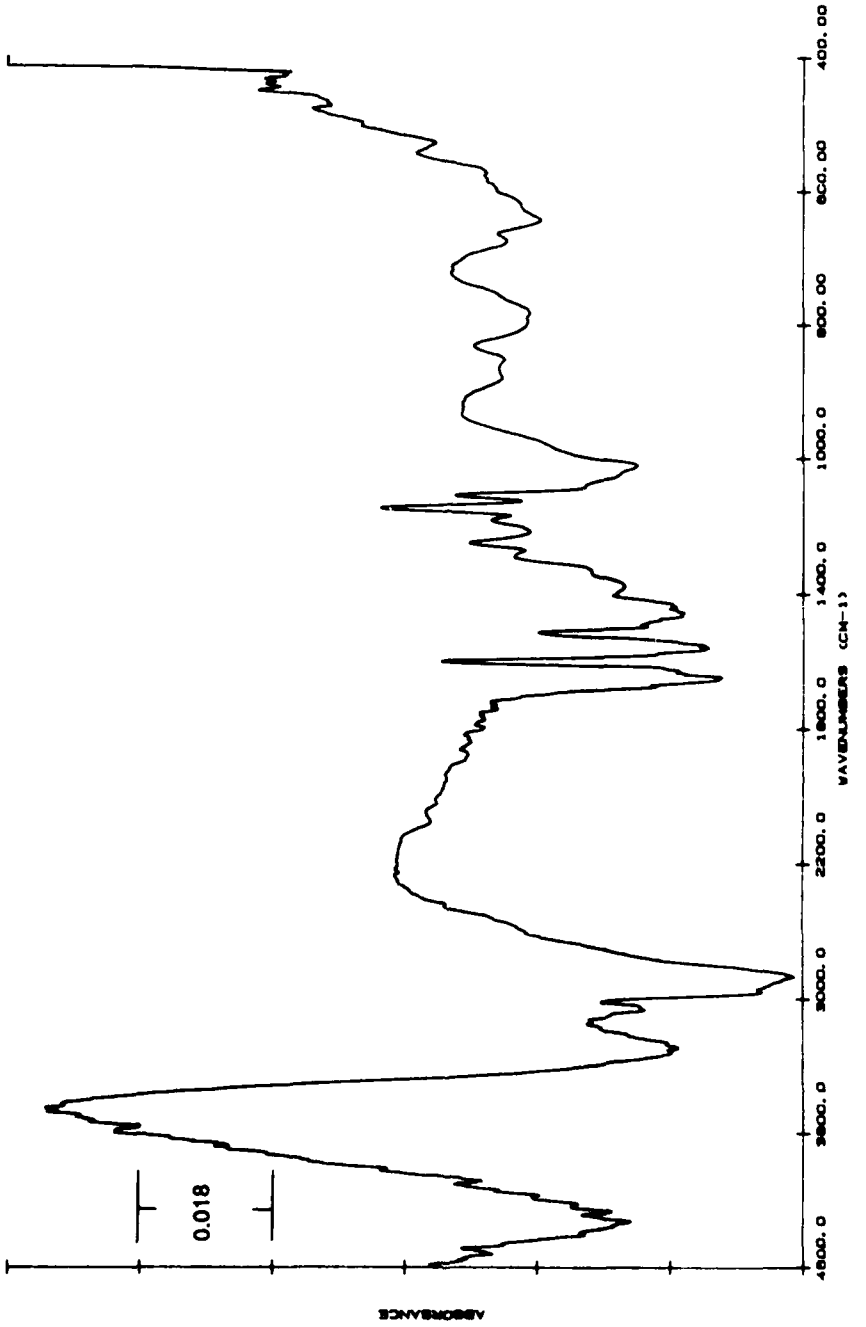

Figure 86. Grazing angle FTIR spectrum of cured EPON 828/DDS film on ferrotype plates.

TABLE XLI

Grazing Angle FTIR Peak Positions and Assignments for Cured EPON 828/DDS Films on Ferrotype Plates

Cured EPON 828/DDS (cm^{-1})	Peak Assignment
3779	-OH str
3642	
3144	
3013	
1598	aromatic C-C str. quadrant str. benzene ring
1512	semicircle str. benzene ring C=C str. benzene ring
1404	
1292	-OH in-plane def. $-CH_2-$ twisting
1250	O=S=O asym str. aryl-O str. C-O-C asym str.
1182	C-H inplane def. C-C str. of Ar-C-Ar
1148	O=S=O sym str.
1109	
926	
866	
833	out of plane bending of p-disubstituted benzene ring
719	
664	

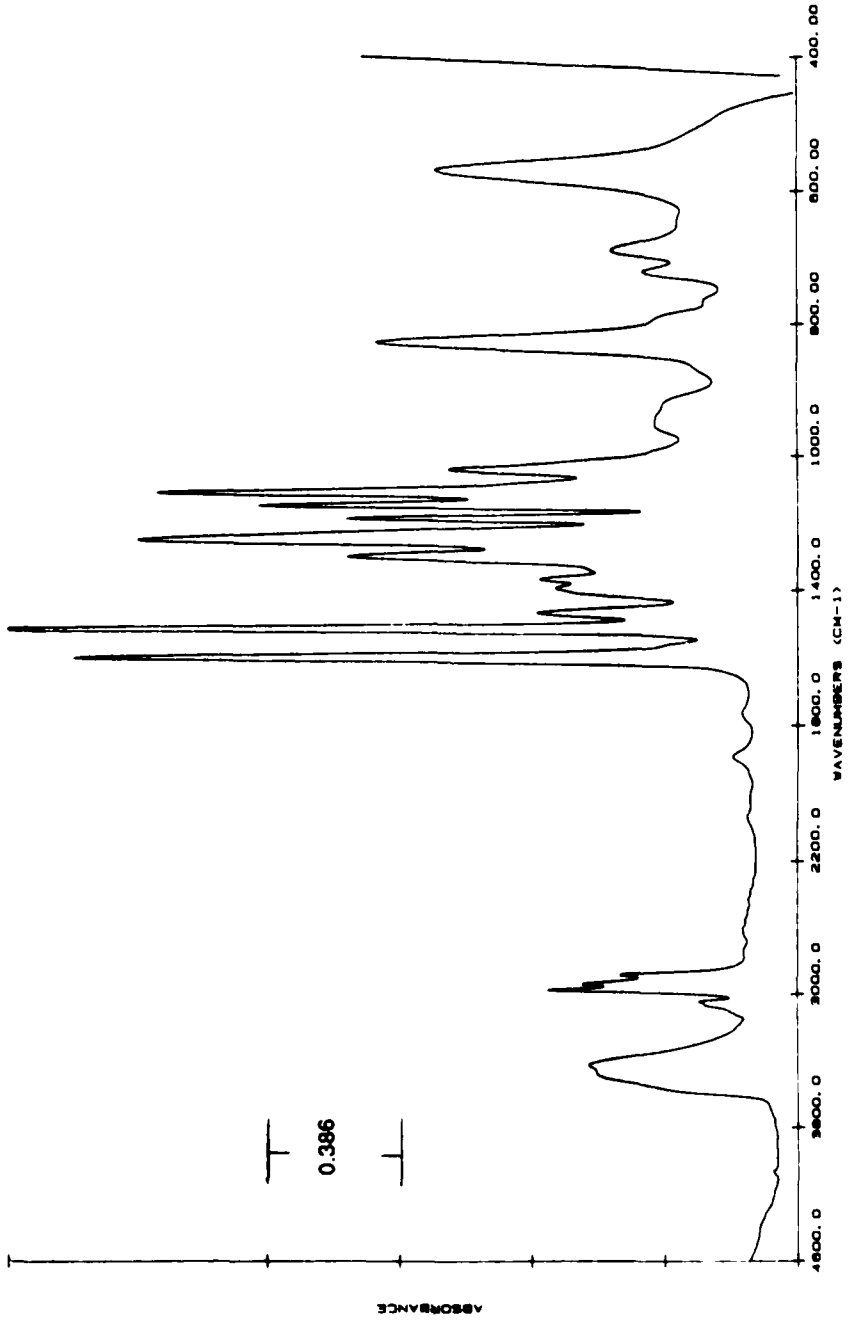

Figure 87. Transmission FTIR spectrum of EPON 828/DDS free-standing film.

TABLE XLII

Transmission FTIR Peak Positions and Assignments for EPON 828/DDS Free Standing Film

EPON828/DDS (cm^{-1})	Peak Assignment
3491	-OH str.
3420	-OH str.
3042	C-H asym. str. CH_3
2969	C-H asym. str. $-CH_2$
2932	C-H sym. str. CH_3
2876	C-H sym. str. $-CH_2$
1595	substituted aromatics
1510	substituted aromatics C=C str. benzene ring
1464	
1391	
1364	methyl gp CH_3 bend of gem-dimethyl
1296	
1246	aryl-O str. C-O-C asym. str.
1182	C-H inplane def. C-C of isopropylidene gp
1144	
1105	phenyl ether
1040	substituted aromatics C-O str. C-O-C sym. str.
953	
916	epoxy gp
827	out of plane bending of p-disubstituted benzene ring
721	
689	
571	

Comparing peak intensities, the peak at 1595 cm^{-1} is smaller than the peak at 1510 cm^{-1} in the transmission spectrum, while the relative intensities are reversed in the film spectrum. The peak at 1040 cm^{-1} is more intense in the transmission spectrum than in the film spectrum. The film spectra are collected under polarized light parallel to the plane of incidence. Those molecules oriented parallel to the surface will not interact strongly with the infrared radiation with an electric vector perpendicular to the sample. Thus, the change in intensities could simply be due to orientation effects of the polymer backbone.

Another interesting feature in comparing the two spectra is the size of the -OH stretch region. The -OH region is shifted to higher wavenumbers and is markedly more intense in the film spectrum compared to the neat transmission spectrum. This enhance peak intensity could be due to the -OH groups orienting perpendicular to the sample surface, both at the EPON 828/ferrotype interface and at the air interface. The orientation of hydroxyl groups perpendicular to the sample surface implies enhanced interaction between the epoxy and the ferrotype surface. While the quality of the spectrum is not as good as the ferrotype substrate spectra, the Ti-6-4 substrate samples show a similar phenomenon where the -OH stretch region is enhanced over the transmission spectrum, as shown in Figure 88.

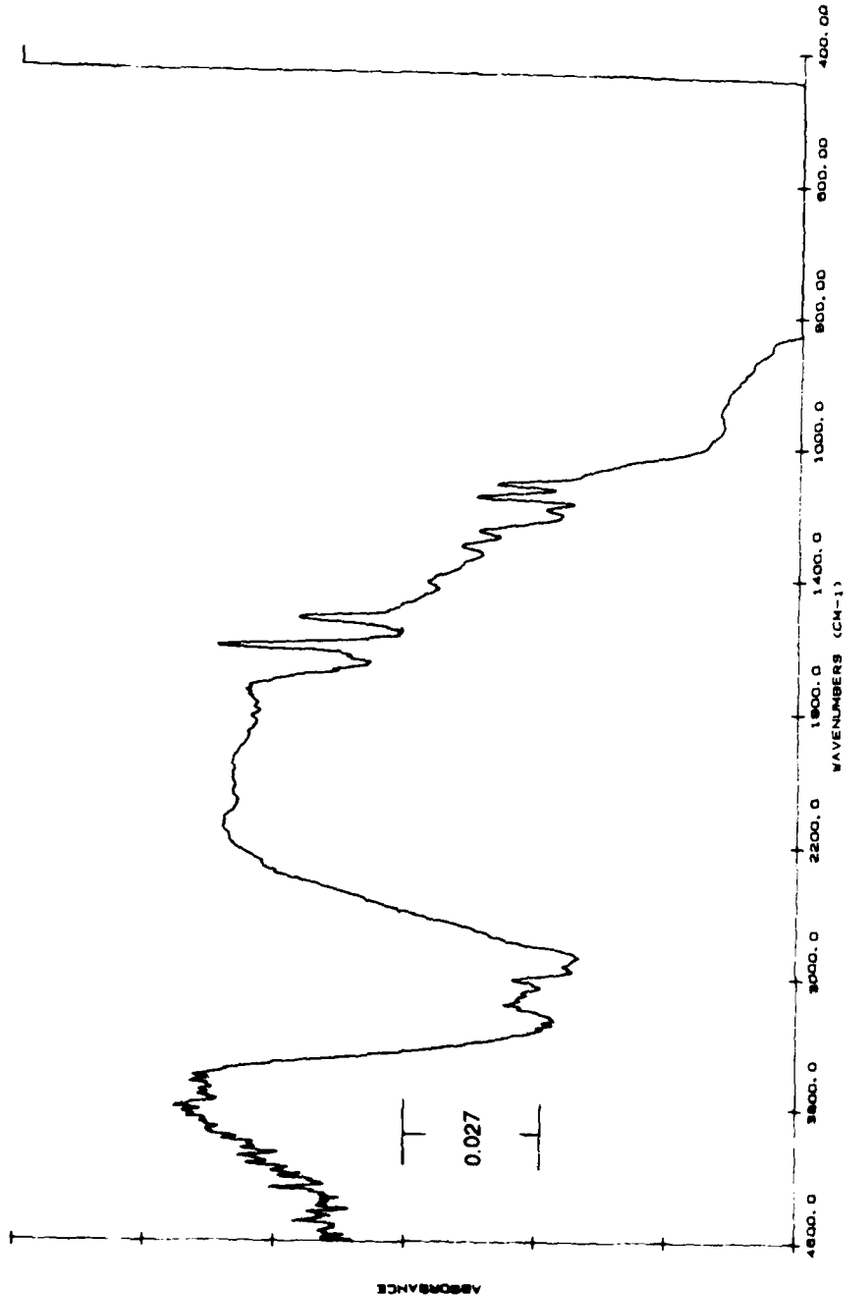

Figure 88. Grazing angle FTIR spectrum of cured EPON 828/DDS film on polished Ti-6-4 plates.

b. **EPON 828 / DDS on E-8385**

Figures 89 and 90 are spectra of ferrotype plate and polished Ti-6-4 as substrates with 1 wt% E-8385 spuncoat on the reflective plates, followed by 0.2 wt% EPON 828/DDS solution spun coat on the E-8385 film. The peak positions and relative intensities of the sandwich films match each other except for the increased intensity of the -OH band in the film on the polished Ti-6-4 and the absence of the band at 1254 cm^{-1}.

Comparing these sandwich film spectra to the EPON 828/DDS film spectra, the peak at 1258 cm^{-1} is present on the EPON film spectra as well. The presence of the aluminum alkoxide masks the epoxide region at 916 cm^{-1}, so that conclusions to the degree of cure cannot be made. Although not exhaustive, this infrared study shows no evidence for chemical reaction between the epoxy and the alkoxide surface. There is, however, a strong -OH stretch in the model epoxy surfaces indicating ample opportunity to hydrogen bonding with the aluminum alkoxide.

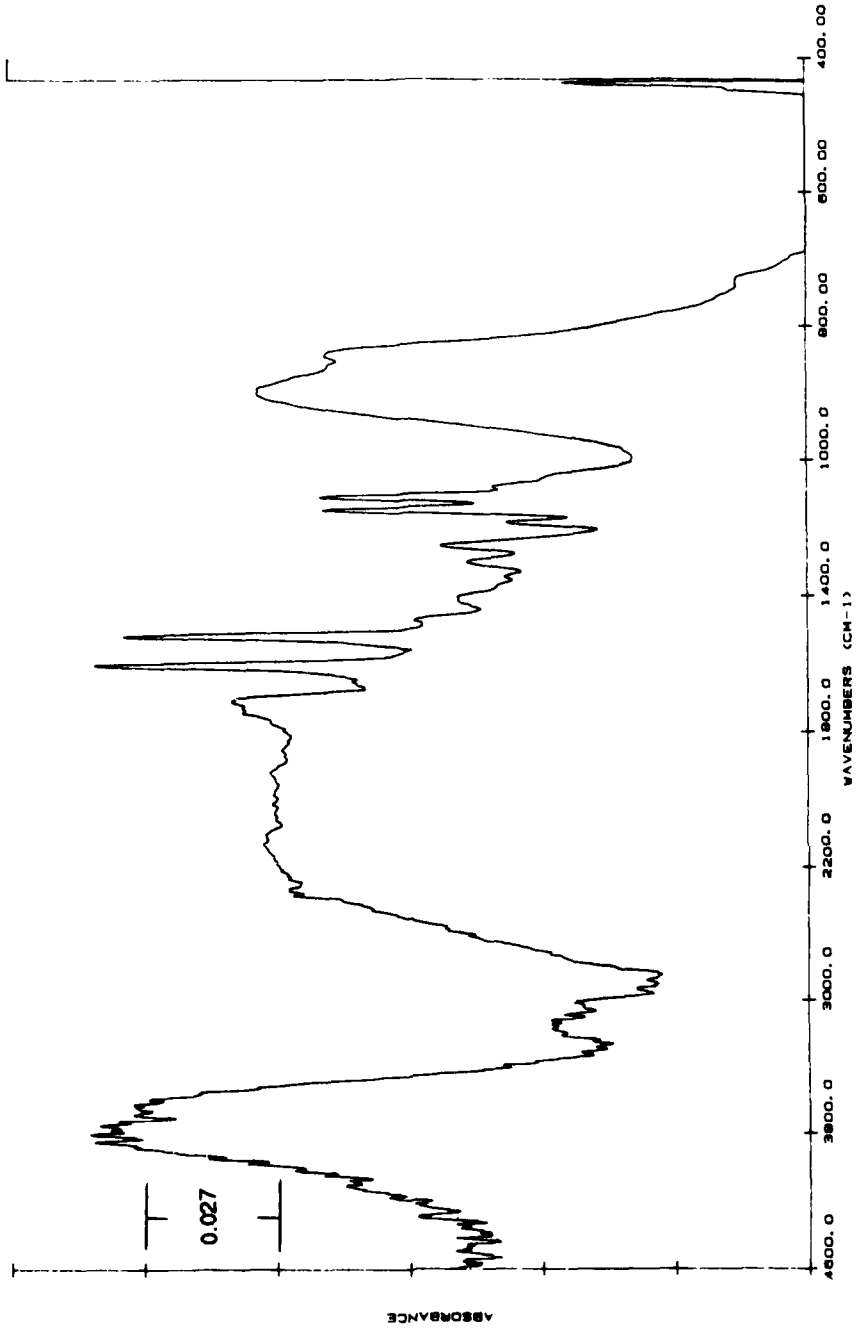

Figure 89. Grazing angle FTIR spectrum of cured EPON 828/DDS film on 1 wt% E-8385 on polished Ti-6-4.

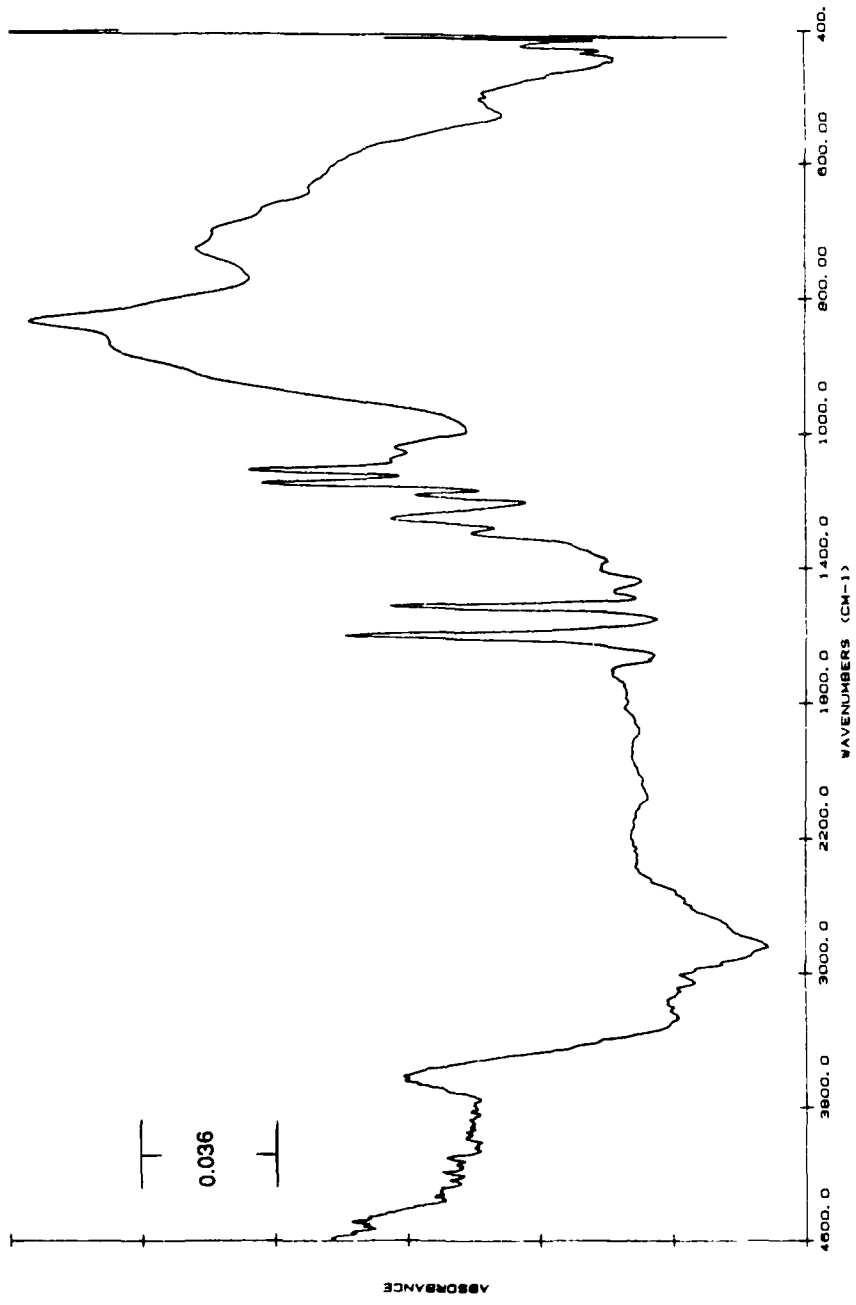

Figure 90. Grazing angle FTIR spectrum of cured EPON 828/DDS film on 1 wt% E-8385 on ferrotype plates.

V. SUMMARY

The four pretreatments used, CAA, SHA, P/F, and TURCO created surface oxides with different properties. The results from profilometry, SEM, and contamination experiments indicate the surface area of the pretreatments in increasing order is P/F << TURCO < CAA = SHA. The acidity/basicity also differed between pretreatments with the order of decreasing acidity CAA > P/F > TURCO > SHA. This apparent acidity/basicity can result from two types of hydroxyls existing on the surface - the acidic bridging hydroxyls and the basic terminal hydroxyls. The acidity/basicity could also be due to low levels of adsorbed etchant or electrolyte, undetectable by surface analysis, but present enough to influence the indicator dye tests. The residuals that could be detected by surface analysis techniques were chemically reproducible, with characteristic elements of fluorine for CAA, phosphorous for P/F, iron and silicon for TURCO and calcium and silicon for SHA.

Adhesive bond testing of these pretreated surfaces by lap shear showed no significant difference between the pretreatments; however, when exposed to hot, wet conditions, there was a profound difference in durability. Thus, the lap shear test is not a surface sensitive technique and should not be used to evaluate surface pretreatments. The locus of failure for the lap shear test samples, while

showing similar strengths, differed. The CAA samples failed within the oxide layer while the P/F and the TURCO samples failed within the epoxy, close to the metal oxide. The locus of failure for the wedge and stress durability tests agreed with each other, but differed from the ambient conditions lap shear test. The environmentally tested samples showed interfacial failure at the epoxy/titanium interface, indicating water destroys the interaction between the epoxy and titanium oxide as predicted thermodynamically. The durability of these pretreatments followed the same trend as the assumed surface areas, namely: CAA = SHA > TURCO >> P/F. Thus the durability is controlled by the area of interaction between the epoxy and surface oxide. These interactions will include acid/base interactions between acidic hydroxyls on the oxide with the amines and ethers in the epoxy and between the basic hydroxyls on the oxide with the hydroxyls in the epoxy.

The metal alkoxides as adhesion promoters showed mixed success. The titanium alkoxides showed no enhancement in bond durability with the titanium alkoxide/epoxy interface being the weak link. The aluminum alkoxide on the other hand showed a striking enhancement in bond durability of the P/F treated bonds indicating a strong bond at both the Ti-6-4/alkoxide and alkoxide/epoxy interfaces. FTIR showed a higher concentration of hydroxyl groups on the surface of

the aluminum alkoxide compared to the titanium alkoxides, therefore, a higher concentration of hydrogen bonding available to interact with the epoxy.

Thus, the surface area of the pretreated Ti-6-4 adherends and the concentration of hydroxyl groups on the surface of the alkoxide primers are the dominant factors which affect the durability of Ti-6-4/FM-300 bonds.

VI. REFERENCES

1. A. J. Kinlock in "Durability of Structural Adhesives", A. J. Kinlock, ed. Applied Science Publishers, London, 1983.

2. W. C. Wake, "Adhesion and the Formulation of Adhesives, 2nd Edition", Applied Science Publishers, London, 1982.

3. F. A. Cotton and G. Wilkinson, "Basic Inorganic Chemistry", John Wiley & Sons, Inc., New York, 1976.

4. R. M. Brick, A. W. Pense, R. B. Gordon, "Structure and Properties of Engineering Materials", 4th Edition, McGraw-Hill Book Company, New York, 1977.

5. F. A. Cotton and G. Wilkinson, "Advanced Inorganic Chemistry, 2nd Edition", Interscience Publishers, New York, 1967.

6. F. Izumi, **Bull. Chem. Soc. Jpn.**, **51**, 1771(1978).

7. H. P. Boehm, in **Adv. Catal.**, D. D. Eley, H. Pines, P. B. Weisz, ed., Vol. 16, Academic Press, New York, 1966.

8. F. Kover and M. J. Musselin, **Thin Solid Films**, 2, 211(1968).

9. A. Navrotsky and O. J. Kleppa, **J. Am. Ceram. Soc.**, 50, 626(1967).

10. T. Mitsuhashi and O. J. Kleppa, **J. Am. Ceram. Soc.**, 62, 356(1979).

11. M. Primet, P. Pichat, M. V. Mathieu, **J. Phys. Chem.**, 75, 1216(1971).

12. M. Shiojiri, T. Miyano, C. Kaito, **Jpn. J. Appl. Phys.**, **18**, 1937(1979).

13. T. R. Hayes and J. F. Evans, **J. Phys. Chem.**, **88**, 1963(1984).

14. Y. Suda, T. Morimoto, M. Nagao, **Langmuir**, 3, 99(1987).

15. T. K. Sham and M. S. Lazarus, **Chem. Phys. Lett.**, **68**, 426(1979).

16. B. M. Ditchek, K. R. Breen, J. D. Venables, "Bondability of Ti Adherends", MML TR-80-17C, Final Report 4/1/79-3/31/80.

16a. M. Ditchek, K. R. Breen, T. S. Sun, J. D. Venables, S. R. Brown, "Bondability of Ti Adherends", 12th National SAMPE Technical Conference, Oct. 7-9, 1980, 882-895.

17. R. F. Wegman, D. W. Levi, "Evaluation of Titanium Prebond Treatments by Stress Durability Testing", 27th National SAMPE Symposium, May 4-6, 440-452 (1982).

18. S. R. Brown, "An Evaluation of Titanium Bonding Pretreatments with a Wedge Test Method", 27th National SAMPE Symposium, May 4-6, 363-376, (1982).

19. A. C. Kennedy, R. Kohler, P. Poole, **Int. J. Adhes. and Adhes.**, 3(2), 133(1983).

20. N. R. Armstrong, R. K. Quinn, **Surf. Sci.**, 67, 451(1977).

21. A. M. Cheng, "Anodic Oxide Formation on Ti-6Al-4V in Chromic Acid for Adhesive Bonding", Virginia Tech Thesis, 1983.

22. J. I. Goldstein, H. Yakowitz, D. E. Newbury, Chapter 1, in "Practical Scanning Electron Microscopy", J. I. Goldstein and H. Yakowitz, ed., Plenum Press, New York, 1975.

23. J. I. Goldstein, Chapter 2, in "Practical Scanning Electron Microscopy", J. I. Goldstein and H. Yakowitz, ed., Plenum Press, New York, 1975.

24. J. I. Goldstein, Chapter 3, in "Practical Scanning Electron Microscopy", J. I. Goldstein and H. Yakowitz, ed., Plenum Press, New York, 1975.

25. D. E. Newbury, Chapter 4, in "Practical Scanning Electron Microscopy", J. I. Goldstein and H. Yakowitz, ed., Plenum Press, New York, 1975.

26. L. D. Peachy, Norelco Reporter, 27, 19, 1980.

27. D. E. Newbury and H. Yakowitz, Chapter 6, in "Practical Scanning Electron Microscopy", J. I. Goldstein and H. Yakowitz, ed., Plenum Press, New York, 1975.

28. A. Miller, Boeing Commercial Airplane Company, personal communication.

29. D. Briggs and M. P. Seah, ed. "Practical Surface Analysis by Auger and X-ray Photoelectron Spectroscopy", John Wiley and Sons, Chichester, 1983.

30. C. D. Wagner, W. M. Riggs, L. E. Davis, J. F. Moulder, "Handbook of X-ray Photoelectron Spectroscopy", G. E. Mullenberg, ed., 1979.

31. D. Briggs, ed, "Handbook of X-ray and Ultraviolet Photoelectron Spectroscopy", Heyden & Son Ltd., London, 1977.

32. S. Kohiki and K. Oki, J. Electron Spectrosc. Relat. Phenom., 33, 375(1984).

33. G. D. Davis, M. Natan, K. A. Anderson, Appl. Surf. Sci., 15, 321(1983).

34. J. S. Solomon and W. L. Baun, Surf. Sci., 51, 228(1975).

35. D. W. Fischer, Phys. Rev. B, Solid State, 5, 4219(1972).

36. S. Thomas, Surf. Sci., 55, 754(1976).

37. C. S. Fadley, R. J. Baird, W. Siekhaus, T. Novakov, S. Å. L. Bergstrom, J. Electron Spectrosc. Relat. Phenom., 4, 93(1974).

38. C. J. Powell and P. E. Larson, Appl. Surf. Sci., 1, 186(1978).

39. R. F. Reilman, A. Msezane, and S. T. Manson, J. Electron Spectrosc. Relat. Phenom., 8, 389(1976).

40. D. R. Penn, J. Electron Spectrosc. Relat. Phenom., 9, 29(1976).

41. M. P. Seah and W. A. Dench, Surf. Interface Anal., 1, 2(1979).

42. C. D. Wagner, L. E. Davis, W. M. Riggs, Surf. Interface Anal., 2, 53(1980).

43. J. C. Ashley and C. L. Lung, Surf. Interface Anal., 4, 52(1982).

44. H. Tokutaka, K. Nishimori, H. Hayashi, Surf. Sci., 149, 349(1985).

45. C. Battistoni, G. Mattogno, E. Paparazzo, Surf. Interface Anal., 7, 117(1985).

46. C. D. Wagner, J. Electron Spectrosc. Relat. Phenom., 32, 99(1983).

47. J. H. Schofield, J. Electron Spectrosc. Relat. Phenom., 8, 129(1976).

48. S. Hofmann, Surf. Interface Anal., 9, 3(1986).

49. A. Benninghoven, CRC Crit. Rev. Solid State Sci., 291, June, 1976.

50. D. E. Newbury, in" Quantitative Surface Analysis of Materials, ASTM STP 643", N. S. McIntyre, ed., American Society for Testing and Materials, 127, 1978.

51. A. Brown and J. C. Vickerman, Surf. Interface Anal., 6, 1(1984).

52. K. W. Allen in "Adhesion 8", Elsevier Scientific Publishing Company, Amsterdam, 1983.

53. J. C. Rivière, Mém. Sci. Rev. Métall., 759, Décembre, 1979.

54. I. D. Ward and M. Strathman, Ind. Res. Dev., 154, September, 1983.

55. J. M. Lang and F. Degrève, Surf. Interface Anal., 7, 53(1985).

56. J. F. Rabek, "Experimental Methods in Polymer Chemistry", John Wiley and Sons, Chichester, 1980.

57. J. R. Dyer, "Applications of Absorption Spectroscopy of Organic Compounds", Prentice-Hall, Inc., New Jersey, 1965.

58. T. Nguyen, Prog. Org. Coat., 13, 1(1985).

59. D. E. Leyden and R. S. Shreedhara Murthy, Spectroscopy, 2, 28(1987).

60. P. R. Griffiths and J. A. deHaseth, "Fourier Transform Infrared Spectrometry", John Wiley & Sons, New York, 1986.

61. R. G. Greenler, **J. Chem. Phys.**, **44**, 310(1966).

62. N. J. Harrick, **Am. Lab.**, 78, November, 1986.

63. J. F. Rabolt, M. Jurich, J. D. Swalen, **Appl. Spectrosc.**, 39, 269(1985).

64. A. Ishitani, H. Ishida, F. Soeda, V. Nagasawa, **Anal. Chem.**, **54**, 682(1982).

65. D. L. Allara, A. Baca, C. A. Pryde, **Macromolecules**, **11**, 1215(1978).

66. G. Socrates, "Infrared Characteristic Group Frequencies", John Wiley and Sons, Chichester, 1980.

67. J. F. Rabolt, F. C. Burns, N. E. Schlotter, J. D. Swalen, **J. Chem. Phys.**, 78, 946(1983).

68. H. Kollek, **Int. J. Adhes. and Adhes.**, 5, 75(1985).

69. A. Zecchina, S. Coluccia, C. Morterra, **Appl. Spectrosc. Rev.**, 21, 259(1985).

70. H. O. Finklea and R. Vithanage, **J. Phys. Chem.**, 86, 3621(1982).

71. M. Primet, J. Basset, M. V. Mathieu, M. Prettre, **J. Phys. Chem.**, **74**, 2868(1970).

72. H. Knozinger and P. Ratnasamy, **Catal. Rev. -Sci. Eng.**, 17, 31(1978).

73. "The Sadtler Standard Spectra", Vol. 34, 33830K, Sadtler Research Laboratory, Philadelphia, 1974.

74. "The Sadtler Standard Spectra", Vol. 16, 15547K, Sadtler Research Laboratory, Philadelphia, 1974.

75. C. T. Lynch, K. S. Mazdiyasni, J. S. Smith, W. J. Crawford, **Anal. Chem.**, 36, 2332(1964).

76. J. V. Bell, J. Heisler, H. Tannenbaum, J. Goldenson, **Anal. Chem.**, **25**, 1720(1953).

77. D. C. Bradley, R. C. Mehrotra, D. P. Gaur, "Metal Alkoxides", Academic Press, London, 1978.

78. C. G. Barraclough, D. C. Bradley, J. Lewis, I. M. Thomas, J. Chem. Soc., 503, 2601(1961).

79. H. H. Zeiss and M. Tsutsui, J. Amer. Chem. Soc., 75, 897(1953).

80. H. W. van der Marel and H. Beutelspacher, "Atlas of Infrared Spectroscopy of Clay Minerals and Their Admixtures", Elsevier Scientific Publishing Company, Amsterdam, 1976.

81. "The Sadtler Standard Spectra", Vol. 48, 47948P, Sadtler Research Laboratory, Philadelphia, 1976.

82. A. J. Maeland, R. C. Rittenhouse, K. Bird, Plat. Surf. Finish., 56, May 1976.

83. B. E. Yoldas, Ceram. Bull., 54, 286(1975).

84. T. Mole and E. A. Jeffrey, "Organoaluminum Compounds", Elsevier, Amsterdam, 1972.

85. H. Lee and K. NeVille, "Handbook of Epoxy Resins", McGraw-Hill Book Company, New York, 1967.

86. T. Nguyen and W. E. Byrd," XIth Int. Cong. Organic Coatings Science and Technology, Proceedings", Greece, 235, July 1985.

87. S. Yoshida and H. Ishida, J. Adhesion, 16, 217(1984).

88. J. Schultz, K. Tsutsumi, J. Donnet, J. Colloid Interface Sci., 59, 272(1977).

89. W. C. Hamilton, J. Colloid Interface Sci., 47, 672(1974).

90. W. C. Hamilton, J. Colloid Interface Sci., 40, 219(1972).

91. A. Carre and J. Schultz, J. Adhesion, 15, 151(1983).

92. J. Schultz, K. Tsutsumi, J. Donnet, J. Colloid Interface Sci., 59, 277(1977).

93. M. E. R. Shanahan, C. Cazeneuve, A. Carrot, J. Schultz, J. chim. phys., 79,n° 3 (1982).

94. F. M. Fowkes, **Ind. Eng. Chem.**, 56, 40(1964).

95. D. K. Owens and R. C. Wendt, J. Appl. Polym. Sci., 13, 1741(1969).

96. S. Wu, **J. Polym. Sci.: Part C**, 34, 19(1971).

97. J. Comyn in "Durability of Structural Adhesives", A. J. Kinlock, ed. Applied Science Publishers, London, 1983.

98. F. M. Fowkes in "Surface Treatments for Improved Performance and Properties", J. J. Burke & V. Weiss, ed., Plenum Publishing Corp., 1982, pp. 75-84.

99. J. C. Bolger, in "Adhesion Aspects of Polymeric Coatings", K. L. Mittal, ed., Plenum Press, New York, 1983.

100. F. M. Fowkes, D. O. Tischler, J. A. Wolfe, L. A. Lannigan, C. M. Ademu-John, M. J. Halliwell, J. **Polym. Sci.: Polym. Chem. Ed.**, 22, 547(1984).

101. K. Tanabe, "Solid Acids and Bases", Academic Press, New York, 1970.

102. C. Walling, **J. Am. Chem. Soc.**, 72, 1164(1950).

103. E. Bányai in "Indicators", E. Bishop, ed., Pergamon Press, Oxford, 1972.

104. D. M. Brewis, J. Comyn, R. J. A. Shalash, **Int. J. Adhes. and Adhes.**, October, 1982.

105. J. P. Sargent, K. H. G. Ashbee, J. **Phys. D**, 14, 1933(1981).

106. W. Brockmann, O. -D. Henneman, H. Kollek, **Int. J. Adhes. and Adhes.**, 33, January, 1982.

107. M. Natan, J. D. Venables, J. **Adhesion**, 15, 125(1983).

108. R. A. Gledhill and A. J. Kinloch, J. **Adhesion**, 6, 315(1974).

109. W. Brockmann, "Xth International Conference in Organic Coatings Science and Technology", July, 1984, Athens, Greece, pp. 11-21.

110. D. L. Hunston and W. D. Bascom, in "ACS Advances in Chemistry Series, No. 208, Rubber Modified Thermoset Resins", C. K. Riew and J. K. Gillham, Ed., 1984.

111. A. V. Pocius, in "Structural Adhesives Chemistry and Technology", S. R. Hartshorn, Ed., Plenum Press, NY, 1986.

112. C. W. Jennings, **J. Adhesion, 4**, 25(1972).

113. D. E. Packham, in "Adhesion Aspects of Polymeric Coatings", K. L. Mittal, Ed., Plenum Press, 1983.

113a. W. Brockmann, O. -D. Hennemann, H. Kollek, "Adhesive Joints", K. L. Mittal, Ed., Plenum Publishing Corporation, 1984.

114. J. A. Marceau, Y. Moji, and J. C. McMilliam, **Adhes. Age**, 28, October, 1977.

115. S. R. Brown and G. J. Pilla, Report No. NADC - 82032-60, March, 1982.

116. M. H. Stone and T. Peet, Technical Memorandum Mat 349, Controller HMSO, London, July, 1980.

117. ASTM Designation: D 1002 - 72, 1973.

118. G. P. Anderson, S. J. Bennett and K. L DeVries, "Analysis and Testing of Adhesive Bonds", Academic Press, New York, 1977.

119. R. A. Pike and F. P. Lamm, Presentation at ACS Meeting, Denver, April 1987.

120. R. A. Pike, **Int. J. Adhes. and Adhes.**, **6**, 21(1986).

121. R. A. Pike, S.A.M.P.E., October, 1985.

122. R. A. Pike, **Int. J. of Adhesion and Adhesives**, 5, 3(1985).

123. B. E. Yoldas, **J. Amer. Cer. Soc.**, 65, 387(19[illegible].

124. B. E. Yoldas, **J. Mater. Sci.**, 21, 1087(19[illegible].

125. B. E. Yoldas, **J. Mater. Sci.**, 14, [illegible].

126. B. E. Yoldas, **Ceram. Bull.**, 54, [illegible].

AD-A189 503 AN INTERDISCIPLINARY APPROACH TO PREDICTIVE MODELING OF 4/4
STRUCTURAL ADHESI..(U) VIRGINIA TECH CENTER FOR
ADHESION SCIENCE BLACKSBURG J A FILBEY ET AL. OCT 87
UNCLASSIFIED CAS/CHEM-87-7 N00014-82-K-0105 F/G 11/1 NL

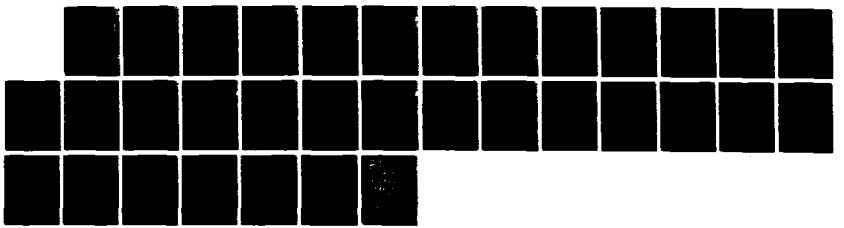

127. R. K. Dwivedi, G. Gowda, J. of Mater. Sci. Lett., 4, 331(1985).

128. H. F. Webster,II, "Characterization of Thin Silicone Films Formed by Migration Across Defined Polymer Substrates", Virginia Tech, Master's Thesis, 1985.

129. H. O. Finklea and J. A. Melendez, Spectroscopy, 1, 47(1986).

130. J. G. Mason, R. Siriwardane, J. P. Wightman, J. Adhesion, 11, 315(1981).

131. H. L. Youmans, "Statistics for Chemistry", Charles E. Merrill Publishing Co., Columbus, Ohio, 1973.

132. R. C. Weast, ed, "Handbook of Chemistry and Physics", 57th edit., CRC Press, Cleveland, Ohio, 1976.

133. E. Roman, M. Sánchez-Avedillo, J. L. de Segovia, Appl. Phys. A, 35, 35(1984).

134. Personal communication, G. Davis, H. Clearfield, K. Shaffer, Martin Marietta Laboratories.

135. J. A. Skiles and J. P. Wightman, "Chromic Acid Anodized Ti-6Al-4V: Its characterization and its single lap bond strength to heat resistant adhesives", Summary Report, Va Tech, June, 1987.

136. H.-P. Boehm, Angew. Chem. Internat. Edit., 5(6), 533(1966).

137. M. Natan, J. D. Venables, "Bondability of Ti Adherends", MML TR-82-20C, Final Report 8/15/81-8/15/82.

138. D. K. Shaffer, H. M. Clearfield, J. S. Ahearn, "Surface and Interface Characterization for High-Temperature Adhesive Systems", MML TR-86-47c, Quarterly Report No. 3, June, 1986.

139. Personal communication, D. LeFebvre, Virginia Tech and C. Matz, MBB Transport Aircraft.

140. BASIC program written by L. H. Arney, Jr.

141. S. C. Lin, B. J. Bulkin, E. M. Pearce, J. of Polym. Sci.: Polym. Ed., 17, 3121(1979).

142. J. Comyn, A. J. Kinlock, C. C. Herley, R. R. Mallik, D. P. Oxley, R. G. Pritchard, S. Reynolds, C. R. Werrett, J. Adhesion, 12, 171(1981).

APPENDIX A

Chromic Acid Anodization (CAA)

1. Gritblast with an Econoline gritblaster at approximately 100 psi and held approximately 5 cm from the coupon.
2. Wipe the coupons with methyl ethyl ketone, MEK.
3. Soak in sodium hydroxide solution (13g/250ml) at 70° C for 5 min.
4. Rinse three times in deionized water.
5. Pickling step: Immerse in pickle solution (15 ml conc. HNO_3, 3 ml 49% w/w HF, 82 ml H_2O.
6. Rinse three times in deionized water.
7. Anodize in room temperature for 20 min at 10 V, 26.9 amp/m^2 (2.5 amp/ft^2) in a chromic acid solution (50 g/1000 ml) with Ti-6-4 as the cathode. 49% w/w HF is added to attain the desired current density.
8. Rinse three times in deionized water, soaking for 5 min in the final rinse.
9. Blow dry with prepurified nitrogen gas until visibly dry.

Phosphate/Fluoride Etch (P/F)

1. Gritblast as above.
2. Wipe with MEK.
3. Soak in Sprex AN-9 or Super Terj solution (30 g/1000 ml) at 80° C for 15 min.
4. Rinse three times in deionized water.
5. Immerse in pickle solution (31 ml 49% w/w HF, 213 ml conc HNO_3/1000 ml) at room temperature for 2 min.
6. Rinse three times in deionized water.
7. Soak in phosphate fluoride solution (50.5 g Na_3PO_4, 20.5 g KF, 29.1 ml 49% w/w HF/1000 ml) at room temperature for 2 min.
8. Rinse three times in deionized water.
9. Soak in deionized water at 65° C for 15 min.
10. Blow dry as above.

TURCO Basic Etch (TURCO)

1. Gritblast as above.
2. Wipe with MEK.
3. Soak in TURCO 5578 solution (37.6 g/1000 ml) at 70° - 80° C for 5 min.
4. Rinse three times in deionized water.
5. Soak in TURCO 5578 solution (360 g/1000 ml) at 80° - 100° C for 10 min.
6. Rinse three times in deionized water.
7. Soak in deionized water at 60° - 70° C for 2 min.
8. Blow dry as described above.

Sodium Hydroxide Anodization (SHA)

1. Gritblast as above.
2. Rinse with methanol or acetone.
3. Immerse in Super Terj solution (30 g/1000 ml) at 80° C for 15 min.
4. Rinse three times in deionized water.
5. Soak in water at 50° - 60° C for 15 min.
6. Anodize at 20° C for 30 min at 10 V in 5.0M sodium hydroxide solution with Ti-6-4 as cathode. The current density is not controlled.
7. Rinse in running tap water for 20 min.
8. Blow dry as above.

TABLE B-I

XPS Analysis of CAA Pretreated Ti-6-4

Sample	Element	B.E.(ev)	A.P.
CAA	C	285.	38
Poly Sci	O	530.2	40
	Ti	458.8	16
	F	684.8	2.6
CAA	C	285.	59
KRATOS	O	530.3	31
	Ti	458.8	7.8
	F	684.7	2.1
CAA	C	285.	61
KRATOS	O	530.5	30
	Ti	459.0	7.6
	F	685.3	1.2
CAA	C	285.	60
KRATOS	O	530.7	29
	Ti	459.1	7.4
	F	685.6	2.1
	Al	74.9	1.6
CAA	C	285.	36
KRATOS	O	530.4	44
	Ti	458.9	14
	F	684.8	4.8
CAA	C	285.	41
KRATOS	O	530.3	43
	Ti	458.8	13
	F	684.9	2.9
CAA	C	285.	52
KRATOS	O	530.3	36
	Ti	459.9	11
	F	685.3	1.8
CAA	C	285.	48
KRATOS	O	530.3	37
	Ti	458.7	11
	F	684.7	3.2
CAA	C	285.	44
PHI	O	530.2	40
	Ti	458.8	12
	F	684.8	3.8

TABLE B-II

XPS Analysis of P/F Pretreated Ti-6-4

Sample	Element	B.E.(ev)	A.P.
P/F	C	285.	44
Poly Sci	O	530.4	39
	Ti	458.6	12
	P	132.6	2.2
P/F	C	285.	59
KRATOS	O	529.9	32
	Ti	458.3	6.4
	P	132.8	2.2
P/F	C	285.	56
KRATOS	O	530.7	35
	Ti	459.0	7.7
	P	133.4	1.8
P/F	C	285.	59
KRATOS	O	530.1	30
	Ti	458.7	8.4
	P	133.1	1.3
	Si	105.4	1.1
	N	400.5	0.8
P/F	C	285.	31
KRATOS	O	530.2	53
	Ti	458.8	13
	P	133.2	3.3
P/F	C	285.	40
KRATOS	O	529.7	46
	Ti	458.3	12
	P	133.0	1.4
P/F	C	285.	35
PHI	O	530.4	50
	Ti	458.8	13
	P	133.5	2.4

TABLE B-III

XPS Analysis of TURCO Pretreated Ti-6-4

Sample	Element	B.E.(ev)	A.P.
TURCO Poly Sci	C	285.	61
	O	529.0	30
	Ti	458.4	4.1
	Si	103.6	4.5
TURCO KRATOS	C	285.	55
	O	530.3	33
	Ti	458.5	3.5
	Si	103.7	7.5
	Fe	714.7	1.1
TURCO KRATOS	C	285.	62
	O	530.2	28
	Ti	458.7	4.8
	Si	104.3	3.1
	Fe	710.8	1.3
TURCO KRATOS	C	285.	45
	O	530.1	33
	Ti	458.6	5.6
	Si	105.1	18
	Fe	711.8	0.8
	Pb	137.9	0.2
TURCO KRATOS	C	285.	45
	O	529.8	43
	Ti	458.1	7.2
	Si	104.1	4.7
	Fe	710.4	TR
TURCO PHI	C	285.	43
	O	530.4	47
	Ti	458.8	8.3
	Fe	711.5	2.1

TABLE B-IV

XPS Analysis of SHA Pretreated Ti-6-4

Sample	Element	B.E.(ev)	A.P.
SHA	C	285.	31
KRATOS	O	529.9	46
	Ti	458.3	8.1
	F	688.5	0.8
	Si	102.8	8.5
	P	133.2	1.4
	Ca	347.1	3.8
SHA	C	285.	30
PHI	O	530.3	48
	Ti	458.7	11
	Si	102.9	5.5
	Ca	347.3	5.8

TABLE B-V

XPS Analysis of PSHA Pretreated Ti-6-4

Sample	Element	B.E.(ev)	A.P.
PSHA	C	285.	37
KRATOS	O	530.5	45
	Ti	458.8	11
	F	689.1	1.4
	Si	102.3	1.4
	P	133.7	1.9
	Ca	347.4	2.8
PSHA	C	285.	38
PHI	O	530.3	46
	Ti	458.7	11
	Si		TR
	Ca	347.4	5.7

TABLE B-VI

SIMS Results for CAA Pretreated Ti-6-4 Surface

Mass/Charge	+ SIMS Assignment
16	O^+
19	F^+
23	Na^+
24	C_2^+, Ti^{++}
27	Al^+
28	N_2^+
39	NaO^+
43	AlO^+
46	Ti^+
47	Ti^+, TiH^+
48	Ti^+, TiH^+
49	Ti^+, TiH^+
50	Ti^+, TiH^+
51	TiH^+, V^+
52	Cr^+
56	CaO^+
62	TiO^+
63	TiO^+, $TiOH^+$
64	TiO^+, $TiOH^+$
65	TiO^+, $TiOH^+$
66	TiO^+, $TiOH^+$
67	$TiOH^+$, VO^+, TiF^+
68	CrO^+
69	
80	TiO_2^+

TABLE B-VII

SIMS Results for P/F Pretreated Ti-6-4 Surface

Mass/Charge	+ SIMS Assignment
16	O^+
19	F^+
23	Na^+
24	C_2^+, Ti^{++}
27	Al^+
28	N_2^+
29	
32	O_2^+
39	NaO^+, K^+
40	Ar^+, Ca^+
41	
43	AlO^+
44	SiO^+
46	Ti^+
47	Ti^+, TiH^+
48	Ti^+, TiH^+
49	Ti^+, TiH^+
50	Ti^+, TiH^+
51	TiH^+, V^+
52	
54	
56	CaO^+
62	TiO^+
63	TiO^+, $TiOH^+$
64	TiO^+, $TiOH^+$
65	TiO^+, $TiOH^+$
66	TiO^+, $TiOH^+$
67	$TiOH^+$, VO^+

TABLE B-VII, continued

SIMS Results for P/F Pretreated Ti-6-4 Surface

Mass/Charge	+ SIMS Assignment
68	
69	
70	
75	AlO_3^+
78	TiO_2^+
79	TiO_2^+, TiO_2H^+
80	TiO_2^+, TiO_2H^+
81	TiO_2^+, TiO_2H^+
82	TiO_2^+, TiO_2H^+
83	VO_2^+, TiO_2H^+
91	
96	TiO_3^+

TABLE B-VIII

SIMS Results for TURCO Pretreated Ti-6-4 Surface

Mass/Charge	+ SIMS Assignment
16	O^+
23	Na^+
27	Al^+
28	N_2^+
40	Ar^+, Ca^+
44	SiO^+
46	Ti^+
47	Ti^+, TiH^+
48	Ti^+, TiH^+
49	Ti^+, TiH^+
50	Ti^+, TiH^+
51	TiH^+, V^+
52	
54	
56	Fe^+, CaO^+
57	
62	TiO^+
63	TiO^+, $TiOH^+$
64	TiO^+, $TiOH^+$
65	TiO^+, $TiOH^+$
66	TiO^+, $TiOH^+$
67	$TiOH^+$, VO^+
72	FeO^+
80	TiO_2^+, TiO_2H^+

TABLE B-IX

SIMS Results for SHA Pretreated Ti-6-4 Surface

Mass/Charge	+ SIMS Assignment
7	N^{++}
14	N^{+}
16	O^{+}
20	HF^{+}, Ca^{+}
23	Na^{+}
24	C_2^{+}, Ti^{++}
25	
26	
27	Al^{+}
28	N_2^{+}, Si^{+}
29	
30	
39	NaO^{+}, K^{+}
40	Ar^{+}, Ca^{+}
41	
42	
43	AlO^{+}
44	SiO^{+}
45	
46	Ti^{+}
47	Ti^{+}, TiH^{+}
48	Ti^{+}, TiH^{+}
49	Ti^{+}, TiH^{+}
50	Ti^{+}, TiH^{+}
51	TiH^{+}, V^{+}
56	CaO^{+}
57	
58	

TABLE B-IX, continued

SIMS Results for SHA Pretreated Ti-6-4 Surface

Mass/Charge	+ SIMS Assignment
59	
60	SiO_2^+
62	TiO^+
63	TiO^+, $TiOH^+$
64	TiO^+, $TiOH^+$
65	TiO^+, $TiOH^+$
66	TiO^+, $TiOH^+$
67	$TiOH^+$, VO^+
72	CaO_2^+
80	TiO_2^+
88	CaO_3^+

TABLE B-X

SIMS Results for PSHA Pretreated Ti-6-4 Surface

Mass/Charge	+ SIMS Assignment
7	N^{++}
16	O^{+}
20	HF^{+}, Ca^{++}
23	Na^{+}
24	C_2^{+}, Ti^{++}
25	
26	
27	Al^{+}
28	N^{+}, $_2Si^{+}$, AlH^{+}
39	NaO^{+}, K^{+}
40	Ar^{+}, Ca^{+}
41	
42	
43	AlO^{+}
44	SiO^{+}, $AlOH^{+}$
45	
46	Ti^{+}
47	Ti^{+}, TiH^{+}
48	Ti^{+}, TiH^{+}
49	Ti^{+}, TiH^{+}
50	Ti^{+}, TiH^{+}
51	TiH^{+}, V^{+}
56	CaO^{+}
57	
59	

TABLE B-X, continued

SIMS Results for PSHA Pretreated Ti-6-4 Surface

Mass/Charge +	SIMS Assignment
60	SiO_2^+
62	TiO^+
63	TiO^+, $TiOH^+$
64	TiO^+, $TiOH^+$
65	TiO^+, $TiOH^+$
66	TiO^+, $TiOH^+$
67	$TiOH^+$, VO^+
80	TiO_2^+

TABLE B-XI

SIMS Results for TiO_2 Powder

Mass/Charge	+ SIMS Assignment
16	O^+
23	Na^+
26	
27	
32	O_2^+
39	NaO^+, K^+
40	Ar^+, Ca^+
46	Ti^+
47	Ti^+, TiH^+
48	Ti^+, TiH^+
49	Ti^+, TiH^+
50	Ti^+, TiH^+
51	TiH^+
56	CaO^+
62	TiO^+
63	TiO^+, $TiOH^+$
64	TiO^+, $TiOH^+$
65	TiO^+, $TiOH^+$
66	TiO^+, $TiOH^+$
67	$TiOH^+$
78	TiO_2^+
80	TiO^+, $TiOH^+$
81	TiO^+, $TiOH^+$
113	
115	In^+

TABLE B-XII

XPS Analysis of Heating Study for CAA Pretreated Ti-6-4

Sample	Element	B.E.	A.P.	FWHM
CAA	C	285	36.	
Coupon	O	530.4	44.	
25° C	Ti	458.9	14.	1.5
	F	684.8	4.8	
CAA	C	285	41.	
Coupon	O	530.3	43.	
25° C	Ti	458.8	13.	1.5
	F	684.4	2.9	
CAA	C	285	38.	
Foil	O	530.4	43.	
25° C	Ti	458.8	14.	1.6
	F	684.9	2.8	
	Al	74.0	3.1	
CAA	C	285	25.	
Foil	O	530.4	50.	
25° C	Ti	459.0	17.	1.7
	F	685.0	5.2	
	Al	74.5	3.2	
CAA	C	285	42.	
Coupon	O	530.7	43.	
340° C	Ti	459.2	14.	1.5
	F	685.3	1.7	
CAA	C	285	32.	
Coupon	O	530.9	43.	
450° C	Ti	459.4	22.	1.8
	F	685.8	2.6	

TABLE B-XII, continued

XPS Analysis of Heating Study for CAA Pretreated Ti-6-4

Sample	Element	B.E.	A.P.	FWHM
CAA	C	285	18.	
Foil	O	530.8	52.	
450° C	Ti	459.4	19.	1.8
	F	685.4	6.0	
	Al	74.6	5.2	
CAA	C	285	38.	
Foil	O	530.9	44.	
450° C	Ti	459.4	11.	1.8
	F	685.5	4.2	
	Al	119.6	3.1	
CAA	C	285	23.	
Foil	O	530.8	49.	
450° C	Ti	459.3	18.	1.8
	F	685.4	6.0	
	Al	74.8	4.2	

TABLE B-XIII

XPS Analysis of Heating Study for PSHA Pretreated Ti-6-4

Sample	Element	B.E.	A.P.	FWHM
PSHA	C	285	24.	
Foil	O	530.7	51.	
25° C	Ti	459.0	13.	1.6
	Ca	347.8	6.1	
	P	133.9	1.2	
	Si	102.4	1.5	
	Mg	89.4	1.0	
	Al	74.4	3.1	
PSHA	C	285	18.	
Foil	O	530.9	55.	
25° C	Ti	459.3	12.	1.7
	Ca	347.9	7.7	
	P	134.4	3.1	
	Si	102.2	1.9	
	Al	74.5	1.8	
PSHA	C	285	22.	
Foil	O	530.7	54.	
450° C	Ti	459.3	15.	1.6
	Ca	347.9	6.6	
	F	685.3	1.2	
	Si	102.3	2.0	
PSHA	C	285	24.	
Foil	O	530.8	55.	
450° C	Ti	459.3	12.	1.6
	Ca	347.7	6.2	
	F	685.1	1.1	
	Si	102.3	1.8	
PSHA	C	285	19.	
Foil	O	531.0	51.	
450° C	Ti	459.3	13.	1.7
	Ca	348.0	8.3	
	P	133.9	3.5	
	Si	102.8	3.0	
	Al	75.1	2.2	

TABLE B-XIV

XPS Analysis of Heating Study for P/F Pretreated Ti-6-4

Sample	Element	B.E.	A.P.	FWHM
P/F	C	285	26.	
Coupon	O	530.2	45.	
25° C	Ti	458.8	12.	1.5
	P	133.2	2.8	
	Na	61.8	14.	
P/F	C	285	28.	
Foil	O	530.5	53.	
25° C	Ti	458.9	14.	1.7
	P	133.3	3.5	
	N	400.5	1.2	
P/F	C	285	24.	
Foil	O	530.4	55.	
25° C	Ti	459.0	16.	1.8
	P	133.6	2.4	
	Al	74.0	2.0	
P/F	C	285	23.	
Coupon	O	530.6	39.	
450° C	Ti	457.4	15.	5.2
	P	133.5	1.7	
	Na	61.4	22.	
P/F	C	285	23.	
Foil	O	530.8	52.	
450° C	Ti	459.3	22.	4.4
	P	133.9	1.6	
	F	685.1	1.2	
	Al	119.3	0.8	
P/F	C	285	61.	
Foil	O	530.7	27.	
450° C	Ti	459.0	9.7	3.7
	P	133.7	1.4	
	Al	74.3	1.8	
P/F	C	285	19.	
Foil	O	530.8	58.	
450° C	Ti	459.2	17.	3.0
	P	133.9	3.1	
	Al	74.7	3.5	

TABLE B-XV

XPS Analysis of Heating Study for TURCO Pretreated Ti-6-4

Sample	Element	B.E.	A.P.	FWHM
TURCO	C	285	36.	
Coupon	O	530.1	47.	
25° C	Ti	458.6	6.6	1.5
	Si	105.1	8.9	
	Fe	711.8	1.9	
	Pb	137.9	0.1	
TURCO	C	285	30.	
Coupon	O	530.5	48.	
350° C	Ti	458.9	12.	2.2
	Si	105.2	8.8	
	Fe	709.6	1.6	
	Pb	138.7	0.1	
TURCO	C	285	38.	
Foil	O	530.3	44.	
25° C	Ti	458.6	5.3	2.6
	N	397.2	9.1	
	Fe	711.1	3.0	
	S	169.0	0.7	
TURCO	C	285	29.	
Foil	O	530.2	58.	
25° C	Ti	458.7	9.3	1.8
	Fe	711.1	2.5	
	Al	73.5	1.7	
TURCO	C	285	36.	
Foil	O	530.6	44.	
450° C	Ti	459.0	17.	3.0
	Fe	709.9	1.5	
	Al	118.9	2.0	
TURCO	C	285	83.	
Foil	O	531.4	11.	
450° C	Ti	459.1	2.4	Broad
	N	396.8	1.9	
	Al	74.1	1.9	
TURCO	C	285	26.	
Foil	O	530.5	54.	
450° C	Ti	458.9	14.	2.2
	Fe	709.6	4.0	
	Al	74.4	2.4	

TABLE B-XVI

XPS Analysis of Lap Shear Failure Surfaces

Sample	Element	B.E.(ev)	A.P.
CAA	C	285	57.
MFS	O	530.4	30.
	Ti	458.8	8.8
	F	684.8	0.7
	N	400.0	2.9
CAA	C	285	56.
AFS	O	530.6	21.
	Ti	459.2	8.4
	F	685.0	12.
	N	401.8	3.1
CAA	C	285	69.
MFS	O	530.8	25.
	Ti	459.2	5.2
	Al	75.0	1.5
CAA	C	285	61.
AFS	O	531.2	20.
	Ti	459.8	5.8
	F	686.1	9.7
	Al	75.6	2.2
	N	400.5	2.2
CAA	C	285	59.
MSS	O	530.0	32.
	Ti	458.4	7.6
	Al	74.0	1.4
P/F	C	285	95.
MFS	O	533.0	2.8
	Br	70.1	1.9
P/F	C	285	96.
AFS	O	533.4	3.9
	Br	TR	

TABLE B-XVI, Continued

XPS Analysis of Lap Shear Failure Surfaces

Sample	Element	B.E.(ev)	A.P.
TURCO	C	285	91.
MFS	O	533.0	4.8
	Br	70.7	0.8
	N	399.6	1.0
	Si	101.8	2.4
TURCO	C	285	91.
AFS	O	533.0	4.7
	Br	70.5	0.9
	N	399.1	1.1
	Si	102.0	2.6
CAA	C	285	90.
with	O	533.2	8.1
Soak	F	689.8	0.3
MFS	Br	70.3	0.7
	Si	103.2	1.1
CAA	C	285	88.
with	O	533.3	8.0
Soak	F	689.0	1.2
AFS	Br	71.7	0.4
	N	400.3	0.7
	Si	103.3	1.6
CAA	C	285	79.
with	O	533.2	17.
Soak	Ti	460.1	1.9
MSS	Br	69.9	0.8
	N	401.1	2.2

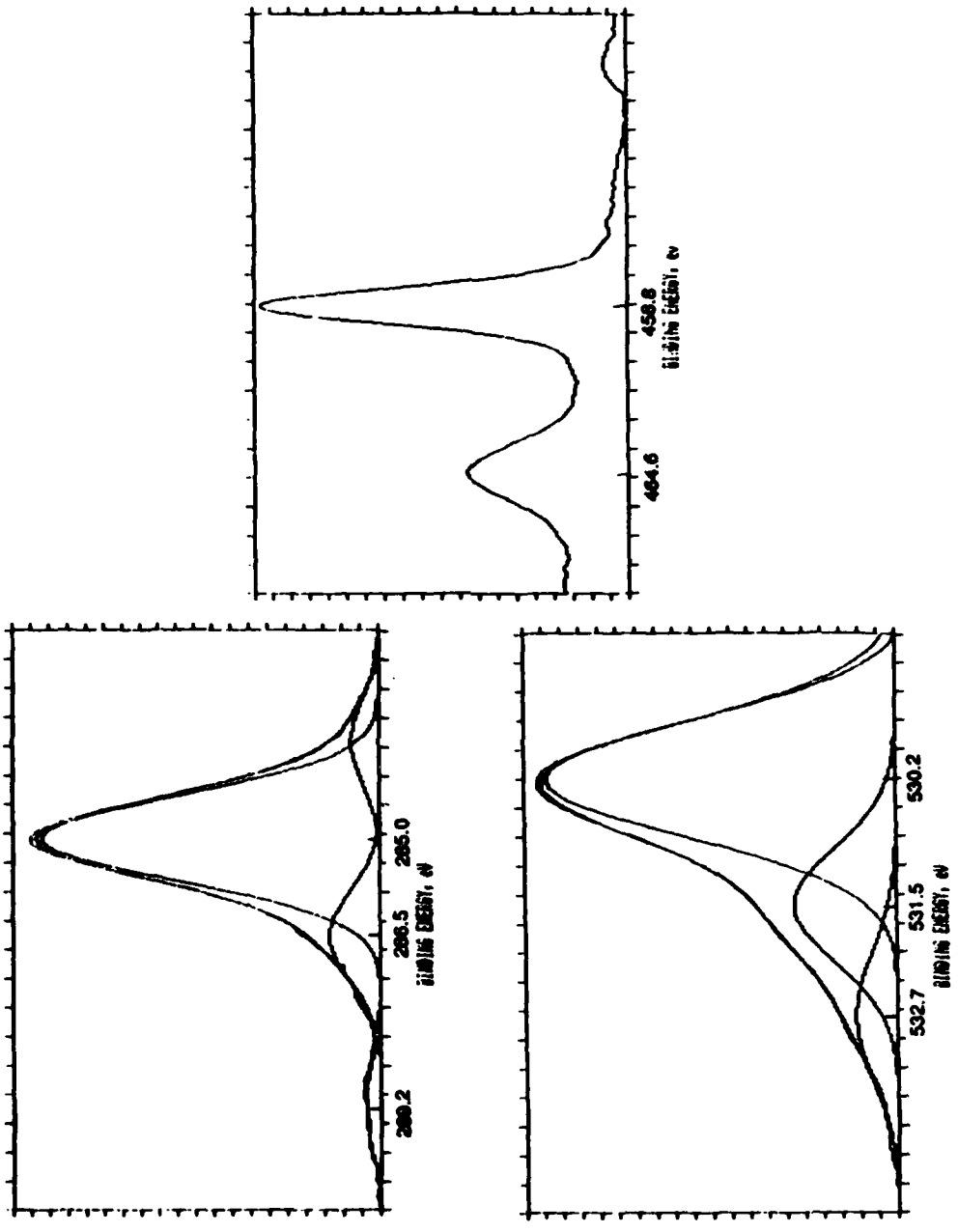

Figure C1. Representative spectra of C 1s, O 1s and Ti 2p peaks from a CAA pretreated surface.

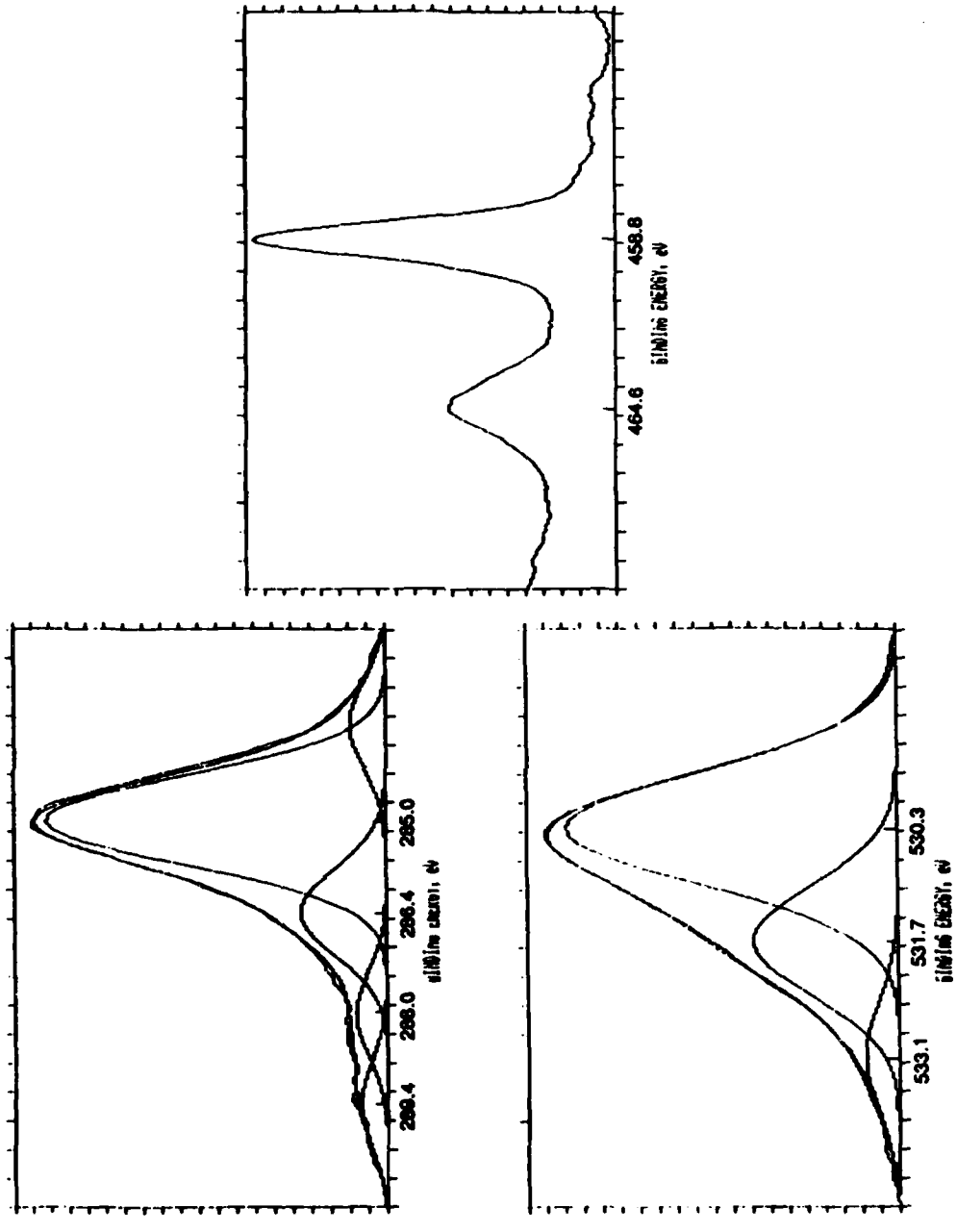

Figure C2. Representative spectra of C 1s, O 1s and Ti 2p peaks from a P/F pretreated surface.

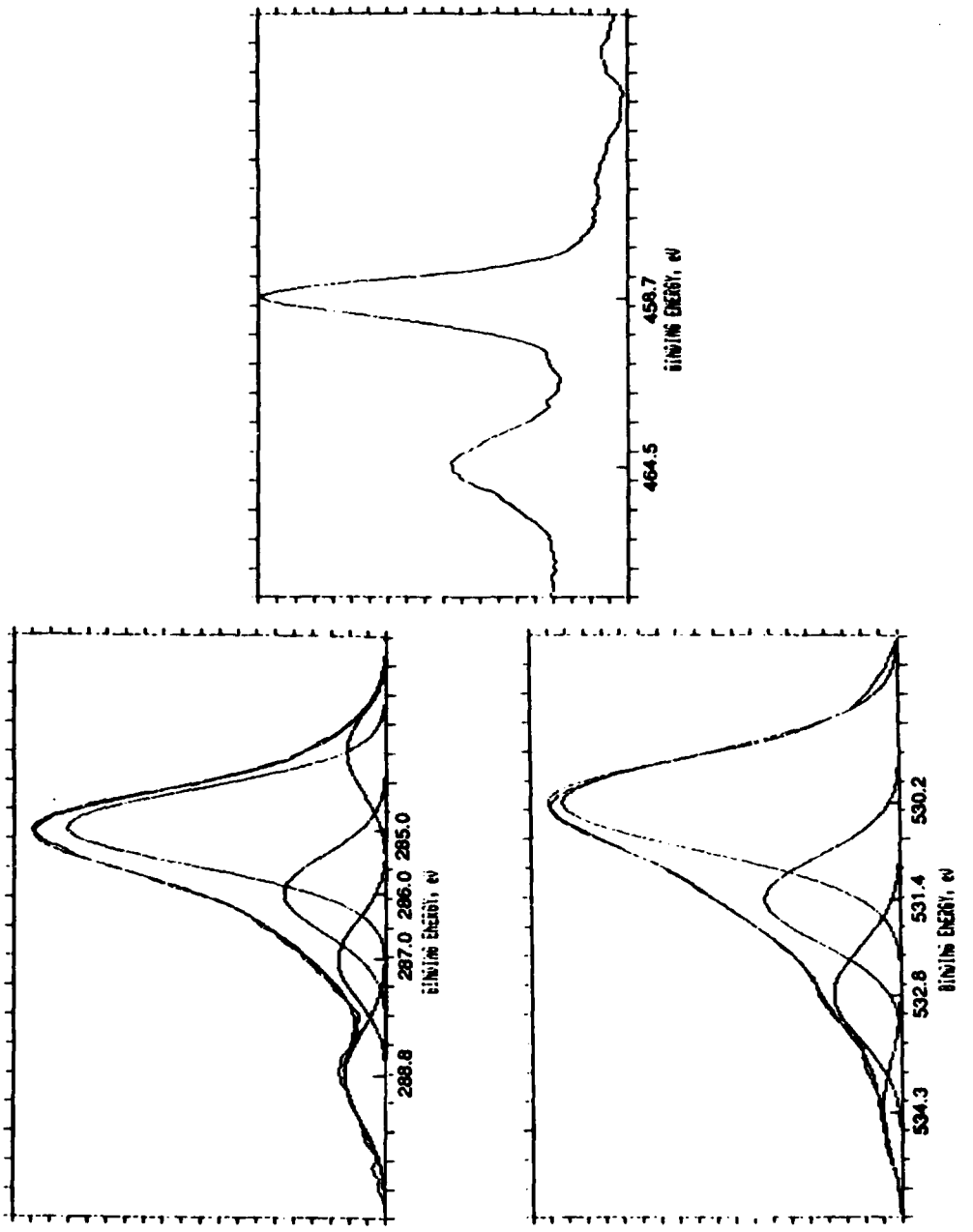

Figure C3. Representative spectra of C 1s, O 1s and Ti 2p peaks from a TURCO pretreated surface.

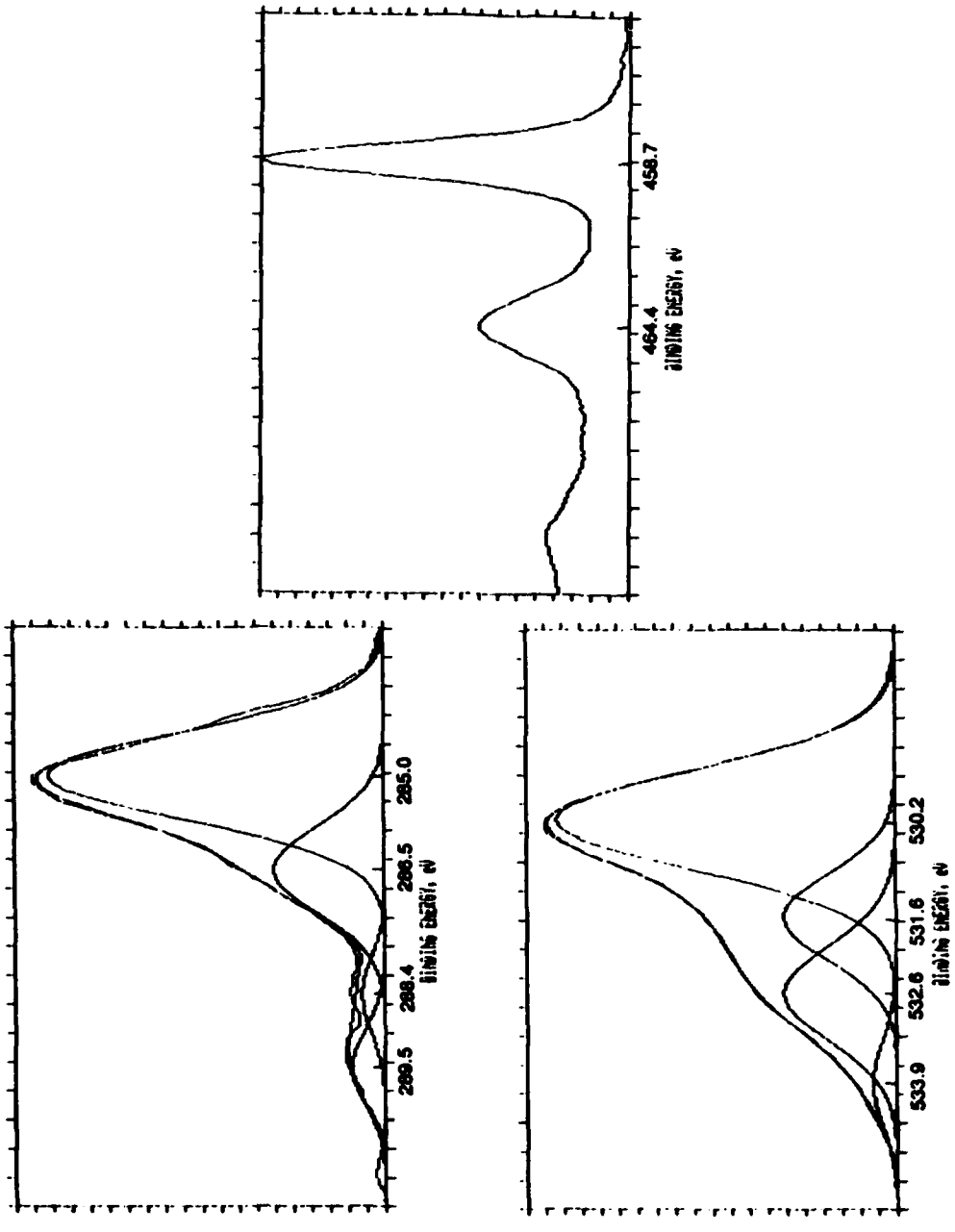

Figure C4. Representative spectra of C 1s, O 1s and Ti 2p peaks from a SHA pretreated surface.

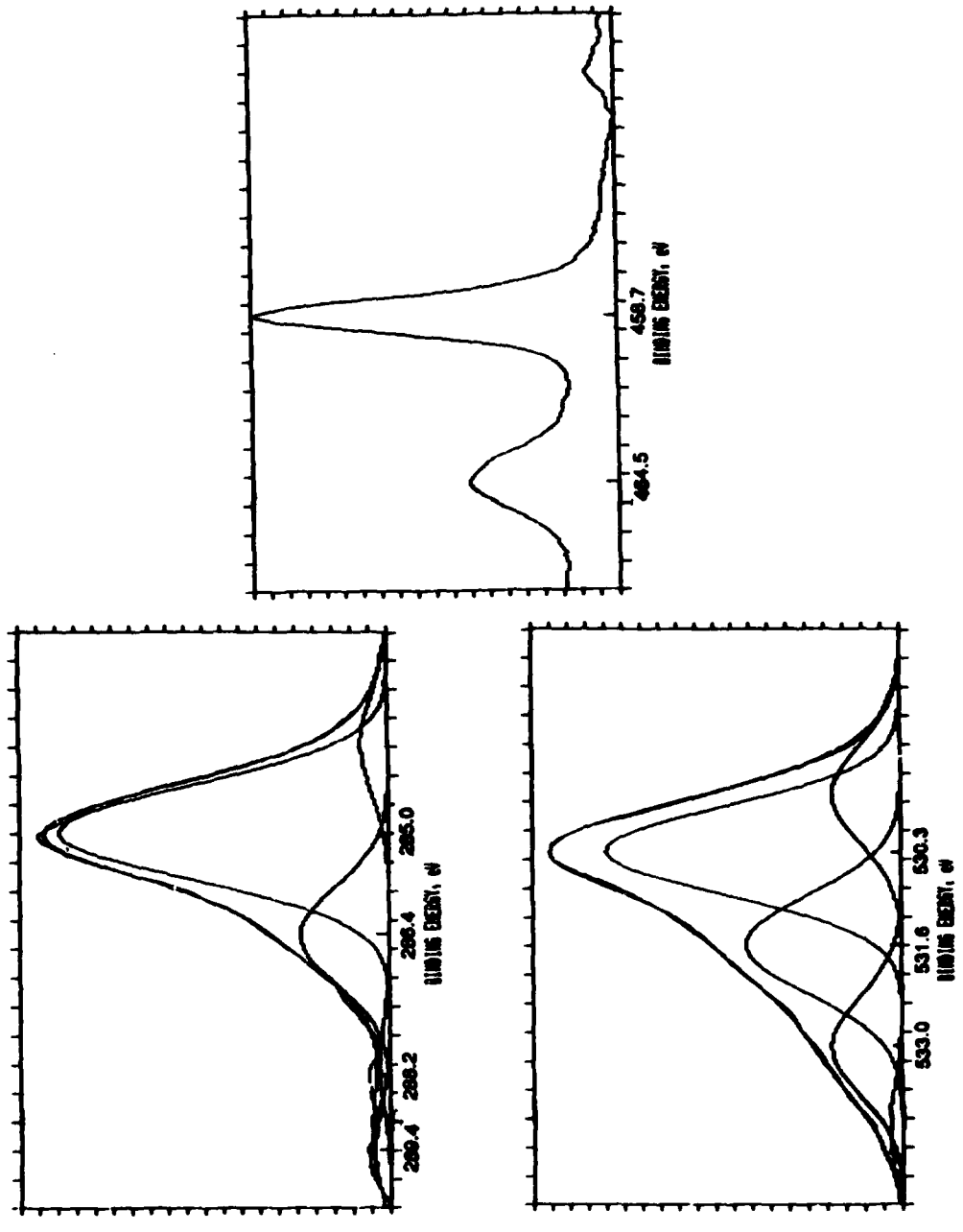

Figure C5. Representative spectra of C 1s, O 1s and Ti 2p peaks from a PSHA pretreated surface.

APPENDIX D

```
10      REM    ARXOPT2  12-5-86
25      REM   FOR AL OXIDE OVERLAYER, MFP = 100
30      PRINT "ENTER SAMPLE NAME"
35      INPUT D$
60      REM   FOR EACH SAMPLE, ENTER AP(AL)/AP(CR) FOR EACH
              ANGLE AS A()
61      REM   MAKE SURE THERE IS A CORRESPONDING ANGLE IN
              LINE 80 T()
62      REM   AT LINE 220, ALLOW FOR NUMBER OF ANGLES
70      A(1) = 2.85 : A(2) = 4.46 : A(3) = 6.48
80      T(1) = 90*π/180 : T(2) = 30*π/180 : T(3) = 10*π/180
90      ZMIN = 99999
100     FOR I = 25 TO 200 STEP 5
101     REM   I = THICKNESS IN ANGSTROMS
110     FOR J = .7 TO 1 STEP .05
111     REM   J = GAMMA % COVERAGE
120     REM   Z = (I-25)^2 + (J-64)^2
130     GOSUB 200
140     IF Z < ZMIN THEN ZMIN = Z : XMIN = I : VMIN = J :
        PRINT ZMIN, XMIN, YMIN
150     NEXT J : NEXT I
152     OPEN 1,4
154     PRINT#1,D$
160     PRINT#1, "MIN VALUE:"; ZMIN; "THICKNESS="; XMIN; " &
        GAMMA="; YMIN
162     PRINT#1:CLOSE1
164     PRINT "MIN VALUE:"; ZMIN; "THICKNESS="; XMIN; " &
        GAMMA="; YMIN
165     IF XMIN = 25 OR XMIN = 200 OR YMIN = .7 THEN PRINT
        "CAUTION - RESET LIMITS!'
170     STOP
200     REM   SUBROUTINE THAT RETURNS A MINIMUM Z VALUE
201     REM
210     Z=0
220     FOR K = 1 TO 3
225     E = EXP (-I/(100 * SIN(T(K))))
226     REM   [CR] = 0.055,  [AL] = 0.0343
230     AC = 90.055*J*(1-E))/(0.0343*(1-J+J*E))
240     Z = Z + ABS(AC-A(K))
250     NEXT K
260     RETURN
```

AD-A189 503

BIBLIOGRAPHIC DATA SHEET	1. Report No.	2.	3. Recipient's Accession No.

4. Title and Subtitle: Summary Report
An Interdisciplinary Approach to Predictive Modeling of Structural Adhesive Bonding - Factors Affecting the Durability of Titanium/Epoxy Bonds

5. Report Date: November 1987

6.

7. Author(s): Filbey, J. A. and Wightman, J. P.

8. Performing Organization Rept. No. CAS/CHEM-87-7

9. Performing Organization Name and Address
Virginia Polytechnic Institute and State University
Center for Adhesion Science and
Department of Chemistry
Blacksburg, VA 24061

10. Project/Task/Work Unit No.

11. Contract/Grant No.: N00014-82-K-0185

12. Sponsoring Organization Name and Address
Office of Naval Research
800 N. Quincy St.
Arlington, VA 22217

13. Type of Report & Period Covered

14.

15. Supplementary Notes

16. Abstracts

Factors influencing the durability of Ti-6-4/epoxy and Ti-6-4/metal alkoxide/epoxy interphases were studied by first determining chemical and physical properties of Ti-6-4 adherend surfaces; second by characterizing the strength and durability of Ti-6-4/epoxy bonds; and third by using aluminum and titanium alkoxides as possible adhesion promoters.

Ti-6-4 adherend surfaces were oxidized either by chemical etch or anodization. Four principal pretreatments were studied: Chromic acid anodization (CAA), sodium hydroxide anodization (SHA), phosphate fluoride acid etch (P/F), and TURCO basic etch (TURCO). The oxides were characterized physically by SEM, STEM, profilometry, and contact angles; and chemically by XPS, AES, SIMS, and indicator dyes. The two anodically produced oxides were porous, with pore diameters of 40 to 50 nm, while P/F and TURCO pretreated adherends showed no porosity. Good reproducibility of oxide composition was seen by XPS. The acidity/basicity of the surfaces was found to be in

(Abstract continued on attached Sheet)

17. Key Words and Document Analysis. 17a. Descriptors

17b. Identifiers/Open-Ended Terms

17c. COSATI Field Group

18. Availability Statement	19. Security Class (This Report)	21. No. of Pages
Unlimited	UNCLASSIFIED	296
	20. Security Class (This Page) UNCLASSIFIED	22. Price

Abstract continued

order of increasing basicity CAA < P/F <TURCO < SHA

All adhesive bonding was done with a structural epoxy, FM-300. Lap shear strengths showed no significant difference between pretreatments, reinforcing the opinion that the lap shear test is not surface sensitive. The stress durability and wedge test, however, showed vast differences in bond durability. The SHA and CAA pretreatments were equally durable in 80° C, 95% r.h. The TURCO pretreatment was slightly less durable than the P/F pretreatment which exhibited no durability in hot-wet environments. The characterization results point to the surface area of contact between the adhesive and adherend as the reason for variation in bond durability. CAA and SHA pretreated Ti-6-4 adherends were porous and thus possessed the highest surface area. TURCO was the roughest surface and therefore had a higher surface area than the smoother P/F surface.

Because the P/F surface was not durable, it was chosen as the substrate for testing the possible durability enhancement by titanium and aluminum alkoxide coatings. Sec-butyl aluminum alkoxide significantly enhanced the bond durability of the P/F pretreated bonds, while the titanium alkoxide primers showed no improvement in durability. The locus of failure and infrared studies indicate the enhancement in durability by the aluminum alkoxide was due to the high concentration of hydroxyl groups in the alkoxide available to interact with the titanium oxide and the epoxy.

END

DATE

FILMED

MARCH

1988

DTIC